INSTITUTE OF LOW TEMPERATURE AND STRUCTURE RESEARCH
POLISH ACADEMY OF SCIENCES

Wrocław Doctoral School
of Institutes of Polish
Academy of Sciences

Doctoral dissertation

Polymorphism in lead halides comprising protonated methylhydrazine: hybrid organic-inorganic compounds with tunable structural and optoelectronic properties

Polimorfizm w halogenkach ołowiu zawierających protonowaną metylohydrazynę: organiczno-nieorganiczne związki hybrydowe o przestrajalnych właściwościach strukturalnych i optoelektronicznych

In the form of a thematically consistent series of articles published in scientific journals

mgr inż. Dawid Drozdowski

Supervisor: dr hab. Anna Gągor, prof. INTiBS PAN

Wrocław, 2024

Acknowledgments

Chciałbym serdecznie podziękować:

promotorce – Ani Gągor oraz prof. Mirosławowi Mączce za nieocenione
wsparcie, mentoring oraz umożliwienie realizacji badań i samorozwoju

współpracownikom z projektu i badań wszelakich, za wartościowe i rzeczowe dyskusje

koleżankom i kolegom z Oddziału Badań Strukturalnych, za bezcenną pomoc
w rozwiązywaniu problemów natury krystalograficznej i nie tylko

Panu dr. Damianowi Szymańskiemu za rzetelne pomiary analizy składu chemicznego
oraz niemniej rzetelne dyskusje na temat stanu polskiej piłki

mojej wspaniałej rodzinie, przyjaciołom (pozdrawiam *Szymony*), znajomym
oraz wszystkim osobom, które przyczyniły się do powstania owej pracy

oraz, *last but not least*, mojej ukochanej małżonce Kasi, która najlepiej zna moje
doktoranckie przeżycia i zawsze okazuje ogrom wsparcia i miłości.

Niniejszą pracę pragnę **zadedykować** mojemu dziadkowi Władysławowi
(pisząc ową dedykację w dzień jego urodzin), którego jednym z marzeń jest,
by móc zwracać się do mnie per *Panie Doktorze* :)

The research presented herein was supported by the National Science Centre in Poland under the OPUS 18 project (2019/35/B/ST5/00043).

NATIONAL SCIENCE CENTRE
POLAND

Table of Contents

1. Abstract

In recent years hybrid organic-inorganic perovskites (HOIPs) based on lead halides gained substantial interest in materials science and industry due to exceptional properties, such as high power conversion and quantum efficiencies, long carrier diffusion lengths, etc. combined with costly efficient synthesis. However, their potential for applications is limited by several factors, including high vulnerability to moisture or chemicals, resulting in rapid degradation. As the unique properties of molecular lead halides arise directly from the intermolecular interactions and depend on the crystal composition, the attention of researchers is increasingly directed toward new analogs by substituting the A- B-, and X- sites in the perovskite ABX_3 structure.

The family of lead halide HOIPs has been recently expanded with compounds comprising methylhydrazinium (MHy^+) cation. The crystal structure of $MHyPbX_3$ perovskites (X = Br, Cl) consists of a three-dimensional (**3D**) network of corner-sharing PbX_6 octahedra, which are heavily distorted due to interactions with MHy^+ cations situated within the voids. Unlike their counterparts, $MHyPbX_3$ crystallize in noncentrosymmetric, polar space groups, thus opening the possibilities for observations of nonlinear optical and ferroic features. MHy^+ has also been found to act as a spacer in MHy_2PbX_4 (X = Br, I) two-dimensional (**2D**) HOIPs. The current state of the art on MHy-based lead halide hybrids calls for developing new compounds using the A- and X-site compositional engineering.

The effects of substitution and alloying of the A and X sites on crystal structure and selected optoelectronic properties are described in six articles (**D1** – **D6**). In **D1**, halide-alloying introduced to $MHyPbBr_xCl_{3-x}$ **3D** HOIPs prompts the stabilization of both high-temperature polymorphs of single-halide analogs and enables tuning of bandgap value, ionic conductivity, and the characteristics of photoluminescence bands. The same approach is used in **D2** for $MHy_2PbBr_{4-x}I_x$ **2D** HOIPs, inducing a rich polymorphism driven by the temperature and halides contribution. In **D3**, layered MHy_2PbCl_4 is characterized. This compound shows a unique sequence of temperature-induced polymorphs, starting from high-temperature centrosymmetric, intermediate modulated, and low-temperature polar phase. The concurrence of MHy^+ and imidazolium cation in **D4** promotes a formation of **2D** perovskites with (110)-oriented layers, featuring a profound tilting arising from interactions with organic cations. Finally, articles **D5** and **D6** describe the hybrid compounds of lower dimensionality of octahedra connections, i.e., $MHyPbI_3$ **1D** compound with parallel double-chains, and $Cs_2MHy_2PbX_6$ (X = Br, I) **0D** analog with isolated octahedra, respectively.

2. Streszczenie

Organiczno-nieorganiczne związki halogenków ołowiu o strukturze perowskitu zyskują w ostatnich latach coraz większą popularność w nauce oraz przemyśle ze względu na ich unikalne właściwości m.in. wysoką wydajność konwersji energii, wydłużone drogi dyfuzji nośników ładunku oraz niski koszt i łatwość otrzymywania. Potencjał aplikacyjny jest jednak ograniczony przez wysoką wrażliwość tych materiałów na działanie wilgoci i związków chemicznych, co przekłada się na obniżoną stabilność opartych na nich urządzeń. Właściwości fizykochemiczne perowskitów hybrydowych wynikają bezpośrednio z budowy (wymiarowości) struktury nieorganicznej oraz oddziaływań między częścią molekularną i nieorganiczną, w związku z tym są determinowane składem kryształu. Dlatego coraz więcej uwagi poświęca się poszukiwaniu nowych analogów stosując podstawienia chemiczne w pozycjach A, B oraz X w trójwymiarowej strukturze perowskitu opisanej wzorem ABX_3.

Do wąskiej grupy kationów organicznych, mogących stabilizować strukturę perowskitu w halogenkach ołowiu, należy kation metylohydrazyniowy (MHy^+). Struktura krystaliczna $MHyPbX_3$ (X = Br, Cl) zbudowana jest z trójwymiarowej (**3D**) sieci połączonych narożami oktaedrów PbX_6, które cechują się silną dystorsją ze względu na oddziaływania z kationami MHy^+ obsadzającymi przestrzenie między oktaedrami. Perowskity $MHyPbX_3$ wyróżniają się spośród innych 3D HOIPs krystalizacją w układach niecentrosymetrycznych, stwarzając tym samym możliwość obserwacji efektów optyki nieliniowej oraz właściwości ferroicznych. MHy^+ krystalizuje również w układach **2D** o wzorze MHy_2PbX_4 (X = Br, I), w których znajduje się w przestrzeniach między warstwami oktaedrów. Dotychczasowe wyniki wskazują na duży potencjał otrzymania nowych związków hybrydowych halogenków ołowiu na bazie MHy^+ o unikalnych właściwościach poprzez modyfikację składu chemicznego w pozycjach A lub X.

Wpływ podstawiania halogenków i obecności dwóch jonów na pozycji A lub X na strukturę krystaliczną oraz na wybrane właściwości optoelektroniczne opisano w sześciu artykułach (**D1** – **D6**) stanowiących treść niniejszej rozprawy. W artykule **D1** dotyczącym serii związków **3D** o wzorze $MHyPbBr_xCl_{3-x}$, obecność dwóch halogenków pozwala na stabilizację faz wysokotemperaturowych. Poprzez zmianę stężenia halogenków uzyskano przestrajalność szerokości przerwy energetycznej, przewodnictwa jonowego oraz położenia i intensywności pasm emisji fotoluminescencji. Układy dwuhalogenkowe **2D** o wzorze $MHy_2PbBr_{4-x}I_x$, opisywane w pracy **D2**, charakteryzują się bogatym polimorfizmem regulowanym temperaturą oraz składem. W artykule **D3** opisany został związek **2D** o wzorze MHy_2PbCl_4, który charakteryzuje się rzadką sekwencją przemian fazowych indukowanych temperaturą tj. wysokotemperaturową fazą centrosymetryczną, przejściową fazą modulowaną oraz niskotemperaturową fazą polarną. Artykuł **D4** opisuje związki o wzorze $IMMHyPbX_4$ (X = Br, Cl) zawierające dwa kationy organiczne, imidazoliowy (IM^+) oraz MHy^+. Materiały te należą do nielicznej grupy perowskitów **2D** typu (110) i cechują się znaczącą dystorsją warstw nieorganicznych w wyniku oddziaływań wodorowych z kationami organicznymi. Artykuły **D5** i **D6** opisują związki hybrydowe o niższej wymiarowości połączeń oktaedrów – odpowiednio **1D** o wzorze $MHyPbI_3$ z łańcuchową budową części nieorganicznej, oraz **0D** o wzorze $Cs_2MHy_2PbX_6$ (X = Br, I) z izolowanymi oktaedrami.

3. Aims and Objectives

The following dissertation focuses on a specific class of **hybrid organic-inorganic materials**, i.e., **lead halides comprising methylhydrazinium (MHy^+) cation.** The already reported **3D** perovskites ($APbX_3$) with A = MHy^+ and X = Br^-, Cl^- offer enhanced stability compared to their well-known analogs and reveal exceptional properties arising from noncentrosymmetric and strongly distorted alignment. The MHy-based lead halides with inorganic layers (**2D**, A_2PbX_4, X = Br^-, I^-) are characterized, for instance, by record-breaking low interlayer distances.

This dissertation aims to **develop and characterize** newcomers to this emerging class of hybrids that demonstrate novel tunable properties. The general scientific goal is to understand the structure-property relationships and mechanisms of structural phase transitions that determine the physicochemical properties of the synthesized materials.

The proposed paths for the development of new compounds are as follows:

- **Halide substitution**: compositions with one of the following halide anions: Cl^-, Br^-, I^-.
- **Halide alloying**: coexistence of two halides at the X site.
- **A-site cation alloying**: introducing the second organic or inorganic cation to the MHy-based systems.

These compositional engineering techniques have already demonstrated their usability for the flagship lead halide perovskites in terms of modification of crystal structure and tunability of the optoelectronic features. In the case of the titular compounds, A- and X-site engineering is expected to alter the intermolecular interactions, yielding specific structural alignments, and consequently affecting the physicochemical properties. Apart from **3D** and **2D** structures, it is likely that the synthesized compounds may adopt other types of dimensionalities, including **1D** and **0D**.

To address the aims and objectives set in the dissertation, detailed studies of the crystal structure are provided via X-ray diffraction measurements on single-crystal and powdered samples, conducted in a broad temperature range (from 100 K to the temperature of decomposition of the sample). Apart from the structural studies, the articles constituting the thesis also describe the linear and nonlinear optical properties and the dielectric characterization, performed by the collaborators.

4. Author Resume

Dawid Drozdowski, MSc Eng.

Date of birth: 09/12/1996

ORCID: 0000-0001-5918-5503

Scopus Author Identifier: 57292246800

Educational background

10/2020 – 07/2024	**PhD Candidate** Wrocław Doctoral School of Institutes of Polish Academy of Sciences Institute of Low Temperature and Structure Research, Polish Academy of Sciences Division of Structure Research
02/2019 – 07/2020	**Master Studies** Wrocław University of Science and Technology Faculty of Chemistry Field of study: Materials Engineering Specialization: Advanced Functional Materials
10/2015 – 01/2019	**Bachelor (Engineering) Studies** Wrocław University of Science and Technology Faculty of Chemistry Field of study: Chemical and Process Engineering

Projects

07/2024 – present	**NCN Preludium 22 (2023/49/N/ST5/00521)** Layered hybrid perovskites with broadband luminescence and tuneable optoelectronic properties. **Principal Investigator (PI)**
10/2020 – present	**NCN OPUS 18 (2019/35/B/ST5/00043)** Synthesis and physicochemical properties of lead halides comprising protonated methylhydrazine: three-dimensional and layered perovskites with tunable optoelectronic properties (PI: prof. Mirosław Mączka) **Investigator**

List of publications constituting the content of the dissertation

(IF = 2-year impact factor, MP – ministerial points, * – corresponding author)

D1 *Three-Dimensional Methylhydrazinium Lead Halide Perovskites: Structural Changes and Effects on Dielectric, Linear, and Nonlinear Optical Properties Entailed by the Halide Tuning*

D. Drozdowski, A. Gągor, D. Stefańska, J. K. Zaręba, K. Fedoruk, M. Mączka*, A. Sieradzki

The Journal of Physical Chemistry C, **2022**, 126, 3, 1600–1610, DOI: 10.1021/acs.jpcc.1c07911, https://pubs.acs.org/doi/full/10.1021/acs.jpcc.1c07911 (IF: 3.3, MP: 140)

D2 *Layered methylhydrazinium lead halide perovskites: new crystal polymorphs with a tailored band gap and photoluminescence colour via halide substitution*

D. Drozdowski*, A. Kabański, M. Mączka, A. Gągor*

Journal of Materials Chemistry C, **2024**, 12, 6653-6662, DOI: 10.1039/D4TC00865K, https://pubs.rsc.org/en/content/articlehtml/2024/tc/d4tc00865k (IF: 5.7, MP: 140)

D3 *[Methylhydrazinium]$_2$PbCl$_4$ a Two-dimensional Perovskite with Polar and Modulated Phases*

K. Fedoruk, **D. Drozdowski**, M. Mączka*, J. K. Zaręba, D. Stefańska, A. Gągor, A. Sieradzki*

Inorganic Chemistry, **2022**, 61, 39, 15520–15531, DOI: 10.1021/acs.inorgchem.2c02206, https://pubs.acs.org/doi/full/10.1021/acs.inorgchem.2c02206 (IF: 4.3, MP: 140)

D4 *Broadband yellow and white emission from large octahedral tilting in (110)-oriented layered perovskites: imidazolium-methylhydrazinium lead halides*

D. Drozdowski*, K. Fedoruk, A. Kabański, M. Mączka, A. Sieradzki, A. Gągor*

Journal of Materials Chemistry C, **2023**, 11, 4907-4915, DOI 10.1039/D3TC00401E, https://pubs.rsc.org/en/content/articlehtml/2018/89/d3tc00401e (IF: 5.7, MP: 140)

D5 *Methylhydrazinium lead iodide – one-dimensional chain phase with excitonic absorption and large energy band gap*

D. Drozdowski*, A. Gągor, M. Mączka

Journal of Molecular Structure, 1249, **2022**, 131660 DOI: 10.1016/j.molstruc.2021.131660, https://www.sciencedirect.com/science/article/pii/S0022286021017889 (IF: 4.0, MP: 70)

D6 *Zero-dimensional mixed-cation hybrid lead halides with broadband emissions*

M. Mączka*, **D. Drozdowski**, D. Stefańska, A. Gągor

Inorganic Chemistry Frontiers, **2023**, 10, 7222-7230, DOI: 10.1039/D3QI01749D, https://pubs.rsc.org/en/content/articlehtml/2023/qi/d3qi01749d (IF: 6.1, MP: 140)

List of the remaining publications

(IF = 2-year impact factor, MP – ministerial points, * – corresponding author)

---

1) *Effect of Dimensionality on Photoluminescence and Dielectric Properties of Imidazolium Lead Bromides*

S. Smółka*, M. Mączka*, **D. Drozdowski**, D. Stefańska, A. Gągor, A. Sieradzki, J. K. Zaręba, M. Ptak *Inorganic Chemistry,* **2022***,* 61, 38, 15225–15238, DOI: 10.1021/acs.inorgchem.2c02496 (IF: 4.3, MP: 140)

2) *Hybrid Organic-Inorganic Crystals of [Methylhydrazinium]$M^{II}Cl_3$ (M^{II} = Co, Ni, Mn)*

J. A. Zienkiewicz*, M. Ptak, **D. Drozdowski**, K. Fedoruk, M. Stefański, A. Pikul

The Journal of Physical Chemistry C, **2022***,* 126, 37, 15809-15818, DOI: 10.1021/acs.jpcc.2c04893 (IF: 3.3, MP: 140)

3) *Hybrid Chlorides with Methylhydrazinium Cation: $[CH_3NH_2NH_2]CdCl_3$ and Jahn-Teller Distorted $[CH_3NH_2NH_2]CuCl_3$*

J. A. Zienkiewicz*, D. A. Kowalska, **D. Drozdowski**, A. Pikul, M. Ptak*

Molecules, **2023***,* 28, 2, 473 DOI: 10.3390/molecules28020473 (IF: 4.2, MP: 140)

4) *Multi-noncentrosymmetric Two-Dimensional Trilayered Lead Bromide Perovskites With Methylhydrazinium Cations: Lattice Dynamics, Phase Transitions, Dielectric Response and Optical Properties*

M. Mączka*, S. Smółka, D. Stefańska, A. Gągor, J. K. Zaręba, K. Fedoruk-Piskorska, M. Ptak, **D. Drozdowski**, A. Sieradzki

Chemistry of Materials, **2024**, 36, 17, 8286–8299, DOI: 10.1021/acs.chemmater.4c01174 (IF = 7.1, MP: 200)

Conference presentations

International

1) 34th European Crystallographic Meeting, **Padova (Italy)**, 26-30/08/2024

Oral presentation

Title: *Polymorphism in lead halide hybrids comprising methylhydrazinium cation*

Authors: **D. Drozdowski**, A. Gągor, M. Mączka

2) XXV Jubilee Polish-Czech Seminar on Structural and Ferroelectric Phase Transitions, **Lake Dymaczewskie (Poland)**, 06-10/05/2024

Oral presentation

Title: *Phase transitions, optical and dielectric properties in layered hybrid perovskites of ACI and (110)-oriented type*

Authors: **D. Drozdowski**, A. Kabański, K. Fedoruk-Piskorska, M. Mączka, A. Sieradzki, A. Gągor

3) 26th Congress and General Assembly of the International Union of Crystallography, **Melbourne (Australia)**, 22-29/08/2023

Oral presentation

Title: *Old Trick for new dogs – modification of structural and optoelectronic properties in layered methylhydrazinium lead halide perovskites via halide mixing.*

Authors: **D. Drozdowski**, A. Gągor, K. Fedoruk, M. Mączka, D. Stefańska, J. K. Zaręba, A. Sieradzki

4) 33rd European Crystallographic Meeting, **Versailles (France)**, 23-28/08/2022

Poster presentation

Title: *Two-dimensional methylhydrazinium lead chloride perovskites with temperature-controlled centrosymmetric, modulated, and polar crystal phases.*

Authors: **D. Drozdowski**, A. Gągor

5) XXIV Czech-Polish Seminar on Structural and Ferroelectric Phase Transitions, **Harrachov (Czechia)**, 23-27/05/2022

Poster + 2 minutes oral presentation

Title: *Effect of halide mixing on structural and optoelectrical properties of the 3D and 2D methylhydrazinium lead halide perovskites.*

Authors**: D. Drozdowski**, A. Gągor, M. Mączka

Nationwide

1) 65th Polish Crystallographic Meeting, **Wrocław**, 26-28/06/2024

Poster presentation

Title: *Phase transitions and polymorphism in lead halide hybrids comprising methylhydrazinium*

Authors: **D. Drozdowski**, A. Gągor, M. Mączka

2) VII Conference of Doctoral Students of the PAS (KonDokPAN 2023), **Wrocław**, 13-15/10/2023

Oral presentation

Title: *Flexible solar cells and other phenomena - the world of hybrid perovskites*

Authors: **D. Drozdowski**, M. Mączka, A. Gągor

3) 64th Polish Crystallographic Meeting, **Wrocław**, 05-07/07/2023

Oral presentation

Title: *Two-dimensional hybrid perovskites with (110)-oriented layers and large octahedra tilting.*

Authors: **D. Drozdowski**, A. Gągor, M. Mączka

4) X Łódzkie Sympozjum Doktorantów Chemii, **Łódź**, 18-19/05/2023

Poster presentation

Title: *Szerokopasmowa emisja w warstwowych perowskitach hybrydowych – halogenkach ołowiu z kationami organicznymi.*

Authors: **D. Drozdowski**, K. Fedoruk, A. Kabański, M. Mączka, A. Sieradzki, A. Gągor

5) VI Conference of Doctoral Students of the PAS (KonDokPAN 2022), **Kraków**, 21-23/10/2023

Oral presentation

Title: *Layered methylhydrazinium lead halide perovskites*

Authors: **D. Drozdowski**

6) 63rd Polish Crystallographic Meeting, **Wrocław**, 29/06-01/07/2022

Oral presentation

Title: *Chlorek ołowiu z kationem metylohydrazoniowym - synteza i właściwości strukturalne warstwowego perowskitu hybrydowego*

Authors: **D. Drozdowski**, K. Fedoruk, M. Mączka, J. K. Zaręba, D. Stefańska, A. Sieradzki, A. Gągor

7) XIX Wrocławskie Studenckie Sympozjum Chemiczne, **Wrocław**, 21-22/05/2022

Oral presentation

Title: *Metody otrzymywania perowskitowych kropek kwantowych*

Authors: **D. Drozdowski**

8) IX Łódzkie Sympozjum Doktorantów Chemii, **Łódź**, 19-20/05/2022

Oral presentation

Title: *Wpływ mieszania halogenków na właściwości strukturalne i optoelektroniczne trój- i dwuwymiarowych ołowiowych perowskitów hybrydowych zawierających metylohydrazynę.*

Authors: **D. Drozdowski**, A. Gągor, M. Mączka

9) VIII Łódzkie Sympozjum Doktorantów Chemii, **Łódź**, 24/09/2021

Poster presentation

Title: *3D methylhydrazinium lead halide perovskites: Structural changes and effects on dielectric, linear, and optical properties entailed by the halide tuning.*

Authors: D. Drozdowski, A. Gągor, D. Stefańska, J. K. Zaręba, K. Fedoruk, M. Mączka, A. Sieradzki

10) 62nd Polish Crystallographic Meeting, **Wrocław**, 23-25/06/2021

Poster presentation

Title: *Tuning of crystal structures and optical properties via halide substitution in non-centrosymmetric 3D hybrid perovskites comprising methylhydrazinium cations.*

Authors: D. Drozdowski, A. Gągor, D. Stefańska, J. K. Zaręba, K. Fedoruk, M. Mączka, A. Sieradzki

Awards and scholarships

- Ludo Frevel Crystallography Scholarship for the year 2023
- Distinction in the Max Born Scholarship for the year 2023
- Travel bursary (IUCr Young Scientists Awards) for the 26th Congress and General Assembly of the International Union of Crystallography and 33rd European Crystallographic Meeting
- 2nd place for "best presentation award" at XXIV Czech-Polish Seminar on Structural and Ferroelectric Phase Transitions
- 2nd place for "best poster presentation" at the 62nd Polish Crystallographic Meeting
- Distinction of the poster presentation during the Annual Scientific Session of the Wrocław Doctoral School of Institutes of PAS (twice – 2021/22 and 2022/23)

Additional activity

- Council Member PhD Students Council of the Polish Academy of Sciences (PAS) (11/2022-11/2023)
- President of the organizing committee of the VII Conference of Doctoral Students of PAS (13-15/10/2023)
- President of the PhD Students Council of the Institute of Low Temperature and Structure Research (PAS) (01/2021-12/2023)
- Member of the Polish Crystallographic Association (PCA) and Young Crystallographers Section (YCS) (03/2023 – present)
- Member of the organizing committee of the *1st Scientific Session of YCS PCA* (05/07/2023)
- Member of the organizing committee of *the 62nd, 63rd, 64th and 65th Polish Crystallographic Meeting*
- Participation in the international school: *19th BCA/CCG Intensive Teaching School in X-Ray Structure Analysis*, Durham (United Kingdom), 25/03-02/04/2023
- Preparation and performance of the powder X-ray diffraction experiments in the *European Synchrotron Radiation Facility (ESRF)*, Grenoble (France), 26-28/10/2022
- Preparation of the workshops and chemical experiments during two editions of the *Niskie Łąki* scientific workshop and *Dolnośląski Festiwal Nauki* festival

5. List of abbreviations and symbols

Abbreviation	Full form
ACI	Alternating cation in the interlayer space
BA (BA^+)	Butylammonium (cation)
BDS	Broadband dielectric spectroscopy
DJ	Dion-Jacobson
DRS	Diffusive reflectance spectra
DSC	Difference scanning calorimetry
EDAX	Energy dispersive X-ray analysis
FA (FA^+)	Formamidinium (cation)
FE	Free exciton
FWHM	Full width at half maximum
HBs	Hydrogen bonds
HOIPs	Hybrid organic-inorganic perovskites
HT	High temperature
IBA (IBA^+)	Isobutylammonium (cation)
IM (IM^+)	Imidazolium (cation)
KDP	Potassium dihydrogen phosphate
LT	Low temperature
MA (MA^+)	Methylammonium (cation)
MHy (MHy^+)	Methylhydrazinium (cation)
PCE	Power conversion efficiency
PL	Photoluminescence
PT	Structural phase transition, polymorphic transition
RP	Ruddlesden-Popper
RT	Room temperature
SCXRD	Single-crystal X-ray diffraction
SHG	Second harmonic generation
STEx	Self-trapped exciton
TF	Goldschmidt tolerance factor
XRD	X-ray diffraction

SYMBOL	DESCRIPTION	UNIT
a, b, c	Lattice parameters	Å
d_{in}	180° – θ_{in}	deg (°)
d_{out}	180° – θ_{out}	deg (°)
E_g	Energy band gap	eV
q^*	Modulation vector	–
ΔC_p	Heat capacity	$\mathrm{Jmol^{-1}K^{-1}}$
Δ_d	Bond length distortion	–
ε'	Dielectric constant	–
θ_{in}	In-plane Pb–X–Pb angle	deg (°)
θ_{link}	Pb–X–Pb angle for (110)-oriented type	deg (°)
θ_{out}	Out-of-plane Pb–X–Pb angle	deg (°)
σ^2	Octahedra angle variance	deg^2

6. Introduction

6.1. Hybrid organic-inorganic compounds

Materials that combine inorganic and organic units present significant prospects for developing novel and functional materials for scientific investigation and technological utilization. Inorganic materials may demonstrate high electrical mobility, intriguing magnetic behavior, notable mechanical strength, thermal robustness, etc. They also exhibit a broad range of band gap (E_g) widths, resulting in a vast group of superconductors, semiconductors, and insulators [1]. The organic compounds, in turn, are characterized by highly effective luminescence, flexible mechanical characteristics, considerable polarizability, and, as in the case of their inorganic counterparts, conductivity or superconductivity [2]. The research on organic-inorganic hybrids generally aims to benefit from the diverse interaction mechanisms inherent in both inorganic and organic chemistry. This leads to new materials with enhanced properties than those attainable with either of the subgroups. In certain scenarios, the objective is to explore novel phenomena arising from the intermolecular forces between the organic and inorganic species.

Hybrid materials may be roughly classified concerning the bonding relations between the abovementioned, as depicted in Fig. 1. The first group includes the weaker intermolecular interactions, such as hydrogen bonds (HBs), van der Waals, and subtle electrostatic forces. In this type of structures, the linking distances between the electrically neutral organic and inorganic frameworks are relatively long, resembling the physisorption process [3,4]. The second class is defined by stronger organic-inorganic interactions, i.e., coordination, ionic, and covalent bonds. In ionic compounds, the organic moiety is integral to the inorganic structure and is essential for maintaining overall charge neutrality. In contrast to the previous class, these materials generally reveal smaller bonding distances and well-defined stoichiometries, with the organic cations occupying specific sites in the lattice. While all the presented types of hybrid compounds hold significant scientific and technological interest, a particular group has garnered attention from researchers and industry in recent decades due to its strong potential for optoelectronic (i.e., light-emitting, photovoltaic, dielectric, etc.) applications – ionically interacting systems built on the perovskite framework.

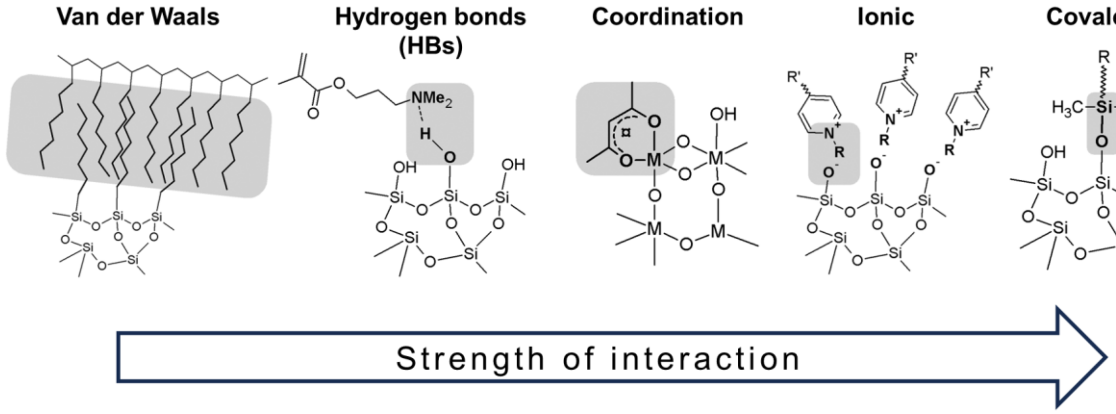

Figure 1. Classification of the hybrid organic-inorganic materials based on the strength of the intermolecular interactions [3].

6.2. Hybrid perovskites

Perovskite, a calcium titanium oxide mineral with the chemical formula $CaTiO_3$, was discovered in 1839 by the Prussian mineralogist Gustav Rose in the Ural Mountains and named in honor of Lev Perovski – the initiator of the Russian Geographical Society [5]. Today, the ‘perovskite’ term broadly refers to materials sharing the same structure as $CaTiO_3$, expressed by the general chemical formula ABX_3 [6,7]. The crystal structure is built of BX_6 octahedra, which through corner-sharing, form a three-dimensional framework accommodating A-site cations in the 12-fold coordinated cavities (Fig. 2). The archetypal perovskite structure adopts cubic O_h symmetry described in $Pm\overline{3}m$ space group. Within a great diversity of perovskite oxide compositions, one may find examples with lower symmetry. For instance, the crystal structure of barium titanate ($BaTiO_3$) is described in the trigonal $R3m$ space group at ambient conditions [8]. The displacement of Ti^{4+} from the octahedra center induces ferroelectric ordering and spontaneous polarization. This feature has placed the $BaTiO_3$ as one of the most widely used ferroelectric ceramics [9–11]. Other examples, such as $BiFeO_3$ and $LaMnO_3$ demonstrate advisable properties (enormous magnetoresistance effect, multiferroicity, etc.) in terms of spintronics, storage devices, and other electronic and magnetic applications [12,13].

The A-, B-, and X-sites of the perovskite structure are not restricted only to metal cations and oxygen anions. They can adopt a variety of compositions, as long as the charge balance and lattice compatibility are preserved. Substituting the A- and X-site ions with organic compounds creates a subclass of perovskite materials known as **hybrid organic-inorganic perovskites (HOIPs)** [14]. Incorporating organic components into the perovskite alignment notably alters their electronic nature and structural flexibility compared to their inorganic counterparts. These features may enable novel properties and functionalities absent in perovskite oxides. Moreover, a vast structural and chemical variability of HOIPs offers multipurpose physicochemical properties and substantial opportunities for their tunability and controllability through simple bottom-up chemical synthesis.

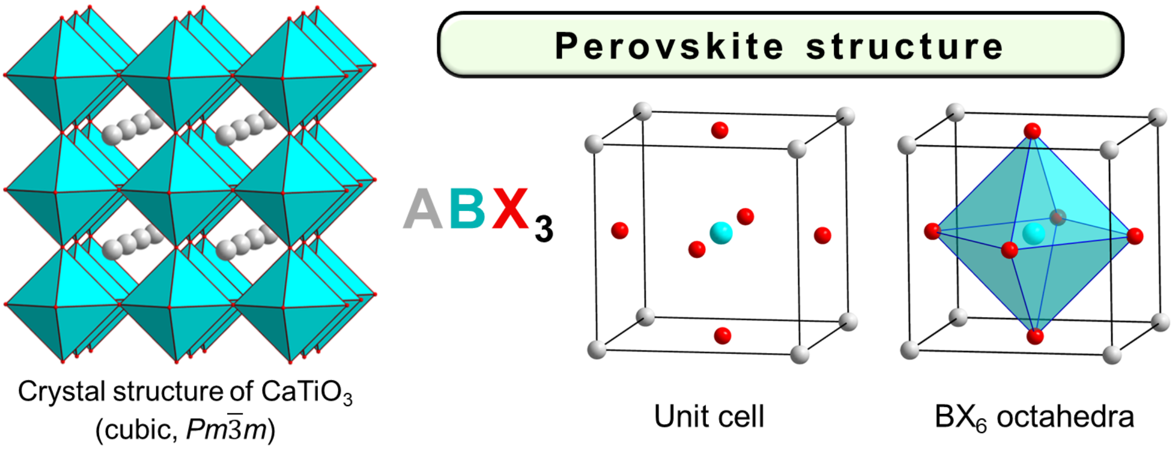

Figure 2. The crystal structure of perovskite (calcium titanate, $CaTiO_3$) with the characteristic features.

An extensive variety of the components on the A-, B-, and X-site results in numerous combinations of HOIPs, with the compositions spanning over a large section of the periodic table. Regarding the crystal structure, one may distinguish several subcategories apart from the ABX_3 cubic exemplar, including ABX_3 hexagonal perovskites (6H, 4H), A_3BX anti-perovskites, $A_2BB'X_6$ double perovskites, and other [7,15–17]. Another path of classification refers to the type of the mono- or multiatomic anion at the X site, as illustrated in Fig. 3. This type of categorization encompasses anions such as halides (Cl^-, Br^-, I^-), cyanides (CN^-), formates ($HCOO^-$), hypophosphites ($H_2PO_2^-$), azides (N_3^-), etc. [18].

HOIPs, much like their inorganic counterparts, can demonstrate a wide range of physical properties based on their unique configurations. Perovskite formates are attractive due to their multiferroic properties [19–21], whereas azides, cyanides, and hypophosphites exhibit switchable dielectric behavior, as well as versatile magnetic, luminescent, and non-linear optical features [22–25]. Nevertheless, one specific class, namely **3D lead halide HOIPs** (with Pb^{2+} metal centers and comprising small organic cations at the A site, often referred to as ‘perovskitizers’) has captured the largest attention of both material science and industry, demonstrating exceptional optoelectronic properties, thoroughly investigated and rapidly improved over the last 15 years.

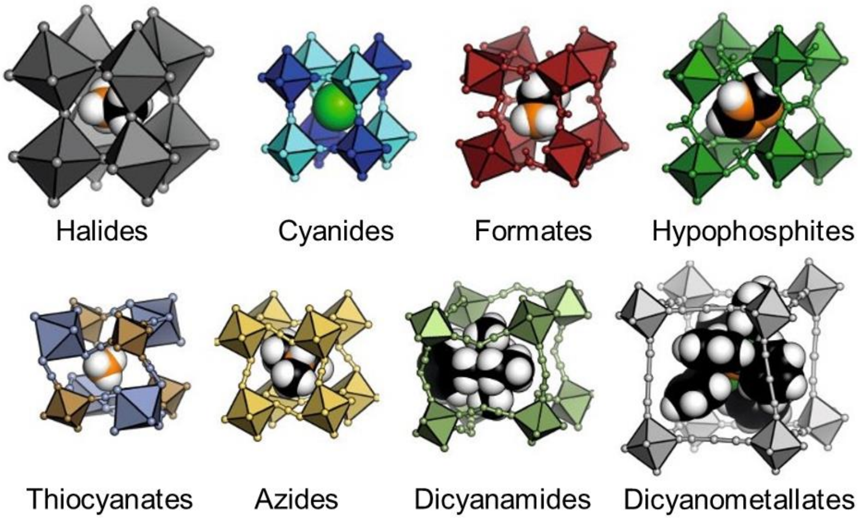

Figure 3. Classification of HOIPs centered on the type of introduced X-site anion [18].

6.3. 3D lead halide HOIPs

3D lead halide HOIPs comprising methylammonium (MA^+, $CH_3NH_3^+$) or formamidinium (FA^+, $CH(NH_2)^+$) started to attract worldwide attention in 2009, when the $MAPbI_3$-based solar cell device was reported, exhibiting the power conversion efficiency (PCE) of 3.8% [26]. Since then, the PCE of the perovskite solar cells has promptly grown to 26.1%, matching the conventional devices based on silicone [27,28]. Such rapid progress is driven by the exceptional photoelectronic properties of $MAPbX_3$ and $FAPbX_3$ absorbers, e.g., high extinction and absorption coefficients, and long carrier diffusion lengths. [29–31]. With all these features and low-cost fabrication, lead halide HOIPs constitute the core for thin, flexible, and semitransparent solar cells. They are considered for contemporary and future applications in optoelectronics, photodynamic therapy, etc. [32–34]. However, the commercialization process of $MA/FAPbX_3$-based photovoltaics still faces critical issues, mainly regarding their high sensitivity to moisture and other external factors, resulting in poor long-term stability and performance [35]. Thus, several strategies have evolved throughout the years to address these issues.

The first approach involves the substitution of the organic cation at the A site, an essential tool for achieving highly tunable HOIP properties. However, such modifications are limited due to steric hindrance from the three-dimensional inorganic substructure. The stability of the **3D** perovskite can be parametrized using the Goldschmidt tolerance factor (*TF*) [36]. Bearing in mind that the A-site cations are not spherical ions but molecular groups, the *TF* has been adjusted in this case to the following formula [37]:

$$TF = \frac{r_{A,eff} + r_X}{\sqrt{2}(r_B + r_X)}$$

where $r_{A,eff}$ is the effective radius of the A-site molecule, and r_B and r_X represent the radius of B and X ions, respectively. Typical *TF* values for the perovskites span between ~0.8 and ~1.0. In the case of **3D** lead halides, only moieties with a moderately small $r_{A,eff}$ may fulfill the above rule. Thus far, four A-site cations have been reported to fit into the **3D** structure, namely MA^+, FA^+, aziridinium (AZr^+) and methylhydrazinium (MHy^+) ($r_{A,eff}$ provided in Fig. 4). When compared to the well-known MA- and FA-based compounds, $AZrPbX_3$ **3D** HOIPs possess the favored cubic phase down to the lowest temperatures (132 – 162 K) and demonstrate the optical band gap values (1.51 eV for $AZrPbI_3$) more preferable for the photovoltaics [38–41]. The MHy-based compositions, despite exceeding the *TF* (1.01, 1.03, and 1.05 for I, Br, and Cl, respectively), adopt two stable **3D** structures of $MHyPbBr_3$ and $MHyPbCl_3$ formula [42,43]. With the largest $r_{A,eff}$ of MHy^+ among all mentioned cations (Fig. 4), **$MHyPbX_3$ (X = Br, Cl) are the only 3D lead halide HOIPs that crystallize and adopt noncentrosymmetric phases with severely distorted perovskite substructure.** Combined with the order-disorder phase transitions, observed in $MHyPbBr_3$, this specific family demonstrates the greatest potential for the studies of the crystal structure and its rearrangement upon varying temperature. Furthermore, the lack of the center of symmetry is manifested in the non-linear optical phenomena, ferroic properties, etc., paving the way for new fields of optoelectronic applications.

Another approach that has gained significant interest in recent years is the A- and X-site alloying, which involves the coexistence of two constituents at a single site. Several studies have reported enhanced stability and performance of HOIPs through the incorporation of secondary organic cations [44–46]. For instance, doping of imidazolium (IM^+) or its derivatives to the MA-based **3D** HOIPs results in improved PCE and moisture resistance, benefiting from the hydrophobic nature of the introduced moiety [47,48]. In the case of halide-mixing, an expanding body of reports on $MAPbX_nX'_{3-n}$ and $FAPbX_nX'_{3-n}$ **3D** hybrids reveals the anion-tunable characteristics [49–52]. Halide alloying offers tunability of E_g, PL bands, and extended charge carrier diffusion lengths, maintaining facile and low-cost synthesis and fabrication [53,54]. Similarly to A-site alloying, mixed-halide compositions can address a critical issue of poor stability, e.g., in the way of incorporation of Br^- to the $MAPbI_3$ films [55]. In general, site alloying is regarded as an influential tool to strengthen the tunability of physicochemical properties, in some cases controlling them by changing the ratio of halides. While this technique proved its usefulness for the analogs with MA^+ and FA^+, **there is a lack of studies on the A- and X-site alloying impact on the systems comprising MHy^+**.

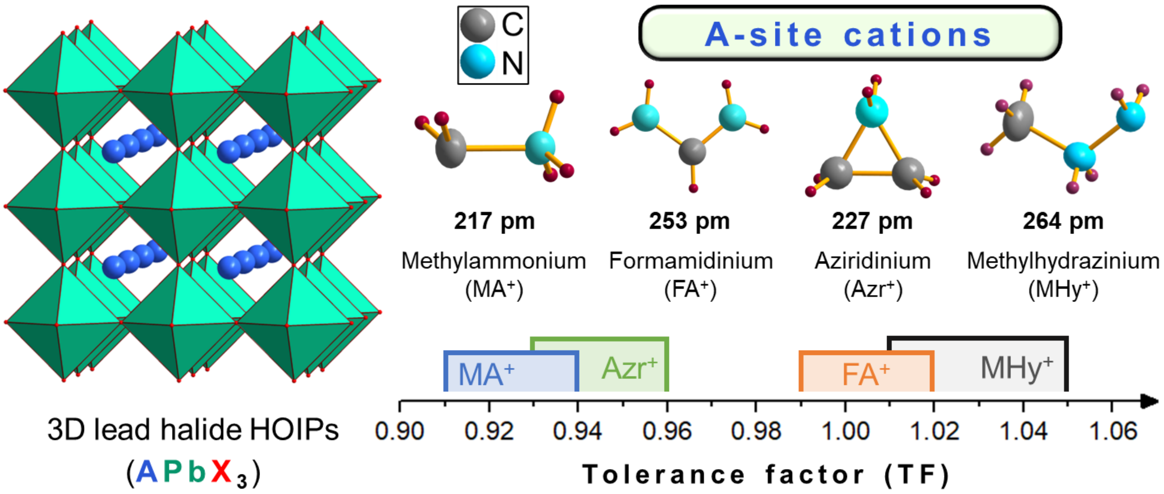

Figure 4. Three-dimensional (**3D**) lead halide HOIPs with four A-site cations introduced thus far. Under each cation its $r_{A,eff}$ is provided, adapted from ref. [21,41,56]. *TF* values are calculated for B = Pb and X = Cl, Br, I.

6.4. The hybrids of low dimensionality

A limited number of A-site cations that maintain a stable perovskite structure has led to a focus on lead halide hybrids with reduced dimensionality. As outlined above, the inorganic substructure in perovskite consists of BX_6 octahedra propagating along each of the three spatial dimensions. Accordingly, the octahedra may connect along two dimensions, one dimension, or even be separated from each other, creating **2D**, **1D**, and **0D** subclasses, as presented in Fig. 5. This path of modification offers more degrees of freedom and allows for the introduction of more moieties, particularly larger organic cations. Reduced dimensionality generally leads to thermodynamically preferred and therefore more stable alignments, addressing one of the main concerns regarding the potential of lead halide hybrids for diverse applications. Before describing each subclass, a brief explanation regarding the 'perovskite' term is provided. The question of which lower-dimensional subgroups can be regarded as perovskites remains contentious, leading to several publications on the topic. [57–59]. Some papers consider each of the **0D-2D** groups as perovskites [60–63], whereas others suggest limiting this term only to structures with three-dimensionally linked octahedra and describe the remaining ones as e.g., perovskite-related materials or simply lower-dimensional hybrid compounds [57,58]. Without a clear definition provided by any international committees or institutions and bearing in mind the similarities in the properties and scope of applications (further explained in the following paragraph), **here the term ‘perovskite’ is preserved for the 3D and 2D subgroups**, by analogy with ref. [64].

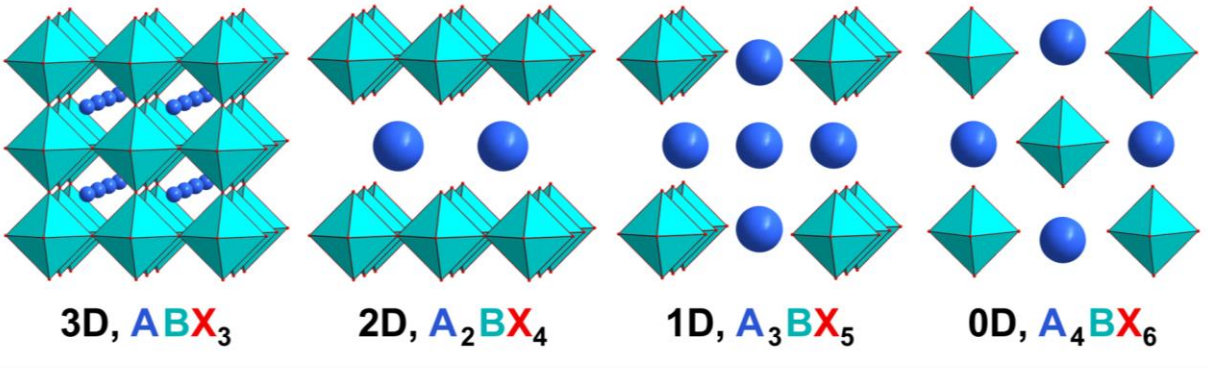

Figure 5. The classification of hybrid compounds based on the dimensionality of octahedra connections.

Two-dimensional hybrid perovskites (**2D** HOIPs, general formula of A_2BX_4), which consist of octahedra propagating along two directions (‘layers’) separated by organic cations (‘spacers’), are emerging as promising alternatives to their **3D** counterparts. These materials offer considerably better stability and resistance to moisture, due to the higher formation energy and the hydrophobic properties of the organic spacers [65–67]. The distinctive alignment of **2D** HOIPs is characterized by the electronic structure directly controlled by the inorganic components. Owing to the separation of inorganic layers, they are described as natural (in some cases even perfect) quantum wells with two-dimensional electronic confinement [68]. This effect can be manifested in increased photoluminescence quantum yield (PLQY ca. 80%) and profoundly narrower PL bandwidths (< 20 nm) in comparison to **3D** counterparts [69,70]. Conversely, the presence of insulating spacers induces the formation of stable electron-hole pairs (excitons), resulting in significantly increased exciton binding energies (typically >150 meV and ~10 meV for **2D** and **3D** perovskites, respectively) [71,72]. These characteristics are highly preferable for light-emitting applications; however, large binding energy leads to lower PCE, which is an undesirable feature for photovoltaics. Nevertheless, one may find reports describing the **2D-3D** multidimensional perovskite solar cells that demonstrate relatively high PCE and long-term usability simultaneously [73].

An unquestionable advantage of **2D** perovskites over their **3D** analogs is presumably countless A-site organic cations that can act as spacers. A plethora of diverse reported and calculated types of crystal structures that one might classify concerning different characteristic features. One of the possible criteria involves the ‘slicing’ of parental **3D** inorganic structure along a specific direction of propagation, forming the subgroup known as the single-layered **2D**

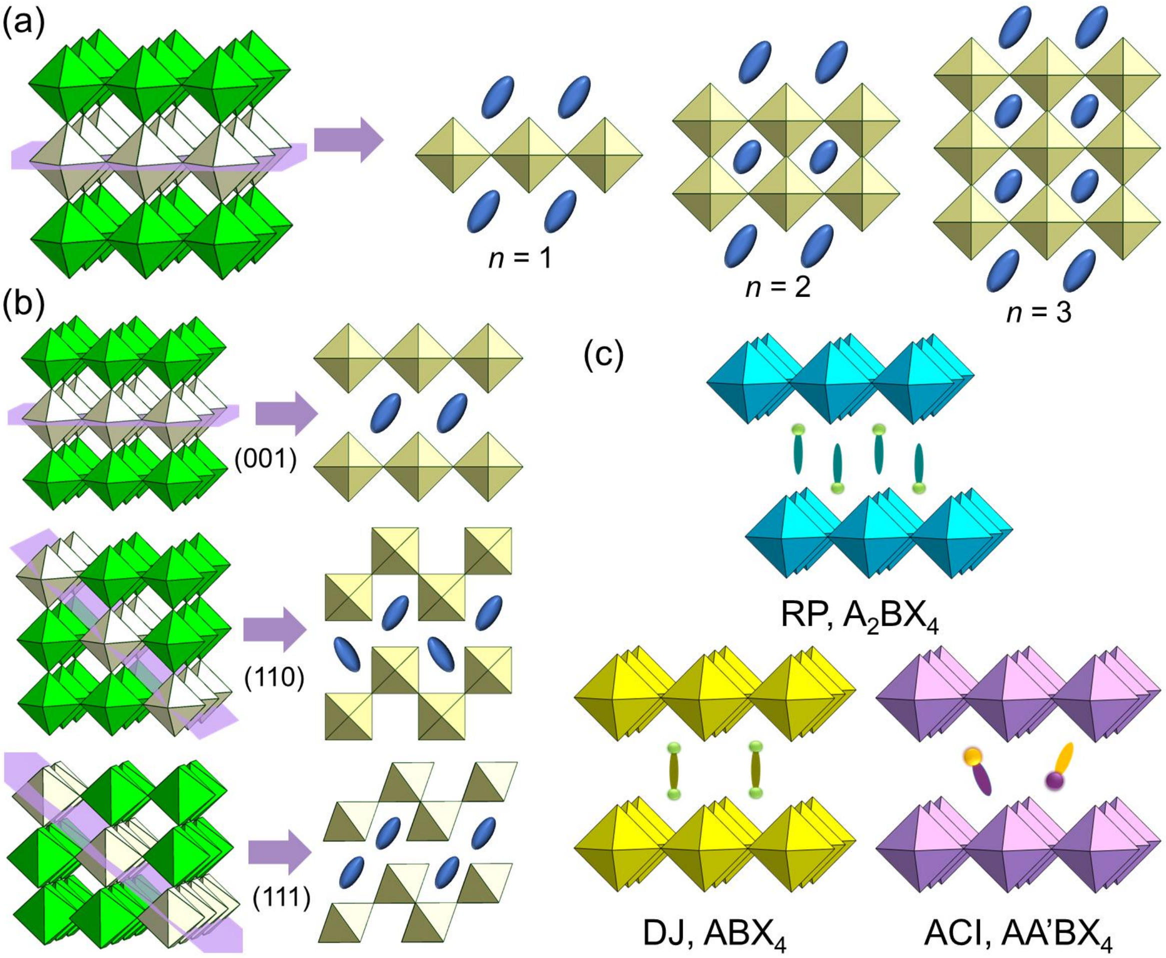

Figure 6. Classification of single-layered **2D** HOIPs based on (a) multiplicity of the inorganic layers along the direction perpendicular to the propagation, (b) 'slicing' the **3D** parental structure along (001), (110), and (111) planes, respectively, and (c) a valency of the introduced organic cation and a shift between the adjacent layers. RP = Ruddlesden-Popper, DJ = Dion-Jacobson, ACI = Alternating Cation in the Interlayer space.

HOIPs (octahedra layers isolated from each other, $n = 1$) or multi-layered analogs (share the halide corners with one, two, etc. adjacent layers, $n > 1$), as illustrated in Fig. 6a. **The single-layered compounds are regarded as the most stable and easily synthesized phase pure, with the most natural quantum-well character** [68]**, and therefore are the only group considered in this thesis.** Another way of categorization is based on slicing as well, but made along particular crystallographic planes, generating the (001)-, (110)-, and (111)-oriented subclasses (Fig. 6b). A vast majority of structures (over 600 lead halides in the online **2D** perovskites database [74]) is (001)-oriented (sliced across the octahedral corners), making this configuration the most favorable and adaptable to the chemical substitution. The (110)-oriented compounds (sliced across the octahedra edges, 25 records in the database) deserve attention, exhibiting broadband and white-light colored PL with superior PLQY and Stokes shifts than the (001)-type counterparts, owing to higher dielectric confinement and octahedra distortion [75–78]. The (111)-oriented **2D** perovskites are not a part of this thesis, as they can only be formed with the B^{3+} metals from group 15, like Bi, Sb, As, etc. [79]. The last proposed way of classification refers to the valency of the organic cation(s) and a relative stacking of the adjacent layers (Fig. 6c), resulting in the Ruddlesden-Popper (RP, A_2BX_4, A is monovalent) phases with a characteristic shift of the adjacent layers [80,81], Dion-Jacobson (DJ, ABX_4) with divalent cation [82,83], and the Alternating Cation in the Interlayer space (ACI, $AA'BX_4$, A and A' are monovalent) compounds [84]. The RP hybrids demonstrate the ability to tune the E_g across a broad spectral range (410 – 760 nm) and increased light absorption coefficient [85,86]. The presence of a divalent cation in DJ structures allows the creation of HBs involving two ends of an organic moiety, leading to improved stability. They may also exhibit a prolonged carrier lifetime twice as for RP counterparts [87–89]. The last subclass, *i.e.*, ACI is relatively new and the least common, however, the coexistence of two different organic cations has already demonstrated the potential to reduce dielectric and electronic confinement [84,90]. Consequently, ACI-type compounds may serve as a crucial link between solar cells and light-emitting applications.

In semiconducting materials exhibiting strong coupling of electrons and holes to the lattice, a carrier can become self-trapped within its lattice distortion field. An electron-hole pair with such a carrier is referred to as a self-trapped exciton (STEx) – a frequently common phenomenon in the metal halide hybrids, which greatly affects the energy transport and luminescent properties of these materials [91]. Owing to phonon-exciton interaction, STEx is crucially dependent on the dimensionality of the crystal structure [92]. Lowering the dimensionality to **1D** and **0D** systems (Fig. 5c, d) facilitates the self-trapping process, giving rise to broadband PL from STEx with large Stokes shifts (approx. 1 eV) and high PLQY [93,94]. **1D** structures, composed of PbX_6 octahedra propagating along a single direction surrounded by organic moieties, may be regarded as quantum wire systems with semiconducting inorganic chains surrounded by insulating organic barriers, interacting with each other via HBs. The chains may be formed differently, including single/double or corner-, edge-, and face-sharing chains, etc. (Fig. 7). Due to their unique structural and chemical characteristics, **1D** hybrid lead halides form highly stable excitons with large exciton binding energies of several hundred meV, benefiting from heavy quantum confinement [93]. The **0D** analogs, built of lead halide clusters or isolated PbX_6^{4-} octahedra, also demonstrate substantial exciton binding energies with increased radiative recombination. Both alignments are usually more stable than their **3D** and **2D** counterparts under ambient conditions [95,96].

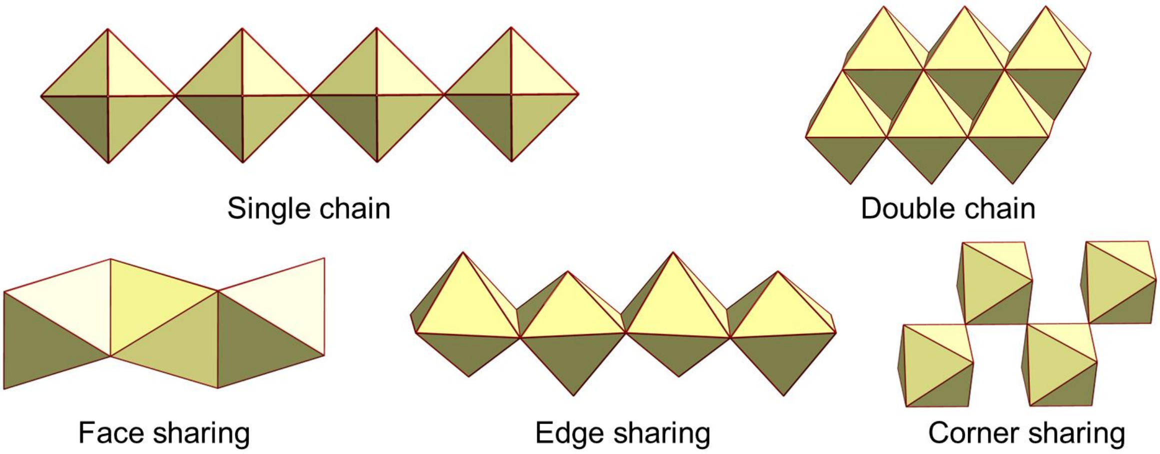

Figure 7. Examples of typical alignments of the octahedra chains reported for **1D** hybrid metal halide compounds.

6.5. Lead halide hybrids comprising methylhydrazinium

All of the **3D** and lower-dimensional subgroups of lead halides demonstrate unique properties and deserve to be developed. If compounds from each subclass contain the same organic cation, their intermolecular interactions and observed physicochemical properties can be compared. Among four known perovskitizers in lead halide HOIPs (MA^+, FA^+, AZr^+, and MHy^+), perovskites comprising MHy^+ demonstrate exceptional structural features and, according to the database [74], MHy^+ is the sole reported so far to be a spacer for the (001) single-layered **2D** structures without introducing the secondary moiety (layered MA-based materials are stabilized with SCN^- anions, whereas FA_2PbBr_4 adopts (110)-oriented corrugated layers [97,98]). This section is dedicated to the description of already reported hybrid perovskites and perovskite-related compounds comprising MHy^+.

As mentioned above (subchapter 6.3.), **3D** HOIPs of the $MHyPbX_3$ (X = Br, Cl) formula crystallize in a strongly noncentrosymmetric phase (monoclinic, $P2_1$), unlike the other analogs (e.g., cubic $Pm\overline{3}m$ for $FAPbBr_3$ and $AZrPbBr_3$, tetragonal $I4/mcm$ for $MAPbBr_3$, all centrosymmetric [38,99–101]). This peculiarity is associated with the largest $r_{A,eff}$ of MHy^+ (264 pm, [21]) among all four perovskitizers. In $MHyPbX_3$ (X = Br, Cl), the presence of a sizeable cation in the space limited by the octahedra induces the formation of the anisotropic **3D** structure. Two inequivalent positions of Pb are distinguished, creating perovskite [001] layers composed of $Pb(1)X_6$ and $Pb(2)X_6$, as presented in Fig. 8a. The terminal NH_2^+ group of MHy^+ violates the coordination sphere of metal centers unequally, bringing more deformations to the Pb(2) layers, which surround the $NH_2–NH_2^+$ group (Fig. 8b). The $Pb(2)\cdots NH_2^+$ coordination bonds are 2.92 and 3.04 Å (2.83 and 2.89 Å) for Br (Cl), which is under the limit for this type of interaction [42,43]. Besides the coordination bonds, the position of MHy^+ is stabilized via N–H···X HBs with the halide acceptors (Fig. 8b).

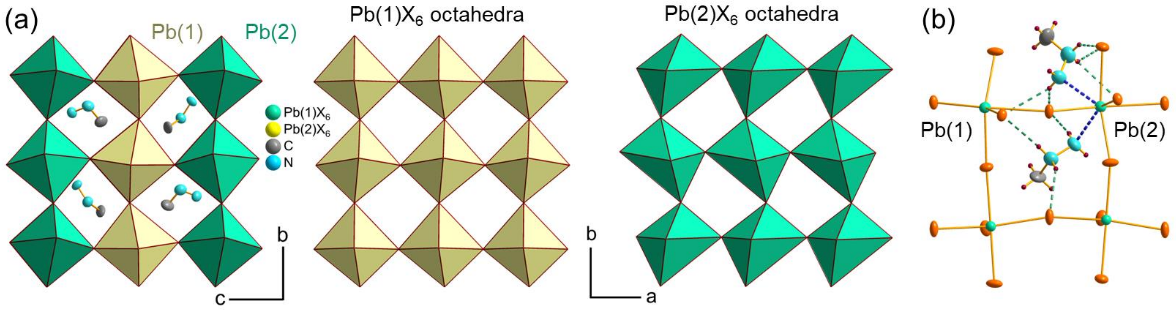

Figure 8. The crystal structure of $MHyPbX_3$ (X = Br, Cl) **3D** HOIPs at RT (monoclinic, $P2_1$). (a) View along [100] and [001] directions, presenting layers of two symmetrically inequivalent positions of Pb. (b) Intermolecular interactions between MHy^+ cations and the inorganic substructure. Green and blue dashed lines represent N–H···X HBs and Pb(2)–NH_2^+ coordination bonds, respectively [42,43].

Deformations of the octahedra can be expressed using various criteria. **In this thesis, distortions of the single octahedra are characterized by the bond length distortion (Δ_d) and octahedra angle variance (σ^2)**. Both parameters have been calculated according to Fleet's method [102], with the formulas provided below:

$$\Delta_d = \frac{1}{6}\sum_{i=1}^{6}\left(\frac{l_i - \bar{l}}{\bar{l}}\right)^2 \qquad \sigma^2 = \frac{1}{11}\sum_{i=1}^{12}(\theta_i - 90°)^2$$

where l_i denotes the mean bond length. Generally, greater Δ_d and σ^2 values indicate a larger deviation of the Pb–X bond lengths and X–Pb–X angles from the ideal O_h octahedron characteristic for the cubic $Pm\overline{3}m$ phase, as depicted in Fig. 9a. In the $MHyPbX_3$ systems, the largest distortions are reported for X = Cl and are as follows: $\Delta_d = 2.2\cdot10^{-4}$ ($11.4\cdot10^{-4}$) and $\sigma^2 =$ 21 deg^2 (314 deg^2) for the $Pb(1)Cl_6$ ($Pb(2)Cl_6$) octahedra at RT. The calculated values are far greater than for the counterparts with other perovskitizers (e.g., Δ_d of $Pb(2)Br_6$ is roughly 50 times bigger than for the most distorted phase of $MAPbBr_3$ [42]), depicting a greater influence of MHy^+ on the octahedra geometry.

The most common deformations occurring in the systems of linked octahedra are associated with the tilting along the in-plane or out-of-plane direction (Fig. 9b), identified through the Pb–X–Pb angles concerning Pb atoms of the adjacent octahedra (***θ_{in}*** and ***θ_{out}*** respectively, also expressed as $\boldsymbol{D_{in}} = 180° - \boldsymbol{\theta_{in}}$ and $\boldsymbol{D_{out}} = 180° - \boldsymbol{\theta_{out}}$). It is important to note, that the deviations from 180° do not have to entail tilting but may originate from the single octahedra distortions. Tilting in itself refers mainly to the relative rotation against each of the neighboring octahedra, which does not occur for the $MHyPbX_3$, but is present in several **2D** systems (*vide infra*).

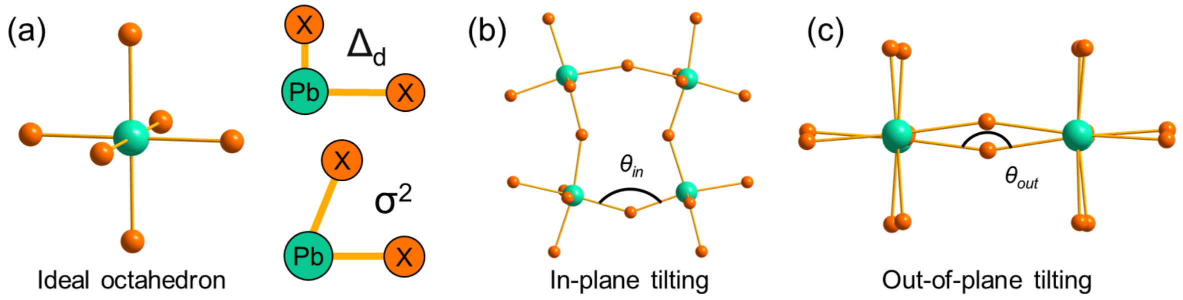

Figure 9. Parameters describing the distortions of (a) a single octahedra and (b) the linked octahedra systems [102].

The hallmark of the **3D** HOIPs comprising MHy^+, *i.e.*, a lack of a center of symmetry, induces the effects that require this specific structural property (examples illustrated in Fig. 10). The first of the described phenomena is a nonlinear optical process, where two photons with the same energy interact with the material, producing a new photon with doubled energy of the initial photons (equivalently: doubled frequency and half of the wavelength). This process, known as the **Second Harmonic Generation (SHG)** occurs for the noncentrosymmetric structures (besides the 432, 422, and 622 point groups) [103,104], and it may be utilized as a proving tool for the existence or absence of the center of symmetry. In both $MHyPbBr_3$ and $MHyPbCl_3$, the SHG response is present, with the intensity at RT equal to 0.18 and 0.03 of KDP, respectively (KDP = potassium dihydrogen phosphate, a reference material used in the Kurtz-Perry test [105]). Noncentrosymmetric materials may also exhibit, for instance, pyro-, piezo-, and ferroelectricity, opening new ways of applications in optoelectronics, including lasers, sensors, photodetectors, etc.

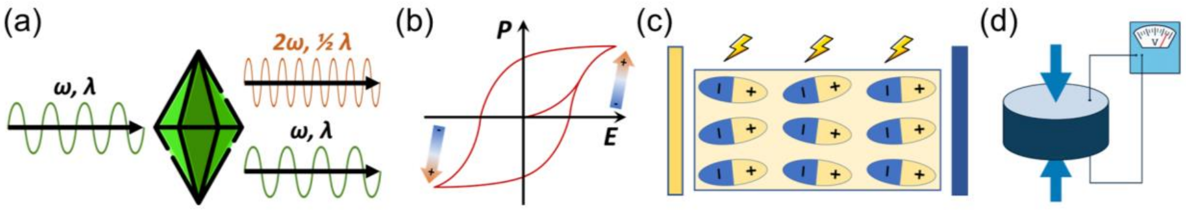

Figure 10. Examples of the phenomena that occur (or may occur) in the crystalline materials that adopt noncentrosymmetric phases: (a) Second Harmonic Generation (SHG), (b) ferroelectricity, (c) pyroelectricity and (d) piezoelectricity.

A genuinely exceptional feature of the MHy^+ lies in its size small enough to be a perovskitizer for **3D** structures, but **also sufficiently large to be a spacer for the 2D counterparts without the introduction of a second organic cation**. To the present day, **2D** lead halide HOIPs of the MHy_2PbX_4 formula have been reported for X = Br, Cl, I [106–108]. Ref. [108] describing MHy_2PbCl_4 is also a part of the thesis (**D3**) and thus, this section is limited to the description of the Br- and I-based compounds only.

Analogously to the **3D** analogs, MHy_2PbBr_4 crystallizes at RT in a polar symmetry. The crystal structure is presented in Fig. 11a. One may distinguish two types of intermolecular forces that anchor the organic moieties, namely N–H···N HBs and, similarly to **3D** perovskite, N–H···Br HBs. However, due to the reduced dimensionality of the inorganic part, only the apical Br^- ligands act as acceptors. The influence of MHy^+ on the octahedra geometry is therefore undermined, which is manifested in lower Δ_d and σ^2 ($2.2\cdot10^{-4}$ and 18.6 deg^2) as well as the decreased deviation of the Pb–Br–Pb angles from 180°. Consequently, MHy_2PbBr_4 is described in higher symmetry, *i.e.*, orthorhombic $Pmn2_1$ [42,107]. This phase is stable from the LT region (measured to 100 K) and upon 350 K on heating. Its polar character is confirmed by the SHG response. Contrarily to **3D** compounds, **MHy_2PbBr_4 demonstrates ferro-, pyro-, and piezoelectric properties** as well, originating from the existence of non-compensated MHy^+ dipoles and a spontaneous polarization along the polar [001] direction (Fig. 11a).

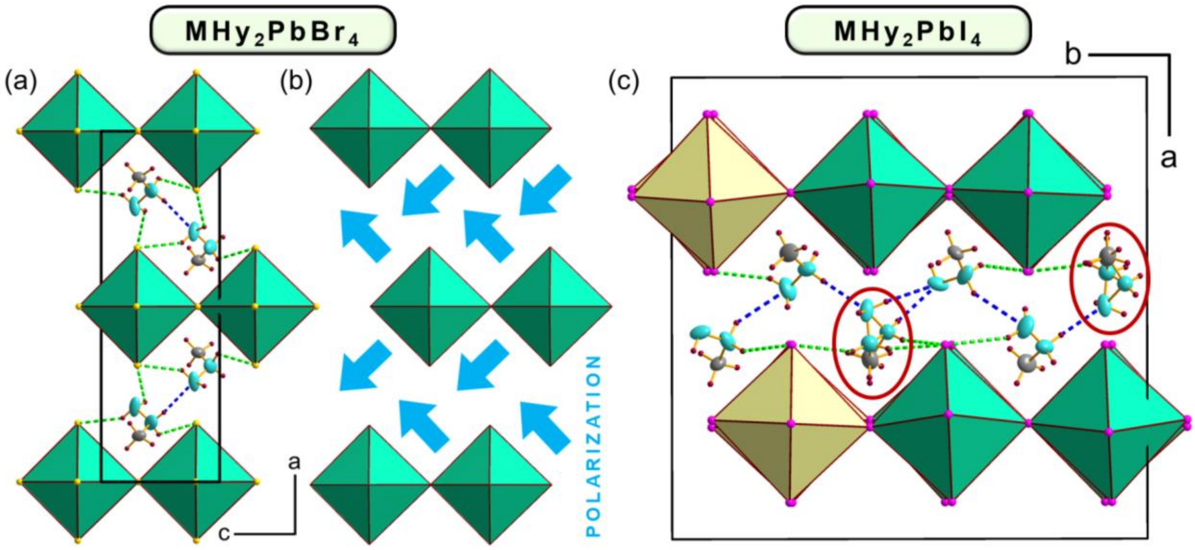

Figure 11. RT phases of (a) MHy_2PbBr_4 ($Pmn2_1$) and (b) MHy_2PbI_4 ($Pccn$). Green (blue dashed) lines represent N–H···X (N–H···N) HBs. Arrows in (a) represent locations of MHy^+ dipoles, oriented along the polar [001] direction. Red ovals in (b) indicate disordered MHy^+ cations [107,109].

MHy_2PbI_4 crystallizes in the orthorhombic, *Pccn* symmetry, with the unit cell markedly expanded when compared to the Br^- analog. This phase is stable from ca. 230 K up to nearly 300 K, at which exceeding the PT occurs (further described in the subchapter 6.6.). Nonetheless, a centrosymmetric character of MHy_2PbI_4 remains at all observed crystal phases [109]. The crystal structure at 280 K is depicted in Fig. 11b. Dynamic behavior of MHy^+ cations differs from the abovementioned compounds, as every third cation is disordered over two positions with a 0.7 to 0.3 ratio. Another distinguishing attribute is the existence of out-of-plane tilting, with D_{out} up to 7.9° along the [010] direction. The observed tilting system is thoroughly analyzed in ref. [64], pointing out that every third octahedron along the *b* direction is unique (marked with yellow color in Fig. 11b). Despite lower translational symmetry and more distorted perovskite layers, both Δ_d and σ^2 ($1.4 \cdot 10^{-4}$ and 11.9 deg^2 for the most distorted octahedron at 280 K) are reduced regarding MHy_2PbBr_4, which is a direct consequence of increased interatomic distances associated with the incorporation of the larger anion (I^-). Lastly, **MHy_2PbI_4 demonstrates an E_g of 2.20 eV – an exceptionally low value compared to other A_2PbI_4 2D HOIPs** [110–112]**, which is beneficial from the viewpoint of applications in photovoltaics.**

Benefiting from a high ability of MHy^+ to create an HBs network and its smaller $r_{A,eff}$ in comparison to other spacers (e.g., dimethylammonium – 272 pm, ethylammonium – 274 pm, guanidinium – 278 nm [56]), **MHy_2PbX_4 2D systems reveal record-breaking low interlayer distances among the lead halide 2D HOIPs.** They also exhibit a variety of PL emission colors upon changing temperature [107–109]. Apart from the single-layered RP structures, MHy^+ has also been reported to co-create multilayered (*n* = 3) **2D** compounds of the $BA_2MHy_2Pb_3Br_{10}$ formula (BA = butylammonium), in which it is situated in the intralayer space [113]. This material crystallizes in the noncentrosymmetric *Cc* group with a distorted inorganic substructure and reveals narrow PL associated with a shoulder peak originating from the trap states. In another trilayered material, *i.e.*, $IBA_2MHy_2Pb_3Br_{10}$ (IBA = isobutylammonium), a lone pair of electrons in MHy^+ induces the creation of directional dipoles, thereby generating bulk photovoltage and leading to polarization-dependent photocurrent [114]. This observation is beneficial for constructing polar multilayer materials and creating opportunities for highly sensitive polarized photodetection.

In the case of both **1D** and **0D** compounds, there are no reports on lead halide hybrids comprising MHy^+ hitherto. Nonetheless one may find papers regarding **1D** analogs with other metals. For chlorides with B = Co, Ni, Mn, and Cu, MHy^+ not only interacts with the inorganic part via HBs but also the terminal NH_2^+ group participates in a rare $[BCl_5N]$ coordination sphere [115,116]. MHy^+ has also been reported to embed in the **1D** materials with face-sharing double octahedra chains for $MHyCdCl_3$ and edge-sharing for MHy_2SbI_5 [117]. The second material exhibits notably low E_g of 2.01 eV (2.12 eV) for the polar (centrosymmetric) polymorph.

To summarize this subchapter, MHy^+ demonstrates exceptional ability to stabilize the **3D** and **2D** lead halide HOIPs, and the **1D** metal halide hybrids. **One may therefore presume the potential of MHy^+ to cocreate lower-dimensional structures with lead halides, as well as**

other structural types (e.g., ACI, (110)-oriented), giving rise to a wide variety of atomic alignments with notable structural and optoelectronic characteristics.

6.6. Polymorphism and phase transitions

In crystallography, polymorphism refers to the condition where a solid chemical compound can exist in multiple crystalline forms. These forms may vary in physical properties, although the chemical composition remains identical. Typically, one polymorph is stable within a certain temperature and pressure range, while another one is stable under different surrounding conditions [118]. At a specific temperature and pressure (namely inversion point) a reversible transition from one crystalline phase to another occurs. This process is known as **structural phase transition** or **polymorphic transition (PT, PTs for plural)** [119]. This paragraph, as well as the whole thesis, is aimed at the structural transformations as the function of temperature. The polymorphs for each material exhibiting PTs are annotated as I, II, III, etc., from higher to lower temperatures.

One of the first and widely known paths of classification of PTs was proposed by Ehrenfest in 1933, referring to discontinuity in the first or second derivative of the Gibbs free energy concerning a specific thermodynamic variable (e.g., temperature), thereby forming first-order and second-order PTs, respectively [120]. In other terms, a first-order transition is linked with an exchange of energy (latent heat) with the surroundings. The Ehrenfest classification does not need to be compliant with the alternations at the molecular level. A more adequate and also frequently encountered way of categorization, associated with structural modifications, was established by Buerger in 1961 and distinguishes [121]:

- **reconstructive PT** – involves a significant reorganization of the crystal structure, achieved by breaking and reforming the adjacent coordination bonds. One polymorph transforms into another with an unrelated structure.
- **displacive PT** – atoms and molecules exhibit small shifts. The main bonds are not broken, whereas changes in the coordination spheres may occur. Both polymorphs are symmetrically related (group-subgroup).
- **order-disorder PT** – a certain molecule adopts several positions in one polymorph and becomes ordered in the second one, and vice versa.

It should be noted that for most cases both polymorphs are described in different symmetry, however, one may also find examples of compounds with transitions occurring without a change of the space group, which is defined as the isostructural PT [122].

The most prevalent cause of temperature-induced PTs in lead halide hybrids is a change in the dynamics of the organic moieties, including their order-disorder behavior. This also applies to $MHyPbBr_3$, where the earlier mentioned RT phase ($P2_1$, **II**) is characterized by ordered MHy^+ cations. When heated, increasing interatomic distances diminish the intermolecular forces that stabilize the positions of MHy^+, eventually leading to PT above 418 K to the cubic $Pm\overline{3}m$ polymorph (**I**), in which the MHy^+ cations freely rotate within the perovskite cavities (Fig. 12a). The inorganic substructure in **I** consists of the ideal octahedra of O_h symmetry, with all Pb–Br bond lengths the same (3.018(1) Å at 430 K) and without octahedra distortions [42]. Phase **I** is centrosymmetric and isotypic to the $MAPbBr_3$ and $FAPbBr_3$ analogs [123,124]. The **II → I** PT is of an order-disorder type and is associated with a breaking of both HBs and $Pb(2)\cdots NH_2^+$ coordination bonds. It is also defined by the transition between polar and centrosymmetric polymorphs. The last feature is reflected in switchable dielectric and nonlinear optical behavior, i.e., step-like change of the dielectric constant (ε', Fig. 12b). The SHG signal vanishes in the area of the transition temperature and appears again after cooling down from HT to RT due to the PT [42].

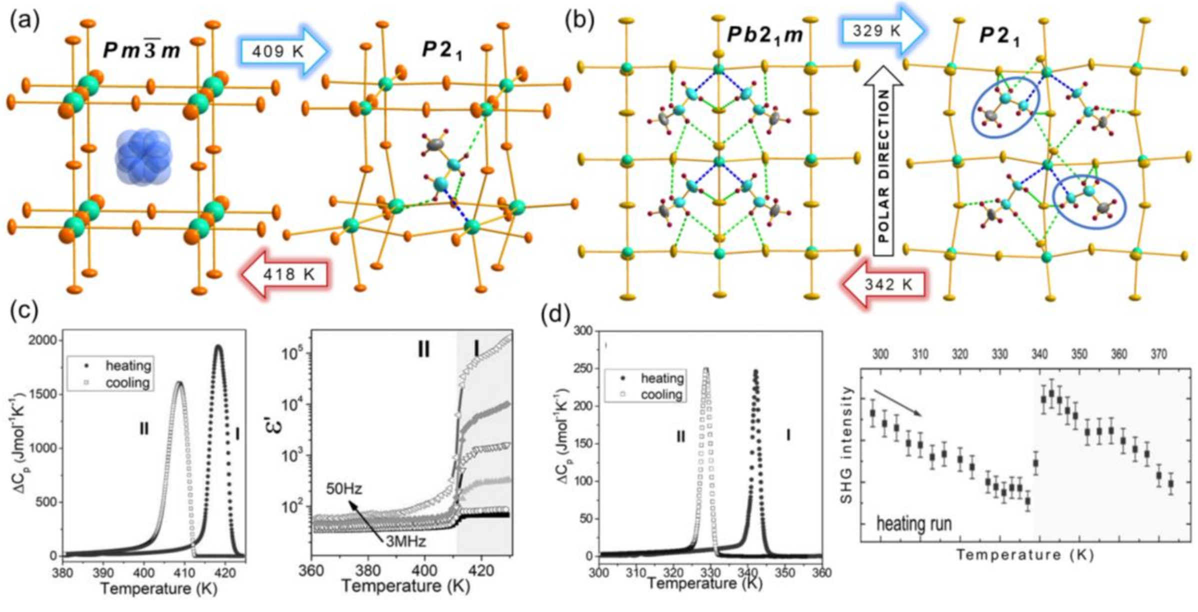

Figure 12. (a, b) HT and RT polymorphs of (a) $MHyPbBr_3$ ($Pm\overline{3}m$ and $P2_1$, respectively) and (b) $MHyPbCl_3$ ($Pb2_1m$ and $P2_1$, respectively) with the temperatures of PTs on cooling and heating. Reoriented MHy^+ cations upon PT are marked with a blue oval in (b). (c) Change in heat capacity (ΔC_p) and dielectric constant (ε') in $MHyPbBr_3$. (d) Change in ΔC_p and intensity of SHG signal on a heating run in $MHyPbCl_3$. All plots in (c, d) are presented as a function of temperature [42,43].

The strength of intermolecular interactions in $MHyPbCl_3$ ($P2_1$ at RT, **II**) is greater than in Br^- analog, owing to reduced bond lengths. In this case, therefore, there is no transition to the structure with heavily disordered organic moieties upon heating. In turn, above 342 K a PT occurs to another polar polymorph – orthorhombic, $Pb2_1m$ (**I**) [43]. The MHy^+ cations in **I** are still ordered, the number of inequivalent Pb atoms remains the same, and the distortions of the perovskite substructure are marginally changed in comparison to **II**. Nevertheless, the rearrangement of every second MHy^+ cation and the HBs system occurs, as presented in Fig. 12c. The reorganization is also manifested in a reduction of the independent positions of MHy^+ from two to one, prompting the formation of new N–H···Cl HBs involving the middle NH_2 group. The Pb(2)···NH_2^+ coordination bond length remains unchanged at 2.88 Å. According to Buerger classification and the International Tables for Crystallography [125], the **I** → **II** PT is of displacive type with the group-subgroup relation – $P2_1$ is the maximal subgroup of $Pb2_1m$. From the perspective of MHy^+ dipoles, the spontaneous polarization along the polar direction increases upon the **II** → **I** PT. This translates to an exceptional nonlinear property. As depicted in Fig. 12d, the intensity of the SHG signal progressively decreases when heated until ca. 337 K, where it then abruptly increases by ~50% due to the **II** → **I** PT. Accordingly, upon cooling from HT to RT, the signal decreases by ~40% around 330 K, confirming the reversibility of PT. Hence, $MHyPbCl_3$ demonstrates switching between two SHG-active states, with greater activity exhibited by the HT phase **II** [43].

In the **2D** material of the MHy_2PbBr_4 formula, the polar RT polymorph ($Pmn2_1$, **III**) undergoes two PTs, both in the HT area, as illustrated in Fig. 13a. The first PT occurs when heated above 351 K. The low-intensity diffraction peaks appear, indicating the modulated structure with the modulation vector $\boldsymbol{q^*} = 0.25b^*$. This corresponds to a fourfold increase of the *b* parameter and the unit cell expansion along the [010] direction. The modulated HT polymorph **II** is stable only within a narrow temperature range (15 – 20 K) and thus may be considered as a metastable phase. Adding this to the very weak intensity of satellite peaks, the structure model has not been obtained. Nevertheless, the averaged structure was determined in the *Pmnm* centrosymmetric space group, suggesting the disruption of the ferroelectric ordering characteristic for **III**. Upon heating above 371 K, the modulations disappear, and the symmetry of the averaged structure becomes the proper one. The characteristic feature of the HT polymorph **I** (*Pmnm*) is the disorder of MHy^+ cations, which are split into two equivalent positions with equal probability over the mirror plane. The thermally induced disorder prevents the formation of a stable network of the N–H···Br and N–H···N HBs. The weakened interactions mitigate the octahedra distortion, expressed in lower σ^2 for **I** (11.3 deg^2 at 380 K) in comparison to **III** (18.6 deg^2 at 300 K) [107]. Another difference between phases **I** and **III** is the off-center displacement of Pb in the polar polymorph, which produces net dipoles contributing to the ferroelectric properties.

Analyzing the crystal structure alternations in MHy$_2$PbBr$_4$ one may assume that the modulated phase **II** also demonstrates unique dynamics of the organic moieties, and therefore the PTs are of order-disorder type. Analogously to the **3D** Br-based analog, structural transitions are coupled with the presence of a center of symmetry. It is revealed in the absence of SHG response in phases **I** and **II** (Fig. 13b), thus confirming their centrosymmetric nature. In the case of dielectric measurements, a step-like change of ε' around the temperatures of PTs is observed, and, with the implementation of Curie-Weiss law, it is concluded that the PT has a ferroelectric (**III**) to paraelectric (**I**) character [107].

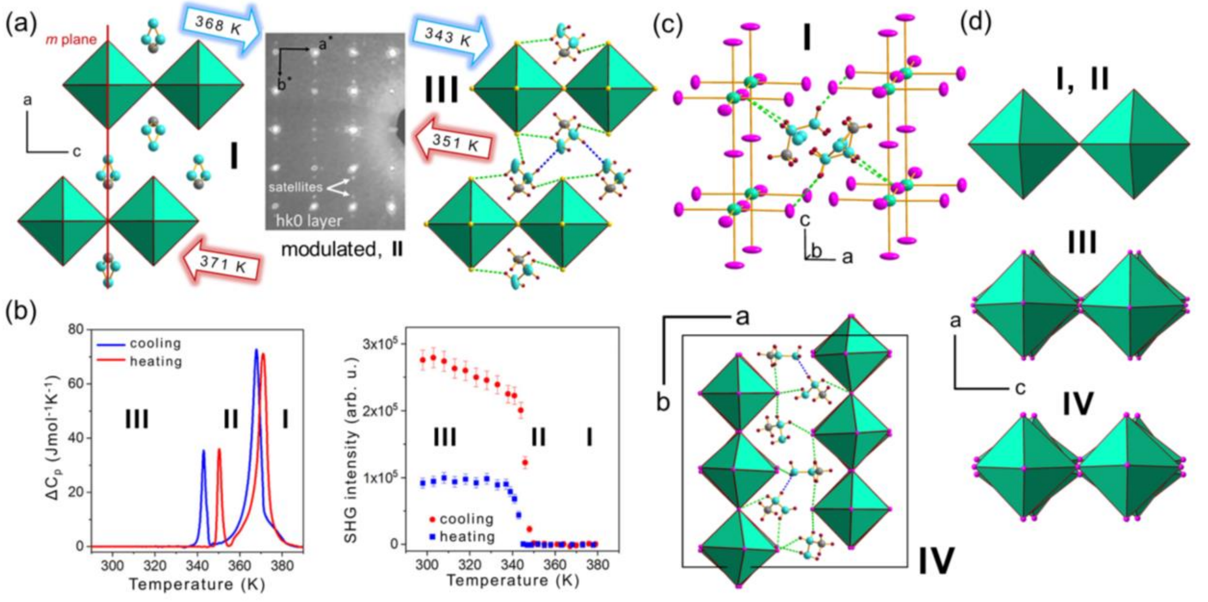

Figure 13. (a) The crystal structures of MHy$_2$PbBr$_4$ in *Pmnm* (**I**) and $Pmn2_1$ (**III**) with the temperatures of PTs upon cooling (blue arrows) and heating (red arrows). (b) The change in ΔC_p associated with PTs and integral intensities of the SHG signal of MHy$_2$PbBr$_4$ for heating (red) and cooling (blue) runs. (c) The crystal structures of MHy$_2$PbBr$_4$ in *Pmmn* (**I**) and $P\bar{1}$ (**IV**). The tilting of $[PbI_6]^{4-}$ octahedra in subsequent polymorphs projected along the [010] direction [107,109].

The last compound in this subchapter, i.e., MHy$_2$PbI$_4$ **2D** HOIP is the only one described herein that exhibits the PTs in both heating and cooling starting from the RT phase. To maintain clarity, the polymorphs are described starting from the highest temperature. The HT polymorph **I** (stable above ~320 K) is isostructural to the HT phase of MHy$_2$PbBr$_4$, adopting an orthorhombic *Pmmn* symmetry. However, the dynamics of MHy$^+$ differs from the one for Br analog, as the organic moieties are disordered not over two, but three positions linked to a rotation along the long axis (Fig. 13c). The first PT occurs after cooling below 318 K and is of isostructural type, leading to another polymorph of the same symmetry (*Pmmn*, **II**). Further cooling induces the **II** → **III** PT below 295 K to the RT polymorph (*Pccn*, **III**), described previously. **III** is characterized by notably expanded unit cell volume when compared to **II**, as the *b* and *c* are tripled and doubled, respectively [109]. This is a consequence of a partial stabilization of MHy^+ positions, i.e., one of three independent cations remains disordered over two positions with a 0.7 to 0.3 ratio (*vide infra*, Fig. 11b). The last PT occurs below 233 K, leading to the triclinic LT polymorph of $P\overline{1}$ symmetry (**IV**). In **IV**, all atoms are ordered. The abundant network of N–H···I HBs is created, involving each of the 24 inequivalent iodides as acceptors. Both symmetry reduction and anchoring of the MHy^+ cations provoke out-of-plane tilting, which is present in **III** and **IV**, reaching the max. D_{out} values of 7.9° and 13.5°, respectively. Despite the lack of noncentrosymmetric phases, MHy_2PbI_4 demonstrates a switchable dielectric behavior arising from the order-disorder nature of PTs, displayed in a step-like change of the dielectric permittivity around 295-300 K. The ordering of MHy^+ upon **III → IV** PT is responsible for the dipolar relaxation process observed ~250 K [109].

Recognizing the significant impact of halide substitution on revealed structural and optoelectronic properties of MHy-based hybrid perovskites, **both the A-site and especially X-site alloying approaches may be incorporated into these materials. This might potentially open the way for new materials with retained benefits of their single-site parental structures**.

7. Experimental section

Details about every experimental method are given in the **D1** – **D6** articles. Herein, a general overview of the synthesis, crystallization, and structural analysis, is provided.

7.1. Synthesis and Crystallization Methods

All the chemical reagents and solvents, i.e., PbX_2 (X = Br, Cl, I, all 98% pure), HCl (37% wt. in H_2O), HBr (48% wt. in H_2O), HI (37% wt. in H_2O, stabilized with H_3PO_2), methylhydrazine (MHy, 98%), imidazole (IM, 99.5%), *N*, *N*-dimethylformamide (DMF, 99.8%), methyl acetate (99.5%) and propylene carbonate (99.7%) were commercially available (purchased from Sigma-Aldrich) and utilized without further purification.

All compounds investigated in the presented papers were synthesized using wet chemical methods. The precursor solution, containing methylhydrazine, lead halide salts, HX acids (X = Br, Cl, I), and other chemical compounds (depending on the final composition and the crystallization method) was vigorously stirred at 30-50 °C, until the complete dissolving of the reagents. Three different crystallization techniques have been used in total (Fig. 14). In the antisolvent approach, utilized in **D1**, **D3**, and **D5**, the solution was placed in a glass vial, which was then placed inside a larger vial containing methyl acetate. The outer vial was sealed tightly, while the inner vial's lid was loosened to enable the diffusion of the methyl acetate to the precursor solution. In **D1** and **D3**, this technique required the additional solvent (DMF), introduced after prior neutralization (pH = 7) of the precursor mixture. In **D2**, **D4**, and **D6**, the

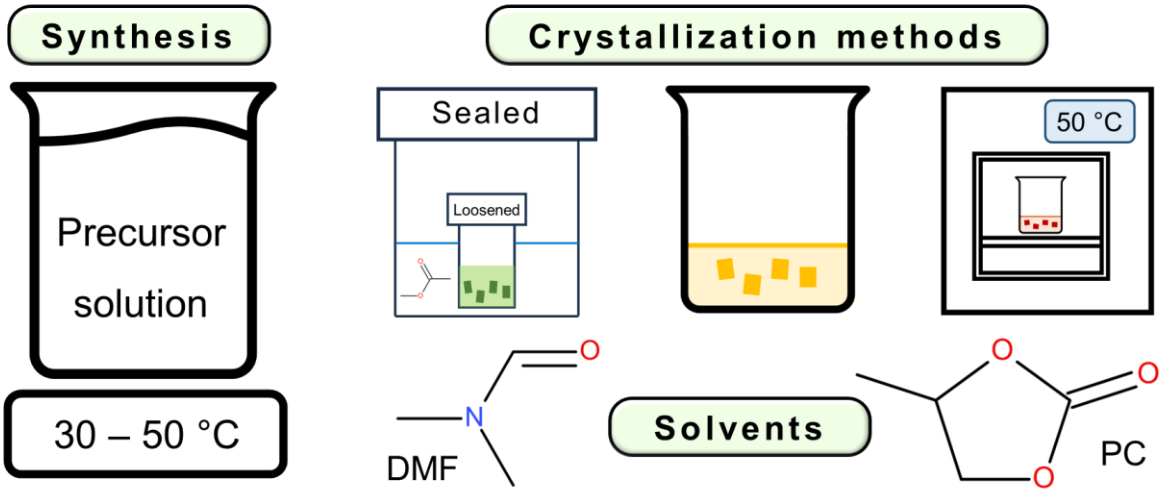

Figure 14. (left) Illustration of the synthesis of the compounds reported in **D1** – **D6**. (upper right) methods of crystallization: antisolvent, crystallization ambient conditions, and storage at 50 °C. (lower right) additional solvents used: *N*,*N*-dimethylformamide (DMF, **D1** – **D4**) and propylene carbonate (PC, **D2**, **D6**).

precursor solution, containing the DMF (**D2**, **D4**) or PC (**D6**) was left undisturbed at RT. To synthesize the compounds with greater iodine contribution in **D2**, the clear solution dissolved in PC was stored in a glass vial at 50 °C. Single crystals were harvested after 2-7 days, extracted from the mother liquid, and dried at RT. The series of mixed-halide single crystals (**D1**, **D2**) is presented in Fig. 15.

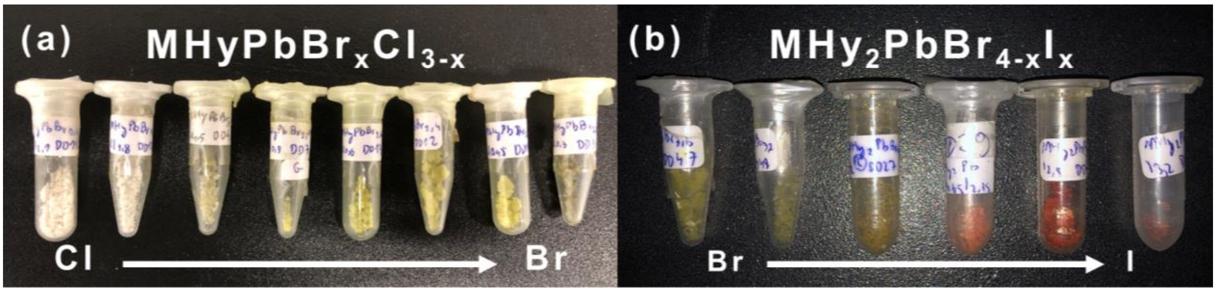

Figure 15. Series of single crystals with two halides at the 'X' site. (a) **3D** HOIPs of the $MHyPbBr_xCl_{3-x}$ formula (x = 0.40, 0.58, 0.85, 1.33, 1.95, 2.25, 2.55) – **D1**. (b) **2D** HOIPs of the $MHy_2PbBr_{4-x}I_x$ formula (x = 0.25, 0.3, 0.4, 1.1, 2.35, 2.5, 3.1) – **D2**.

7.2. X-ray diffraction

Single-crystal X-ray diffraction (SCXRD) experiments were conducted using an Xcalibur four-circle diffractometer (Oxford Diffraction) equipped with an Atlas CCD detector and graphite-monochromated MoKα radiation (λ = 0.7107 Å). SCXRD experiments in nonambient conditions were carried out with the Oxford Cryostream open-flow cooler. Absorption was corrected using multi-scan methods with CrysAlis PRO 1.171.41.93a (Rigaku Oxford Diffraction, 2020). Empirical absorption correction was employed, utilizing spherical harmonics, executed in the SCALE3 ABSPACK scaling algorithm. All crystal structures were solved in the Olex2 software with the SHELXT program [126,127]. For all non-modulated phases, the least-squares refinement was performed using SHELXL [128]. Hydrogen atoms were inserted at calculated positions and treated as riding atoms. Refinement of the modulated phases (**D2**, **D3**) was conducted in Jana2020 [129], with the application of the (3 + 1) superspace approach. In both cases, the refinement started from the inorganic part, modulated assuming positional modulation with first-order harmonics. The same procedure was applied to the organic part in **D2**, whereas in **D3** the occupational modulation was adopted to MHy^+, using a crenel function ($\Delta x_4 = 0.5$) and positional modulation functions described as harmonics within the (0,1) interval. The tables containing the main experimental details from the SCXRD measurements are provided in the supplementary information in all publications. The crystal structures are deposited in the Cambridge Crystallographic Data Centre (CCDC [130]).

Powder X-ray diffraction patterns of the grounded samples were measured in reflection mode using an X'Pert PRO X-ray diffraction system equipped with a PIXcel ultrafast line detector and Soller slits for CuKα radiation (λ = 1.5406 Å). High-temperature (HT) experiments (**D2**, **D5**) were conducted with the Anton Paar Oven Chamber.

7.3. Initial characterization

Initial characterization of the synthesized materials involved Raman spectroscopy (Bruker FT MultiRam spectrometer with the YAG:Nd laser excitation at 1064 nm) and powder X-ray diffraction of bulk samples (described above).

For the mixed-halide systems (**D1**, **D2**), the examination of the chemical composition via Energy Dispersive X-ray Analysis (EDAX) was applied, with the FEI Nova NanoSEM 230 scanning electron microscope. The measurements were performed by Dr Damian Szymański from ILT&SR PAS. The results obtained from the EDAX were compared with the calculations of the halide occupancy on SCXRD models (Fig. 16). The accuracy of EDAX measurements is specified below, provided by the manufacturer.

Quantitative analysis accuracy for standardless analysis

Results (in wt.%)	**Description**	**Relative %**
20 – 100	Main element	2%
5 – 20	Major element	4%
1 – 5	Minor element	10 – 20%
0.2 – 1	Trace element	50 – 100%

Example: Pb = 21.13% ± 2% of 21.13% (0.42%)
Result: 21.13 ± 0.42%

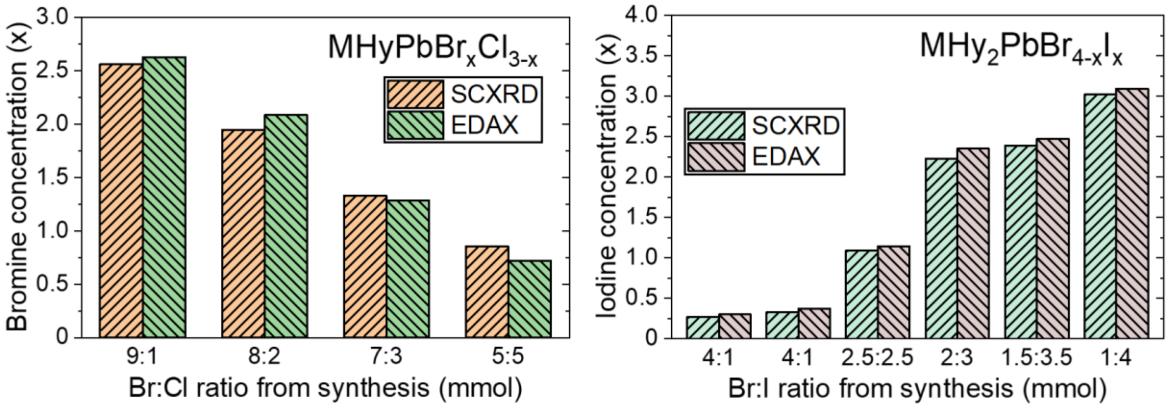

Figure 16. Comparison of halide concentration determined via SCXRD experiments and EDAX analysis for (left) $MHyPbBr_xCl_{3-x}$ (**D1**) and (right) $MHy_2PbBr_{4-x}I_x$ (**D2**). For SCXRD models compositions were determined through free variables refinement of the halides site occupancy.

8. Results published in the series of D1-D6 articles

The summaries of each publication constituting the thesis are provided in this section. Full versions are included in the Appendices.


THE JOURNAL OF PHYSICAL CHEMISTRY C
A JOURNAL OF THE AMERICAN CHEMICAL SOCIETY

pubs.acs.org/JPCC
Article

Three-Dimensional Methylhydrazinium Lead Halide Perovskites: Structural Changes and Effects on Dielectric, Linear, and Nonlinear Optical Properties Entailed by the Halide Tuning

Dawid Drozdowski, Anna Gągor, Dagmara Stefańska, Jan K. Zaręba, Katarzyna Fedoruk,
Mirosław Mączka,* and Adam Sieradzki

D1

The **D1** article describes the synthesis of seven new mixed-halide **3D** HOIPs of the $MHyPbBr_xCl_{3-x}$ formula ($x = 0.40$, 0.58, 0.85, 1.33, 1.95, 2.25, and 2.55) and a Br−I co-doped material – $MHyPbBr_{2.8}I_{0.2}$ (formulas determined from the EDAX analysis). The study involves the preparation of a (x, T) phase diagram based on SCXRD and differential scanning calorimetry (DSC) experiments. The impact of the structural changes and X-site alloying on dielectric, linear, and second-order nonlinear optical properties is examined, utilizing the Broadband Dielectric Spectroscopy (BDS), measurements of absorption and PL emission, and examination of the SHG response via Kurtz-Perry test. **D1** refers to previous studies on $MHyPbBr_3$ and $MHyPbCl_3$ [42,43]. Despite large TF values (1.05 and 1.03) both materials adopt **3D** perovskite alignment and stand out among lead halide HOIPs by crystallizing in polar ($P2_1$) symmetry with profoundly distorted inorganic substructure. $MHyPbBr_3$ undergoes a $P2_1 \rightarrow Pm\bar{3}m$ PT at 418 K, exhibiting a switchable dielectric behavior, whereas $MHyPbCl_3$ displays $P2_1 \rightarrow Pb2_1m$ PT, manifested in a unique feature, i.e., enhanced SHG response in HT phase. **This work examines and underscores the potential of halide-alloying in MHy-based 3D perovskites, demonstrating a substantial tunability of structural, optical, and dielectric characteristics.**

As shown in the (x, T) phase diagram (Fig. 17g), $MHyPbBr_xCl_{3-x}$ systems abundant in bromine ($x \geq 1.33$) exhibit three polymorphic phases – cubic $Pm\bar{3}m$ (**I**), orthorhombic $Pb2_1m$ (**II**) and monoclinic $P2_1$ (**III**), whereas two polymorphs (**II** and **III**) are observed in the chloride-rich area. Phase **I**, which appears at $T_1 \geq 409$ K, is centrosymmetric and isostructural to the HT phase of $MHyPbBr_3$. The MHy^+ cations freely rotate, exerting no noticeable influence on the shape of the inorganic substructure, and thus the $[PbX_6]^{4-}$ octahedra (X = halide) are of O_h symmetry (Fig. 17a, d). It is worth mentioning that the cubic $Pm\bar{3}m$ symmetry is an aristotype of both inorganic and hybrid perovskites. The noncentrosymmetric **II** (HT analog of $MHyPbCl_3$) is stable at $T_2 \geq 318$ K. The **I → II** PT involves the positional ordering of MHy^+, leading to their spontaneous polarization along the polar [010] direction (Fig. 17b). Further reorganization of the organic cations occurs in **III** (also polar, RT polymorph of both $MHyPbBr_3$ and $MHyPbCl_3$), with every second MHy^+ dipole aligning more in (010) planes rather than along the [010] direction (Fig. 17c). In the polar polymorphs, MHy^+ disrupts the coordination sphere of $Pb(2)X_6$, bringing a heavy distortion to these octahedra (Fig. 17 e, f).

The σ^2 values for $MHyPbBr_xCl_{3-x}$ series are in the range of 14–21 deg^2 and 301–314 deg^2 for $Pb(1)X_6$ and $Pb(2)X_6$, respectively, increasing along with Cl contribution. The $Pb(2)\cdots NH_2^+$ coordination bonds elongate with increasing Br content, consequently diminishing the strength of intermolecular interactions. Along with x, the volume of the void housing the organic cations expands, reaching the minimum value (~77 Å^3) to allow the free rotation of MHy^+ (crucial condition for stable phase **I**) for $x \geq 1.95$ (Fig. 17h), which agrees with the experimental observations.

$MHyPbBr_{2.8}I_{0.2}$ crystallizes in polar $P2_1$ symmetry, isostructural to **III**. Above 411 K (390 K) on heating (cooling) a PT to cubic $Pm\overline{3}m$ phase occurs, with lattice parameter $a = 6.046(5)$ Å at 400 K. This transition occurs at lower temperatures compared to Br^- analog, (418 K (409 K) on heating (cooling)), indicating the role of the iodine in the stabilization of the cubic phase at lower temperature. Further observation of this trend was not possible, as the syntheses towards higher iodide content led to a non-perovskite phase, described in **D5**.

The halide substitution in $MHyPbBr_xCl_{3-x}$ remarkably changes the electric properties. The activation energy of Cl^- ionic conductivity rises with growing Br^- content in phases **II** and **III**, while in **I**, the conductivity of Br^- ion heightens with increasing Cl^- content. In the case of optical properties, the E_g narrows, and PL bands display a redshift when going from Cl^- to Br^- and subsequently to I^-. PL color shifts from greenish blue for Cl-rich samples to yellowish-green for $MHyPbBr_{2.8}I_{0.2}$. SHG measurements reveal that the incorporation of Br to $MHyPbCl_3$ reduces the disparity in SHG signal intensities between phases **I** and **II**. The relative SHG efficiencies of Br−Cl mixed materials at RT enhance with increasing Br content.

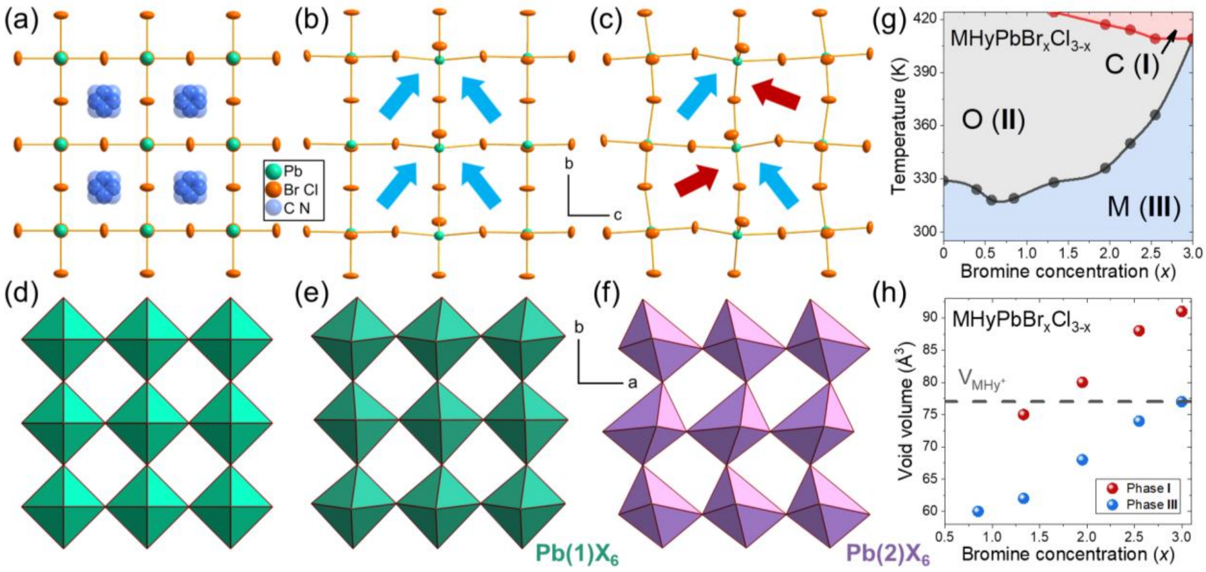

Figure 17. (a-c) Crystal structure of MHyPbBr$_x$Cl$_{3-x}$ in phases **I**, **II**, and **III**, respectively. Arrows in (b, c) represent MHy$^+$ dipoles. (d-f) Single [100] PbX$_6$ octahedra (X = Br, Cl) layer. (g) (*x*, T) phase diagram. (h) Void volume vs *x* – dashed line denotes the volume of freely-rotating MHy$^+$ cation.

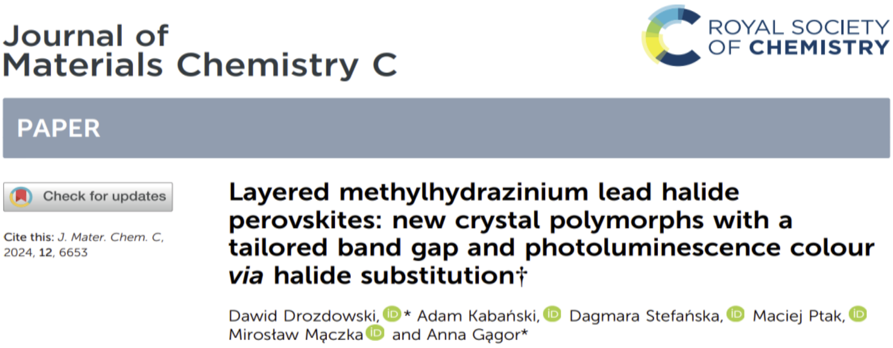

Journal of
Materials Chemistry C

ROYAL SOCIETY
OF CHEMISTRY

PAPER

Check for updates

Cite this: *J. Mater. Chem. C*, 2024, 12, 6653

Layered methylhydrazinium lead halide perovskites: new crystal polymorphs with a tailored band gap and photoluminescence colour *via* halide substitution†

Dawid Drozdowski,* Adam Kabański, Dagmara Stefańska, Maciej Ptak, Mirosław Mączka and Anna Gągor*

D2

This report includes a synthesis of the **2D** HOIPs series of MHy$_2$PbBr$_{4-x}$I$_x$ formula across a wide concentration (*x* = 0.25, 0.3, 0.4, 1.1, 2.35, 2.5, 3.1, formulas derived from the EDAX analysis). The study involves the crystal structure determination on both single-crystal and powdered samples, preparation of the (*x*, T) phase diagram, Raman and diffuse reflectance spectroscopy (DRS), and the PL properties as a function of temperature and halide concentration. The choice of the Br-I system is dictated by the previous studies on MHy$_2$PbBr$_4$ and MHy$_2$PbI$_4$ [107,109]. Both compounds are characterized by exceptionally low interlayer distances among **2D** lead halide HOIPs. MHy$_2$PbBr$_4$ is ferroelectric in a broad temperature range (*Pmn*2$_1$ phase below 343 K) and undergoes two PTs on heating – through the modulated intermediate phase to centrosymmetric *Pmnm*. MHy$_2$PbI$_4$ reveals two polymorphs besides the *Pmmn*, namely *Pccn* (below 295 K) and $P\overline{1}$ (below 233 K), and exhibits a distinctive octahedra tilting system with remarkably low E_g of 2.20 eV. Notably different symmetries of both materials result in an **abundant polymorphism in MHy$_2$PbBr$_{4-x}$I$_x$ driven by the temperature and halides ratio.**

Furthermore, D2 once again demonstrates the facile tunability of selected physicochemical properties accomplished via X-site alloying.

$MHy_2PbBr_{4-x}I_x$ crystallize in RP **2D** perovskite alignment with corner-sharing $[PbX_6]^{-4}$ (X = Br, I) octahedra creating (010) slabs, spaced by the MHy^+ cations. The (*x*, T) phase diagram is presented in Fig. 18a, segmented into 3 areas with varying iodine content. The boundaries are determined by the symmetry of LT (RT) phases between the 1st and 2nd (2nd and 3rd) zones.

The HT phase in the 1st and 2nd region ($0.2 < x < 2.2$) is of *Pmmn* orthorhombic symmetry (**II**), being isostructural to other halide-based analogs [107–109]. The crystal structure consists of slightly distorted octahedra layers with the MHy^+ moieties divided into two symmetrically equivalent positions with equal probability. The RT phase (**III**), for $0.2 < x < 2.2$, is of orthorhombic *Pnma* symmetry, ($a' = 2a$ superstructure of **II**). The individual octahedra contain three symmetrically inequivalent halide positions, i.e., X1, X2 (bridging along [001] and [100] directions, respectively) and an apical X3. In both **II** and **III**, the octahedra are marginally distorted with $\Delta_d = 2.6 \cdot 10^{-4}$ and $\sigma^2 = 13.8$ deg^2. The MHy^+ cations remain disordered in **III** but occupy two nonequivalent positions with unequal probabilities (0.65:0.35). A few N–H···N and N–H···X HBs form, primarily involving the apical halides as acceptors.

The ferroelectric ordering, an attribute of MHy_2PbBr_4, is disrupted even for the compositions with $x = 0.25$. For $0.2 < x < 1$ and below 220–230 K, a PT occurs, with the symmetry reduction to the monoclinic $P2_1/c$ space group (**IV**, $c' = 2c$ superstructure of **III**). The crystal structure in **IV** is shown in Fig. 18c. All atoms are situated in general positions, and the MHy^+ cations are ordered, being anchored via N–H···N and N–H···X HBs. The symmetry breaking also strengthens the intermolecular interactions, manifested in Δ_d and σ^2 parameters increasing to $8.7 \cdot 10^{-4}$ and $\sigma^2 = 26.9$ deg^2, respectively, and provokes the out-of-plane tilting of the perovskite layers with D_{out} up to 17.9°. For $1 < x < 2.2$ the *mmmF*1 symmetry reduction (following the Aizu notation [131]) occurs upon cooling, leading to the LT phase of triclinic, $P\overline{1}$ space group (**V**). Analogously to **IV**, **V** is $c' = 2c$ superstructure of **III**, but the lower symmetry and augmented iodine contribution lead to a greater number of inequivalent positions of MHy^+ (8 vs 4) and moderate suppression of the octahedra deformation ($\Delta_d = 5.5 \cdot 10^{-4}$, $\sigma^2 = 16.5$ deg^2 and $D_{out} = 16.5°$).

In the iodine-rich area ($x > 2.2$), a reconstructive transformation occurs in the HT zone – the layered structure transforms into the **3D** perovskite with heavily disordered organic cations (Fig. 18d). For the $MHy_2PbBr_{1.5}I_{2.5}$ composition, the crystal structure was refined in the cubic

$Pm\overline{3}m$ symmetry (**I**) with a = 6.270(3) Å at 350 K. Phase **I** was also recorded for powdered $MHy_2PbBr_{3.7}I_{0.3}$ with a = 5.992(3) Å at RT, preceded by heating to 420 K. **The presence of the 3D phase addresses the stabilization challenge of lead iodide hybrids (the 3D has not been obtained through chemical synthesis thus far), offering a resolution by incorporating bromine**, as in the previous reports on FA-based analogs [132].

The RT phase for $x > 2.2$ is incommensurately modulated, described in $Pnma(00\gamma)0s0$ superspace symmetry (**VI**) with the modulation vector $\boldsymbol{q^*}$ decreasing along with increasing iodine contribution – from 0.46 for $x = 2.35$ to 0.44 for $x = 3.1$. The modulation involves positional shifts of all atoms along the [010] direction. The largest displacement amplitude is observed for the halides at the X2 site (Fig. 18e-f). Considering that both X1 and X3 sites serve as proton acceptors in N–H···X HBs, bromides are favored at these positions. Consequently, X2 is almost entirely occupied by iodide, being less affected by the intermolecular forces (Fig. 18f). Unlike phase **III**, **VI** exhibits tilted octahedral layers with a maximum D_{out} of 14.45°, marginally lower than in **IV** and **V**. The MHy^+ moieties are well-ordered in **VI**, evidenced by the absence of a PT upon cooling. The average symmetry of **VI** differs from the intermediate phase of MHy_2PbBr_4 (*Pmnm*) and is stabilized in a wide temperature range.

The impact of halide substitution on geometric parameters in $MHy_2PbBr_{4-x}I_x$ is depicted in Fig. 18g. As mentioned above, iodine prefers to occupy the X2 site (non-involved in HBs), which is particularly evident in the $x > 2.2$ range. The occupancy at X2 for low x values does not notably alter the distances between the layers. The lattice parameter b (perpendicular to the layers) increases substantially for higher x values at the apical X3 site. The increasing I^- contribution also mitigates octahedral deformation and influences thermal equilibrium, stabilizing LT phases of different symmetry (**IV** and **V**) at comparable temperatures. The juxtaposition of RT structures and single-halide analogs reveals a relationship between lattice parameters and iodine concentration: a doubling of the a occurs initially, and in phase **VI**, the $\boldsymbol{q^*}$ approaches $0.33c^*$, corresponding to the $3c$ supercell, characteristic of the RT phase of MHy_2PbI_4 (Fig. 18b).

Raman spectroscopy confirmed the altered MHy^+ dynamics at RT in mixed-halide compounds compared to single-halide compounds, with MHy^+ movements freezing at low temperatures. Linear optical analysis revealed a redshift in excitonic absorption bands at RT (from 445 to 554 nm) and a reduction of E_g from 2.91 eV to 2.31 eV for $0.3 \leq x \leq 3.1$ (Fig. 18h). In addition, a noticeable change in PL color is observed – from bluish green for $x = 0.3$ to yellow-green for $x = 2.5$, alongside a shift in PL bands from 478 nm ($x = 0.3$) to 557 nm ($x = 2.5$).

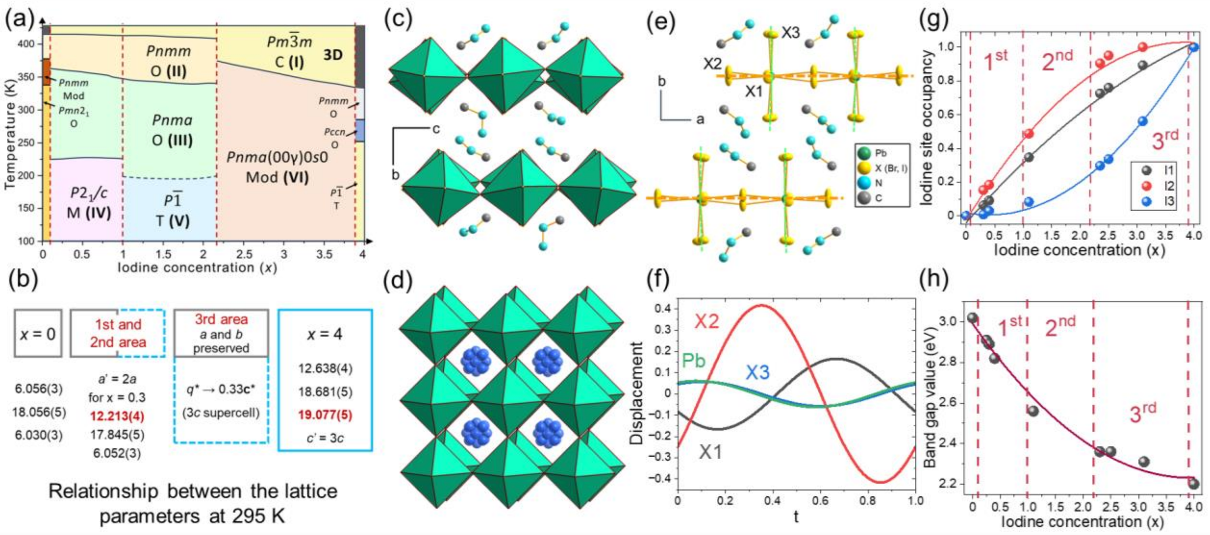

Figure 18. (a) The (x, T) phase diagram of $MHy_2PbBr_{4-x}I_x$ divided into three regions based on the halide concentration. (b) The relationship between lattice parameters of $MHy_2PbBr_{4-x}I_x$ series at RT. (c) $MHy_2PbBr_{3.7}I_{0.3}$ in $P2_1/c$ (**IV**, 100 K) with ordered MHy^+ cations. (d) The crystal structure for $x = 2.5$ at 350 K in $Pm\bar{3}m$ (**I**), after the **2D → 3D** reconstructive transition. (e) $MHy_2PbBr_{0.9}I_{3.1}$ in the incommensurately modulated symmetry ($Pnma(00\gamma)0s0$, **VI**) at 295 K. Dashed lines depict the coordinates of X1 (orange) and X3 (green). (f) The displacement curves of Pb and halide (X) atoms along the b direction. (g) Iodine site occupancy and (h) band gap value at 295 K vs x.

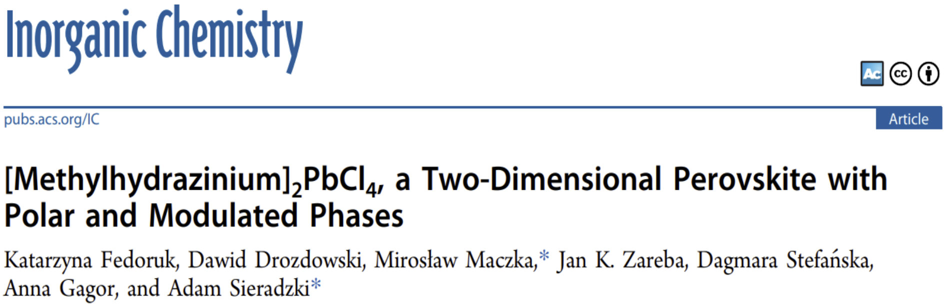

Inorganic Chemistry

pubs.acs.org/IC

Article

[Methylhydrazinium]$_2$PbCl$_4$, a Two-Dimensional Perovskite with Polar and Modulated Phases

Katarzyna Fedoruk, Dawid Drozdowski, Mirosław Mączka,* Jan K. Zaręba, Dagmara Stefańska, Anna Gągor, and Adam Sieradzki*

D3

The **D3** article outlines the synthesis and structure-property relations of the newcomer to the **2D** HOIPs family – MHy_2PbCl_4. The multi-technique investigation is performed, including the crystal structure analysis via XRD combined with DSC, electrical measurements (BDS and the field-dependent polarization), Raman spectroscopy, and the examination of nonlinear (SHG) and linear optical (DRS, PL) properties. **Studies on MHy_2PbCl_4 serve as another illustration of MHy-directed creation of the polar polymorphs in 2D perovskites, coupled with the centrosymmetric and rarely observed modulated phase.**

MHy_2PbCl_4 represents the Ruddlesden-Popper structural type of **2D** compounds and is characterized by complex HT to LT phase behavior. Three distinct crystal polymorphs are observed – HT phase **I** of orthorhombic, centrosymmetric $Pmmn$ symmetry, modulated RT phase **II** (below 332 K), described in $Pmmn(00\gamma)s00$ superspace group, and the LT phase (**III**) of monoclinic, polar $P2_1$ symmetry (below 205 K).

The structure of **I** (Fig. 19a) consists of corner-sharing $[PbCl_6]^{4-}$ octahedra layers, propagating along [010] direction, interspersed with MHy^+ cations. MHy^+ is disordered over the *m* mirror plane, occupying two positions with equal probability. Phase **I** exhibits the same symmetry as the HT polymorphs of the MHy_2PbX_4 (X = Br, I) [107,109]. The smaller ionic radius of Cl^- leads to a decrease in the interlayer distance (8.97 Å at 350 K) and stronger intermolecular interactions, evidenced by heightened Δ_d and σ^2 parameters ($1.6 \cdot 10^{-3}$ and 14.4 deg^2) when compared to Br- and I-based analogs.

Lowering the temperature results in the interlayer distance reduction to 8.66 Å at RT and triggers a PT to the modulated $Pmmn(00\gamma)s00$ phase (**II**) with the modulation vector $\boldsymbol{q^*} \cong 0.25c^*$. The 4-fold approximant of **II** is depicted in Fig. 19b. In comparison to **I**, the inorganic part slightly deviates from the mirror plane towards the [100] direction, with the maximum deviation from 180° of the Pb−Cl−Pb angle equal to 14.2°. Furthermore, both Δ_d and σ^2 values increase to the maximum of $1.73 \cdot 10^{-3}$ and 24.7 deg^2, respectively. The MHy^+ cations are ordered, and their distribution in the structure is directed by the supplementary translation component of the superspace group (intrinsic phase shift of 1/2) related to the 2-fold axis (bottom part of Fig. 19b). This arrangement leads to the formation of N−H···N and N−H···Cl HBs, however, in the crystal structure, of **II** there are NH_2^+ groups not involved in hydrogen bonding, pointing out to the instability of the HBs network. Phase **II** is likely to be isostructural to the intermediate phase of MHy_2PbBr_4, where a narrow temperature window (~350 – 370 K) prevents the determination of the crystal structure from SCXRD experiments. Nevertheless, in both cases $\boldsymbol{q^*}$ is ca. 0.25 along the same direction and the symmetry reduction from the *Pmmn* HT polymorph occurs.

As temperature decreases further, the **II → III** PT leads to the LT phase **III** with a $P2_1$ polar space group (Fig. 19c). In **III**, certain MHy^+ cations undergo spontaneous rotation, resulting in uncompensated MHy^+ dipoles and polarization along the [010] direction. The reduced interatomic distances facilitate the creation of a stable network of both N−H···Cl and N−H···N HBs. Enhanced intermolecular interactions and symmetry reduction impact the shape of the perovskite layers, reflected in arisen distortion parameters ($\Delta_d = 3.4 \cdot 10^{-3}$ and $\sigma^2 = 61.4$ deg^2) and an appearance of the out-of-plane tilting with $\theta_{link} = 161°$.

The interlayer gap reaches ~8.52 Å at 100 K, surpassing the previous record (held by MHy_2PbBr_4) for the shortest distance between layers in the **2D** lead halide HOIPs. Unlike its bromine and iodine analogs, a short interlayer span in MHy_2PbCl_4 does not convert to an unusually low exciton binding energy. Instead, it reaches 366 meV, falling within the typical range for **2D** perovskites. The estimated E_g of 3.75 eV is also the largest among the MHy_2PbX_4 (X = Br, Cl, I) series. The acentric arrangement in **III** is supported by SHG investigations and the pyroelectric effect, displaying the decay of spontaneous polarization along the [010] direction following the PT. Contrary to the Br^- analog, MHy_2PbCl_4 does not reveal the ferroelectric properties. This may be explained when the types of symmetry-breaking PTs are compared. MHy_2PbBr_4 undergoes the ferroelectric PT of the *mmm*F*mm*2 type, whereas MHy_2PbCl_4 exhibits the *mmm*F2 PT, associated with the presence of ferroelastic domains [131]. This type of PT combined with heavier octahedra distortion and stronger HBs network might be the reason for the adverse attempts of polarization switching in MHy_2PbCl_4.

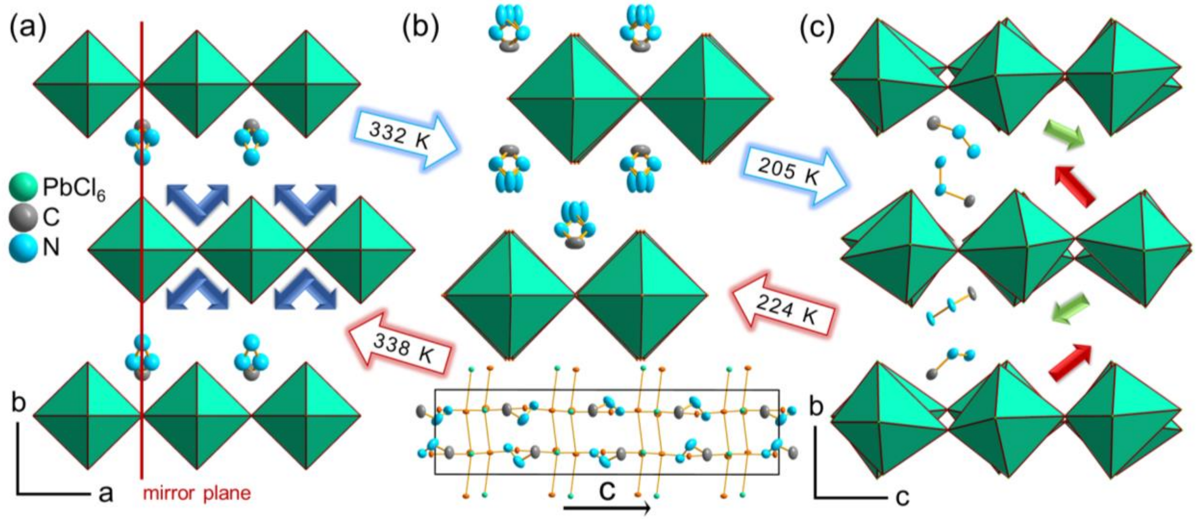

Figure 19. Crystal structure of MHy_2PbCl_4 in (a) centrosymmetric *Pmmn*, (b) modulated *Pmmn*(00*γ*)*s*00, and (c) polar $P2_1$ symmetry. Arrows in (a, c) represent the locations of compensated (dark blue) and non-compensated (red and green) MHy^+ dipoles. The temperatures of PTs are determined via DSC measurements.

Journal of Materials Chemistry C

ROYAL SOCIETY OF CHEMISTRY

PAPER

Check for updates

Cite this: *J. Mater. Chem. C*, 2023, 11, 4907

Broadband yellow and white emission from large octahedral tilting in (110)-oriented layered perovskites: imidazolium-methylhydrazinium lead halides†

Dawid Drozdowski, *[a] Katarzyna Fedoruk, [b] Adam Kabanski, [a] Mirosław Maczka, [a] Adam Sieradzki [b] and Anna Gagor *[a]

D4

This work includes the synthesis of new **2D** lead halide HOIPs with two A-site constituents – $IMMHyPbBr_4$ (**IMPB**, IM = imidazolium) and $IMMHyPbCl_4$ (**IMPC**). Utilizing the XRD, DSC, BDS, PL absorption, and temperature-dependent emission measurements, the crystal structures, PT mechanisms, and dielectric and linear optical properties of the obtained materials are investigated. **This article describes another feature of MHy^+ in lead halides, i.e., an**

ability to occupy the intralayer sites in the ACI-type 2D HOIPs with heavily distorted, (110)-oriented layers.

Both **IMPB** and **IMPC** adopt the ACI structural alignment, with IM^+ in the interlayer site and MHy^+ in the intralayer site. The HT phases (**I**) are of monoclinic *P*2/*c* symmetry. The inorganic part consists of corrugated, (110)-oriented inorganic layers comprising $[PbX_6]^{4-}$ octahedra (X = Br, Cl) bound by *cis* ligands (Fig. 20a). Both organic cations and the linking halides display the dynamic disorder. The distortion parameters $\Delta_d = 8.3\cdot10^{-4}$ ($10.5\cdot10^{-4}$) and $\sigma^2 = 13.7$ deg^2 (15.1 deg^2) for **IMPB** (**IMPC**) are common of the (110)-oriented **2D** lead halide HOIPs.

On cooling, both compounds undergo a PT to the monoclinic $P2_1/c$ polymorph (**II**, Fig. 20b). The **I** → **II** PT involves the translational symmetry breaking (formation of the 2*b* superstructure) The IM^+ cations are well-ordered and involved in N–H···X and C–H···X HBs. The heightened intermolecular forces induce the tilting of the octahedra layers with the Pb–X_{link}–Pb angle (θ_{link}, X_{link} = linking halide) equal to 158° (153°) for **IMPB** (**IMPC**) at 295 K. The Δ_d and σ^2 parameters rise to $13.5\cdot10^{-4}$ ($31.5\cdot10^{-4}$) and 28.7 deg^2 (44.7 deg^2) for **IMPB** (**IMPC**) at 100 K. **Both compounds are characterized by considerably greater tilting and extraordinarily low Pb–Pb intralayer distances in comparison to the literature analogs.** MHy^+ cations still exhibit disorder at RT, nonetheless, notably reduced in comparison to **I**, being split into three positions with the same probability. A partial stabilization of MHy^+ may be caused by the formation of N–H···N HBs between IM^+ and N atoms from NH_2^+. On further cooling, a gradual ordering of the MHy^+ arises with anchoring one position at 100 K. This occurs without altering the symmetry of the structure.

The progressive positional ordering of the MHy^+ moieties, taking place in the LT region, induces the single dipolar relaxation process, observed on the BDS spectra (Fig. 20c) from 150 K (170 K) to 188 K (230 K) for **IMPB** (**IMPC**). A uniquely large distortion of the perovskite layers is responsible for broad PL bands (Full Width at Half Maximum (FWHM) = 160 nm (166 nm) for **IMPB** (**IMPC**) at 80 K), accompanied by significant Stokes shifts (178 nm (252 nm) for **IMPB** (**IMPC**)) and one of the widest energy band gaps among (110)-oriented **2D** lead halide hybrids (3.22 eV and 3.79 eV for **IMPB** and **IMPC**, respectively). A shift in PL emission color is noted with changing temperature, particularly notable for **IMPB**, varying from yellow at 80 K to white at 200 K (Fig. 20d). While the white-light PL was documented in several (110)-oriented compounds [76,133,134], this is the first report of such a phenomenon among ACI-type perovskites.

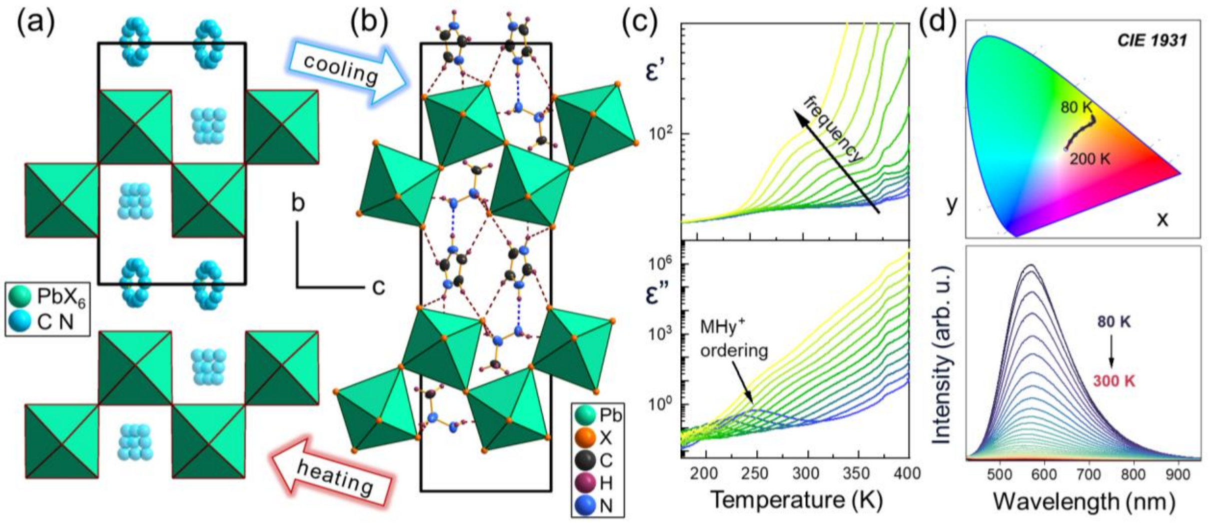

Figure 20. (a-b) The crystal structures of **IMPB** and **IMPC** in (a) HT phase ($P2/c$, **I**) and (b) LT phase ($P2_1/c$, **II**) at 100 K. Dashed lines in (b) represent HBs: blue for N–H⋯N and dark red for N–H⋯X and C–H⋯X. (c) Dielectric curves for **IMPC** with the anomaly arising from the ordering of the MHy$^+$. (d) Linear optical properties of **IMPB** with broad PL and white-light emission at 200 K (0.34, 0.37; 5226 K).

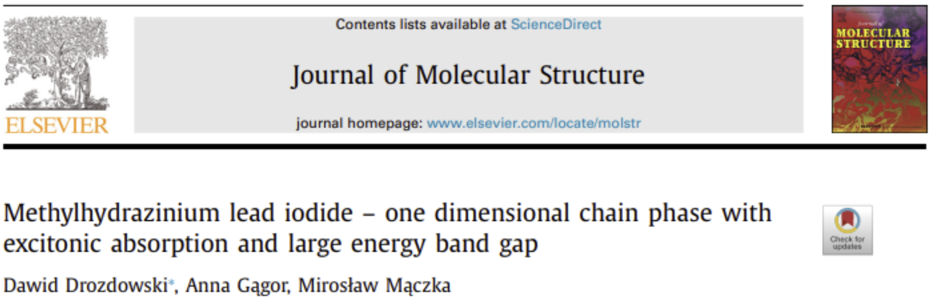
Contents lists available at ScienceDirect
Journal of Molecular Structure
journal homepage: www.elsevier.com/locate/molstr
ELSEVIER

Methylhydrazinium lead iodide – one dimensional chain phase with excitonic absorption and large energy band gap

Dawid Drozdowski*, Anna Gągor, Mirosław Mączka

D5

Despite a more suitable TF value (1.01) of iodine-based compounds compared to other halides – 1.03 (1.05) for MHyPbBr$_3$ (MHyPbCl$_3$), the **3D** perovskite of MHyPbI$_3$ formula has not been synthesized yet. Anti-solvent crystallization attempts targeting MHyPbI$_3$ or MHyPbBr$_x$I$_{3-x}$ (with iodine content above ~7%) **3D** HOIPs lead to yellow needle-like crystals with **1D** inorganic substructure, adopting the same formula – MHyPbI$_3$. This paper describes in detail the crystal structure of the obtained material. DSC and HT powder diffractometry were employed to examine the PTs. The RT absorption spectra were recorded to estimate the E_g value. **As the phase reported herein is a predominant (or sole) outcome of the syntheses conducted to MHy-based lead iodide HOIPs, comprehending the thermodynamically favored alignments is vital for ongoing quests to discover novel hybrids.**

At RT MHyPbI$_3$ adopts monoclinic symmetry described in the $P2_1/c$ space group. Its structure consists of parallel double chains of edge-sharing [PbI$_6$]$^{4-}$ octahedra extending along the [100] direction, with MHy$^+$ cations situated in between. Three inequivalent iodine positions are distinguished and the Pb–I bond lengths are 3.07–3.43 Å. The intermolecular interactions are expressed in N–H···I HBs involving only I3 acceptor (H···A (D···A) distances of 2.96–3.04 Å (3.48–3.56 Å)). The weakly-developed network of HBs and low σ^2 (6.32 deg^2) indicate a weaker influence on intermolecular forces on the shape and symmetry of inorganic substructure when compared to other MHy-based lead halides. The analogous crystal packing was reported for several lead halide hybrid compounds, including $HyPbI_3$, $MAPbI_3 \cdot DMF$, and $(NH_4)PbI_3$ (Hy = hydrazinium) [135–137].

When heated above 357 K, a PT occurs, causing a multi-domain twinning of the single-crystal sample. The powder diffraction patterns recorded at 363 K are indexed in monoclinic $P2_1/m$ symmetry – a maximal non-isomorphic supergroup of $P2_1/c$ for $a' = 2a$ [125]. The doubling of lattice parameter a takes place without significant alteration in interatomic distances compared to the pristine phase. Given that this direction represents the propagation of the chains, they undergo marginal alternations in geometry. Notable changes occur in the remaining directions, associated with the relative positions of the adjacent chains, as evidenced by the unit cell elongation (contraction) of by ca. 5.2% (9.9%) along [010] ([001]) direction. Fig. 21 depicts potential modifications of the unit cell at HT, likely prompted by increased dynamics of the MHy^+ cations. The HT polymorph is metastable – the first traces of the initial phase reappear after approx. 20 min after cooling to RT, with complete structural restoration occurring ca. 50 minutes post-cooling. According to DSC traces, the metastable polymorph adopts its sequence of PTs when immediately cooled down below RT, with heat anomaly at 277 (269) K on heating (cooling).

The **1D** $MHyPbI_3$ hybrid exhibits no PL activity at either RT or 77 K. The estimated E_g equals 3.11 eV – significantly higher than for **2D** MHy_2PbI_4 perovskite (2.20 eV [109]), likely due to the lower dimensionality of the inorganic substructure.

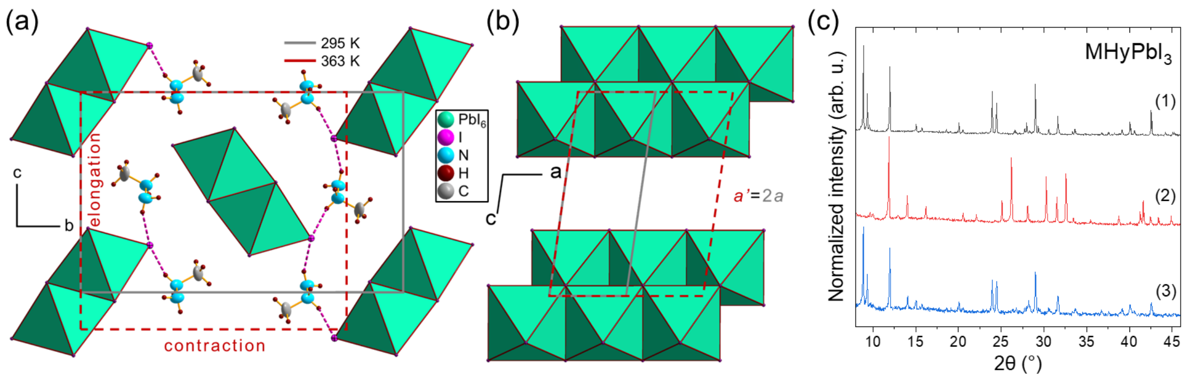

Figure 21. Crystal structure of $MHyPbI_3$ along (a) [100] and (b) [010] direction. Grey and red lines represent the unit cell at RT and 363 K, respectively. (c) Powder diffractograms at (1) RT (virgin sample), (2) 363 K, and (3) 50 minutes after cooling down from 363 K to RT.

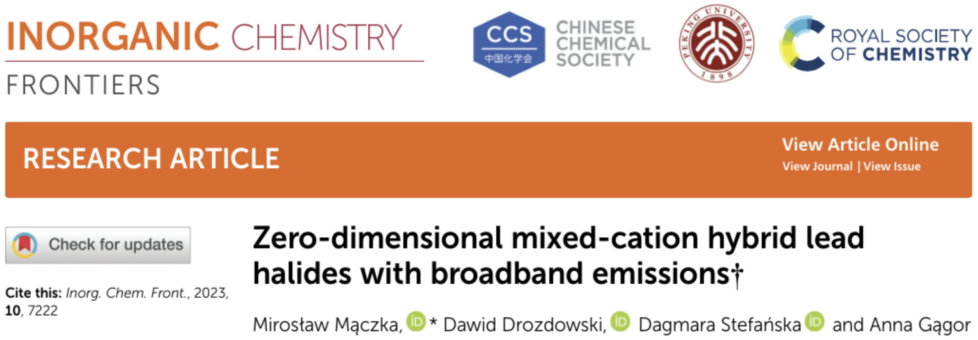
INORGANIC CHEMISTRY FRONTIERS

CCS CHINESE CHEMICAL SOCIETY

ROYAL SOCIETY OF CHEMISTRY

RESEARCH ARTICLE

View Article Online
View Journal | View Issue

Check for updates

Cite this: *Inorg. Chem. Front.*, 2023, **10**, 7222

Zero-dimensional mixed-cation hybrid lead halides with broadband emissions†

Mirosław Mączka,* Dawid Drozdowski, Dagmara Stefańska and Anna Gągor

D6

The D6 article encompasses the synthesis, crystal structures, and phonon and linear optical examination of three new entrants in the group of **0D** lead halides – $Cs_2MHy_2PbBr_6$, $Cs_2MHy_2PbI_6$, and $Cs_2MHy_2PbBr_3I_3$, marking the initial instances of **0D** lead halide hybrids with mixed A-site cations. The findings presented herein illustrate that the mixed-cation method demonstrates a potential for the development of **new 0D lead halides exhibiting efficient broadband PL. The MHy^+ cations reveal the ability to serve as a 'spacer' in the structural subgroup with isolated octahedra.**

$Cs_2MHy_2PbX_6$ (X = Br, I) crystallize in the structure isostructural to the high-pressure phase of Cs_4PbX_6 ternary compound, i.e., orthorhombic *Cmce* [138]. The all-inorganic analog adopts rhombohedral ($R\bar{3}c$) packing upon standard conditions [139,140], and the $R\bar{3}c$ → *Cmce* PT is associated with increased octahedra distortion. For the hybrid compound, this effect is attained through the incorporation of larger and anisotropic counterion, i.e., MHy^+, creating internal pressure. The presence of MHy^+ is also manifested in expanded unit cell parameters.

The crystal packing is presented in Fig. 22. MHy^+ cations selectively replace Cs^+ and form HBs layers with the inorganic substructure through N–H···X bonds (Fig. 22a). The characteristic feature of $Cs_2MHy_2PbX_6$, not observed in materials from **D1-D5**, is a **statistical disorder of**

MHy$^+$, resulting in two equivalent positions related by a mirror plane, making the terminal CH_3 and NH_2 groups indistinguishable. This effect is observed at both RT and 100 K. Another intriguing feature is the **selective substitution of halides appearing in $Cs_2MHy_2PbI_3Br_3$**. The HB acceptor positions are preferably occupied by Br, whereas the non-interacting sites were refined with the I (Br) occupancy of 0.75 (0.25). The proposed halide distribution is also supported by similar Pb–Br bond lengths in the mixed-halide (3.037 Å) and bromine (3.011 Å) analogs (Fig. 22b). The selective substitution results in a markedly increased octahedra distortion, as the Δ_d arises from $0.12{\cdot}10^{-5}$ in $[PbBr_6]^{4-}$ to $29.9{\cdot}10^{-5}$ in $[PbBr_3I_3]^{4-}$.

The Raman studies confirm the preferential occupation of anionic sites in the mixed-halide analog, as well as the static character of MHy$^+$ disorder in all compounds. Linear optical studies reveal that $Cs_2MHy_2PbBr_6$ and $Cs_2MHy_2PbI_6$ reveal broad orange-yellow PL (FWHM of 158 nm and 175 nm, respectively), accompanied by significant Stokes shifts of 342 nm (280 nm) for Br$^-$ (I$^-$). A superior octahedra distortion in $Cs_2MHy_2PbI_3Br_3$ induces a redshift and broadens the PL (FWHM = 280 nm, Fig. 22c).

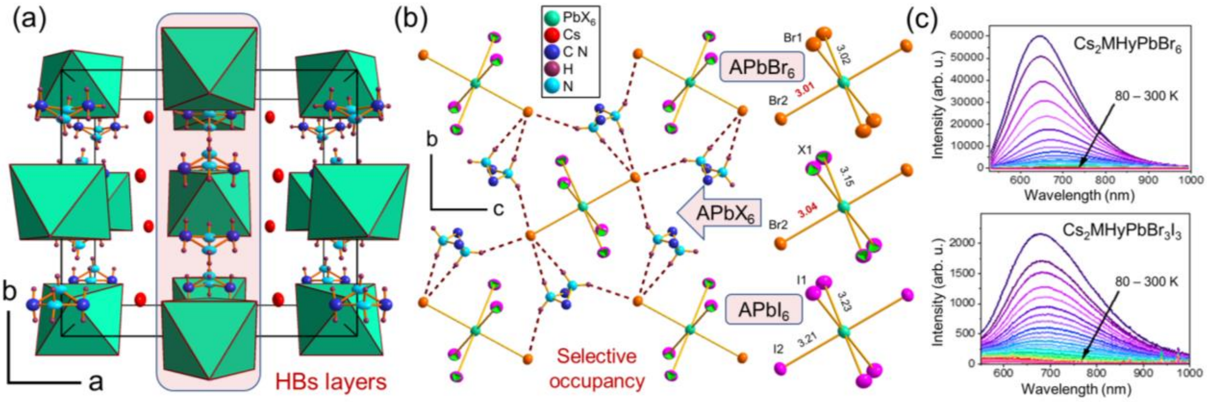

Figure 22. (a-b) The crystal structure of $Cs_2MHy_2PbX_6$ (X = Br, I). (a) Isolated $[PbX_6]^{4-}$ octahedra form HBs with MHy$^+$ moieties perpendicular to the [100] direction. (b) Selective occupancy and the N–H···Br HBs in $Cs_2MHy_2PbBr_3I_3$. (c) Mixed-halide $Cs_2MHy_2PbBr_3I_3$ reveals broadened PL associated with a greater octahedra distortion when compared to single-halide $Cs_2MHy_2PbBr_6$.

9. Discussion

To study the relationships between crystal structure and optoelectronic properties (including their tunability) of the MHy-based lead halide hybrid materials, one may consider several factors on the structural level, i.e., intermolecular interactions (here HBs mainly), voids volumes (for **3D** compounds), interlayer spacing (for **2D**) and interatomic distances in general. All these aspects are dependent on the temperature and may also abruptly change upon the PTs. For a better understanding of demonstrated features, the effect of several chemical engineering strategies is discussed, including halide substitutions (for single-halide compositions), halide alloying, and the incorporation of second cation (IM^+, Cs^+) beside MHy^+ (A-site cation alloying). The dimensionality of inorganic substructure also serves an important role in structural and physicochemical characterization.

9.1. Halide substitution

The strength of HBs with halide acceptor arises with higher electronegativity and smaller ionic radius, resulting in enhanced attraction of the H atom and reduced distances. One may determine decreasing strength and tendency to create the HBs in the following order of acceptors: Cl^-, Br^-, I^-, with the electronegativity of 3.16, 2.96, and 2.66 eV in Pauling scale, and ionic radii of 181, 196, and 220 pm, respectively [141]. Halide exchange may therefore impact the symmetry and physicochemical properties of lead halide hybrids.

As previously discussed, MHy_2PbX_4 **2D** HOIPs with X = Br, I, exhibit distinct sequences of phase transitions and polymorphic phases, despite adopting the same disordered orthorhombic aristotype with *Pmmn* symmetry at high temperatures. This behavior underscores the significant influence of halide substitution on their physicochemical properties [107,109]. Article **D3** investigates MHy_2PbCl_4, which also displays a unique sequence of phase transitions. The HT *Pmmn* phase is stabilized above 338 K upon heating – a higher temperature than observed in the iodine analog (320 K). This discrepancy may be attributed to shorter interatomic and interlayer distances in MHy_2PbCl_4, which shift the transformation to the disordered phase towards higher temperatures. In contrast, this explanation does not apply to MHy_2PbBr_4 where the disordered *Pmmn* phase emerges at an even higher temperature, above 371 K. This behavior is potentially related to the presence of ferroelectric order, which stabilizes the room-temperature polymorph of the bromine analog ($Pmn2_1$) at elevated temperatures.

The modulated phase **II** ($Pmmn(00\gamma)s00$) in MHy_2PbCl_4 is stable over a broad temperature range, up to 224 K during heating, and is characterized by positionally ordered MHy^+ cations.

A similar modulated phase is observed in MHy_2PbBr_4 (HT polymorph **II**). Given the identical average structure (*Pmmn*) and comparable modulation vector ($\boldsymbol{q}^*$ ~0.25**c***), it can be inferred that both phases are isostructural. Therefore, substituting Br with Cl promotes the stabilization of the modulated phase, likely due to the increased strength of HBs. A PT to a polar phase occurs for both materials – $P2_1$ ($Pmn2_1$) for X = Cl (Br). In the case of Br, this transition is of ferroelectric nature, whereas for Cl, the transition involves symmetry reduction accompanied by the formation of ferroelastic domains. The increased octahedral distortion, driven by stronger HBs in the Cl analog, results in the loss of ferroelectric properties upon substituting Br with Cl. It is worth noting that the $P2_1$ phase with distorted layers was reported for MHy_2PbBr_4 in high-pressure studies, with $Pmn2_1 \rightarrow P2_1$ PT occurring at ca. 4 GPa [142]. Reduced interatomic distances in MHy_2PbCl_4 are also manifested in the lowest interlayer distances among the MHy_2PbX_4 series – 8.66 Å for MHy_2PbCl_4 at 295 K.

Halide substitution effects are also evident in ACI-type **2D** HOIPs, as discussed in **D4**. The phase transition from phase **II** to phase **I** is associated with the order-disorder behavior of the organic moieties and occurs at a higher temperature for $IMMHyPbCl_4$ (IMPC) – 383 K, compared to Br-based IMPB (357 K). IMPC exhibits a greater degree of octahedral distortion and tilting relative to IMPB. In contrast, for the **0D** compositions examined in **D6**, i.e., $CsMHyPbX_6$ (X = Br, I), halide substitution does not significantly impact the crystal structure. The symmetry remains consistent, and the distortion parameters show only slight variations (Δ_d = $0.12\cdot10^{-5}$ and $1.1\cdot10^{-5}$ for $[PbBr_6]^{4-}$ and $[PbI_6]^{4-}$, respectively).

In the case of linear optical properties, MHy_2PbCl_4 (**D3**) demonstrates a substantially larger E_g (3.75 eV) than Br (2.75 eV) and I (2.20 eV) analogs [107,109]. The band gap reduction from 3.79 eV to 3.20 eV upon Cl to Br substitution is also observed in the $IMMHyPbX_4$ (**D4**). In general, the E_g decreases with the increasing ionic radius of the halogen atom (Fig. 23a), which is related to the increase of the covalent character of Pb – X bonding (the order from the most covalent to the least covalent character of the bond is: Pb – I > Pb – Br > Pb – Cl). Additionally, the degree of octahedral distortion, which is influenced by halide substitution, also affects E_g and other optical properties [70]. The positions of excitonic absorption and the maximum of PL emission bands can be modulated, typically exhibiting a red shift in the sequence of X = Cl, Br, I (**D3, D4**). This trend is similarly observed in MHy-based **3D** perovskites and various other lead halide hybrids [42,43,143,144]. The redshifts in PL maxima correspond to changes in emission color. This phenomenon is particularly noteworthy in ACI **2D** HOIPs, where substituting Cl with Br enabled the observation of white-light PL emission, as depicted in Fig. 23b, c (**D4**, [143]).

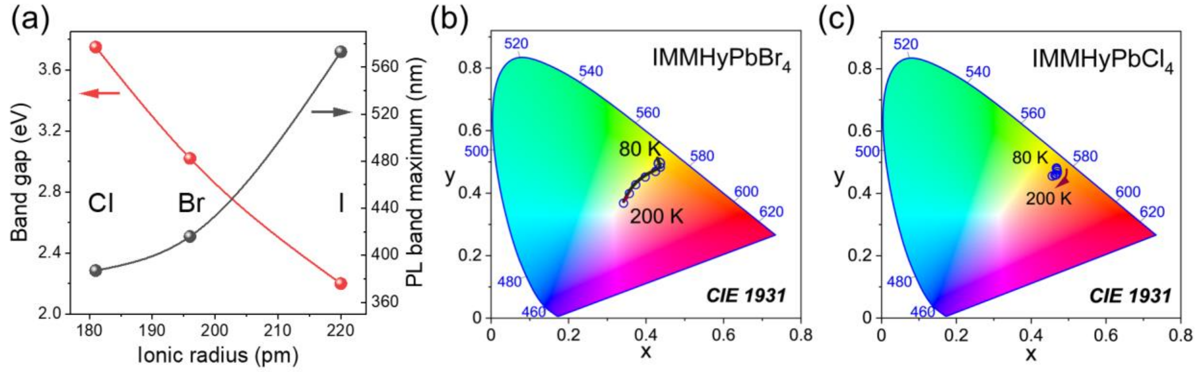

Figure 23. Impact of the halide substitution on linear optical properties of studied materials. (a) Position of PL band related to free exciton (FE) recombination in MHy_2PbX_4 (X = Cl, Br, I) **2D** HOIPs. (b, c) CIE diagrams for $IMMHyPbBr_4$ and $IMMHyPbCl_4$ (article **D4**) – (110)-oriented and ACI-type **2D** HOIPs [107–109,143].

9.2. Halide alloying

The halide alloying approach has been applied to the series of **3D** and **2D** HOIPs ($MHyPbBr_xCl_{3-x}$ – **D1**, $MHy_2PbBr_{4-x}I_x$ – **D2**) and the $Cs_2MHy_2PbBr_3I_3$ **0D** compound (**D6**). In the **3D** systems, halide mixing does not result in the emergence of new polymorphs that have not already been reported for single-halide prototypes. However, the HT phases of both $MHyPbBr_3$ and $MHyPbCl_3$ are stabilized for compositions with $x \geq 1.33$, which is associated with the minimum volume of the perovskite voids necessary to allow free rotation of MHy^+ cations. Notably, even at a low chlorine content (~15% atomic), the sample adopts the HT phase of $MHyPbCl_3$. This stabilization is likely due to increased intermolecular forces resulting from reduced distances, which facilitate the reorientation of organic cations. Halide alloying combined with temperature variations induces rich polymorphism in the Br-I series of **2D** perovskites, resulting in four new RP phases that are not observed in either of the single-halide analogs (as detailed in the Results chapter for **D2**). **Additionally, it is crucial to emphasize that the incorporation of Br into MHy_2PbI_4 represents the only known method for forming the 3D perovskite phase with a significant iodide content.**

The series described in the **D1** and **D2** exhibit a linear relationship between the unit cell volume and halide concentration, consistent with Vegard's law on solid solutions [144]. However, Vegard's law also traditionally predicts a linear change in lattice parameters, which is not observed for parameter *b* in the $MHy_2PbBr_{4-x}I_x$ systems. As discussed in **D2**, this anomaly arises from the **selective substitution of the halide sites (Fig. 24)**. Halide positions that interact with the MHy^+ are preferentially occupied by the one that forms stronger HBs, in this case, Br^-.

Preferred halide occupancy has also been discussed and reported for other layered metal halide hybrids [145–147], and similarly observed in the **0D** compound, leading to a relevant increase in Δ_d in $Cs_2MHy_2PbBr_3I_3$ (**D6**). This selective occupancy in **2D** and **0D** compounds suggests a need to revisit the **3D** series in light of this phenomenon. In fact, in the **3D** systems, halides occupy all six inequivalent sites non-uniformly, as illustrated in Fig. 24a. Similar to the previously mentioned examples, positions that are weakly involved or not involved in hydrogen bonding (e.g., X6) are preferentially occupied by the larger halide, Br. Conversely, Cl predominantly occupies positions that are actively engaged in hydrogen bonding, such as X1. However, this selective occupancy effect is less pronounced in the **3D** systems compared to their **2D** counterparts and becomes progressively diminished as the Br concentration increases, owing to the expansion of interatomic distances.

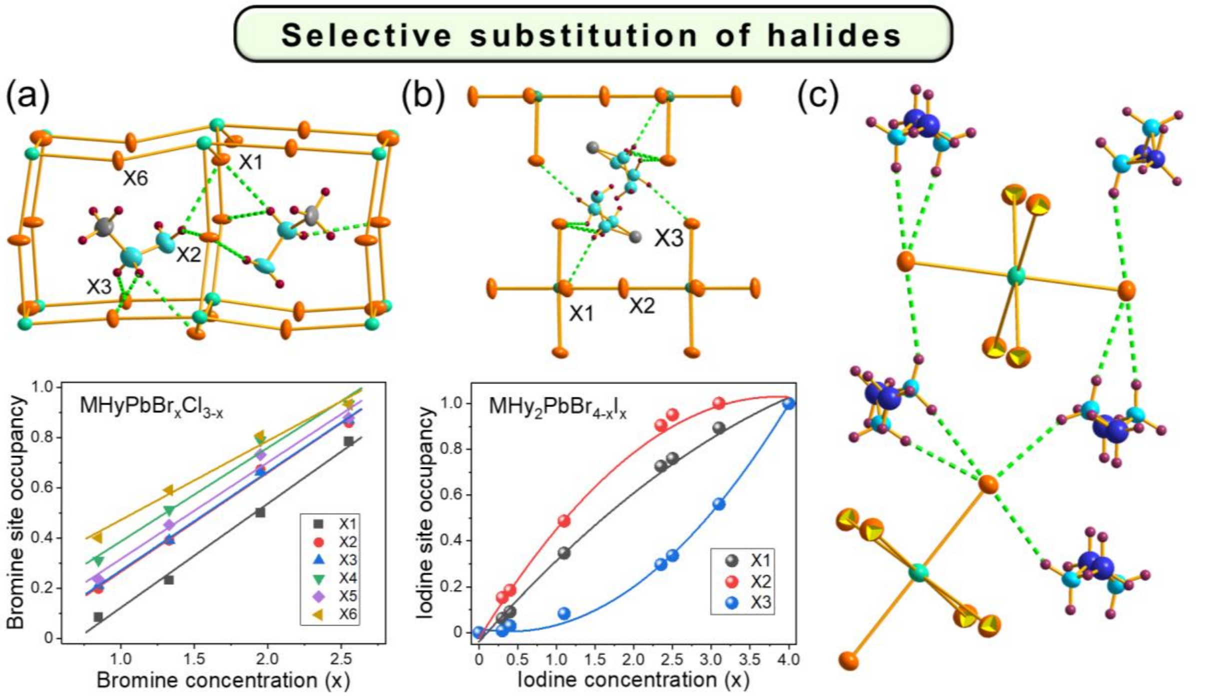

Figure 24. Selective occupying of the halide sites occurring for the halide-alloyed compounds: (a) $MHyPbBr_xCl_{3-x}$ **3D** HOIPs (**D1**), (b) $MHy_2PbBr_{4-x}I_x$ **2D** HOIPs (**D2**), and (c) $Cs_2MHy_2PbBr_3I_3$ **0D** hybrids (**D6**). Sites occupied with I (0.75) and Br (0.25) in (c) are displayed as octants. Positions involved in the creation of HBs (dashed lines) are preferred by smaller halides [148–150].

As described in the previous subchapter, substituting halides at the X site may significantly alter optical properties, such as E_g and position of absorption and PL bands. The application of the halide alloying in **3D** and **2D** HOIPs enhances the tunability of these properties. In mixed-halide compositions, the optical parameters tend to fall between the values observed for the corresponding single-halide analogs, as illustrated in Fig. 25.

For the Br-Cl series described in **D1**, a continuous redshift in the exciton absorption band occurs with increasing Br content (from 389 nm to 457 nm). This trend is also evident for the $MHyPbBr_{2.8}I_{0.2}$ (484 nm), despite a relatively low concentration of I^-. The E_g and a maximum of PL emission bands exhibit a linear dependence on the halide ratio x for $MHyPbBr_xCl_{3-x}$ (Fig. 25a, b). **This linear relationship allows not only for the fine-tuning of optical parameters but also for the precise control of these properties by adjusting the halide composition ratio.**

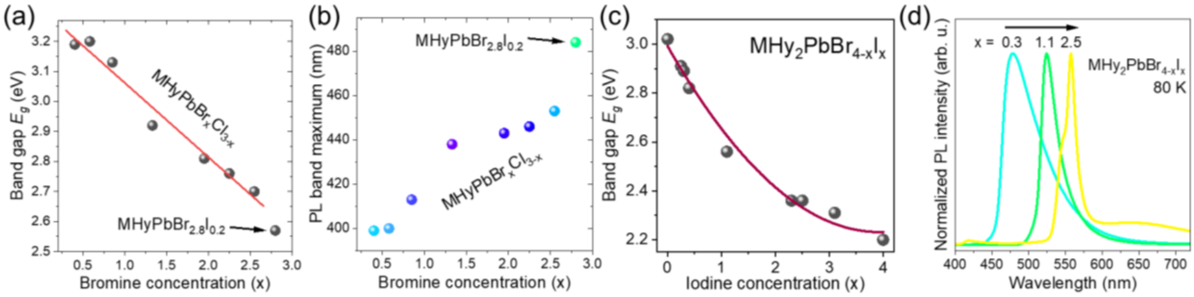

Figure 25. Dependence of E_g at RT and position of PL bands at 80 K on halide concentration in (a, b) $MHyPbBr_xCl_{3-x}$ **3D** HOIPs (**D1**) and (c, d) $MHy_2PbBr_{4-x}I_x$ **2D** HOIPs (**D2**). The colors of dots in (b, d) represent the positions of maxima on CIE chromaticity diagrams [148,149].

The same series also exhibits varying intensities of the SHG response, with values falling between those reported for $MHyPbX_3$ and $MHyPbCl_3$ [42,43]. In the $MHy_2PbBr_{4-x}I_x$ layered compounds E_g shows different trends across the entire range of halide concentrations, with the most significant decrease occurring in Br-rich compositions as x increases, as depicted in Fig. 25c. This behavior is particularly relevant for optoelectronic applications, where the development of mixed-halide materials with enhanced stability and reduced bandgap (characteristic features of Br- and I-based hybrids, respectively) can be advantageous. In the iodine-dominated region, the E_g curve flattens, approaching the value calculated for MHy_2PbI_4 (2.20 eV) [109]. The impact of halide alloying is also apparent in $Cs_2MHy_2PbBr_3I_3$ where increased octahedral distortions, driven by selective halide occupancy, lead to the broadening of PL emission bands. This is reflected in the FWHM of the PL emission, which increases from 158 nm (175 nm) for X = Br (I) to 230 nm (**D6**, [150]).

As observed, all the halide-alloyed systems discussed in this subchapter incorporate Br^- in their compositions. Notably, there is still an absence of compounds based solely on Cl^- and I^- ions that include MHy^+. This contrasts with the behavior of analogs based on MA^+ and FA^+, where examples of Cl-I systems are available [151,152]. One possible explanation for this distinction is the significant difference in ionic radii between Cl^- and I^-, which may have a more pronounced effect on MHy-based compounds. Additionally, the absence of Cl-I systems in

MHy^+ compounds could be attributed to the lack of an appropriate solvent or limitations in the methods of synthesis or crystallization.

9.3. A-site cation alloying

The impact of incorporating a second A-site cation into MHy-based lead halide hybrids is explored in articles **D4** and **D6**, which introduce imidazolium (IM^+) and cesium (Cs^+), respectively. Imidazolium derivatives are becoming increasingly common additives in **3D** perovskite materials. IM-based ionic liquids are effective in developing high-quality and moisture-resistant perovskite films, owing to their hydrophobic nature and ability to prevent rapid crystallization [44,153]. Analogously to MHy^+, IM^+ has been reported to stabilize lead bromide compounds of various structural alignments, including 4H-hexagonal, **1D** double-chain, and **1D** single-chain structures [15]. Partial replacement of organic cation with inorganic Cs^+ (5-20% wt.) has been described as a powerful strategy to increase the thermal stability of HOIPs by forming primary bonds with PbX_6, much stronger than HBs [154,155]. $CsPbX_3$ quantum dots with **3D** structure exhibit bright PL with remarkable PLQY and exceedingly narrow FWHM but simultaneously are characterized by poor durability [156,157]. More stable **0D** compounds of the Cs_4PbX_6 formula demonstrate attractive optical properties as well, including strong excitonic absorption in the UV region.

As described in **D4**, the introduction of IM^+ to MHy-based lead halides results in the formation of a single-layered **2D** perovskite phase of the ACI type, with both cations residing in the interlayer space. This perovskite structure features layers aligned along the (110) direction, which is an orientation rarely observed among lead halide hybrids. As illustrated in Fig. 26a, IM^+ cations serve as typical spacers in these **2D** compounds, engaging in hydrogen bonding with the adjacent inorganic slabs. MHy^+ occupies the spaces between the adjacent octahedra within the corrugated layers. Analogous alignment was reported for $IMGUAPbBr_4$ (GUA = guanidinium) with GUA^+ situated in the intralayer area [158]. However, as the GUA^+ is a symmetrical ion with a dipole moment equal to zero, it marginally affects the geometry of octahedra (θ_{link} = 180°). For compounds in **D4,** a notable tilting of the perovskite layers is present owing to the polar character of MHy^+. Another interesting property related to the presence of two organic A-site cations is the system of N–H···N HBs between IM^+ and the terminal group of MHy^+, which presumably contributes to the partial stabilization of the second moiety at RT, and its final anchoring at LT (*vide supra*). While there are no reports of the ACI- and (110)-oriented **2D** compositions comprising MHy^+, one may find two examples with IM^+ in the literature, including the aforementioned $IMGUAPbBr_4$ and $IMTzPbBr_4$ (Tz = 1,2,4-

triazolium), which reveals an enhanced (i.e., 3 x 3) corrugation [158,159]. Overall, the A-site cation alloying in **D4** generates the **new 2D HOIPs with (110)-oriented layers**.

An interplay of specific alignment and heavy distortions is manifested in significantly broadened PL emission bands in comparison to MHy-based analogs of (001)-type (FWHM of 160 nm (168 nm) and 5 nm (60 nm) for the main PL band in the (110)- and (001)- oriented lead bromides (chlorides), respectively), which are attributed more likely to the STEx states rather than FE recombination [143].

Although both MHy^+ and Cs^+ demonstrate the ability to stabilize the **3D** perovskite structures, a combination of these two cations leads to the formation of **0D** compounds with isolated octahedra, similar to the most stable all-inorganic analog of Cs_4PbX_6 formula. The insights of A-site cation alloying on the crystal structure of $Cs_2MHy_2PbX_6$ (**D6**) are presented in Fig. 26b. MHy^+ through a selective substitution of Cs^+ sites (both cations are in a 1:1 ratio), affects the geometry of the inorganic part. Consequently, the compounds adopt *Cmce* symmetry – a high-pressure analog of Cs_4PbX_6 [138]. As derived from DRS measurements, the A-site cation alloying induces a redshift of excitonic absorption, especially for the $Cs_2MHy_2PbI_6$ [150].

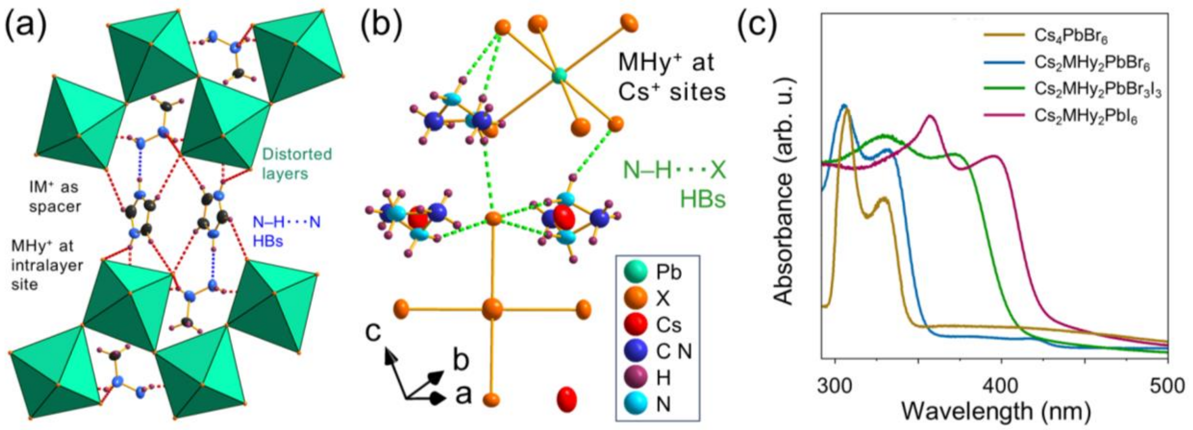

Figure 26. Effects of A-site cation alloying. (a) In $IMMHyPbX_4$ (**D4**, X = Br, Cl) **2D** HOIPs MHy^+ is situated at intralayer space due to the presence of IM^+ spacer. The location of MHy^+ brings heavy distortions to the inorganic part. Both cations interact with each other via N–H···N HBs. (b) In $Cs_2MHy_2PbX_6$ (**D6**, X = Br, I) **0D** hybrids MHy^+ selectively substitutes for Cs^+ sites and interacts with halides via N–H···X HBs. (c) The presence of MHy^+ provokes a redshift of excitonic absorption compared to all-inorganic Cs_4PbX_6 [143,150].

9.4. Role of dimensionality

The final subsection focuses on the influence of octahedral connectivity on the structural and optoelectronic properties of the materials under investigation. Fig. 27 displays the distortion parameters of the octahedra for each halide subgroup as a function of dimensionality and, for **2D** structures, the type of structure. Given the significant impact of selective halide occupancy on octahedral geometry in halide-alloyed systems, only single-halide analogs are considered for this comparison.

For chlorides and bromides, a notable decrease in angle variance (σ^2) is observed in lower-dimensional hybrids compared to their **3D** counterparts. Specifically, bromides exhibit a smaller, yet still significant, reduction in σ^2 when comparing **0D** to **2D** analogs, while iodides show a decrease in σ^2 for **0D** and **1D** structures relative to **2D**. Among **2D** HOIPs, compounds with (110)-oriented layers are characterized by marginally lower σ^2 compared to those with (001)-oriented layers. Regarding bond lengths, the relationship between Δ_d and dimensionality is inconsistent. For chlorides (X = Cl^-), distortions increase in **2D** phases compared to **3D** phases, whereas for bromides (X = Br^-), Δ_d decreases across the sequence of **3D**, **2D**, and **0D** phases. In iodides, no clear trend is observed in Δ_d values, with the largest deviations in bond lengths reported for **1D** structures.

Varying dimensionality of the octahedra connections leads to different spatial arrangements of MHy^+ within the crystal structure, which in turn affects the intermolecular forces between organic and inorganic components. The characteristics of these interactions may be expressed in the **strength of HBs** involving MHy^+ donors and halide acceptors, and the **distances between NH_2 groups and Pb centers**. The first factor has been investigated via Raman spectroscopy in article **D6**, comparing the modes for terminal NH_2^+ groups in **3D** $MHyPbBr_3$, **2D** MHy_2PbBr_4, **1D** $MHyPbI_3$, and **0D** $Cs_2MHy_2PbBr_6$. The obtained results indicate the following order of decreasing HB strength: **3D** > **1D** > **0D** > **2D** [150]. Considering the second factor, only for the **3D** perovskites the Pb – NH_2 lengths (in the range of 2.83 – 3.04 Å) may be regarded as coordination bonds, whereas the analogous distances in the hybrids of lower dimensionality exceed 4 Å. It may be concluded, therefore, that the heaviest octahedra distortions, which are observed for **3D** compounds, are attributed to the strongest interactions of the inorganic part with MHy^+. However, when excluding **3D** analogs from the comparison, the classification of hydrogen bond strength does not fully align with the observed trends in distortion parameters. In such cases, the explanations for these discrepancies become more complex and should be evaluated on a case-by-case basis. For instance, increased Δ_d values in (110)-oriented **2D** compounds versus (001)-type may arise from a greater out-of-plane tilting of the layers (**D4**). In iodides, enhanced Δ_d for the **1D** structures might emerge from the fact that only the apical I^- are involved in HBs, which brings an asymmetry in bond lengths (**D5**).

The role of dimensionality is also noted in several aspects of the optical properties. In general, E_g increases with decreasing dimensionality in all of the halide subgroups. An enhanced band gap is also recorded for (110)-oriented (ACI type) chlorides and bromides versus their (001)-oriented (RP) counterparts (**D3**). The ACI-type **2D** HOIPs and **0D** hybrids are characterized by broader PL emission bands than **3D** and **2D** RP perovskites (**D1** – **D4**, **D6**). The only representant of **1D** phases, i.e., $MHyPbI_3$, is optically inactive (**D5**). Altogether, the dimensionality of octahedra connections can be regarded as another contributor to the tunability of structural and optoelectronic properties of the studied materials.

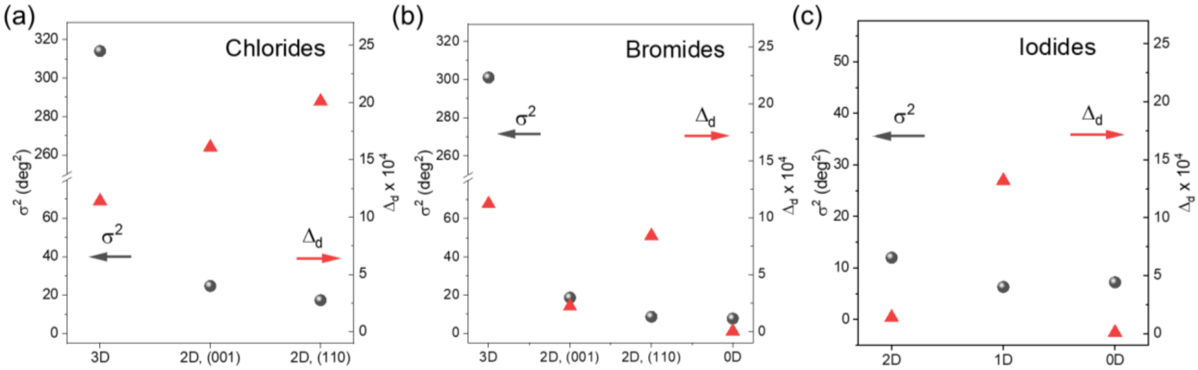

Figure 27. Octahedra distortion parameters as a function of dimensionality of octahedra connections in MHy-based lead halide hybrids. The RT phases of single-halide compounds are taken into consideration, i.e.: (a) $MHyPbCl_3$, MHy_2PbCl_4, and $IMMHyPbCl_4$ ([43], **D3**, **D4**), (b) $MHyPbBr_3$, MHy_2PbBr_4, $IMMHyPbBr_4$, and $Cs_2MHy_2PbBr_6$ ([42,107], **D4**, **D6**), (c) MHy_2PbI_4, $MHyPbI_3$, and $Cs_2MHy_2PbI_6$ ([109], **D5**, **D6**).

10. Summary

One of the aims of the studies associated with the dissertation was a synthesis of new hybrid organic-inorganic lead halides comprising MHy^+ cation. Selected compositional engineering techniques (substitution and alloying of the A- and X-site ions), and three crystallization methods (with varying ratios of lead halide salts and MHy to Pb) have been utilized to obtain compounds with varying dimensionality of the octahedra connections and, for the layered systems, different type of crystal structures. The crystal structure analysis has been provided regarding the intermolecular interactions and polymorphs stabilized upon varying temperature. The structure-property relationships have been analyzed, herein limited to the optical characteristics.

The described materials cover the whole range of dimensionality, according to the classification illustrated in Fig. 5. In the case of **2D** HOIPs solely, two types of compounds based on relative stacking and two based on 'slicing' along the planes (Fig. 6) are reported, as outlined below:

Compound formula	Dimensionality (type)	Article
$MHyPbBr_xCl_{3-x}$ (x = 0.40, 0.58, 0.85, 1.33, 1.95, 2.25, 2.55) $MHyPbBr_{2.8}I_{0.2}$	**3D**	**D1**
$MHy_2PbBr_{4-x}I_x$ (x = 0.25, 0.3, 0.4, 1.1, 2.35, 2.5, 3.1)	**2D** (RP, (001)-oriented)	**D2**
MHy_2PbCl_4	**2D** (RP, (001)-oriented)	**D3**
$IMMHyPbX_4$ (X = Br, Cl)	**2D** (ACI, (110)-oriented)	**D4**
$MHyPbI_3$	**1D**	**D5**
$Cs_2MHy_2PbX_6$ (X = Br, I)	**0D**	**D6**

All the mixed-halide compounds include Br^- in their composition. Further studies, possibly requiring a design of the new synthesis paths, shall be provided to obtain compounds with I^- and Cl^-.

The MHy^+ cation has been found to serve as the perovskitizer in **3D** systems and as the spacer for **2D** compounds of RP type and **1D** systems without introducing the second A-site moiety. By definition, the coexistence of two cations at the A site is required to synthesize the ACI type **2D** HOIPs, which is herein achieved via integrating MHy^+ with IM^+. Development of the remaining **0D** class is feasible by incorporating the inorganic Cs^+ cation, which has already been found in the literature to form the structures with isolated octahedra.

Three paths for the development of new compounds have been utilized, including **halide substitution**, **halide alloying**, and **A-site cation alloying**. Below the impact of each of the approaches on structural and optoelectrical properties is summarized.

Halide substitution in **2D** RP perovskites of MHy_2PbX_4 (X = Cl, Br, I) formula results in distinct sequences of structural PTs for each halide. Despite these differences, certain common features emerge, such as the HT orthorhombic *Pmmn* polymorph observed across all three systems. Both MHy_2PbBr_4 and MHy_2PbCl_4 transform to a modulated phase upon cooling. For MHy_2PbBr_4 this modulated phase exists within a narrow temperature range (approx. 20 K), while for MHy_2PbCl_4, it is stabilized over a much broader range (approx. 130 K). Both compounds subsequently undergo a phase transition to noncentrosymmetric polymorphs, specifically $Pmn2_1$ for MHy_2PbBr_4 and $P2_1$ for MHy_2PbCl_4. The introduction of smaller halides leads to decreased interatomic distances and strengthened intermolecular interactions. This is particularly evident in MHy_2PbCl_4, which exhibits the smallest interlayer spacing and the highest degree of octahedral distortion among the compounds studied. Additionally, the more distorted geometry of the perovskite slabs is noticeable in (001)-oriented $IMMHyPbCl_4$ compared to its $IMMHyPbBr_4$ analog. The substitution of Br with Cl affects the phase equilibrium, resulting in a shift of the phase transition temperature from 357 K to 383 K upon heating.

In linear optical characteristics, a general trend of band gap narrowing and a redshift of both absorption and PL emission bands is observed along with increasing ionic radius of halides (Cl → Br → I). Another factor affecting the optical properties is the increased octahedral distortion that accompanies the introduction of smaller halides. This highlights the impact of halide substitution on optical features and underscores the direct relationship between the observed optical characteristics and the crystal structure. The shifts of the PL bands correspond to changes in emission color. In the ACI **2D** HOIPs, substituting Cl with Br induces the white-light PL emission observed near 200 K. This makes the $IMMHyPbBr_4$ the first report of hybrid perovskite with two organic cations that reveals this feature.

In the **halide-alloyed** $MHyPbBr_xCl_{3-x}$ **3D** systems both HT phases of the single-halide analogs ($Pb2_1m$ and $Pm\bar{3}m$ for Cl and Br, respectively) are reported for $x \geq 1.33$ and the HT polymorph of $MHyPbCl_3$ is present for all compositions. Stabilization of the cubic phase is determined by the volume of voids hosting MHy^+. In the $MHy_2PbBr_{4-x}I_x$ series of **2D** hybrids, four new polymorphs are reported, including RT phases of orthorhombic *Pnma* and incommensurately modulated $Pnma(00\gamma)0s0$ symmetry, and the LT phases described in monoclinic $P2_1/c$ and triclinic $P\overline{1}$ space group. The halide-mixing approach turned out to be a solution to form the **3D** perovskite phase with a large contribution of iodide, which could not be achieved through chemical synthesis. In the $Cs_2MHy_2PbBr_3I_3$ **0D** material a coexistence of two halides is manifested in a notable increased distortion of Pb–X bond length. A characteristic feature of all halide-mixed compounds described herein is the preferential occupation of the halide sites. The positions interacting with MHy^+ are predominantly occupied by the halide forming stronger HBs, in this case, Cl^- for **3D** and Br^- for **2D** and **0D** systems.

The implementation of halide alloying in **3D** and **2D** HOIPs enhances the tunability of optical properties. A redshift of the excitonic absorption band from 389 nm to 457 nm is demonstrated with increasing x in $MHyPbBr_xCl_{3-x}$, further enhanced to 484 nm for $MHyPbBr_{2.8}I_{0.2}$. In the same series, the values of E_g and positions of the PL emission maxima vary linearly on x. In the $MHy_2PbBr_{4-x}I_x$ **2D** HOIPs E_g drops rapidly with x in the Br-dominated systems, eventually tending to the value of 2.20 eV, reported for MHy_2PbI_4. Increased octahedral distortions related to the selective occupancy broaden the PL emission bands in $Cs_2MHy_2PbBr_3I_3$, with FWHM increasing from 158 – 175 nm to 230 nm.

The introduction of IM^+ as an A-site cation into MHy-based lead halides results in the formation of a **2D** phase of the ACI type. This structure features corrugated inorganic layers oriented along the (110) direction, with IM^+ and MHy^+ cations occupying interlayer and intralayer positions, respectively. Two polymorphs, described in monoclinic $P2/c$ and $P2_1/c$ (HT (**I**) and LT (**II**) phase, respectively) are observed in both $IMMHyPbX_4$ (X = Cl, Br) compounds. The existence of N–H···N HBs between IM^+ and MHy^+ provides gradual stabilization of the second cation on cooling. The inorganic slabs in **II**, influenced by interactions with MHy^+, are distinguished by the heaviest tilting of the perovskite layers reported to date for the (110)-oriented ACI-type lead halides. The unique structural features are manifested in broadened PL emission bands compared to MHy-based analogs of (001)-type. This demonstrates another example of the relationship between crystal structure and optical properties.

The combination of MHy^+ and Cs^+ at the A site prompts the formation of **0D** structures with isolated octahedra, analogously to the Cs_4PbX_6. MHy^+ substitutes the Cs^+ sites, affecting the octahedra geometry via HBs. The compounds adopt orthorhombic *Cmce* symmetry, isostructural to the high-pressure polymorph of Cs_4PbX_6. Here the **A-site cation alloying** is also useful for the tunability of optical properties, revealing a redshift of excitonic absorption against the all-inorganic material.

The role of dimensionality and a type of structure on the structural and optical properties is discussed for single-halide materials. Generally, the σ^2 parameter (octahedra angle variance) decreases in hybrids of lower dimensionality vs **3D** and **2D** perovskites for all studied lead halides. In **2D** HOIPs, the (110)-oriented materials reveal lower σ^2 compared to (001)-type analogs. Contradictory dependencies are observed in bond length distortions, with Δ_d increasing in **2D** chlorides against **3D**, decreasing in the **3D**, **2D**, and **0D** order in bromides, and reaching the highest values for the **1D** structures in iodides. The HB's strengths decrease in the following order: **3D**, **1D**, **0D**, and **2D**. The largest octahedra distortions, which are observed for **3D** structures, are most likely attributed to the largest degree of intermolecular interactions, as only for **3D** systems the Pb – NH_2 distances are small enough to be treated as coordination bonds. In the case of linear optical properties, the band gap increases with decreasing dimensionality. Chlorides and bromides of the ACI-type structures with (110)-oriented layers reveal larger E_g than the (001)-oriented RP analogs. ACI-type **2D** HOIPs and **0D** hybrids also exhibit broader PL emission bands than **3D** and **2D** RP perovskites. The sole **1D** phase, $MHyPbI_3$, does not reveal luminescent properties.

In conclusion, the studies presented in this thesis demonstrate that both A-site and X-site engineering approaches are effective for developing new MHy-based lead halide hybrids. The described compounds are characterized by rich polymorphism, influenced by temperature variations and site-specific substitution or site mixing. A detailed analysis of their crystal structures reveals the significant impact of organic-inorganic intermolecular forces on both structural features and phase transition behaviors. By employing the compositional engineering methods discussed, one can precisely tune and control various bulk optoelectronic properties, including band gap, absorption and photoluminescence (PL) emission band positions and shapes, second harmonic generation (SHG) intensity, and ionic conductivity. Ultimately, the structure-property relationships highlighted in this study underscore the importance of comprehensive characterization techniques to enhance the understanding and applicability of this emerging subclass of hybrid materials.

11. References

1. Mitzi, D.B. Synthesis, Structure, and Properties of Organic-Inorganic Perovskites and Related Materials. In *Progress in Inorganic Chemistry*; John Wiley & Sons, Ltd, **1999**; Vol. 48, pp. 1–121, doi:10.1002/9780470166499.ch1.
2. Saparov, B.; Mitzi, D.B. Organic-Inorganic Perovskites: Structural Versatility for Functional Materials Design. *Chem. Rev.* **2016**, *116*, 4558–4596.
3. Kickelbick, G. Introduction to Hybrid Materials. In *Hybrid Materials: Synthesis, Characterization, and Applications*; John Wiley & Sons, Ltd, **2007**; pp. 1–48, doi:10.1002/9783527610495.CH1.
4. Schroeder, G. Hybrydowe Nieorganiczno-Organiczne Zmiatacze Molekularne - Synteza, Właściwości, Zastosowanie. *Chemik* **2016**, *70*, 81–88.
5. Rose, G. *De Novis Quibusdam Fossilibus Quae in Montibus Uraliis Inveniuntur*; AG Schade, **1839**.
6. Wenk, H.-R.; Bulakh, A. *Minerals: Their Constitution and Origin*; 11th ed.; Cambridge University Press, **2015**.
7. Li, W.; Stroppa, A.; Wang, Z.; Gao, S. *Hybrid Organic–Inorganic Perovskites*; John Wiley & Sons, Ltd, **2020**., doi:10.1002/9783527344338.CH1.
8. Megaw, H.D. Crystal Structure of Barium Titanate. *Nature* **1945**, *155*, 484–485.
9. Garbarz-Glos, B.; Lisińska-Czekaj, A.; Czekaj, D.; Bak, W. Effect of Semiconductor Element Substitution on the Electric Properties of Barium Titanate Ceramics. *Arch. Metall. Mater.* **2016**, *61*, 887–890.
10. Reavley, M.J.H.; Guo, H.; Yuan, J.; Ng, A.Y.R.; Ho, T.Y.K.; Tan, H.T.; Du, Z.; Gan, C.L. Ultrafast High-Temperature Sintering of Barium Titanate Ceramics with Colossal Dielectric Constants. *J. Eur. Ceram. Soc.* **2022**, *42*, 4934–4943.
11. Arlt, G.; Hennings, D.; De With, G. Dielectric Properties of Fine-grained Barium Titanate Ceramics. *J. Appl. Phys.* **1985**, *58*, 1619–1625.
12. Kubel, F.; Schmid, H. Structure of a Ferroelectric and Ferroelastic Monodomain Crystal of the Perovskite $BiFeO_3$. *Acta Crystallogr.* **1990**, *B46*, 698–702.
13. Norby, P.; Andersen, I.G.K.; Andersen, E.K.; Andersen, N.H. The Crystal Structure of Lanthanum Manganate(III), $LaMnO_3$, at Room Temperature and at 1273 K under N_2. *J. Solid State Chem.* **1995**, *119*, 191–196.

14. Li, W.; Wang, Z.; Deschler, F.; Gao, S.; Friend, R.H.; Cheetham, A.K. Chemically Diverse and Multifunctional Hybrid Organic-Inorganic Perovskites. *Nat. Rev. Mater.* **2017**, *2*, 16099.

15. Smółka, S.; Mączka, M.; Drozdowski, D.; Stefańska, D.; Gągor, A.; Sieradzki, A.; Zaręba, J.K.; Ptak, M. Effect of Dimensionality on Photoluminescence and Dielectric Properties of Imidazolium Lead Bromides. *Inorg. Chem.* **2022**, *61*, 15225–15238.

16. Cepeda, J.; Pérez-Yáñez, S.; Beobide, G.; Castillo, O.; Luque, A.; Wright, P.A.; Sneddon, S.; Ashbrook, S.E. Exploiting Synthetic Conditions to Promote Structural Diversity within the Scandium(III)/Pyrimidine-4,6-Dicarboxylate System. *Cryst. Growth Des.* **2015**, *15*, 2352–2363.

17. Wei, Z.; Liao, W.Q.; Tang, Y.Y.; Li, P.F.; Shi, P.P.; Cai, H.; Xiong, R.G. Discovery of an Antiperovskite Ferroelectric in $[(CH_3)_3NH]_3(MnBr_3)(MnBr_4)$. *J. Am. Chem. Soc.* **2018**, *140*, 8110–8113.

18. Boström, H.L.B.; Senn, M.S.; Goodwin, A.L. Recipes for Improper Ferroelectricity in Molecular Perovskites. *Nat. Commun.* **2018**, *9*, 1–7.

19. Jain, P.; Ramachandran, V.; Clark, R.J.; Hai, D.Z.; Toby, B.H.; Dalal, N.S.; Kroto, H.W.; Cheetham, A.K. Multiferroic Behavior Associated with an Order-Disorder Hydrogen Bonding Transition in Metal-Organic Frameworks (MOFs) with the Perovskite ABX_3 Architecture. *J. Am. Chem. Soc.* **2009**, *131*, 13625–13627.

20. Gómez-Aguirre, L.C.; Pato-Doldán, B.; Mira, J.; Castro-García, S.; Senñarís-Rodríguez, M.A.; Sánchez-Andújar, M.; Singleton, J.; Zapf, V.S. Magnetic Ordering-Induced Multiferroic Behavior in $[CH_3NH_3][Co(HCOO)_3]$ Metal-Organic Framework. *J. Am. Chem. Soc.* **2016**, *138*, 1122–1125.

21. Mączka, M.; Gągor, A.; Ptak, M.; Paraguassu, W.; Da Silva, T.A.; Sieradzki, A.; Pikul, A. Phase Transitions and Coexistence of Magnetic and Electric Orders in the Methylhydrazinium Metal Formate Frameworks. *Chem. Mater.* **2017**, *29*, 2264–2275.

22. Du, Z.-Y.; Xu, T.-T.; Huang, B.; Su, Y.-J.; Xue, W.; He, C.-T.; Zhang, W.-X.; Chen, X.-M.; Du, Z.; Huang, B.; et al. Switchable Guest Molecular Dynamics in a Perovskite-Like Coordination Polymer toward Sensitive Thermoresponsive Dielectric Materials. *Angew. Chemie Int. Ed.* **2015**, *54*, 914–918.

23. Trzebiatowska, M.; Gągor, A.; Macalik, L.; Peksa, P.; Sieradzki, A. Phase Transition in the Extreme: A Cubic-to-Triclinic Symmetry Change in Dielectrically Switchable Cyanide Perovskites. *Dalt. Trans.* **2019**, *48*, 15830–15840.

24. Xu, W.J.; Li, P.F.; Tang, Y.Y.; Zhang, W.X.; Xiong, R.G.; Chen, X.M. A Molecular Perovskite with Switchable Coordination Bonds for High-Temperature Multiaxial Ferroelectrics. *J. Am. Chem. Soc.* **2017**, *139*, 6369–6375.
25. Mączka, M.; Gągor, A.; Pikul, A.; Stefańska, D. Novel Hypophosphite Hybrid Perovskites of $[CH_3NH_2NH_2][Mn(H_2POO)_3]$ and $[CH_3NH_2NH_2][Mn(H_2POO)_{2.83}(HCOO)_{0.17}]$ Exhibiting Antiferromagnetic Order and Red Photoluminescence. *RSC Adv.* **2020**, *10*, 19020–19026.
26. Kojima, A.; Teshima, K.; Shirai, Y.; Miyasaka, T. Organometal Halide Perovskites as Visible-Light Sensitizers for Photovoltaic Cells. *J. Am. Chem. Soc.* **2009**, *131*, 6050–6051.
27. NREL Best Research-Cell Efficiency Chart https://www.nrel.gov/pv/assets/pdfs/best-research-cell-efficiencies-rev211011.pdf (accessed on 5 June 2024).
28. Liang, Z.; Zhang, Y.; Xu, H.; Chen, W.; Liu, B.; Zhang, J.; Zhang, H.; Wang, Z.; Kang, D.H.; Zeng, J.; et al. Homogenizing Out-of-Plane Cation Composition in Perovskite Solar Cells. *Nature* **2023**, *624*, 557–563.
29. Ball, J.M.; Lee, M.M.; Hey, A.; Snaith, H.J. Low-Temperature Processed Meso-Superstructured to Thin-Film Perovskite Solar Cells. *Energy Environ. Sci.* **2013**, *6*, 1739–1743.
30. Sun, S.; Salim, T.; Mathews, N.; Duchamp, M.; Boothroyd, C.; Xing, G.; Sum, T.C.; Lam, Y.M. The Origin of High Efficiency in Low-Temperature Solution-Processable Bilayer Organometal Halide Hybrid Solar Cells. *Energy Environ. Sci.* **2013**, *7*, 399–407.
31. Stranks, S.D.; Eperon, G.E.; Grancini, G.; Menelaou, C.; Alcocer, M.J.P.; Leijtens, T.; Herz, L.M.; Petrozza, A.; Snaith, H.J. Electron-Hole Diffusion Lengths Exceeding 1 Micrometer in an Organometal Trihalide Perovskite Absorber. *Science* **2013**, *342*, 341–344.
32. Wang, F.; Cao, Y.; Chen, C.; Chen, Q.; Wu, X.; Li, X.; Qin, T.; Huang, W. Materials toward the Upscaling of Perovskite Solar Cells: Progress, Challenges, and Strategies. *Adv. Funct. Mater.* **2018**, *28*, 1803753.
33. Cao, M.; Tian, J.; Cai, Z.; Peng, L.; Yang, L.; Wei, D. Perovskite Heterojunction Based on $CH_3NH_3PbBr_3$ Single Crystal for High-Sensitive Self-Powered Photodetector. *Appl. Phys. Lett.* **2016**, *109*, 233303.
34. Mehdi, H.; Mhamdi, A.; Hannachi, R.; Bouazizi, A. $MAPbBr_3$ Perovskite Solar Cells: Via a Two-Step Deposition Process. *RSC Adv.* **2019**, *9*, 12906–12912.

35. Zhang, Z.; Liu, Y.; Sun, Q.; Ban, H.; Liu, Z.; Yu, H.; Li, X.; Dai, L.; Yang, W.; Shen, Y.; et al. The Importance of Elemental Lead to Perovskites Photovoltaics. *Chem. Inorg. Mater.* **2023**, *1*, 100017.
36. Goldschmidt, V.M. Die Gesetze Der Krystallochemie. *Naturwissenschaften* **1926**, *14*, 477–485.
37. Kieslich, G.; Sun, S.; Cheetham, A.K. An Extended Tolerance Factor Approach for Organic–Inorganic Perovskites. *Chem. Sci.* **2015**, *6*, 3430–3433.
38. Petrosova, H.R.; Kucheriv, O.I.; Shova, S.; Gural'skiy, I.A. Aziridinium Cation Templating 3D Lead Halide Hybrid Perovskites. *Chem. Commun.* **2022**, *58*, 5745–5748.
39. Stefańska, D.; Ptak, M.; Mączka, M. Synthesis, Photoluminescence and Vibrational Properties of Aziridinium Lead Halide Perovskites. *Molecules* **2022**, *27*, 7949.
40. Mączka, M.; Ptak, M.; Gągor, A.; Zaręba, J.K.; Liang, X.; Balciunas, S.; Semenikhin, O.A.; Kucheriv, O.I.; Gural'skiy, I.A.; Shova, S.; et al. Phase Transitions, Dielectric Response, and Nonlinear Optical Properties of Aziridinium Lead Halide Perovskites. *Chem. Mater.* **2023**, *35*, 9725–9738.
41. Zheng, C.; Rubel, O. Aziridinium Lead Iodide: A Stable, Low-Band-Gap Hybrid Halide Perovskite for Photovoltaics. *J. Phys. Chem. Lett.* **2018**, *9*, 874–880.
42. Mączka, M.; Ptak, M.; Gągor, A.; Stefańska, D.; Zaręba, J.K.; Sieradzki, A. Methylhydrazinium Lead Bromide: Noncentrosymmetric Three-Dimensional Perovskite with Exceptionally Large Framework Distortion and Green Photoluminescence. *Chem. Mater.* **2020**, *32*, 1667–1673.
43. Mączka, M.; Gągor, A.; Zaręba, J.K.; Stefańska, D.; Drozd, M.; Balciunas, S.; Šimėnas, M.; Banys, J.; Sieradzki, A. Three-Dimensional Perovskite Methylhydrazinium Lead Chloride with Two Polar Phases and Unusual Second-Harmonic Generation Bistability above Room Temperature. *Chem. Mater.* **2020**, *32*, 4072–4082.
44. Salado, M.; Ramos, F.J.; Manzanares, V.M.; Gao, P.; Nazeeruddin, M.K.; Dyson, P.J.; Ahmad, S. Extending the Lifetime of Perovskite Solar Cells Using a Perfluorinated Dopant. *ChemSusChem* **2016**, *9*, 2708–2714.
45. Zhou, Y.; Zhou, Z.; Chen, M.; Zong, Y.; Huang, J.; Pang, S.; Padture, N.P. Doping and Alloying for Improved Perovskite Solar Cells. *J. Mater. Chem. A* **2016**, *4*, 17623–17635.
46. Ono, L.K.; Juarez-Perez, E.J.; Qi, Y. Progress on Perovskite Materials and Solar Cells with Mixed Cations and Halide Anions. *ACS Appl. Mater. Interfaces* **2017**, *9*, 30197–30246.

47. Wang, Q.; Lin, F.; Chueh, C.C.; Zhao, T.; Eslamian, M.; Jen, A.K.Y. Enhancing Efficiency of Perovskite Solar Cells by Reducing Defects through Imidazolium Cation Incorporation. *Mater. Today Energy* **2018**, *7*, 161–168.
48. Lin, H.; Zhang, X.; Cai, L.; Lao, J.; Qi, R.; Luo, C.; Chen, S.; Peng, H.; Huang, R.; Duan, C. High-Stability Fluorescent Perovskites Embedded in PbBrOH Triggered by Imidazole Derivatives in Water. *J. Mater. Chem. C* **2020**, *8*, 5594–5599.
49. Zhang, M.; Yu, H.; Lyu, M.; Wang, Q.; Yun, J.H.; Wang, L. Composition-Dependent Photoluminescence Intensity and Prolonged Recombination Lifetime of Perovskite $CH_3NH_3PbBr_{3-x}$ Clxfilms. *Chem. Commun.* **2014**, *50*, 11727–11730.
50. Karlsson, M.; Yi, Z.; Reichert, S.; Luo, X.; Lin, W.; Zhang, Z.; Bao, C.; Zhang, R.; Bai, S.; Zheng, G.; et al. Mixed Halide Perovskites for Spectrally Stable and High-Efficiency Blue Light-Emitting Diodes. *Nat. Commun.* **2021**, *12*, 1–10.
51. Madjet, M.E.A.; Akimov, A. V.; El-Mellouhi, F.; Berdiyorov, G.R.; Ashhab, S.; Tabet, N.; Kais, S. Enhancing the Carrier Thermalization Time in Organometallic Perovskites by Halide Mixing. *Phys. Chem. Chem. Phys.* **2016**, *18*, 5219–5231.
52. Ebadi, M.; Sefidi, P.Y.; Samadifar, A.; Salari, D.; Darbandi, M.; Hosseini, M.G. Influence of Lead (II) Chloride and/or Lead (II) Bromide Entrance on the Efficiency and Stability of Methyl Ammonium Lead Triiodide Perovskite Solar Cell: Comparative Study of the Halide Composition and Substitution Percentage. *Opt. Mater.* **2021**, *113*, 110888.
53. Edri, E.; Kirmayer, S.; Kulbak, M.; Hodes, G.; Cahen, D. Chloride Inclusion and Hole Transport Material Doping to Improve Methyl Ammonium Lead Bromide Perovskite-Based High Open-Circuit Voltage Solar Cells. *J. Phys. Chem. Lett.* **2014**, *5*, 429–433.
54. Brivio, F.; Caetano, C.; Walsh, A. Thermodynamic Origin of Photoinstability in the $CH_3NH_3Pb(I_{1-x}Br_x)_3$ Hybrid Halide Perovskite Alloy. *J. Phys. Chem. Lett.* **2016**, *7*, 1083–1087.
55. Noh, J.H.; Im, S.H.; Heo, J.H.; Mandal, T.N.; Seok, S. Il Chemical Management for Colorful, Efficient, and Stable Inorganic-Organic Hybrid Nanostructured Solar Cells. *Nano Lett.* **2013**, *13*, 1764–1769.
56. Kieslich, G.; Sun, S.; Cheetham, A.K. Solid-State Principles Applied to Organic–Inorganic Perovskites: New Tricks for an Old Dog. *Chem. Sci.* **2014**, *5*, 4712–4715.
57. Akkerman, Q.A.; Manna, L. What Defines a Halide Perovskite? *ACS Energy Lett.* **2020**, *5*, 604–610.

58. Breternitz, J.; Schorr, S. What Defines a Perovskite? *Adv. Energy Mater.* **2018**, *8*, 1802366.
59. Mercier, N. Hybrid Halide Perovskites: Discussions on Terminology and Materials. *Angew. Chemie Int. Ed.* **2019**, *58*, 17912–17917.
60. Jodlowski, A.D.; Rodríguez-Padrón, D.; Luque, R.; de Miguel, G.; Jodlowski, A.D.; de Miguel, G.; Rodríguez, D. Alternative Perovskites for Photovoltaics. *Adv. Energy Mater.* **2018**, *8*, 1703120.
61. Almutlaq, J.; Yin, J.; Mohammed, O.F.; Bakr, O.M. The Benefit and Challenges of Zero-Dimensional Perovskites. *J. Phys. Chem. Lett.* **2018**, *9*, 4131–4138.
62. Yuan, Z.; Zhou, C.; Tian, Y.; Shu, Y.; Messier, J.; Wang, J.C.; Van De Burgt, L.J.; Kountouriotis, K.; Xin, Y.; Holt, E.; et al. One-Dimensional Organic Lead Halide Perovskites with Efficient Bluish White-Light Emission. *Nat. Commun.* **2017**, *8*, 1–7.
63. Tu, Q.; Spanopoulos, I.; Vasileiadou, E.S.; Li, X.; Kanatzidis, M.G.; Shekhawat, G.S.; Dravid, V.P. Exploring the Factors Affecting the Mechanical Properties of 2D Hybrid Organic-Inorganic Perovskites. *ACS Appl. Mater. Interfaces* **2020**, *12*, 20440–20447.
64. McNulty, J.A.; Lightfoot, P. Structural Chemistry of Layered Lead Halide Perovskites Containing Single Octahedral Layers. *IUCrJ* **2021**, *8*, 485–513.
65. Dou, L.; Wong, A.B.; Yu, Y.; Lai, M.; Kornienko, N.; Eaton, S.W.; Fu, A.; Bischak, C.G.; Ma, J.; Ding, T.; et al. Atomically Thin Two-Dimensional Organic-Inorganic Hybrid Perovskites. *Science* **2015**, *349*, 1518–1521.
66. Tsai, H.; Nie, W.; Blancon, J.C.; Stoumpos, C.C.; Asadpour, R.; Harutyunyan, B.; Neukirch, A.J.; Verduzco, R.; Crochet, J.J.; Tretiak, S.; et al. High-Efficiency Two-Dimensional Ruddlesden–Popper Perovskite Solar Cells. *Nature* **2016**, *536*, 312–316.
67. Leng, K.; Fu, W.; Liu, Y.; Chhowalla, M.; Loh, K.P. From Bulk to Molecularly Thin Hybrid Perovskites. *Nat. Rev. Mater.* **2020**, *5*, 482–500.
68. Wang, K.; Park, J.Y.; Akriti; Dou, L. Two-Dimensional Halide Perovskite Quantum-Well Emitters: A Critical Review. *EcoMat* **2021**, *3*, e12104.
69. Gong, X.; Voznyy, O.; Jain, A.; Liu, W.; Sabatini, R.; Piontkowski, Z.; Walters, G.; Bappi, G.; Nokhrin, S.; Bushuyev, O.; et al. Electron–Phonon Interaction in Efficient Perovskite Blue Emitters. *Nat. Mater.* **2018**, *17*, 550–556.
70. Quan, L.N.; Rand, B.P.; Friend, R.H.; Mhaisalkar, S.G.; Lee, T.W.; Sargent, E.H. Perovskites for Next-Generation Optical Sources. *Chem. Rev.* **2019**, *119*, 7444–7477.
71. Smith, M.D.; Connor, B.A.; Karunadasa, H.I. Tuning the Luminescence of Layered Halide Perovskites. *Chem. Rev.* **2019**, *119*, 3104–3139.

72. Miyata, A.; Mitioglu, A.; Plochocka, P.; Portugall, O.; Wang, J.T.W.; Stranks, S.D.; Snaith, H.J.; Nicholas, R.J. Direct Measurement of the Exciton Binding Energy and Effective Masses for Charge Carriers in Organic–Inorganic Tri-Halide Perovskites. *Nat. Phys.* **2015**, *11*, 582–587.
73. Kim, E.B.; Akhtar, M.S.; Shin, H.S.; Ameen, S.; Nazeeruddin, M.K. A Review on Two-Dimensional (2D) and 2D-3D Multidimensional Perovskite Solar Cells: Perovskites Structures, Stability, and Photovoltaic Performances. *J. Photochem. Photobiol. C Photochem. Rev.* **2021**, *48*, 100405.
74. Marchenko, E.I.; Fateev, S.A.; Petrov, A.A.; Korolev, V. V.; Mitrofanov, A.; Petrov, A. V.; Goodilin, E.A.; Tarasov, A.B. Database of Two-Dimensional Hybrid Perovskite Materials: Open-Access Collection of Crystal Structures, Band Gaps, and Atomic Partial Charges Predicted by Machine Learning. *Chem. Mater.* **2020**, *32*, 7383–7388.
75. Guo, Y.Y.; Elliott, C.; McNulty, J.A.; Cordes, D.B.; Slawin, A.M.Z.; Lightfoot, P. New Variants of (110)-Oriented Layered Lead Bromide Perovskites, Templated by Formamidinium or Pyrazolium. *Eur. J. Inorg. Chem.* **2021**, 3404–3411.
76. Dohner, E.R.; Hoke, E.T.; Karunadasa, H.I. Self-Assembly of Broadband White-Light Emitters. *J. Am. Chem. Soc.* **2014**, *136*, 1718–1721.
77. Mao, L.; Guo, P.; Kepenekian, M.; Hadar, I.; Katan, C.; Even, J.; Schaller, R.D.; Stoumpos, C.C.; Kanatzidis, M.G. Structural Diversity in White-Light-Emitting Hybrid Lead Bromide Perovskites. *J. Am. Chem. Soc.* **2018**, *140*, 13078–13088.
78. Hu, T.; Smith, M.D.; Dohner, E.R.; Sher, M.J.; Wu, X.; Trinh, M.T.; Fisher, A.; Corbett, J.; Zhu, X.Y.; Karunadasa, H.I.; et al. Mechanism for Broadband White-Light Emission from Two-Dimensional (110) Hybrid Perovskites. *J. Phys. Chem. Lett.* **2016**, *7*, 2258–2263.
79. Vargas, B.; Torres-Cadena, R.; Rodríguez-Hernández, J.; Gembicky, M.; Xie, H.; Jiménez-Mier, J.; Liu, Y.S.; Menéndez-Proupin, E.; Dunbar, K.R.; Lopez, N.; et al. Optical, Electronic, and Magnetic Engineering of (111) Layered Halide Perovskites. *Chem. Mater.* **2018**, *30*, 5315–5321.
80. Ruddlesden, S.N.; Popper, P. New Compounds of the K_2NIF_4 Type. *Acta Crystallogr.* **1957**, *10*, 538–539.
81. Stoumpos, C.C.; Cao, D.H.; Clark, D.J.; Young, J.; Rondinelli, J.M.; Jang, J.I.; Hupp, J.T.; Kanatzidis, M.G. Ruddlesden-Popper Hybrid Lead Iodide Perovskite 2D Homologous Semiconductors. *Chem. Mater.* **2016**, *28*, 2852–2867.

82. Dion, M.; Ganne, M.; Tournoux, M. Nouvelles Familles de Phases $M^{I}M^{II}_2Nb_3O_{10}$ a Feuillets "Perovskites." *Mater. Res. Bull.* **1981**, *16*, 1429–1435.

83. Mao, L.; Ke, W.; Pedesseau, L.; Wu, Y.; Katan, C.; Even, J.; Wasielewski, M.R.; Stoumpos, C.C.; Kanatzidis, M.G. Hybrid Dion-Jacobson 2D Lead Iodide Perovskites. *J. Am. Chem. Soc.* **2018**, *140*, 3775–3783.

84. Soe, C.M.M.; Stoumpos, C.C.; Kepenekian, M.; Traoré, B.; Tsai, H.; Nie, W.; Wang, B.; Katan, C.; Seshadri, R.; Mohite, A.D.; et al. New Type of 2D Perovskites with Alternating Cations in the Interlayer Space, $(C(NH_2)_3)(CH_3NH_3)_nPb_nI_{3n+1}$: Structure, Properties, and Photovoltaic Performance. *J. Am. Chem. Soc.* **2017**, *139*, 16297–16309.

85. Chang, Y.H.; Lin, J.C.; Chen, Y.C.; Kuo, T.R.; Wang, D.Y. Facile Synthesis of Two-Dimensional Ruddlesden–Popper Perovskite Quantum Dots with Fine-Tunable Optical Properties. *Nanoscale Res. Lett.* **2018**, *13*, 1–7.

86. Ahmad, S.; Rahil, M.; Rajput, P.; Ghosh, D. Highly Tunable Single-Phase Excitons in Mixed Halide Layered Perovskites. *ACS Appl. Electron. Mater.* **2020**, *2*, 3199–3210.

87. Ghosh, D.; Acharya, D.; Pedesseau, L.; Katan, C.; Even, J.; Tretiak, S.; Neukirch, A.J. Charge Carrier Dynamics in Two-Dimensional Hybrid Perovskites: Dion–Jacobson vs. Ruddlesden–Popper Phases. *J. Mater. Chem. A* **2020**, *8*, 22009–22022.

88. Niu, T.; Ren, H.; Wu, B.; Xia, Y.; Xie, X.; Yang, Y.; Gao, X.; Chen, Y.; Huang, W. Reduced-Dimensional Perovskite Enabled by Organic Diamine for Efficient Photovoltaics. *J. Phys. Chem. Lett.* **2019**, *10*, 2349–2356.

89. Li, X.; Ke, W.; Traoré, B.; Guo, P.; Hadar, I.; Kepenekian, M.; Even, J.; Katan, C.; Stoumpos, C.C.; Schaller, R.D.; et al. Two-Dimensional Dion-Jacobson Hybrid Lead Iodide Perovskites with Aromatic Diammonium Cations. *J. Am. Chem. Soc.* **2019**, *141*, 12880–12890.

90. Mao, L.; Stoumpos, C.C.; Kanatzidis, M.G. Two-Dimensional Hybrid Halide Perovskites: Principles and Promises. *J. Am. Chem. Soc.* **2018**, *141*, 1171–1190.

91. Williams, R.T.; Song, K.S. The Self-Trapped Exciton. *J. Phys. Chem. Solids* **1990**, *51*, 679–716.

92. Georgiev, M.; Mihailov, L.; Singh, J. Exciton Self-Trapping Processes. *Pure Appl. Chem.* **1995**, *67*, 447–456.

93. Trigui, A.; Abid, H.; Mlayah, A.; Abid, Y. Optical Properties and Vibrational Studies of a New Self Assembled Organic–Inorganic Nanowire Crystal $(C_6H_{13}N_3)_2Pb_3I_{10}$. *Synth. Met.* **2012**, *162*, 1731–1736.

94. Chen, D.; Dai, F.; Hao, S.; Zhou, G.; Liu, Q.; Wolverton, C.; Zhao, J.; Xia, Z. Crystal Structure and Luminescence Properties of Lead-Free Metal Halides $(C_6H_5CH_2NH_3)_3MBr_6$ (M = Bi and Sb). *J. Mater. Chem. C* **2020**, *8*, 7322–7329.

95. Rahaman, M.Z.; Ge, S.; Lin, C.H.; Cui, Y.; Wu, T. One-Dimensional Molecular Metal Halide Materials: Structures, Properties, and Applications. *Small Struct.* **2021**, *2*, 2000062.

96. Sun, S.; Lu, M.; Gao, X.; Shi, Z.; Bai, X.; Yu, W.W.; Zhang, Y. 0D Perovskites: Unique Properties, Synthesis, and Their Applications. *Adv. Sci.* **2021**, *8*, 2102689.

97. Dang, Y.; Liu, G.; Song, J.; Meng, L.; Sun, Y.; Hu, W.; Tao, X. Layered Perovskite $(CH_3NH_3)_2Pb(SCN)_2I_2$ Single Crystals: Phase Transition and Moisture Stability. *ACS Appl. Mater. Interfaces* **2020**, *12*, 37713–37721.

98. Fateev, S.A.; Petrov, A.A.; Marchenko, E.I.; Zubavichus, Y. V.; Khrustalev, V.N.; Petrov, A. V.; Aksenov, S.M.; Goodilin, E.A.; Tarasov, A.B. FA_2PbBr_4: Synthesis, Structure, and Unusual Optical Properties of Two Polymorphs of Formamidinium-Based Layered (110) Hybrid Perovskite. *Chem. Mater.* **2021**, *33*, 1900–1907.

99. Schueller, E.C.; Laurita, G.; Fabini, D.H.; Stoumpos, C.C.; Kanatzidis, M.G.; Seshadri, R. Crystal Structure Evolution and Notable Thermal Expansion in Hybrid Perovskites Formamidinium Tin Iodide and Formamidinium Lead Bromide. *Inorg. Chem.* **2018**, *57*, 695–701.

100. Baikie, T.; Barrow, N.S.; Fang, Y.; Keenan, P.J.; Slater, P.R.; Piltz, R.O.; Gutmann, M.; Mhaisalkar, S.G.; White, T.J. A Combined Single Crystal Neutron/X-Ray Diffraction and Solid-State Nuclear Magnetic Resonance Study of the Hybrid Perovskites $CH_3NH_3PbX_3$ (X = I, Br and Cl). *J. Mater. Chem. A* **2015**, *3*, 9298–9307.

101. Poglitsch, A.; Weber, D. Dynamic Disorder in Methylammoniumtrihalogenoplumbates (II) Observed by Millimeter-Wave Spectroscopy. *J. Chem. Phys.* **1987**, *87*, 6373–6378.

102. Fleet, M.E. Distortion Parameters for Coordination Polyhedra. *Mineral. Mag.* **1976**, *40*, 531–533.

103. Franken, P.A.; Hill, A.E.; Peters, C.W.; Weinreich, G. Generation of Optical Harmonics. *Phys. Rev. Lett.* **1961**, *7*, 118.

104. Coda, A.; Pandarese, F. Reliability of Second-Harmonic Generation in Crystalline Powders at Optical Frequencies as a Test of Absence of Centrosymmetry. *J. Appl. Crystallogr.* **1976**, *9*, 193–198.

105. Kurtz, S.K.; Perry, T.T. A Powder Technique for the Evaluation of Nonlinear Optical Materials. *J. Appl. Phys.* **1968**, *39*, 3798–3813.

106. Mączka, M.; Ptak, M. Lattice Dynamics and Structural Phase Transitions in Two-Dimensional Ferroelectric Methylhydrazinium Lead Bromide Investigated Using Raman and IR Spectroscopy. *J. Phys. Chem. C* **2022**, *126*, 7991–7998.

107. Mączka, M.; Zaręba, J.K.; Gągor, A.; Stefańska, D.; Ptak, M.; Roleder, K.; Kajewski, D.; Soszyński, A.; Fedoruk, K.; Sieradzki, A. [Methylhydrazinium]$_2$PbBr$_4$, a Ferroelectric Hybrid Organic-Inorganic Perovskite with Multiple Nonlinear Optical Outputs. *Chem. Mater.* **2021**, *33*, 2331–2342.

108. Fedoruk, K.; Drozdowski, D.; Mączka, M.; Zaręba, J.K.; Stefańska, D.; Gągor, A.; Sieradzki, A. [Methylhydrazinium]$_2$PbCl$_4$, a Two-Dimensional Perovskite with Polar and Modulated Phases. *Inorg. Chem.* **2022**, *61*, 15520–15531.

109. Mączka, M.; Ptak, M.; Gągor, A.; Stefańska, D.; Sieradzki, A. Layered Lead Iodide of [Methylhydrazinium]$_2$PbI$_4$ with a Reduced Band Gap: Thermochromic Luminescence and Switchable Dielectric Properties Triggered by Structural Phase Transitions. *Chem. Mater.* **2019**, *31*, 8563–8575.

110. Febriansyah, B.; Koh, T.M.; Lekina, Y.; Jamaludin, N.F.; Bruno, A.; Ganguly, R.; Shen, Z.X.; Mhaisalkar, S.G.; England, J. Improved Photovoltaic Efficiency and Amplified Photocurrent Generation in Mesoporous n = 1 Two-Dimensional Lead-Iodide Perovskite Solar Cells. *Chem. Mater.* **2019**, *31*, 890–898.

111. Nazarenko, O.; Kotyrba, M.R.; Wörle, M.; Cuervo-Reyes, E.; Yakunin, S.; Kovalenko, M. V. Luminescent and Photoconductive Layered Lead Halide Perovskite Compounds Comprising Mixtures of Cesium and Guanidinium Cations. *Inorg. Chem.* **2017**, *56*, 11552–11564.

112. Du, K.Z.; Tu, Q.; Zhang, X.; Han, Q.; Liu, J.; Zauscher, S.; Mitzi, D.B. Two-Dimensional Lead(II) Halide-Based Hybrid Perovskites Templated by Acene Alkylamines: Crystal Structures, Optical Properties, and Piezoelectricity. *Inorg. Chem.* **2017**, *56*, 9291–9302.

113. Li, X.; Cuthriell, S.A.; Bergonzoni, A.; Dong, H.; Traoré, B.; Stoumpos, C.C.; Guo, P.; Even, J.; Katan, C.; Schaller, R.D.; et al. Expanding the Cage of 2D Bromide Perovskites by Large A-Site Cations. *Chem. Mater.* **2022**, *34*, 1132–1142.

114. Li, R.; Wang, Z.; Zhu, T.; Ye, H.; Wu, J.; Liu, X.; Luo, J. Stereochemically Active Lone Pair Induced Polar Tri-Layered Perovskite for Record-Performance Polarized Photodetection. *Angew. Chemie Int. Ed.* **2023**, *62*, e202308445.

115. Zienkiewicz, J.A.; Kowalska, D.A.; Drozdowski, D.; Pikul, A.; Ptak, M. Hybrid Chlorides with Methylhydrazinium Cation: $[CH_3NH_2NH_2]CdCl_3$ and Jahn-Teller Distorted $[CH_3NH_2NH_2]CuCl_3$. *Molecules* **2023**, *28*, 473.
116. Zienkiewicz, J.A.; Ptak, M.; Drozdowski, D.; Fedoruk, K.; Stefański, M.; Pikul, A. Hybrid Organic-Inorganic Crystals of [Methylhydrazinium]$M^{II}Cl_3$ (M^{II} = Co, Ni, Mn). *J. Phys. Chem. C* **2022**, *126*, 15809–15818.
117. Rowińska, M.; Stefańska, D.; Bednarchuk, T.J.; Zaręba, J.K.; Jakubas, R.; Gągor, A. Polymorphism and Red Photoluminescence Emission from $5s^2$ Electron Pairs of Sb(III) in a New One-Dimensional Organic–Inorganic Hybrid Based on Methylhydrazine: MHy_2SbI_5. *Molecules* **2024**, *29*, 455.
118. Britannica, The Editors of Encyclopaedia. “Polymorphism”. Encyclopedia Britannica, https://www.britannica.com/science/polymorphism-crystals (accessed on 16 June 2024).
119. Toledano, J.C.; Glazer, A.M.; Hahn, T.; Parthe, E.; Roth, R.S.; Berry, R.S.; Metselaar, R.; Abrahams, S.C. Structural Phase Transition Nomenclature Report of an IUCr Working Group on Phase Transition Nomenclature. *Acta Crystallogr.* **1998**, *A54*, 1028–1033.
120. Jaeger, G. The Ehrenfest Classification of Phase Transitions: Introduction and Evolution. *Arch. Hist. Exact Sci.* **1998**, *53*, 51–81.
121. Buerger, M.J. Polymorphism and Phase Transformations. *Fortschritte der Mineral.* **1961**, *39*, 9–24.
122. Schneider, V.E.; Tornau, E.E. On the Theory of Isostructural Phase Transitions in Crystals. *Phys. status solidi* **1982**, *111*, 565–574.
123. Govinda, S.; Kore, B.P.; Swain, D.; Hossain, A.; De, C.; Guru Row, T.N.; Sarma, D.D. Critical Comparison of $FAPbX_3$ and $MAPbX_3$ (X = Br and Cl): How Do They Differ? *J. Phys. Chem. C* **2018**, *122*, 2.
124. Yang, B.; Ming, W.; Du, M.H.; Keum, J.K.; Puretzky, A.A.; Rouleau, C.M.; Huang, J.; Geohegan, D.B.; Wang, X.; Xiao, K. Real-Time Observation of Order-Disorder Transformation of Organic Cations Induced Phase Transition and Anomalous Photoluminescence in Hybrid Perovskites. *Adv. Mater.* **2018**, *30*.
125. *International Tables for Crystallography Volume A: Space-Group Symmetry*; Hahn, T., Ed.; 5th ed.; Springer, **2005**., doi:10.1107/97809553602060000100.
126. Dolomanov, O. V.; Bourhis, L.J.; Gildea, R.J.; Howard, J.A.K.; Puschmann, H. OLEX2: A Complete Structure Solution, Refinement and Analysis Program. *J. Appl. Crystallogr.* **2009**, *42*, 339–341.

127. Sheldrick, G.M. SHELXT – Integrated Space-Group and Crystal-Structure Determination. *Acta Crystallogr.* **2015**, *A71*, 3–8.

128. Sheldrick, G.M. Crystal Structure Refinement with SHELXL. *Acta Crystallogr.* **2015**, *C71*, 3–8.

129. Petříček, V.; Palatinus, L.; Plášil, J.; Dušek, M. Jana 2020 - a New Version of the Crystallographic Computing System Jana. *Zeitschrift fur Krist. - Cryst. Mater.* **2023**, *238*, 271–282.

130. Groom, C.R.; Bruno, I.J.; Lightfoot, M.P.; Ward, S.C. The Cambridge Structural Database. *Acta Crystallogr.* **2016**, *B72*, 171–179.

131. Aizu, K. Possible Species of Ferromagnetic, Ferroelectric, and Ferroelastic Crystals. *Phys. Rev. B* **1970**, *2*, 754.

132. Pratheek, M.; Sujith, P.; Shahul Hameed, T.A.; Predeep, P. Effect of Bromide Doping on the Phase Stability and Shelf Life of the Triple Cation Mixed Halide Perovskite Single-Crystals. *Mater. Lett.* **2022**, *326*, 132903.

133. Dohner, E.R.; Jaffe, A.; Bradshaw, L.R.; Karunadasa, H.I. Intrinsic White-Light Emission from Layered Hybrid Perovskites. *J. Am. Chem. Soc.* **2014**, *136*, 13154–13157.

134. Wu, Z.; Ji, C.; Sun, Z.; Wang, S.; Zhao, S.; Zhang, W.; Li, L.; Luo, J. Broadband White-Light Emission with a High Color Rendering Index in a Two-Dimensional Organic-Inorganic Hybrid Perovskite. *J. Mater. Chem. C* **2018**, *6*, 1171–1175.

135. Campbell, E. V.; Dick, B.; Rheingold, A.L.; Zhang, C.; Liu, X.; Vardeny, Z. V.; Miller, J.S. Structures of a Complex Hydrazinium Lead Iodide, $(N_2H_5)_{15}Pb_3I_{21}$, Possessing $[Pb_2I_9]^{5-}$, $[PbI_6]^{4-}$, and I^- Ions and α- and β-$(N_2H_5)PbI_3$. *Chem. - A Eur. J.* **2018**, *24*, 222–229.

136. Hao, F.; Stoumpos, C.C.; Liu, Z.; Chang, R.P.H.; Kanatzidis, M.G. Controllable Perovskite Crystallization at a Gas-Solid Interface for Hole Conductor-Free Solar Cells with Steady Power Conversion Efficiency over 10%. *J. Am. Chem. Soc.* **2014**, *136*, 16411–16419.

137. Fan, L.Q.; Wu, J.H. NH_4PbI_3. *Acta Crystallogr.* **2007**, *E63*, i189.

138. Castro Ferreira, W.; Araújo, B.S.; Gómez, M.A.P.; Medeiros, F.E.O.; de Araujo Paschoal, C.W.; da Silva, C.B.; Freire, P.T.C.; Kaneko, U.F.; Ardito, F.M.; Souza-Neto, N.M.; et al. Pressure-Induced Structural and Optical Transitions in Luminescent Bulk Cs_4PbBr_6. *J. Phys. Chem. C* **2022**, *126*, 541–550.

139. Møller, C.K. *On the Structure of Cæsium Hexahalogeno-Plumbates (II)*; 3rd ed.; Munksgaard, **1960**.

140. Nitsch, K.; Dušek, M.; Nikl, M.; Polák, K.; Rodová, M. Ternary Alkali Lead Chlorides: Crystal Growth, Crystal Structure, Absorption and Emission Properties. *Prog. Cryst. Growth Charact. Mater.* **1995**, *30*, 1–22.

141. Pauling, L. *The Nature of the Chemical Bond*; 3rd ed.; Cornell University Press, **1960**.

142. Mączka, M.; Sobczak, S.; Ratajczyk, P.; Leite, F.F.; Paraguassu, W.; Dybała, F.; Herman, A.P.; Kudrawiec, R.; Katrusiak, A. Pressure-Driven Phase Transition in Two-Dimensional Perovskite MHy_2PbBr_4. *Chem. Mater.* **2022**, *34*, 7867–7877.

143. Drozdowski, D.; Fedoruk, K.; Kabański, A.; Mączka, M.; Sieradzki, A.; Gągor, A. Broadband Yellow and White Emission from Large Octahedral Tilting in (110)-Oriented Layered Perovskites: Imidazolium-Methylhydrazinium Lead Halides. *J. Mater. Chem. C* **2023**, *11*, 4907–4915.

144. Vegard, L. Die Konstitution Der Mischkristalle Und Die Raumfüllung Der Atome. *Zeitschrift für Phys.* **1921**, *5*, 17–26.

145. Toso, S.; Gushchina, I.; Oliver, A.G.; Manna, L.; Kuno, M. Are Mixed-Halide Ruddlesden-Popper Perovskites Really Mixed? *ACS Energy Lett.* **2022**, *7*, 4242–4247.

146. Ovčar, J.; Leung, T.L.; Grisanti, L.; Skoko, Ž.; Vrankić, M.; Low, K.H.; Wang, S.; You, P.Y.; Ahn, H.; Lončarić, I.; et al. Mixed Halide Ordering as a Tool for the Stabilization of Ruddlesden-Popper Structures. *Chem. Mater.* **2021**, *34*, 42.

147. Yoshio, S.; Hidinori, K. Distribution of Cl^- and Br^- Ions in Mixed Crystals $(CH_3NH_3)_2Cu(Cl_{1-x}Br_x)_4$. *J. Phys. Soc. Jpn* **1983**, *52*, 1420–1426.

148. Drozdowski, D.; Gągor, A.; Stefańska, D.; Zaręba, J.K.; Fedoruk, K.; Mączka, M.; Sieradzki, A. Three-Dimensional Methylhydrazinium Lead Halide Perovskites: Structural Changes and Effects on Dielectric, Linear, and Nonlinear Optical Properties Entailed by the Halide Tuning. *J. Phys. Chem. C* **2022**, *126*, 1600–1610.

149. Drozdowski, D.; Kabański, A.; Stefańska, D.; Ptak, M.; Mączka, M.; Gągor, A. Layered Methylhydrazinium Lead Halide Perovskites: New Crystal Polymorphs with a Tailored Band Gap and Photoluminescence Colour via Halide Substitution. *J. Mater. Chem. C* **2024**, *12*, 6653–6662.

150. Mączka, M.; Drozdowski, D.; Stefańska, D.; Gągor, A. Zero-Dimensional Mixed-Cation Hybrid Lead Halides with Broadband Emissions. *Inorg. Chem. Front.* **2023**, *10*, 7222–7230.

151. Lee, M.M.; Teuscher, J.; Miyasaka, T.; Murakami, T.N.; Snaith, H.J. Efficient Hybrid Solar Cells Based on Meso-Superstructured Organometal Halide Perovskites. *Science* **2012**, *338*, 643–647.

152. Chen, Q.; Zhou, H.; Fang, Y.; Stieg, A.Z.; Song, T. Bin; Wang, H.H.; Xu, X.; Liu, Y.; Lu, S.; You, J.; et al. The Optoelectronic Role of Chlorine in $CH_3NH_3PbI_3$(Cl)-Based Perovskite Solar Cells. *Nat. Commun.* **2015**, *6*, 1–9.

153. Shahiduzzaman, M.; Yamamoto, K.; Furumoto, Y.; Kuwabara, T.; Takahashi, K.; Taima, T. Ionic Liquid-Assisted Growth of Methylammonium Lead Iodide Spherical Nanoparticles by a Simple Spin-Coating Method and Photovoltaic Properties of Perovskite Solar Cells. *RSC Adv.* **2015**, *5*, 77495–77500.

154. Lee, J.-W.; Kim, D.-H.; Kim, H.-S.; Seo, S.-W.; Min Cho, S.; Park, N.-G.; Lee, J.; Kim, D.; Kim, H.; Seo, S.; et al. Formamidinium and Cesium Hybridization for Photo- and Moisture-Stable Perovskite Solar Cell. *Adv. Energy Mater.* **2015**, *5*, 1501310.

155. Ma, X.; Yang, L.; Lei, K.; Zheng, S.; Chen, C.; Song, H. Doping in Inorganic Perovskite for Photovoltaic Application. *Nano Energy* **2020**, *78*, 105354.

156. Li, X.; Wu, Y.; Zhang, S.; Cai, B.; Gu, Y.; Song, J.; Zeng, H. $CsPbX_3$ Quantum Dots for Lighting and Displays: Room-Temperature Synthesis, Photoluminescence Superiorities, Underlying Origins and White Light-Emitting Diodes. *Adv. Funct. Mater.* **2016**, *26*, 2435–2445.

157. Akkerman, Q.A.; Abdelhady, A.L.; Manna, L. Zero-Dimensional Cesium Lead Halides: History, Properties, and Challenges. *J. Phys. Chem. Lett.* **2018**, *9*, 2326–2337.

158. Guo, Y.Y.; McNulty, J.A.; Mica, N.A.; Samuel, I.D.W.; Slawin, A.M.Z.; Bühl, M.; Lightfoot, P. Structure-Directing Effects in (110)-Layered Hybrid Perovskites Containing Two Distinct Organic Moieties. *Chem. Commun.* **2019**, *55*, 9935–9938.

159. Guo, Y.Y.; Yang, L.J.; Biberger, S.; McNulty, J.A.; Li, T.; Schötz, K.; Panzer, F.; Lightfoot, P. Structural Diversity in Layered Hybrid Perovskites, A_2PbBr_4 or $AA'PbBr_4$, Templated by Small Disc-Shaped Amines. *Inorg. Chem.* **2020**, *59*, 12858–12866.

12. Copies of the statements of co-authors

Wrocław, 04.09.2024

mgr inż. Dawid Drozdowski
Institute of Low Temperature and Structure Research
Polish Academy of Sciences
Okolna 2, 50-422 Wroclaw

Declaration of PhD Candidate

Hereby, I confirm my co-authorship in the following publications and describe my contribution to each of the publications constituting the dissertation.

1) Three-Dimensional Methylhydrazinium Lead Halide Perovskites: Structural Changes and Effects on Dielectric, Linear, and Nonlinear Optical Properties Entailed by the Halide Tuning
D. Drozdowski, A. Gągor, D. Stefańska, J. K. Zaręba, K. Fedoruk, M. Mączka*, A. Sieradzki
The Journal of Physical Chemistry C, **2022**, 126, 3, 1600–1610, 10.1021/acs.jpcc.1c07911

- Synthesis of materials
- X-ray diffraction measurements
- Determination of crystal structures, preparation of (x, T) phase diagram
- Raman spectroscopy measurements
- Preparation of the initial draft of the manuscript (introduction, DSC, crystal structure part, and conclusions)
- Unification and formatting of the final version of the manuscript

2) Layered methylhydrazinium lead halide perovskites: new crystal polymorphs with a tailored band gap and photoluminescence colour via halide substitution
D. Drozdowski*, A. Kabański, D. Stefańska, M. Ptak, M. Mączka, A. Gągor*
Journal of Materials Chemistry C, **2024**, 12, 6653-6662, 10.1039/D4TC00865K

- Synthesis of materials
- X-ray diffraction measurements
- Determination of crystal structures, preparation of (x, T) phase diagram
- Preparation of the initial draft of the manuscript (introduction, crystal structure part, and conclusions)
- Unification and formatting of the final version of the manuscript

3) [Methylhydrazinium]$_2$PbCl$_4$ a Two-dimensional Perovskite with Polar and Modulated Phases
K. Fedoruk, D. Drozdowski, M. Mączka*, J. K. Zaręba, D. Stefańska, A. Gągor, A. Sieradzki*
Inorganic Chemistry, **2022**, 61, 39, 15520–15531, 10.1021/acs.inorgchem.2c02206

- X-ray diffraction measurements
- Determination of crystal structures, including modulated phase using the superspace group formalism
- Preparation of the description of crystal structures in the initial draft of the manuscript
- Participation in formatting the final version of the manuscript

4) Broadband yellow and white emission from large octahedral tilting in (110)-oriented layered perovskites: imidazolium-methylhydrazinium lead halides

D. Drozdowski*, K. Fedoruk, A. Kabański, M. Mączka, A. Sieradzki, A. Gągor*
Journal of Materials Chemistry C, **2023**, 11, 4907-4915, 10.1039/D3TC00401E

- X-ray diffraction measurements
- Determination of crystal structures upon varying temperatures
- Preparation of the initial draft of the manuscript (introduction, crystal structure part, and conclusions)
- Unification and formatting of the final version of the manuscript

5) Methylhydrazinium lead iodide – one-dimensional chain phase with excitonic absorption and large energy band gap

D. Drozdowski*, A. Gągor, M. Mączka
Journal of Molecular Structure, 1249, **2022**, 131660, 10.1016/j.molstruc.2021.131660

- Synthesis of materials
- X-ray diffraction measurements
- Determination of crystal structures
- Raman spectroscopy measurements and analysis
- Analysis of the DRS spectra, band gap determination
- Preparation of the initial draft of the manuscript (all parts)
- Unification and formatting of the final version of the manuscript

6) Zero-dimensional mixed-cation hybrid lead halides with broadband emissions

M. Mączka*, D. Drozdowski, D. Stefańska, A. Gągor
Inorganic Chemistry Frontiers, **2023**, 10, 7222-7230, 10.1039/D3QI01749D

- X-ray diffraction measurements
- Determination of crystal structures
- Preparation of the experimental section regarding structural analysis
- Participation in formatting the initial and final version of the manuscript

Dawid Drozdowski
mgr inż. Dawid Drozdowski
PhD Candidate

Anna Gągor
dr hab. Anna Gągor, prof. INTiBS PAN
Supervisor

Wrocław, 04/09/2024

dr hab. Anna Gągor, prof. INTiBS PAN
Institute of Low Temperature and Structure Research
Polish Academy of Sciences
Okolna 2, 50-422 Wroclaw

Declaration of the Supervisor

Hereby, I confirm my co-authorship in the following publications:

Three-Dimensional Methylhydrazinium Lead Halide Perovskites: Structural Changes and Effects on Dielectric, Linear, and Nonlinear Optical Properties Entailed by the Halide Tuning
D. Drozdowski, A. Gągor, D. Stefańska, J. K. Zaręba, K. Fedoruk, M. Mączka*, A. Sieradzki
The Journal of Physical Chemistry C, **2022**, 126, 3, 1600–1610, 10.1021/acs.jpcc.1c07911

Layered methylhydrazinium lead halide perovskites: new crystal polymorphs with a tailored band gap and photoluminescence colour via halide substitution
D. Drozdowski*, A. Kabański, D. Stefańska, M. Ptak, M. Mączka, A. Gągor*
Journal of Materials Chemistry C, **2024**, 12, 6653-6662, 10.1039/D4TC00865K

[Methylhydrazinium]$_2$PbCl$_4$ a Two-dimensional Perovskite with Polar and Modulated Phases
K. Fedoruk, D. Drozdowski, M. Mączka*, J. K. Zaręba, D. Stefańska, A. Gągor, A. Sieradzki*
Inorganic Chemistry, **2022**, 61, 39, 15520–15531, 10.1021/acs.inorgchem.2c02206

Broadband yellow and white emission from large octahedral tilting in (110)-oriented layered perovskites: imidazolium-methylhydrazinium lead halides
D. Drozdowski*, K. Fedoruk, A. Kabański, M. Mączka, A. Sieradzki, A. Gągor*
Journal of Materials Chemistry C, **2023**, 11, 4907-4915, 10.1039/D3TC00401E

Methylhydrazinium lead iodide – one-dimensional chain phase with excitonic absorption and large energy band gap
D. Drozdowski*, A. Gągor, M. Mączka
Journal of Molecular Structure, 1249, **2022**, 131660, 10.1016/j.molstruc.2021.131660

Zero-dimensional mixed-cation hybrid lead halides with broadband emissions
M. Mączka*, D. Drozdowski, D. Stefańska, A. Gągor
Inorganic Chemistry Frontiers, **2023**, 10, 7222-7230, 10.1039/D3QI01749D

My contributions to these publications involved discussing the design of diffraction experiments and obtained results. I also supervised the project and validated the final versions of the manuscripts.

Anna Gągor
dr hab. Anna Gągor, prof. INTiBS PAN

Wrocław, 04/09/2024

prof. dr hab. Mirosław Mączka
Institute of Low Temperature and Structure Research
Polish Academy of Sciences
Okolna 2, 50-422 Wroclaw

Declaration of the co-authorship in the publications

Hereby, I confirm my co-authorship in the following publications:

1. *Three-Dimensional Methylhydrazinium Lead Halide Perovskites: Structural Changes and Effects on Dielectric, Linear, and Nonlinear Optical Properties Entailed by the Halide Tuning*
D. Drozdowski, A. Gągor, D. Stefańska, J. K. Zaręba, K. Fedoruk, M. Mączka*, A. Sieradzki
The Journal of Physical Chemistry C, **2022**, 126, 3, 1600–1610, 10.1021/acs.jpcc.1c07911

2. *Layered methylhydrazinium lead halide perovskites: new crystal polymorphs with a tailored band gap and photoluminescence colour via halide substitution*
D. Drozdowski*, A. Kabański, D. Stefańska, M. Ptak, M. Mączka, A. Gągor*
Journal of Materials Chemistry C, **2024**, 12, 6653-6662, 10.1039/D4TC00865K

3. *Methylhydrazinium lead iodide – one-dimensional chain phase with excitonic absorption and large energy band gap*
D. Drozdowski*, A. Gągor, M. Mączka
Journal of Molecular Structure, 1249, **2022**, 131660, 10.1016/j.molstruc.2021.131660

I reviewed and edited the final version of the manuscripts 1-3, validated the Raman measurements.

4. *[Methylhydrazinium]$_2$PbCl$_4$ a Two-dimensional Perovskite with Polar and Modulated Phases*
K. Fedoruk, D. Drozdowski, M. Mączka*, J. K. Zaręba, D. Stefańska, A. Gągor, A. Sieradzki*
Inorganic Chemistry, **2022**, 61, 39, 15520–15531, 10.1021/acs.inorgchem.2c02206

5. *Broadband yellow and white emission from large octahedral tilting in (110)-oriented layered perovskites: imidazolium-methylhydrazinium lead halides*
D. Drozdowski*, K. Fedoruk, A. Kabański, M. Mączka, A. Sieradzki, A. Gągor*
Journal of Materials Chemistry C, **2023**, 11, 4907-4915, 10.1039/D3TC00401E

6. *Zero-dimensional mixed-cation hybrid lead halides with broadband emissions*
M. Mączka*, D. Drozdowski, D. Stefańska, A. Gągor
Inorganic Chemistry Frontiers, **2023**, 10, 7222-7230, 10.1039/D3QI01749D

I synthesized materials, analyzed Raman data, prepared some drawings, and participated in writing the original drafts and reviewing the final versions of the manuscripts 4-6.

Mączka
....

prof. dr hab. Mirosław Mączka

Wrocław University
of Science and Technology

Department of Experimental Physics

Wrocław, 29/07/2024

dr hab. inż. Adam Sieradzki, prof. PWr
Department of Experimental Physics
Wrocław University of Science and Technology
Wybrzeże Wyspiańskiego 27, 50-370, Wrocław

Declaration of the co-authorships in the publications

Hereby, I confirm my co-authorship in the following publications:

Three-Dimensional Methylhydrazinium Lead Halide Perovskites: Structural Changes and Effects on Dielectric, Linear, and Nonlinear Optical Properties Entailed by the Halide Tuning

D. Drozdowski, A. Gągor, D. Stefańska, J. K. Zaręba, K. Fedoruk, M. Mączka*, A. Sieradzki
The Journal of Physical Chemistry C, **2022**, 126, 3, 1600–1610, 10.1021/acs.jpcc.1c07911

[Methylhydrazinium]$_2$PbCl$_4$ a Two-dimensional Perovskite with Polar and Modulated Phases

K. Fedoruk, D. Drozdowski, M. Mączka*, J. K. Zaręba, D. Stefańska, A. Gągor, A. Sieradzki*
Inorganic Chemistry, **2022**, 61, 39, 15520–15531, 10.1021/acs.inorgchem.2c02206

Broadband yellow and white emission from large octahedral tilting in (110)-oriented layered perovskites: imidazolium-methylhydrazinium lead halides

D. Drozdowski*, K. Fedoruk, A. Kabański, M. Mączka, A. Sieradzki, A. Gągor*
Journal of Materials Chemistry C, **2023**, 11, 4907-4915, 10.1039/D3TC00401E

I supervised and participated in the examination of electrical properties, contributed to the initial draft, and validated the final version of the manuscripts.

Prodziekan ds. promocji i współpracy
dr hab. inż. Adam Sieradzki
(2)

HR EXCELLENCE IN RESEARCH

Wrocław University
of Science and Technology

Faculty of Fundamental Problems
of Technology

Department of Experimental Physics

Wybrzeże Wyspiańskiego 27
50-370 Wrocław, Poland

T: +48 71 320 25 79

wppt.kfd@pwr.edu.pl
www.pwr.edu.pl

REGON: 000001614
NIP: 896-000-58-51
Bank Account
37 1090 2402 0000 0006 1000 0434

Wrocław, 29/07/2024

dr hab. Dagmara Stefańska, prof. INTiBS PAN
Institute of Low Temperature and Structure Research
Polish Academy of Sciences
Okolna 2, 50-422 Wroclaw

Declaration of the co-authorship in the publications

Hereby, I confirm my co-authorship in the following publications:

Three-Dimensional Methylhydrazinium Lead Halide Perovskites: Structural Changes and Effects on Dielectric, Linear, and Nonlinear Optical Properties Entailed by the Halide Tuning
D. Drozdowski, A. Gągor, D. Stefańska, J. K. Zaręba, K. Fedoruk, M. Mączka*, A. Sieradzki
The Journal of Physical Chemistry C, **2022**, 126, 3, 1600–1610, 10.1021/acs.jpcc.1c07911

[Methylhydrazinium]$_2$PbCl$_4$ a Two-dimensional Perovskite with Polar and Modulated Phases
K. Fedoruk, D. Drozdowski, M. Mączka*, J. K. Zaręba, D. Stefańska, A. Gągor, A. Sieradzki*
Inorganic Chemistry, **2022**, 61, 39, 15520–15531, 10.1021/acs.inorgchem.2c02206

Zero-dimensional mixed-cation hybrid lead halides with broadband emissions
M. Mączka*, D. Drozdowski, D. Stefańska, A. Gągor
Inorganic Chemistry Frontiers, **2023**, 10, 7222-7230, 10.1039/D3QI01749D

I performed photoluminescence measurements, analyzed and described linear optical properties, prepared drawings, and participated in writing the original drafts and validating the final versions of the manuscripts.

Layered methylhydrazinium lead halide perovskites: new crystal polymorphs with a tailored band gap and photoluminescence colour via halide substitution
D. Drozdowski*, A. Kabański, D. Stefańska, M. Ptak, M. Mączka, A. Gągor*
Journal of Materials Chemistry C, **2024**, 12, 6653-6662, 10.1039/D4TC00865K

I supervised and participated in the linear optical measurements and reviewed & edited the final version of the manuscript.

Dagmara Stefańska
....
dr hab. Dagmara Stefańska, prof. INTiBS PAN

Instytut Niskich Temperatur i Badań Strukturalnych Institute of Low Temperature and Structure Research
im. Włodzimierza Trzebiatowskiego Polskiej Akademii Nauk Polish Academy of Sciences

• ul. Okólna 2, 50-422 Wrocław | Poland • tel. +48 71 343 5021 • intibs@intibs.pl • www.intibs.pl

Dr hab. Maciej Ptak, prof. INTiBS PAN
Oddział Spektroskopii Optycznej
Instytut Niskich Temperatur i Badań Strukturalnych
Polskiej Akademii Nauk
ul. Okólna 2, 50-422 Wrocław
M.Ptak@intibs.pl

Wrocław, 5 sierpnia 2024 r.

OŚWIADCZENIE

współautora publikacji

Dotyczy:

Layered methylhydrazinium lead halide perovskites: new crystal polymorphs with a tailored band gap and photoluminescence colour via halide substitution
D. Drozdowski*, A. Kabański, D. Stefańska, M. Ptak, M. Mączka, A. Gągor*
Journal of Materials Chemistry C, 2024, 12, 6653–6662, 10.1039/d4tc00865k.

Oświadczam, że mój wkład w powstanie ww. artykułu polegał na wykonaniu pomiarów widm Ramana, ich współanalizie, przygotowywaniu rysunków 5, 6 oraz S17, tabeli S6 oraz fragmentów manuskryptu.

Maciej Ptak

Wrocław, 29/07/2024

Jan K. Zaręba, Ph.D.
Advanced Materials Engineering and Modeling Group
Wrocław University of Science and Technology
Wybrzeże Wyspiańskiego 27, 50-370, Wrocław

Declaration of the co-authorships in the publications

Hereby, I confirm my co-authorship in the following publications:

Three-Dimensional Methylhydrazinium Lead Halide Perovskites: Structural Changes and Effects on Dielectric, Linear, and Nonlinear Optical Properties Entailed by the Halide Tuning

D. Drozdowski, A. Gągor, D. Stefańska, J. K. Zaręba, K. Fedoruk, M. Mączka*, A. Sieradzki
The Journal of Physical Chemistry C, **2022**, 126, 3, 1600–1610, 10.1021/acs.jpcc.1c07911

[Methylhydrazinium]$_2$PbCl$_4$ a Two-dimensional Perovskite with Polar and Modulated Phases

K. Fedoruk, D. Drozdowski, M. Mączka*, J. K. Zaręba, D. Stefańska, A. Gągor, A. Sieradzki*
Inorganic Chemistry, **2022**, 61, 39, 15520–15531, 10.1021/acs.inorgchem.2c02206

I performed temperature-resolved studies on second harmonic generation, Kurtz-Perry powder test at room temperature, described the nonlinear optical properties, prepared drawings, participated in writing the original draft, and validated the final version of the manuscripts.

Jan K. Zaręba, Ph.D.

Instytut Niskich Temperatur i Badań Strukturalnych im. Włodzimierza Trzebiatowskiego Polskiej Akademii Nauk
Institute of Low Temperature and Structure Research Polish Academy of Sciences

• ul. Okólna 2, 50-422 Wrocław Poland • tel. +48 71 343 5021 • intibs@intibs.pl • www.intibs.pl

INTiBSPAN

Wrocław, 29/07/2024

mgr inż. Katarzyna Fedoruk-Piskorska
Department of Experimental Physics
Wrocław University of Science and Technology
Wybrzeże Wyspiańskiego 27, 50-370, Wrocław

Declaration of the co-authorships in the publications

Hereby, I confirm my co-authorship in the following publications:

Three-Dimensional Methylhydrazinium Lead Halide Perovskites: Structural Changes and Effects on Dielectric, Linear, and Nonlinear Optical Properties Entailed by the Halide Tuning

D. Drozdowski, A. Gągor, D. Stefańska, J. K. Zaręba, K. Fedoruk, M. Mączka*, A. Sieradzki
The Journal of Physical Chemistry C, **2022**, 126, 3, 1600–1610, 10.1021/acs.jpcc.1c07911

[Methylhydrazinium]$_2$PbCl$_4$ a Two-dimensional Perovskite with Polar and Modulated Phases

K. Fedoruk, D. Drozdowski, M. Mączka*, J. K. Zaręba, D. Stefańska, A. Gągor, A. Sieradzki*
Inorganic Chemistry, **2022**, 61, 39, 15520–15531, 10.1021/acs.inorgchem.2c02206

Broadband yellow and white emission from large octahedral tilting in (110)-oriented layered perovskites: imidazolium-methylhydrazinium lead halides

D. Drozdowski*, K. Fedoruk, A. Kabański, M. Mączka, A. Sieradzki, A. Gągor*
Journal of Materials Chemistry C, **2023**, 11, 4907-4915, 10.1039/D3TC00401E

I performed broadband dielectric spectroscopy, electric field-dependent polarization, and pyrocurrent measurements. I examined the electrical properties, prepared drawings, contributed to the initial draft, and validated the final version of the manuscripts.

mgr inż. Katarzyna Fedoruk-Piskorska
Katarzyna Fedoruk-Piskorska

Instytut Niskich Temperatur i Badań Strukturalnych Institute of Low Temperature and Structure Research
im. Włodzimierza Trzebiatowskiego Polskiej Akademii Nauk Polish Academy of Sciences

• ul. Okólna 2, 50-422 Wrocław | Poland • tel. +48 71 343 5021 • intibs@intibs.pl • www.intibs.pl

Wrocław, 29/07/2024

mgr inż. Adam Kabański
Institute of Low Temperature and Structure Research
Polish Academy of Sciences
Okolna 2, 50-422 Wroclaw

Declaration of the co-authorship in the publications

Hereby, I confirm my co-authorship in the following publications:

Layered methylhydrazinium lead halide perovskites: new crystal polymorphs with a tailored band gap and photoluminescence colour via halide substitution
D. Drozdowski*, A. Kabański, D. Stefańska, M. Ptak, M. Mączka, A. Gągor*
Journal of Materials Chemistry C, **2024**, 12, 6653-6662, 10.1039/D4TC00865K

Broadband yellow and white emission from large octahedral tilting in (110)-oriented layered perovskites: imidazolium-methylhydrazinium lead halides
D. Drozdowski*, K. Fedoruk, A. Kabański, M. Mączka, A. Sieradzki, A. Gągor*
Journal of Materials Chemistry C, **2023**, 11, 4907-4915, 10.1039/D3TC00401E

I performed photoluminescence measurements, analyzed and described linear optical properties, prepared drawings, participated in writing the original drafts, and validated the final versions of the manuscripts.

Adam Kabański
mgr inż. Adam Kabański

13. Copies of the publications constituting the dissertation

THE JOURNAL OF PHYSICAL CHEMISTRY C
A JOURNAL OF THE AMERICAN CHEMICAL SOCIETY

pubs.acs.org/JPCC Article

Three-Dimensional Methylhydrazinium Lead Halide Perovskites: Structural Changes and Effects on Dielectric, Linear, and Nonlinear Optical Properties Entailed by the Halide Tuning

Dawid Drozdowski, Anna Gągor, Dagmara Stefańska, Jan K. Zaręba, Katarzyna Fedoruk, Mirosław Mączka,* and Adam Sieradzki

Cite This: *J. Phys. Chem. C* 2022, 126, 1600−1610 **Read Online**

ACCESS | Metrics & More | Article Recommendations | Supporting Information

ABSTRACT: Three-dimensional lead halide perovskites are promising materials for optoelectronic applications. The most famous representative comprise methylammonium (MA^+) and formamidinium (FA^+) cations, but recently, this group was enlarged by methylhydrazinium (MHy^+) analogues that crystallize in polar structures at room-temperature. Properties of three-dimensional (3D) perovskites can be tuned by mixing of molecular cations or halide anions. Here, we report synthesis and physicochemical characterization of mixed-halide $MHyPbBr_xCl_{3-x}$ (x = 0.40, 0.58, 0.85, 1.33, 1.95, 2.25, and 2.55) and $MHyPbBr_{2.8}I_{0.2}$ perovskites. X-ray diffraction data show that all materials feature a polar monoclinic $P2_1$ symmetry at room temperature. With the temperature increase, all $MHyPbBr_xCl_{3-x}$ perovskites undergo a displacive phase transition to another polar orthorhombic $Pb2_1m$ phase at $T_2 \geq 318$ K. The bromine rich crystals ($x \geq 1.33$) exhibit an additional order−disorder phase transition to the archetypal cubic $Pm\bar{3}m$ phase at $T_1 \geq 409$ K. In contrast to $MHyPbBr_xCl_{3-x}$ perovskites, $MHyPbBr_{2.8}I_{0.2}$ undergoes a direct $P2_1$ to $Pm\bar{3}m$ phase transition. The temperature at which the cubic phase is stabilized, stability range of the $Pb2_1m$ phase, and distortion of the lead-halide octahedra decrease with the increase of Br^- content. The structural changes affect dielectric, conductivity, and optical properties. In particular, the Br-rich samples show switchable dielectric behavior near 410−420 K. Furthermore, the activation energy of Cl^- ionic conductivity increases with the increase of Br^- content in phases $Pb2_1m$ and $P2_1$, whereas in phase $Pm\bar{3}m$, the conductivity of Br^- ions increases with the increase of Cl^- content. The energy band gap narrows and the photoluminescence (PL) bands exhibit red shift when going from Cl to Br and then to I. Interestingly, whereas PL of the Br-rich and Cl-rich samples is dominated by bound exciton and self-trapped exciton bands, respectively, these bands are suppressed for $2.25 \geq x \geq 0.85$. The PL color is strongly tuned by doping and changes from greenish-blue for the Cl-rich samples to yellowish-green for $MHyPbBr_{2.8}I_{0.2}$. SHG studies demonstrate that doping of $MHyPbCl_3$ with Br^- ions reduces the difference between SHG signal intensities of the monoclinic and orthorhombic phases, to the extent that beyond x = 1.95, the SHG response of these phases becomes essentially the same. The relative SHG efficiencies of Br−Cl mixed materials at room temperature increase with the increase in Br content.

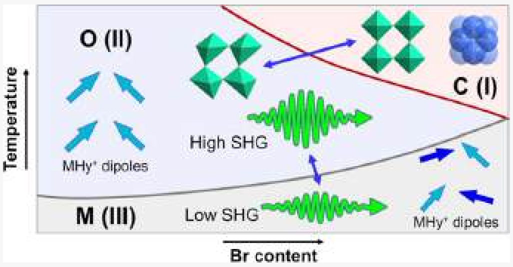

1. INTRODUCTION

Three-dimensional hybrid organic−inorganic perovskites (3D HOIPs) have been the topic of intense research efforts in recent years due to their functional properties. The general formula of 3D HOIPs is the same as for their inorganic analogues, that is, ABX_3, in which "A" cations occupy 12-fold coordinated holes between the corner-sharing BX_6 octahedra.[1−4] In HOIPs, "A" stands for an organic cation, "B" is a metal ion and "X" can be either an organic or inorganic element/group (e.g., halide, formate, azide, dicyanamide, etc.).[5−8] Among these systems, 3D lead halide HOIPs comprising methylammonium (MA^+) and formamidinium (FA^+) cations have grown to be the most explored materials. Numerous studies revealed technologically relevant physicochemical properties, such as high PL yields,[9] power conversion efficiencies of around 25%,[10,11] broad tunability of emission colors,[2] high extinction coefficients,[12] unprecedented mobility of charge carriers,[13] and the like. These properties, combined with low cost and facile synthesis, open up new perspectives for state-of-the-art applications, such as photovoltaics, light emitting devices, photodetectors, or even in photodynamic therapy.[4,14−16]

Another field of research on 3D HOIPs is the improvement of their performance via "A" site cation substitution. Such modification is an indispensable tool to allow for highly tunable modification of HOIP properties, which is usually difficult to obtain with all-inorganic counterparts. However, one should

Received: September 7, 2021
Revised: January 4, 2022
Published: January 16, 2022

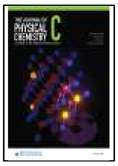

https://doi.org/10.1021/acs.jpcc.1c07911

note that there are some roadblocks to this strategy, as such modifications are limited by the steric hindrance introduced by the cubic inorganic subnetwork. A parameter that allows one to assess the stability of the 3D perovskite is the Goldschmidt tolerance factor (*TF*). Typically, *TF* should be larger than 0.8 and smaller than 1.0 in order to obtain a stable perovskite structure.[1] Thus, for 3D lead halide HOIPs, only organic cations with a relatively small effective radius, e.g., MA^+ and FA^+ (217 and 253 pm, respectively), satisfy the above rule,[3] leading to the discovery of $MAPbX_3$ and $FAPbX_3$ (X stands for Br^-, Cl^-, I^-).[17−21] Nevertheless, a seemingly finite set of small organic cations capable of affording 3D HOIPs has recently been extended by an MHy^+ cation, despite its large effective ionic radius of 264 pm. Indeed, our group has discovered 3D lead halide HOIPs comprising MHy^+ cations, i.e., $MHyPbBr_3$ and $MHyPbCl_3$. Both these perovskites feature tolerance factors higher than 1 (*TF* = 1.03 and 1.05 for Br- and Cl-analogue, respectively) and crystallize in the monoclinic, polar $P2_1$ phase at room temperature (RT).[22,23] $MHyPbBr_3$ undergoes a phase transition at 418 K to the cubic *Pm*-3*m* phase (which is archetypical of 3D perovskites) and exhibits a switchable dielectric behavior, strong second-harmonic generation (SHG) activity, thermochromism, and two-photon excited luminescence under 800 nm excitation.[22] On the other hand, $MHyPbCl_3$ undergoes a phase transition at 342 K to the $Pb2_1m$ orthorhombic space group, which is another polar and noncentrosymmetric phase. This behavior resulted in an exceptional property, i.e., enhancement of an SHG response upon transition from the low-temperature (LT) to the high-temperature (HT) phase, which has been employed to demonstrate HT switching between two SHG-active states.[23]

Recent studies on 3D HOIP analogues also revolved around alloying halogen anions at the "X" site. As a result, there is a growing body of literature demonstrating anion-tunable properties of $MAPbX_{3-x}X'_x$ and $FAPbX_{3-x}X'_x$ (X, X′ = Br^-, Cl^-, I^-) HOIPs.[24−30] For these systems, the mixing-halide approach offer tunability of the optical band gap and emission range, improved PL intensity, enhanced stability, and prolonged charge carriers' diffusion lengths while maintaining facileness of the synthesis and low fabrication cost.[25,31−34] Furthermore, mixed-halide systems can also obviate one of the crucial issues of single-halide $MA/FAPbX_3$ structures, i.e., their poor stability to adventitious water. For instance, Noh et al.[35] reported that a small Br^- content in $MAPbI_3$ thin films results in improved moisture resistance and prolonged decomposition time.

Whereas the mixing-halide approach has proven its utility for $MAPbX_{3-x}X'_x$ and $FAPbX_{3-x}X'_x$, a broader picture on various effects of halide alloying is currently lacking for $MHyPbBr_3$ and $MHyPbCl_3$ systems. Hence, we decided to synthesize mixed-halide $MHyPbBr_xCl_{3-x}$ and $MHyPbBr_xI_{3-x}$ perovskites and investigate their halide-dependent structural, dielectric, linear, and second-order nonlinear optical properties in wide temperature ranges. In particular, it is tempting to see whether this series produces similar or different halide-dependent structural characteristics from those observed for the MA^+ and FA^+-based analogues. A word of explanation is needed for $MHyPbBr_xI_{3-x}$. The 3D $MHyPbI_3$ perovskite has not been synthesized yet (our trials led to formation of yellow $MHyPbI_3$ phase with a chain structure[36]). Perhaps the only way to incorporate I^- anions into the $MHyPbX_3$ framework is to dope the $MHyPbBr_3$ phase with a small amount of I^-. Given the large ionic radius of this anion, it could affect the existence and stability of the cubic phase, which is explored here.

Herein, we report the synthesis of seven mixed-halide $MHyPbBr_xCl_{3-x}$ perovskites (x = 0.40, 0.58, 0.85, 1.33, 1.95, 2.25, and 2.55) as well as a Br−I co-doped material of formula $MHyPbBr_{2.8}I_{0.2}$. We used differential scanting calorimetry (DSC), single crystal X-ray diffraction (SCXRD), and dielectric spectroscopy to determine the uncharted phase diagram of this system and understand impact of halide alloying on the cation dynamics. Also, in this work, the impact of halide mixing on the linear absorption and PL properties was examined to establish prospects for optical band gap engineering and light-emitting applications in MHy^+-based HOIPs. Lastly, we took a closer look at effects that arise from one of the most unusual property of the MHy^+-based 3D HOIPs that is SHG response, associated with structural noncentrosymmetry.[22,23] In this way, not only the acentric identity of studied phases is confirmed but also effect of halide mixing on the relative SHG efficiency is examined.

2. EXPERIMENTAL SECTION

2.1. Materials and Instrumentation.

$PbBr_2$ (98%, Sigma-Aldrich), $PbCl_2$ (98%, Sigma-Aldrich), PbI_2 (98%, Sigma-Aldrich), hydrobromic acid (48 wt % in H_2O, Sigma-Aldrich), hydrochloric acid (37 wt % in H_2O, Sigma-Aldrich), hydroiodic acid (57 wt % in H_2O, Sigma-Aldrich), methylhydrazine (98%, Sigma-Aldrich), *N*-*N*-dimethylformamide (DMF, 99.8%), and methyl acetate (99.5%, Sigma-Aldrich) were commercially available and used without further purification.

Powder XRD patterns were obtained on an X'Pert PRO X-ray diffraction system equipped with a PIXcel ultrafast line detector. The powders were measured in the reflection mode, using CuKα radiation.

SCXRD experiments were carried out with MoKα radiation using an Xcalibur, Atlas diffractometer. Absorption was corrected for by multi-scan methods, CrysAlis PRO 1.171.39.46 (Rigaku Oxford Diffraction, 2018). Empirical absorption correction using spherical harmonics, implemented in the SCALE3 ABSPACK scaling algorithm was applied. H atom parameters were constrained.

Heat capacity was measured using a Mettler Toledo DSC-1 calorimeter with a high resolution of 0.4 μW. Nitrogen was used as a purging gas, and the heating and cooling rates were 5 K/min. The excess heat capacity associated with the phase transitions was evaluated by subtraction from the data the baseline representing variation in the absence of the phase transitions.

Raman spectra were measured using a Bruker FT 100/S spectrometer with the YAG:Nd laser excitation (1064 nm) and were recorded with a spectral resolution of 2 cm^{-1}.

Nonlinear optical studies were performed using a laser system consisting of a Coherent Astrella Ti:Sapphire regenerative amplifier providing 800 nm pulses (75 fs pulse duration, 1 kHz repetition rate) driving a wavelength-tunable TOPAS Prime optical parametric amplifier (OPA). The output of the OPA was set to 1300 nm and was vertically polarized. A laser beam was passed through a 1200 nm longpass dielectric filter (FELH1200, Thorlabs) in order to suppress unwanted short wavelength components typically present in the OPA output.

The Kurtz−Perry test was performed at 298 K. Potassium dihydrogen phosphate (KDP) was used as an SHG reference. The single crystals of $MHyPbBr_xCl_{3-x}$, $MHyPbBr_{2.8}I_{0.2}$, and KDP were crushed with a spatula and sieved through a mini-sieve set (Aldrich), collecting a microcrystal size fraction of 125−177 μm. Next, size-graded samples were fixed in-between microscope glass slides (forming tightly packed layers), sealed, and mounted to the horizontally aligned sample holder. No refractive index matching oil was used. For the Kurtz−Perry test, the average power of 1300 nm beam was equal to 343 mW (spot area of 0.5 cm^2). The employed measurement setup operates in the reflection mode. Specifically, the laser beam was directed onto the sample at 45 degrees to the sample surface and was unfocused. Emission collecting optics consisted of a Ø25.0 mm plano-convex lens of focal length 25.4 mm (Thorlabs) mounted to the 400 μm 0.22 NA glass optical fiber (Ocean Optics) and was placed along the normal to the sample surface. The distance between collection lens and the sample was equal to 30 mm. No polarizer was used; hence, the emission output of any polarization was collected. Scattered pumping radiation was suppressed with the use of a 750 nm shortpass dielectric filter (FESH0750, Thorlabs).

Temperature-resolved SHG study was performed in a separate measurement (1300 nm beam, 130−161 mW, spot area of 0.5 cm^2), in which the temperature control of the sample was performed (2−3 K step) using a Linkam LTS420 Heating/Freezing Stage. Temperature stability was equal to 0.1 K. Excitation geometry, signal collection optics, and the sample preparation protocol were the same as for the Kurtz−Perry test. The emission spectra collected in both experiments were recorded by an Ocean Optics Flame T spectrograph (200 μm slit), with a signal collection time of 2000 ms per temperature point.

Dielectric measurements were carried out using a broad band impedance Novocontrol Alpha analyzer, having a frequency range from 1 Hz up to 1 MHz. Since the obtained single crystals were not large enough to perform single-crystal dielectric measurements, pellets made of well-dried samples were measured instead. The powder was pressed into cylindrical pellets of 5 mm in diameter and from 0.5 to 0.7 mm in thickness. The surfaces of all analyzed samples were painted with silver paste to ensure good electrical contact with the electrodes. Measurements of the dielectric spectra were taken with a step of 1 K over the temperature range from 270 to 380 for the lowest Br content 280 to 440 K for higher Br contents. The temperature was controlled with a Novo-Control Quattro system using a nitrogen gas cryostat. The temperature stability of the samples was better than 0.1 K. All experiments were performed during a heating cycle at a 5 K min^{-1} rate.

The RT diffuse reflectance spectra of the powdered samples were measured using a Varian Cary 5E UV−vis−NIR spectrophotometer. Emission spectra under a 375 nm excitation line from a laser diode were measured with the Hamamatsu photonic multichannel analyzer PMA-12 equipped with a BT-CCD linear image sensor. The temperature of the samples was controlled using a Linkam THMS 600 Heating/Freezing Stage.

The elemental analysis was carried out using the scanning electron microscope FEI Nova NanoSEM 230 (FEI Company, Hillsboro, OR, USA) equipped with an EDS spectrometer (EDAX PegasusXM4) and operating acceleration voltage in the range 3.0−15 kV and spot of 2.5−3.0.

2.2. Synthesis. Single crystals of $MHyPbBr_xCl_{3-x}$ were grown using the antisolvent crystallization method. In this method, a mixture of HBr and HCl (in different ratio, adequate to the ratio of lead halides) was added dropwise to 10 mmol of methylhydrazine until pH = 7. Then, 2 mL of DMF and 10 mmol of mixed $PbBr_2$ and $PbCl_2$ powder were added under continuous stirring and this mixture was heated to 50 °C. Since not all of the lead halide precursors dissolved, 5−10 mL of DMF (depending on a sample) was added until complete dissolution of the mixture. The clear solution was placed into a glass vial, and it was placed in a second, larger vial containing methyl acetate. The lid of the outer vial was thoroughly sealed, whereas the lid of the inner vial was loosened in order to allow diffusion of methyl acetate into the precursor solution. Single crystals of $MHyPbBr_xCl_{3-x}$ were harvested after 4−5 days, filtered from a mother liquor, and dried at RT. EDS analysis revealed that the grown crystals feature bromine content x = 0.40, 0.58, 0.85, 1.33, 1.95, 2.25, and 2.55.

The same method was used for growing single crystals of $MHyPbBr_xI_{3-x}$. However, the precursor was prepared by adding 8.5 mmol of $PbBr_2$ and 1.5 mmol of PbI_2 to a solution containing 10 mmol of methylhydrazine dissolved in 5 mL of HBr and HI (volumetric ratio 8.5:1.5, respectively). After 5 min of continuous stirring at RT, the precursor solution became clear. Orange crystals were harvested after 5 days, filtered from a mother liquor, and dried at RT. EDS analysis revealed that the composition of these crystals is $MHyPbBr_{2.8}I_{0.2}$.

A good match of the powder X-Ray diffraction (PXRD) patterns and Raman spectra of the mixed-halide samples with the patterns and spectra recorded for $MHyPbBr_3$ and $MHyPbCl_3$ (Figures S1 and S2) proved the phase purity of the bulk samples.

3. RESULTS AND DISCUSSION

3.1. Differential Scanning Calorimetry. DSC data show the presence of two types of heat anomalies for the studied compounds (Figure 1 and Figures S3−S10). The first anomaly is observed for all $MHyPbBr_xCl_{3-x}$ samples (Figure 1a). On cooling, the temperature of this anomaly (T_2) is about ∼320 K for the Cl-rich samples (x = 0.40, 0.58, 0.85), but it strongly increases for the Br-rich samples, i.e., from 328 K for x = 1.33 to 368 K for x = 2.55 (Figure 1a). The associated changes in the enthalpy (ΔH) and entropy (ΔS) related to the phase transition at T_2 are listed in Table S1. For x ranging from 0.40 to 2.25, the values of ΔH and ΔS are about 0.65 kJ mol^{-1} and 2.0 J mol^{-1} K^{-1}, respectively. For an order−disorder phase transition, $\Delta S = R \ln(N)$, where R is the gas constant and N is the ratio of the number of configurations in the disordered and ordered phases. Using this formula, the value of N is estimated to be about 1.30. The small value of N is consistent with a displacive character of the phase transition. Since very similar values of ΔH, ΔS, and N (0.70 kJ mol^{-1}, 2.7 J mol^{-1} K^{-1}, and 1.39, respectively) were previously reported for the phase transition observed in $MHyPbCl_3$ at 329 K,[23] it is clear that doping of $MHyPbCl_3$ with Br^- up to x = 2.25 has a weak effect on the phase transition mechanism. Interestingly, this phase transition is observed even for the highest Br^- concentration (x = 2.55), although the values of N = 1.06, ΔH = 0.17 kJ mol^{-1}, and ΔS = 0.50 J mol^{-1} K^{-1} are significantly lower than for the other compositions. Thus, our data show evidence that even a low doping of Cl^- induces a displacive phase transition analogous to that observed in $MHyPbCl_3$. However, lower values of the thermal parameters suggest significantly weaker structural changes when compared to the $MHyPbBr_xCl_{3-x}$ system with x < 2.55.

The second type of heat anomaly is observed for $MHyPbBr_xCl_{3-x}$ with $x \geq 1.33$, and for $MHyPbBr_{2.8}I_{0.2}$ (Figure 1b and Figures S6−S10). In contrast to the former phase transition, the heat anomaly associated with this transition is symmetric and much more intense. Furthermore, this anomaly is observed at much higher temperatures (on cooling, T_1 ranges between 390 and 424 K, see Table S1). The average ΔH, ΔS, and N are very large, i.e., ca. 9.0 kJ mol^{-1}, 23.0 J mol^{-1} K^{-1}, and

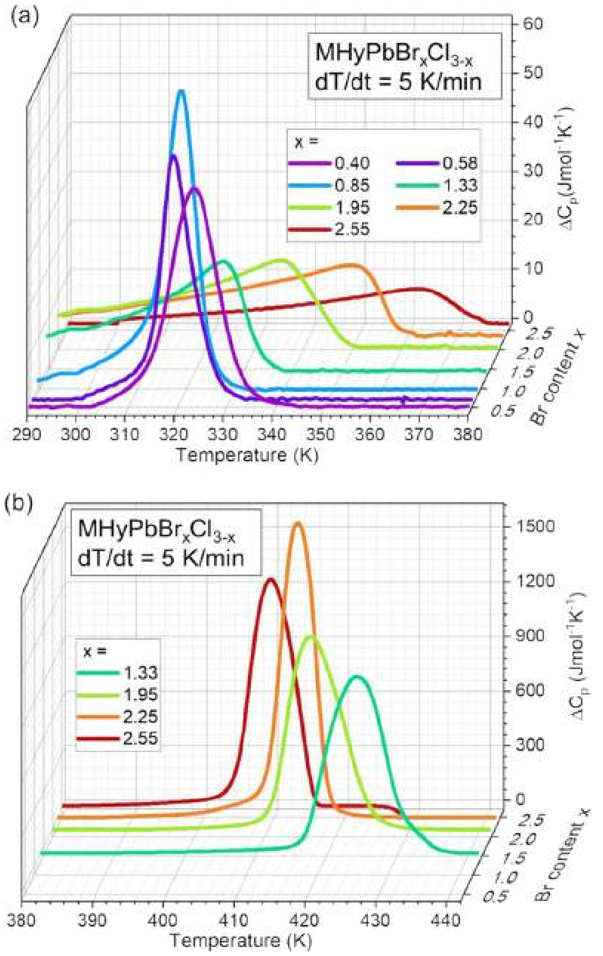

Figure 1. Change in C_p for MHyPbBr$_x$Cl$_{3-x}$ perovskites upon cooling related to the (a) first and (b) second type of a phase transition.

17.0, respectively (Table S1), pointing to the first-order and order−disorder character of this phase transition. A similar anomaly, previously reported for MHyPbBr$_3$ at 409 K (with ΔH, ΔS, and N of 9.9 kJ mol^{-1}, 25.3 J mol^{-1} K^{-1}, and 21.0), was attributed to the $P2_1$ to $Pm\bar{3}m$ phase transition.[22] It is worth noting that doping of MHyPbBr$_3$ with Cl$^-$ leads to the increase in T_1. Opposite behavior is observed on doping with I$^-$ (Table S1).

3.2. Single-Crystal X-ray Diffraction. In order to establish crystal structures of the phases identified in the DSC measurements, SCXRD experiments were performed. The experimental details for MHyPbBr$_x$Cl$_{3-x}$ (x = 0.85, 1.95, 2.55) and MHyPbBr$_{2.8}$I$_{0.2}$ are presented in Tables S2−S5.

MHyPbBr$_x$Cl$_{3-x}$ systems rich in bromine ($x \geq 1.33$) adopt three polymorphic phases, while in the chloride-rich area, only two phases are observed. The HT cubic phase $Pm\bar{3}m$ (phase **I**) is centrosymmetric and isostructural with the HT phase of the MHyPbBr$_3$ analogue (Figure 2a).[22] In **I**, MHy$^+$ cations rotate freely, displaying no noticeable influence on the shape of PbX$_6$ (X = Br, Cl) octahedra. Thus, phase **I** is built of ideal PbX$_6$ octahedra of the O_h symmetry (Figure 2d). The polar orthorhombic $Pb2_1m$ phase (**II**) is isostructural with the HT phase of MHyPbCl$_3$.[23] In contrast to **I**, MHy$^+$ cations in phase **II** are oriented along one direction, giving rise to the onset of spontaneous polarization (Figure 2b). The monoclinic $P2_1$ phase (**III**), which is also polar, corresponds to the RT phases of both MHyPbBr$_3$ and MHyPbCl$_3$. If one compares crystal structures of **II** and **III**, the arrangement of polar cations in the latter is substantially reorganized. Every second MHy$^+$ dipole aligns more to the (010) planes than along the polar [010] direction, which diminishes polarization of this phase relative to **II** (Figure 2c). The synergistic effect of MHy$^+$ size and dipole orientation significantly affects crystal structures of **II** and **III**. In particular, these structures consist of Pb(1)X$_6$ and Pb(2)X$_6$ octahedra (Figure 2e,f) and the terminal N atoms of MHy$^+$ enter the Pb(2)X$_6$ coordination sphere, leading to higher distortion of these octahedra (Figure S11).

Experimental data from the SCXRD and DSC measurements were used together to construct the Br-Cl binary phase diagram of MHyPbBr$_x$Cl$_{3-x}$ perovskites (Figure 3). At RT, all mixed-halide systems crystallize in phase **III**, the same as their single-halide analogues. However, neither MHyPbBr$_3$ nor MHyPbCl$_3$ showed the existence of three temperature-dependent phases.[22,23] For our mixed-halide structures, the region with all three stabilized phases starts when the content of Br$^-$ and Cl$^-$ is nearly equal ($x = 1.33$) and extends to $x = 3$, at which point the phase **II** vanishes. Thus, in order to stabilize phase **II** in the MHyPbBr$_3$ matrix, an incorporation of Cl$^-$ anions appears to be crucial. On the other hand, the phase transition temperature to phase **I** increases with increasing fraction of Cl$^-$, and for $x < 1.33$, the sample decomposition occurs before the crystals reach the cubic phase. On this point, it should be emphasized that these results are opposite to those found for MAPbBr$_x$Cl$_{3-x}$ systems, in which the increase of the Cl fraction induces a stabilization of the $Pm\bar{3}m$ phase at lower temperatures.[37]

To obtain a better grasp of temperature effects on MAPbBr$_x$Cl$_{3-x}$ structural properties, we performed a detailed geometrical analysis of the structures. According to the Vegard's Law, for an ideal substitutional solution, the lattice parameters vary linearly with the concentration of the constituents at constant temperature (for instance, $a_{\mathrm{MHyPbBr1.5Cl_{1.5}}} = 0.5a_{\mathrm{MHyPbBr_3}} + 0.5a_{\mathrm{MHyPbCl_3}}$).[38,39] In the case of our structures in phase **III**, a linear (or quasilinear) dependence of lattice parameters vs Br$^-$ fraction is observed (Figure S12a,b). Thus, the Vegard's law is satisfied.

One should note that the difference between ionic radii of Br$^-$ and Cl$^-$ anions (196 and 181 pm, respectively[40]) is expected to have a non-negligible influence on the geometry of PbX$_6$ coordination spheres. Therefore, the octahedral angle variance (σ^2) and bond length distortion (Δ_d) values for MHyPbBr$_x$Cl$_{3-x}$ in **III** were calculated using the Fleet's approach.[41] A comparison of MHyPbBr$_3$ and MHyPbCl$_3$ structures provides σ^2 values as follows: 14 deg^2 and 301 deg^2 for Pb(1)Br$_6$ and Pb(2)Br$_6$ octahedra, and 21 deg^2 and 314 deg^2 for Pb(1)Cl$_6$ and Pb(2)Cl$_6$.[23] In the MHyPbBr$_x$Cl$_{3-x}$ systems, all σ^2 values for both Pb(1)X$_6$ and Pb(2)X$_6$ octahedra remain between the ones obtained for the single-halide analogues (Figure S12c). The increasing Br$^-$ content leads to the decrease of σ^2 which means that the octahedra become less distorted. The change of Δ_d values with the increasing Br$^-$ fraction is negligible (Δ_d for selected structures in Tables S2−S4).

The presence of the interaction between the terminal N atoms of MHy$^+$ with Pb calls for an investigation of the impact of this interaction on the octahedra distortion. In the single-halide analogues, the Pb(2)···N bond lengths are equal to 2.91 and 3.04 Å (2.83 and 2.89 Å) for MHyPbBr$_3$ (MHyPbCl$_3$). This is below the maximum limit for such interactions based on the survey of CCDC 2020 (Figure S13). Thus, we measured the Pb(2)···N coordination bond lengths (Figure S12d) for the

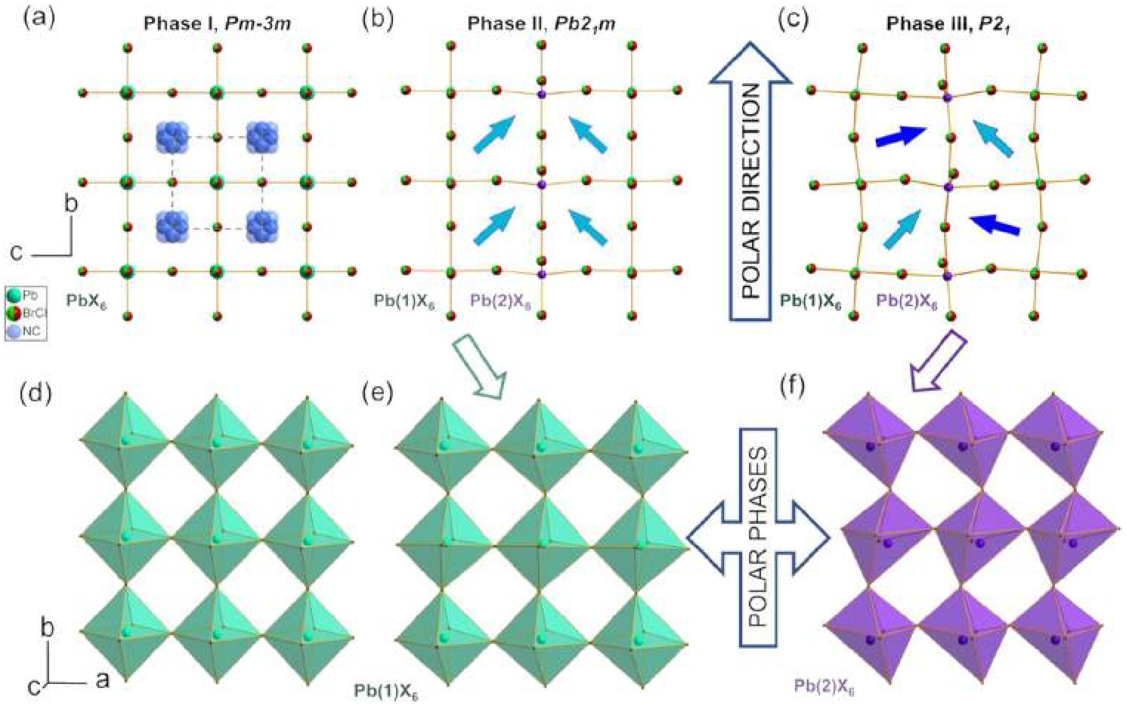

Figure 2. (a−c) Crystal structures of $MHyPbBr_xCl_{3-x}$ for phases **I**, **II**, and **III**, respectively. Arrows in (b, c) represent the location of MHy^+ dipoles. In **II** and **III**, molecules are oriented along the polar direction. (d) Single [100] layer in **I** built of PbX_6 (X = Br, Cl) octahedra. (e, f) [100] layers of (e) $Pb(1)X_6$ and (f) $Pb(2)X_6$ octahedra in both polar phases (**II**, **III**).

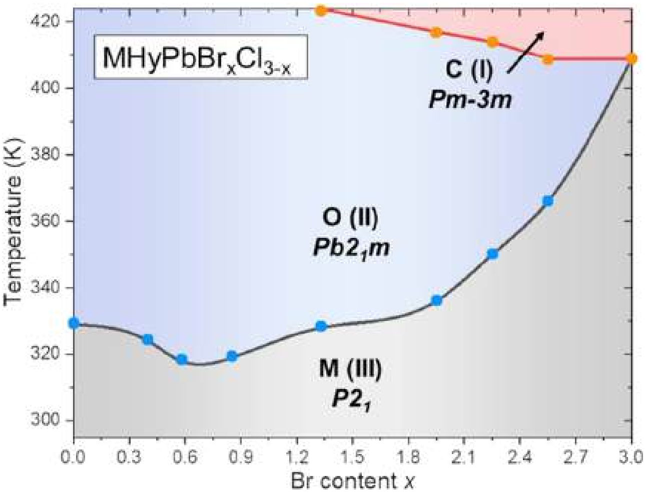

Figure 3. Phase diagram of $MHyPbBr_xCl_{3-x}$ perovskites showing cubic(C) phase **I**, orthorhombic (O) phase **II**, and monoclinic (M) phase **III**. The dots represent transition temperatures upon cooling obtained from the DSC measurements. The curves represent interpolation of the phase boundaries.

$MHyPbBr_xCl_{3-x}$ structures. Both Pb(2)···N(2) and Pb(2)···N(4) bond lengths remain between the values for boundary $MHyPbBr_3$ and $MHyPbCl_3$ structures. This observation is in line with the volume expansion of the unit cell resulting in larger voids between the octahedra. This, in turn, allows more space for the MHy^+ cations and translates to an increased Pb(2)···N distance. In order to verify this relationship, we implemented the PLATON[42] software to calculate void volumes (Figure S14). Considering the volume of the MHy^+ rotation sphere (ca. 77 Å), for our systems with $x \geq 1.95$, the void volume should be large enough to allow the free rotation of MHy^+ inside the structure.

This observation agrees with our SCXRD measurements because for $x = 1.95$, we obtained stable perovskite in phase **I**, while for $x = 1.33$ the sample in **I** started to decompose (both crystals were measured at temperatures right above T_1).

SCXRD measurements of the $MHyPbBr_{2.8}I_{0.2}$ showed that at RT, it crystallizes in the monoclinic phase, space group $P2_1$, which is isostructural to **III**. According to the DSC studies, $MHyPbBr_{2.8}I_{0.2}$ undergoes a phase transition at 411 and 390 K during heating and cooling, respectively. Unfortunately, we could not obtain a model of the HT due to the poor stability of $MHyPbBr_{2.8}I_{0.2}$ above 390 K. Nevertheless, the pre-experiment made at 400 K (preceded by heating at 415 K) proved the existence of the cubic phase $Pm\bar{3}m$ (isostructural to **I**) with the lattice parameter a = 6.046(5) Å. Compared to single- and mixed-halide analogues with Br^- and Cl^-, incorporation of I^- leads to stabilization of phase **I** at lower temperatures, which is in line with the largest ionic radius of I^- (220 pm[40]). The distortion parameters, σ^2 and Δ_d (Table S5), are almost identical to those of $MHyPbBr_3$.[22] Accordingly, approx. 7% fraction of I^- in the $MHyPbBr_{2.8}I_{0.2}$ systems does not affect significantly the octahedral geometry of the Pb center.

3.3. Dielectric Studies. Inspired by the phase diagram, we performed the broad band dielectric spectroscopy (BDS) studies for $MHyPbBr_xCl_{3-x}$ (x = 0.85, 1.33, 1.95, and 2.55) compounds to analyze in depth the mechanism of the observed phase transitions. The representative temperature dependences of the complex dielectric spectra of the samples with $x = 0.85$ and $x = 2.55$ are presented in Figures 4 and 5, respectively. The overall increase of both the ε' (Figures 4a and 5a) and ε'' (Figures 4b and 5b) with temperature results from increasing the contribution of the electrical conductivity and from the enhancement of this effect at higher frequencies. To suppress the effect of the electrode polarization and space charge injection phenomena, the modulus representation ($M^* = 1/\varepsilon^*$) was

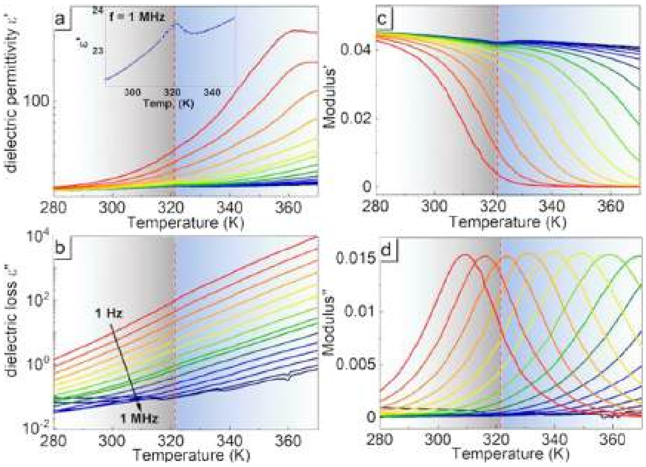

Figure 4. Temperature dependence of the (a) dielectric permittivity, (b) dielectric loss, (c) real M′, and (d) imaginary M″ components of electric modulus spectra as a function of temperature of the $MHyPbBr_{0.85}Cl_{2.15}$ pellet measured on heating. The representative curves are plotted in frequency decades between 1 Hz and 1 MHz. The changes of dielectric permittivity for 1 MHz were enlarged and are presented in the inset in (a). Colors indicate various phases.

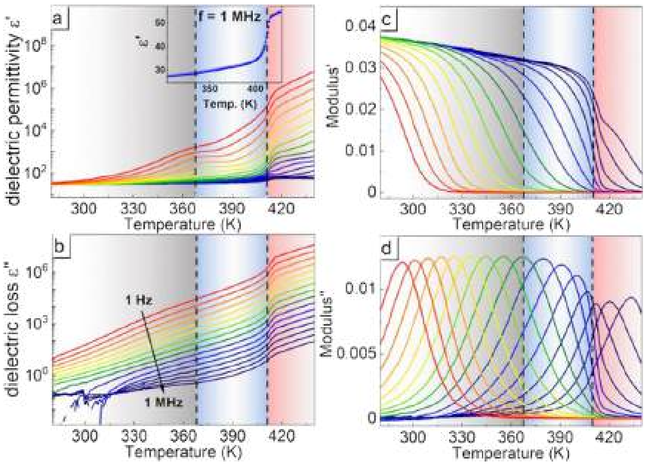

Figure 5. Temperature dependence of the (a) dielectric permittivity, (b) dielectric loss, (c) real M′, and (d) imaginary M″ components of electric modulus spectra as a function of temperature of the $MHyPbBr_{2.55}Cl_{0.45}$ pellet measured on heating. The representative curves are plotted in frequency decades between 1 Hz and 1 MHz. The changes of dielectric permittivity for 1 MHz were enlarged and are presented in the inset in (a). Colors indicate various phases.

applied (Figures 4c,d, and 5c,d).[43] A distinct anomaly of ε' and M′ at $T_2 \approx 321$ K on heating, indicating **III** to **II** phase transition for $MHyPbBr_{0.85}Cl_{2.15}$, can be observed (Figure 4a,c). The dielectric response of $MHyPbBr_{0.85}Cl_{2.15}$ is similar to that of previously published $MHyPbCl_3$.[23] By increasing the Br^- content, the dielectric response approaches the one reported for the $MHyPbBr_3$ compound.[22] Indeed, for $MHyPbBr_{1.33}Cl_{1.67}$, $MHyPbBr_{1.95}Cl_{1.05}$, and $MHyPbBr_{2.55}Cl_{0.45}$ samples, we observe only one step-like anomaly on the dielectric spectra at $T_1 \approx$ 410−430 K on heating (Figure 5a, S15a, S16a), indicating the first-order character of the **II** to **I** phase transition. The dielectric permittivity ε' and dielectric loss ε'' become strongly frequency-dependent above T_1 and increase with temperature, reaching values a few orders of magnitude higher (Figure 5a,b and Figures S15a,b and S16a,b). Furthermore, the shape of the temperature dependent complex electric modulus M* spectra revealed the emergence of an ionic and/or electronic conductivity with increasing temperature (Figure 5c,d and Figures S15c,d and S16c,d). Deeper analysis of the BDS spectra does not reveal a dipolar relaxation response coming from the movements of MHy^+ cations for $MHyPbBr_{1.33}Cl_{1.67}$ and $MHyPbBr_{1.95}Cl_{1.05}$ samples due to the high ionic and/or electronic conductivity present in these materials. Ionic halide migration has been well recognized factor affecting the electric properties in hybrid halide perovskites.[44,45]

The dielectric spectra of the $MHyPbBr_{2.55}Cl_{0.45}$ sample, measured as a function of frequency (Figure S17a−d), reveal the presence of a relaxation process, which can be well approximated by the Havriliak−Negami function (see Figure S18). A quantitative analysis of the frequency domain dielectric data allowed us to obtain the activation energies E_a of the observed processes in all studied compounds. In order to get insight into the activation energy tendency, the values for pure $MHyPbCl_3$ and $MHyPbBr_3$ were also added. It can be noticed that the measured relaxation times exhibit activation-like behavior (see Figure 6a) that can be parameterized using the Arrhenius law:

$$\tau = \tau_0 exp\left(\frac{E_a}{k_B T}\right),$$

where τ_0, E_a, and k_B denote the relaxation time at the HT limit, activation energy, and Boltzmann constant, respectively. The activation energies vs Br^- content in phases I, II, and III, are shown in Figure 6b−d, respectively. If one compares the estimated activation energies for phases II and III of $MHyPbCl_3$, it can be concluded that the symmetry changes weakly affect the energy barrier to activate the Cl^- migration. On the other hand, for $MHyPbBr_3$, the E_a in phase III is almost twice as high as that for phase I. This shows that the observed activation of the Br^- ion migration is strongly suppressed by the $P2_1$ to $Pm\bar{3}m$ symmetry change. In the mixed compounds, depending on the composition, a change in E_a is observed in each phase, which shows that halide replacement modifies the conductivity process in all phases. It can be observed that the E_a of the conductivity of Cl^- ions increases with increasing Br^- content in phases II and III. Likewise, the E_a of the conductivity of Br^- ions decreases with increasing Cl^- content in phase I (Figure 6b−d).

3.4. Linear Optical Properties.

The optical absorption spectra of the investigated perovskites are composed of several bands (Figure 7a). The most red-shifted band of each sample can be attributed to the free excitonic (FE) absorption. For $MHyPbCl_3$ and $MHyPbB_3$, the excitonic absorption was observed at 373 (3.32 eV) and 469 nm (2.64 eV), respectively.[22,23] As can be seen in Figure 7a, the excitonic absorption of the $MHyPbBr_{3-x}Cl_x$ samples exhibits monotonous shift to lower energy with increasing Br^- concentration, i.e., from 389 nm (3.19 eV) for $MHyPbBr_{0.4}Cl_{2.6}$ to 457 nm (2.71 eV) for $MHyPbBr_{2.55}Cl_{0.45}$. However, the most red-shifted excitonic absorption of 484 nm (2.56 eV) is observed for $MHyPbBr_{2.8}I_{0.2}$. Thus, in spite of a small iodine concentration, the excitonic absorption exhibits a significant 15 nm shift to the red compared to pure $MHyPbBr_3$. We have also used the RT absorption spectra and Kubelka−Munk relation to estimate the energy band gaps (E_g) of the investigated perovskites (Figures 7b and 8a). In order to estimate E_g more precisely, the excitonic bands were subtracted from the spectra (Figures S19−S26). As is the case with the excitonic absorption, E_g also exhibits red shift with increasing concentration of Br^- and $MHyPbBr_{2.8}I_{0.2}$ shows

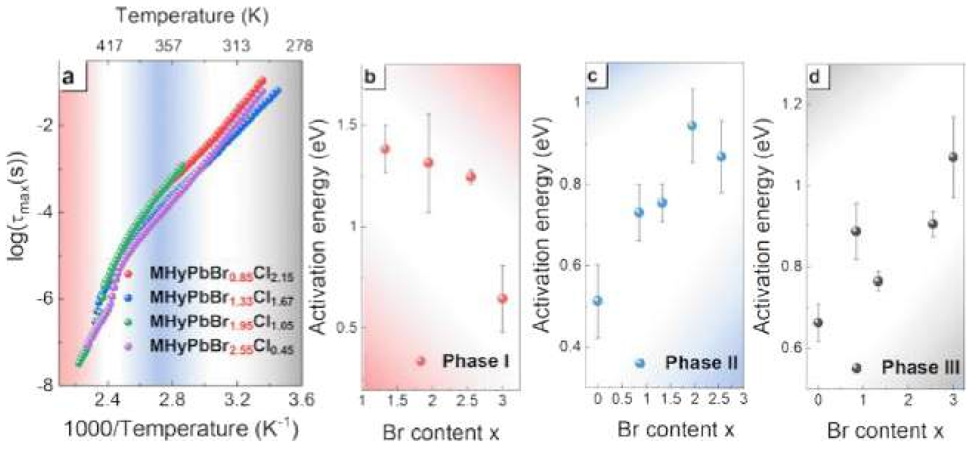

Figure 6. (a) Dependence of the maximum relaxation time as a function of inverse temperature obtained for the studied compounds. Activation energy as a function of the content of Br in (b) **I**, (c) **II**, and (d) **III**.

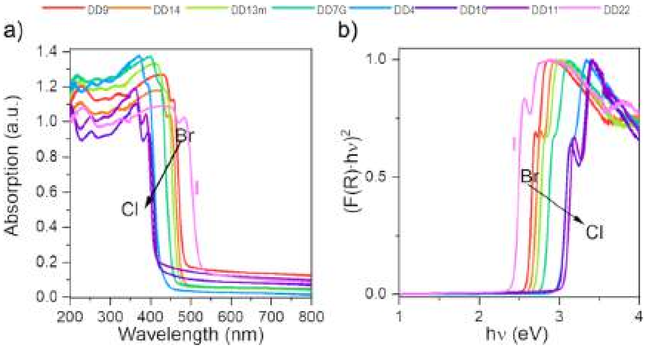

Figure 7. (a) RT diffuse absorption spectra of MHyPbBr$_x$Cl$_{3-x}$ and MHyPbBr$_{2.8}$I$_{0.2}$ and (b) graphical presentation of the Kubelka–Munk function.

the narrowest band gap (Figure 8a). A similar behavior, i.e., narrowing of the band gap when going from Cl to Br and then I, was also reported for other 3D lead halides.[46]

The LT PL spectrum (Figure 8b) of MHyPbBr$_{2.8}$I$_{0.2}$ shows an intense and relatively broad band (FWHM = 46 nm (0.213 eV)) centered at 510 nm characteristic for BE emission.[22,47−49] In addition to this broad band, a small hump appears at 484 nm that overlaps with the excitonic absorption band and can be therefore attributed to FE recombination. The PL spectra of MHyPbBr$_x$Cl$_{3-x}$ samples show both narrow and broad bands (Figure 8b). The narrow and the most blue-shifted band of each sample, attributed to FE recombination, moves from 399 nm for MHyPbBr$_{0.4}$Cl$_{2.6}$ to 453 nm for MHyPbBr$_{2.55}$Cl$_{0.45}$ (Figure 8c). Bands of this kind were observed at 458 and 362 nm for MHyPbBr$_3$ and MHyPbCl$_3$, respectively,[22,23] while for MAPbBr$_3$ and FAPbBr$_3$ analogues, they appeared at 545−550 nm.[50,51] In addition to the FE band, the PL spectrum of the MHyPbBr$_{2.55}$Cl$_{0.45}$ sample shows two additional bands at 470 and 494 nm. Their large Stokes shifts and FWHM values indicate that they can be assigned to BE states. Very similar bands were also reported for MHyPbBr$_3$, but the BE bands of MHyPbBr$_{2.55}$Cl$_{0.45}$ are shifted to higher energies compared to MHyPbBr$_3$ by 15.7 (85 meV) and 11.7 nm (58 meV). The BE emission disappears with increasing Cl$^-$ content, but a new very broad PL appears around 460 nm (Figure 8b). A very large Stokes shift and FWHM value (about 0.95 eV) indicates that it cannot be assigned to a BE emission but rather to STEx states. The origin of this band is associated with the large local structure distortion and the polar nature of the mixed halides.[23]

The changes in the shape and position of the PL bands have pronounced impact on CIE coordinates. As can be seen in Figure 8d, the color of PL varies from deep blue and purplish-blue for bromine content x = 2.55−0.85 to blue and greenish blue for x = 0.58 and x = 0.40. The sample doped with iodine exhibits a yellowish-green emission with a CIE of 0.194; 0.688.

3.5. Second Harmonic Generation Studies. In this section, we move on to the investigation of the halide alloying effect on RT and temperature-resolved SHG properties (TR-SHG) of MHyPbBr$_x$Cl$_{3-x}$ (x = 1.33, 1.95, 2.25, 2.55) and MHyPbBr$_{2.8}$I$_{0.2}$ materials. To this end, we employed a 1300 nm femtosecond laser radiation. While that long wavelengths of laser sources are rarely used in SHG studies of such compounds, that choice is far from accidental. In our previous report on MHyPbBr$_3$, we have observed that the use of shorter laser wavelengths, such as 800 nm, efficiently excites luminescence through the two-photon absorption (2PA) mechanism.[22] As a result, strong up-converted luminescence obscured much weaker in intensity SHG signal. Also, the produced SHG (400 nm) falls directly in the optical band gap and so is effectively attenuated by one-photon absorption resonances. Both these effects are significantly suppressed at 1300 nm, for two reasons. Excitation at 1300 nm corresponds to regions of three-photon and multi-photon absorption, and these processes are weaker than 2PA. Additionally, the produced SHG sits at 650 nm, and as can be seen in the reflectance spectra discussed in the previous section (Figure 7), this spectral region is free of one-photon absorption bands. It follows that the produced SHG is not subject to self-absorption.

RT Kurtz−Perry powder tests[52] on size-graded microcrystalline samples have been performed to reveal the effect of halide mixing of the relative efficiency of generation of second harmonic of radiation (Figure 9a). Experimental spectra are presented in Figure S27. It turns out that relative SHG efficiency (expressed vs that of KDP) for halide-alloyed samples remains within the range imposed by pure-halide phases MHyPbCl$_3$ (0.03·I(2ω)$_{KDP}$) and MHyPbBr$_3$ (0.18·I(2ω)$_{KDP}$). One sees that bromine doping into the MHyPbCl$_3$ matrix starts to impact I$_{SHG}$ values only at x = 1.95 (0.02·I(2ω)$_{KDP}$) and the phase with x = 2.55 features the same relative SHG efficiency (0.21·I(2ω)$_{KDP}$) as MHyPbBr$_3$, within experimental error. In the case of MHyPbBr$_{2.8}$I$_{0.2}$, the obtained I$_{SHG}$ value (0.015·I(2ω)$_{KDP}$) is

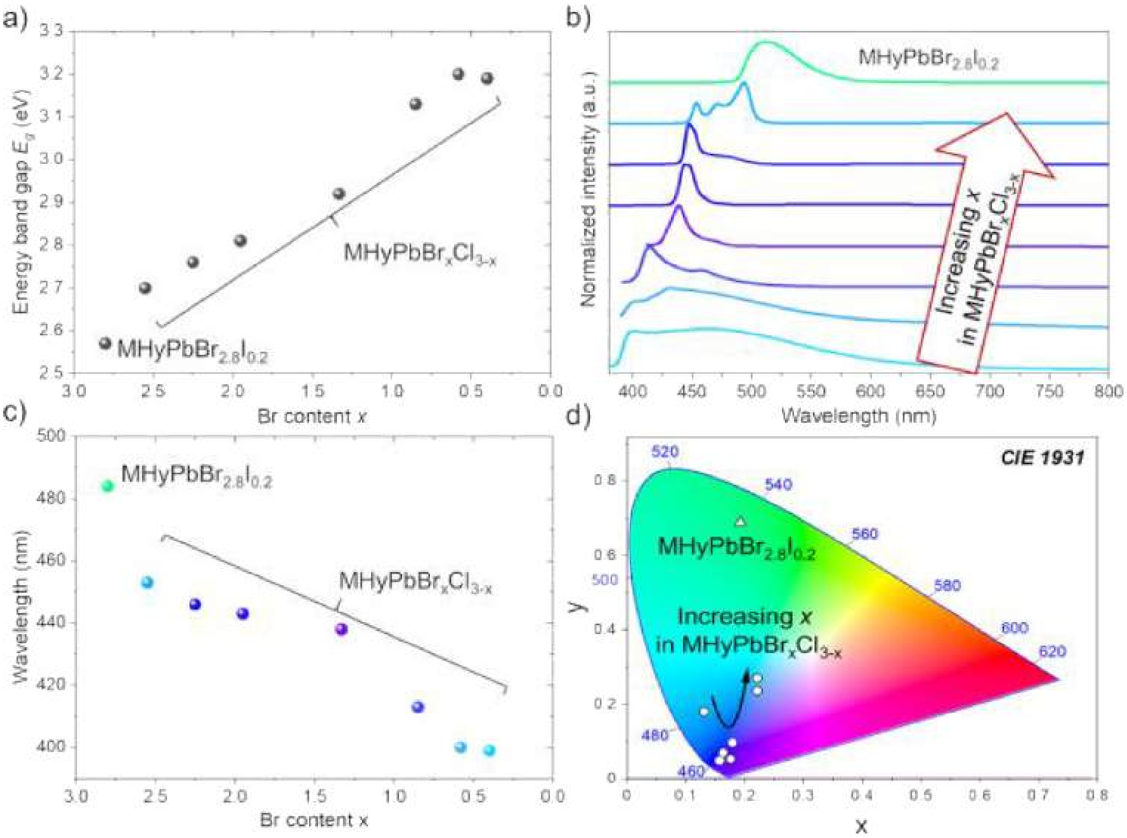

Figure 8. (a) Values of the energy band gap E_g of the investigated compounds. (b) PL spectra of MHyPbBr$_x$Cl$_{3-x}$ and MHyPbBr$_{2.8}$I$_{0.2}$ recorded at 80 K, (c) changes of FE band position with sample composition, and (d) CIE coordinates of the investigated samples.

still close to that of MHyPbBr$_3$, and likely low doping of iodine has little effect on SHG efficiency.

It was tempting to see how the temperature-dependent SHG response evolves in Br−Cl co-doped samples. To this end, TR-SHG measurements have been performed for MHyPbBr$_x$Cl$_{3-x}$ samples with $x = 1.33$, 1.95, 2.25, 2.55 (Figure 9b,c and Figures S28−S37). We will discuss in detail results for MHyPbBr$_{1.33}$Cl$_{1.67}$ and MHyPbBr$_{1.95}$Cl$_{1.05}$ only (Figure 9b,c), since the latter compositions feature essentially similar TR-SHG plots (Figures S32 and S35, respectively), which is in agreement with the derived phase diagram (vide supra, Figure 3).

In the case of MHyPbBr$_{1.33}$Cl$_{1.67}$, one sees that the SHG response rises upon transition from the monoclinic phase **III** to orthorhombic phase **II**. If one compares data points close to the phase transition temperature (ca. 330 K), the SHG enhancement is merely of 5%. The same behavior was previously identified for MHyPbCl$_3$, but for this compound, the SHG signal increased by about 40%; that high difference in signal strengths was sufficient to demonstrate temperature switching between two SHG states.[23] This result gave us a hint that doping of MHyPbCl$_3$ with Br$^-$ decreases the SHG contrast between monoclinic and orthorhombic crystal phases, so we examined materials with higher bromine content to verify this hypothesis.

The TR-SHG plot recorded for MHyPbBr$_{1.95}$Cl$_{1.05}$ shows very weakly marked inflection near 330 K in the heating run, indicative of a phase transition from **III** to **II**. Note that for higher Br$^-$ contents ($x = 2.25$, 2.55, see Figures S32 and S35, respectively), **III** to **II** phase transition is not visible in TR- SHG plots at all (though detectable by DSC, BDS and X-ray crystallography), as the change in SHG response due to phase transition is so small that is obscured by the signal's ripple.

This set of results tells us that stepwise enrichment of the MHyPbCl$_3$ matrix with Br$^-$ suppresses SHG contrast between monoclinic and orthorhombic crystal phases. Application-wise, this effect cannot be seen as useful if a high difference between the SHG signals is required, e.g., in devices employing switching of quadratic NLO response.

Structural studies shown that MHyPbBr$_{1.95}$Cl$_{1.05}$, MHyPbBr$_{2.25}$Cl$_{0.75}$, and MHyPbBr$_{2.55}$Cl$_{0.45}$ feature not only noncentrosymmetric orthorhombic (**II**) and monoclinic (**III**) phases but also a centrosymmetric cubic phase (**I**). Indeed, this is reflected in TR-SHG results (see Figure 9c and Figures S32 and S35, respectively). As seen in these Figures, transition from **II** to **I** results in the complete suppression of the SHG response. An analogous behavior is noted in TR-SHG results for MHyPbBr$_{2.8}$I$_{0.2}$ (Figures S38-S40), which confirms that the cubic phase of this HOIP halide alloy is also centrosymmetric.

Quite a striking observation, which can be made for $x = 1.95$, 2.25, 2.55, and MHyPbBr$_{2.8}$I$_{0.2}$ compositions, is the significant enhancement (3−5-fold) of the SHG response seen in their cooling runs (**I** to **II** transition) relative to heating runs. Note that this is observed only for materials that feature cubic phase **I** and only when samples are heated to cross their respective T_1 temperatures to reach this phase. While at present, we do not know specific origins of this phenomenon, we speculate that transition between these phases generates defects that act as SHG active centers upon restoration of phase **II**.

4. CONCLUSIONS

In this contribution, we took a closer look at effects of halide alloying in HOIPs comprising MHy$^+$ cations: Br−Cl systems of formula MHyPbBr$_x$Cl$_{3-x}$ ($x = 0.40$, 0.58, 0.85, 1.33, 1.95, 2.25,

https://doi.org/10.1021/acs.jpcc.1c07911
J. Phys. Chem. C 2022, 126, 1600−1610

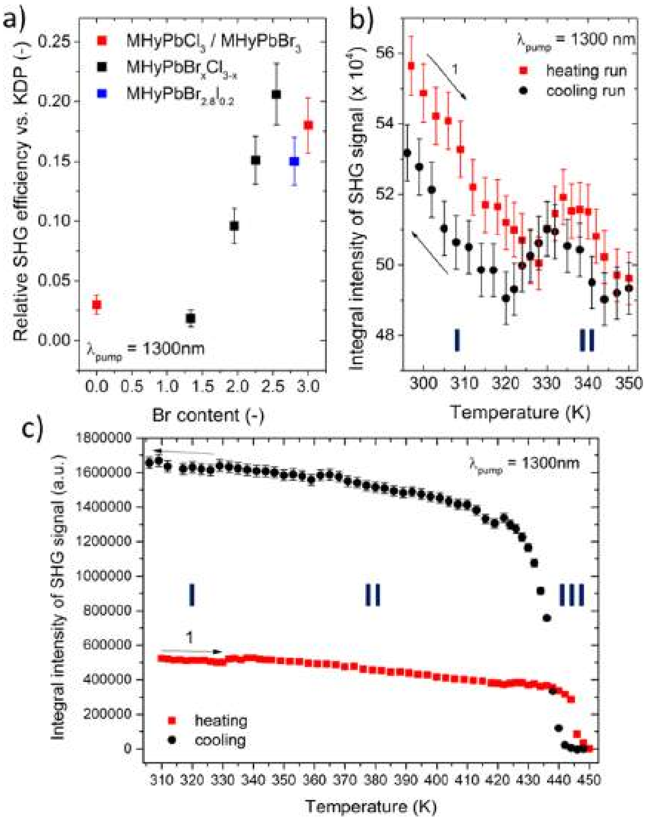

Figure 9. (a) Plot of relative SHG efficiencies expressed vs KDP for MHyPbBr$_x$Cl$_{3-x}$ (x = 0, 1.33, 1.95, 2.25, 2.55, 3) and MHyPbBr$_{2.8}$I$_{0.2}$. Note that relative SHG efficiencies for MHyPbBr$_3$ and MHyPbCl$_3$ are taken from previous reports.[22,23] (b) Plots of integral intensities of the SHG signal of MHyPbBr$_{1.33}$Cl$_{1.67}$ for the heating run (296−350 K, red squares) and cooling run (350−294 K, black squares). (c) Plots of integral intensities of the SHG signal of MHyPbBr$_{1.95}$Cl$_{1.05}$ for the heating run (306−450 K, red squares) and cooling run (450−306 K, black squares).

and 2.55) and a single representative of Br−I compounds, i.e., MHyPbBr$_{2.8}$I$_{0.2}$.

SCXRD data showed that lattice parameters vary linearly with the x value at constant temperature, and thus MHyPbBr$_x$Cl$_{3-x}$ systems fulfill Vegard's Law and can be thought of as ideal substitutional solid-state solutions. X-ray diffraction supported by SHG results evidence that all MHyPbBr$_x$Cl$_{3-x}$ and MHyPbBr$_{2.8}$I$_{0.2}$ perovskites crystallize at RT in a polar $P2_1$ structure (**III**). For the Br-rich compositions ($x \geq 1.33$) both HT phases of MHyPbBr$_3$ and MHyPbCl$_3$ are observed (cubic $Pm\bar{3}m$ (**I**) for $T_1 \geq 409$ K and orthorhombic $Pb2_1m$ (**II**) for $T_2 \geq 318$ K, respectively), while for lower Br content ($x < 1.33$), phase **I** vanishes. This behavior is opposite to that displayed by MAPbBr$_x$Cl$_{3-x}$ systems, for which the increase of Cl$^-$ content induced a stabilization of the cubic phase at lower temperatures. The above observations, as well as the analysis of geometrical parameters, led to a conclusion that the presence of the cubic phase strongly depends on the volume of the voids in-between the PbX$_6$ octahedra, in which MHy$^+$ cations are placed. Phase **II**, which was not observed for MHyPbBr$_3$, starts to appear at small doping of Cl$^-$ ions. In a similar manner to MHyPbBr$_3$, MHyPbBr$_{2.8}$I$_{0.2}$ undergoes a direct phase transition from **III** to **I** but at lower temperature T_1 = 390 K.

Dielectric studies confirm the (x,T) phase diagram and provide evidence for the significant contribution of ionic/electronic conductivity into dielectric response of mixed-halide MHy$^+$-based HOIPs. In phases **II** and **III**, the activation energy of Cl$^-$ conductivity increases along with the Br$^-$ doping, whereas in phase **I**, the activation energy of Br$^-$ conductivity decreases with increasing Cl$^-$ content.

Linear optical studies display systematic narrowing of the optical band gap and red shift of excitonic absorption with increasing Br$^-$ concentration and then on iodine doping, i.e., the excitonic absorption changes from 3.19 eV for MHyPbBr$_{0.4}$Cl$_{2.6}$ to 2.56 eV for MHyPbBr$_{2.8}$I$_{0.2}$. PL properties also depend strongly on the chemical composition. First, the PL spectra of MHyPbBr$_{2.8}$I$_{0.2}$ and MHyPbBr$_{2.55}$Cl$_{0.45}$ samples are dominated by broad bands characteristic for BE emission. The BE emission disappears with increasing Cl$^-$ content, and the spectra are dominated by narrow FE emission for $2.25 \geq x \geq 0.85$. On further increase of Cl$^-$ content, a new very broad PL appears around 460 nm that can be attributed to STEx states. Second, PL bands exhibit red shift with increasing Br$^-$ or I$^-$ content. These changes lead to strong tunability of the PL color, from greenish-blue for the Cl-rich samples to yellowish-green for MHyPbBr$_{2.8}$I$_{0.2}$.

TR-SHG studies revealed that doping of MHyPbCl$_3$ with Br$^-$ gradually decreases the difference between SHG intensities provided by monoclinic and orthorhombic crystal phases, to the point that no measurable difference in SHG intensities between these crystal phases is observed. Comparison of SHG efficiencies measured at RT for MHyPbBr$_x$Cl$_{3-x}$ halide alloys shows that there is no additional gain in SHG efficiency for these hybrids. Indeed, relative SHG efficiencies of halide-alloyed HOIPs remain within the range determined for MHyPbCl$_3$ and MHyPbBr$_3$ and are higher for the Br-rich samples.

Bearing in mind the wide-ranging investigation of 3D HOIPs in terms of numerous technological applications in materials science, our work has clearly revealed the usefulness of the halide alloying approach. We demonstrated large tunability of structural, optical, and dielectric properties of the newcomers in the perovskite family, i.e., lead halide HOIPs comprising MHy$^+$ cations.

■ ASSOCIATED CONTENT

Supporting Information

The Supporting Information is available free of charge at https://pubs.acs.org/doi/10.1021/acs.jpcc.1c07911.

(Tables S1−S6) Parameters obtained from DSC, SCXRD experimental details, and energy band gap values; (Figures S1−S40) PXRD patterns, Raman spectra, DSC traces, geometric parameters, frequency dependences of the complex dielectric permittivity and electrical modulus, Kubelka−Munk functions, experimental SHG spectra, and TR-SHG plots (PDF)

CIF files of MHyPbBr$_x$Cl$_{3-x}$ in **I**, **II**, and **III**, and MHyPbBr$_{2.8}$Cl$_{0.2}$. CCDC 2065131−2065141, 2073876 (ZIP)

■ AUTHOR INFORMATION

Corresponding Author

Mirosław Mączka − *Institute of Low Temperature and Structure Research, Polish Academy of Sciences, 50-422 Wrocław, Poland;* orcid.org/0000-0003-2978-1093; Phone: +48 71 3954 161; Email: m.maczka@intibs.pl; Fax: +48 71 3441 029

Authors

Dawid Drozdowski − *Institute of Low Temperature and Structure Research, Polish Academy of Sciences, 50-422 Wrocław, Poland;* orcid.org/0000-0001-5918-5503

Anna Gągor − *Institute of Low Temperature and Structure Research, Polish Academy of Sciences, 50-422 Wrocław, Poland*

Dagmara Stefańska − *Institute of Low Temperature and Structure Research, Polish Academy of Sciences, 50-422 Wrocław, Poland;* orcid.org/0000-0002-1051-3761

Jan K. Zarȩba − *Advanced Materials Engineering and Modeling Group, Wroclaw University of Science and Technology, 50-370 Wrocław, Poland;* orcid.org/0000-0001-6117-6876

Katarzyna Fedoruk − *Department of Experimental Physics, Wrocław University of Science and Technology, 50-370 Wrocław, Poland*

Adam Sieradzki − *Department of Experimental Physics, Wrocław University of Science and Technology, 50-370 Wrocław, Poland;* orcid.org/0000-0003-4136-5754

Complete contact information is available at: https://pubs.acs.org/10.1021/acs.jpcc.1c07911

Author Contributions

The manuscript was written through contributions of all authors. All authors have given approval to the final version of the manuscript.

Notes

The authors declare no competing financial interest.

■ ACKNOWLEDGMENTS

This research was supported by the National Science Center (Narodowe Centrum Nauki) in Poland under project no. 2019/35/B/ST5/00043. J.K.Z. acknowledges financial support from Wroclaw University of Science and Technology.

■ REFERENCES

(1) Mitzi, D. B. Synthesis, Structure, and Properties of Organic-Inorganic Perovskites and Related Materials. In *Progress in Inorganic Chemistry*; Karlin, K. D.; Wiley, 1999; Vol. *48*, pp. 1−121.

(2) Li, W.; Wang, Z.; Deschler, F.; Gao, S.; Friend, R. H.; Cheetham, A. K. Chemically Diverse and Multifunctional Hybrid Organic-Inorganic Perovskites. *Nat. Rev. Mater.* **2017**, *2*, 16099.

(3) Saparov, B.; Mitzi, D. B. Organic-Inorganic Perovskites: Structural Versatility for Functional Materials Design. *Chem. Rev.* **2016**, *116*, 4558−4596.

(4) Zhao, X.; Ng, J. D. A.; Friend, R. H.; Tan, Z. K. Opportunities and Challenges in Perovskite Light-Emitting Devices. *ACS Photonics* **2018**, *5*, 3866−3875.

(5) Poglitsch, A.; Weber, D. Dynamic Disorder in Methylammonium-trihalogenoplumbates (II) Observed by Millimeter-Wave Spectroscopy. *J. Chem. Phys.* **1987**, *87*, 6373−6378.

(6) Sletten, E.; Jensen, L. H. The Crystal Structure of Dimethylammonium Copper(II) Formate, $NH_2(CH_2)_2[Cu(OOCH)_3]$. *Acta Crystallogr., B* **1973**, *29*, 1752−1756.

(7) Tong, M. L.; Ru, J.; Wu, Y. M.; Chen, X. M.; Chang, H. C.; Mochizuki, K.; Kitagawa, S. Cation-Templated Construction of Three-Dimensional α-Po Cubic-Type $[M(dca)_3]$- Networks. Syntheses, Structures and Magnetic Properties of $A[M(dca)_3]$ (dca = Dicyanamide; for A = Benzyltributylammonium, M = Mn^{2+}, Co^{2+}; for A = Benzyltriethylammonium, M = Mn^{2+}). *New J. Chem.* **2003**, *27*, 779−782.

(8) Zhao, X. H.; Huang, X. C.; Zhang, S. L.; Shao, D.; Wei, H. Y.; Wang, X. Y. Cation-Dependent Magnetic Ordering and Room-Temperature Bistability in Azido-Bridged Perovskite-Type Compounds. *J. Am. Chem. Soc.* **2013**, *135*, 16006−16009.

(9) Wang, W.; Zhang, Y.; Wu, W.; Liu, X.; Ma, X.; Qian, G.; Fan, J. Quantitative Modeling of Self-Assembly Growth of Luminescent Colloidal $CH_3NH_3PbBr_3$ Nanocrystals. *J. Phys. Chem. C* **2019**, *123*, 13110−13121.

(10) Lin, R.; Xiao, K.; Qin, Z.; Han, Q.; Zhang, C.; Wei, M.; Saidaminov, M. I.; Gao, Y.; Xu, J.; Xiao, M.; et al. Monolithic All-Perovskite Tandem Solar Cells with 24. 8% Efficiency Exploiting Comproportionation to Suppress Sn(II) Oxidation in Precursor Ink. *Nat. Energy* **2019**, *4*, 864−873.

(11) NREL *Best Research-Cell Efficiency Chart* https://www.nrel.gov/pv/assets/pdfs/best-research-cell-efficiencies.20190802.pdf (accessed Mar 14, 2021).

(12) Ball, J. M.; Lee, M. M.; Hey, A.; Snaith, H. J. Low-Temperature Processed Meso-Superstructured to Thin-Film Perovskite Solar Cells. *Energy Environ. Sci.* **2013**, *6*, 1739−1743.

(13) Stranks, S. D.; Eperon, G. E.; Grancini, G.; Menelaou, C.; Alcocer, M. J. P.; Leijtens, T.; Herz, L. M.; Petrozza, A.; Snaith, H. J. Electron-Hole Diffusion Lengths Exceeding 1 Micrometer in an Organometal Trihalide Perovskite Absorber. *Science* **2013**, *342*, 341−344.

(14) Mehdi, H.; Mhamdi, A.; Hannachi, R.; Bouazizi, A. $MAPbBr_3$ Perovskite Solar Cells: Via a Two-Step Deposition Process. *RSC Adv.* **2019**, *9*, 12906−12912.

(15) Cao, M.; Tian, J.; Cai, Z.; Peng, L.; Yang, L.; Wei, D. Perovskite Heterojunction Based on $CH_3NH_3PbBr_3$ Single Crystal for High-Sensitive Self-Powered Photodetector. *Appl. Phys. Lett.* **2016**, *109*, 233303.

(16) Wang, F.; Cao, Y.; Chen, C.; Chen, Q.; Wu, X.; Li, X.; Qin, T.; Huang, W. Materials Toward the Upscaling of Perovskite Solar Cells: Progress, Challenges, and Strategies. *Adv. Funct. Mater.* **2018**, *28*, 1803753.

(17) Zhumekenov, A. A.; Saidaminov, M. I.; Haque, M. A.; Alarousu, E.; Sarmah, S. P.; Murali, B.; Dursun, I.; Miao, X. H.; Abdelhady, A. L.; Wu, T.; et al. Formamidinium Lead Halide Perovskite Crystals with Unprecedented Long Carrier Dynamics and Diffusion Length. *ACS Energy Lett.* **2016**, *1*, 32−37.

(18) Eperon, G. E.; Stranks, S. D.; Menelaou, C.; Johnston, M. B.; Herz, L. M.; Snaith, H. J. Formamidinium Lead Trihalide: A Broadly Tunable Perovskite for Efficient Planar Heterojunction Solar Cells. *Energy Environ. Sci.* **2014**, *7*, 982−988.

(19) Liu, M.; Johnston, M. B.; Snaith, H. J. Efficient Planar Heterojunction Perovskite Solar Cells by Vapour Deposition. *Nature* **2013**, *501*, 395−398.

(20) Wu, X.; Trinh, M. T.; Niesner, D.; Zhu, H.; Norman, Z.; Owen, J. S.; Yaffe, O.; Kudisch, B. J.; Zhu, X. Y. Trap States in Lead Iodide Perovskites. *J. Am. Chem. Soc.* **2015**, *137*, 2089−2096.

(21) Hanusch, F. C.; Wiesenmayer, E.; Mankel, E.; Binek, A.; Angloher, P.; Fraunhofer, C.; Giesbrecht, N.; Feckl, J. M.; Jaegermann, W.; Johrendt, D.; et al. Efficient Planar Heterojunction Perovskite Solar Cells Based on Formamidinium Lead Bromide. *J. Phys. Chem. Lett.* **2014**, *5*, 2791−2795.

(22) Mączka, M.; Ptak, M.; Gągor, A.; Stefańska, D.; Zarȩba, J. K.; Sieradzki, A. Methylhydrazinium Lead Bromide: Noncentrosymmetric Three-Dimensional Perovskite with Exceptionally Large Framework Distortion and Green Photoluminescence. *Chem. Mater.* **2020**, *32*, 1667−1673.

(23) Mączka, M.; Gagor, A.; Zarȩba, J. K.; Stefanska, D.; Drozd, M.; Balciunas, S.; Šimėnas, M.; Banys, J.; Sieradzki, A. Three-Dimensional Perovskite Methylhydrazinium Lead Chloride with Two Polar Phases and Unusual Second-Harmonic Generation Bistability above Room Temperature. *Chem. Mater.* **2020**, *32*, 4072−4082.

(24) Rosales, B. A.; Men, L.; Cady, S. D.; Hanrahan, M. P.; Rossini, A. J.; Vela, J. Persistent Dopants and Phase Segregation in Organolead Mixed-Halide Perovskites. *Chem. Mater.* **2016**, *28*, 6848−6859.

(25) Zhang, M.; Yu, H.; Lyu, M.; Wang, Q.; Yun, J. H.; Wang, L. Composition-Dependent Photoluminescence Intensity and Prolonged Recombination Lifetime of Perovskite $CH_3NH_3PbBr_{3-x}Cl_x$ Films. *Chem. Commun.* **2014**, *50*, 11727−11730.

(26) Madjet, M. E. A.; Akimov, A. V.; El-Mellouhi, F.; Berdiyorov, G. R.; Ashhab, S.; Tabet, N.; Kais, S. Enhancing the Carrier Thermalization Time in Organometallic Perovskites by Halide Mixing. *Phys. Chem. Chem. Phys.* **2016**, *18*, 5219−5231.

(27) Gil-Escrig, L.; Miquel-Sempere, A.; Sessolo, M.; Bolink, H. J. Mixed Iodide-Bromide Methylammonium Lead Perovskite-Based Diodes for Light Emission and Photovoltaics. *J. Phys. Chem. Lett.* **2015**, *6*, 3743−3748.

(28) Fedeli, P.; Gazza, F.; Calestani, D.; Ferro, P.; Besagni, T.; Zappettini, A.; Calestani, G.; Marchi, E.; Ceroni, P.; Mosca, R. Influence of the Synthetic Procedures on the Structural and Optical Properties of Mixed-Halide (Br, I) Perovskite Films. *J. Phys. Chem. C* **2015**, *119*, 21304−21313.

(29) Karlsson, M.; Yi, Z.; Reichert, S.; Luo, X.; Lin, W.; Zhang, Z.; Bao, C.; Zhang, R.; Bai, S.; Zheng, G.; et al. Mixed Halide Perovskites for Spectrally Stable and High-Efficiency Blue Light-Emitting Diodes. *Nat. Commun.* **2021**, *12*, 361.

(30) Ebadi, M.; Sefidi, P. Y.; Samadifar, A.; Salari, D.; Darbandi, M.; Hosseini, M. G. Influence of Lead (II) Chloride and/or Lead (II) Bromide Entrance on the Efficiency and Stability of Methyl Ammonium Lead Triiodide Perovskite Solar Cell: Comparative Study of the Halide Composition and Substitution Percentage. *Opt. Mater.* **2021**, *113*, 110888.

(31) Edri, E.; Kirmayer, S.; Kulbak, M.; Hodes, G.; Cahen, D. Chloride Inclusion and Hole Transport Material Doping to Improve Methyl Ammonium Lead Bromide Perovskite-Based High Open-Circuit Voltage Solar Cells. *J. Phys. Chem. Lett.* **2014**, *5*, 429−433.

(32) Hu, Z.; An, Q.; Xiang, H.; Aigouy, L.; Sun, B.; Vaynzof, Y.; Chen, Z. Enhancing the Efficiency and Stability of Triple-Cation Perovskite Solar Cells by Eliminating Excess $PbI_2$from the Perovskite/Hole Transport Layer Interface. *ACS Appl. Mater. Interfaces* **2020**, *12*, 54824−54832.

(33) Yuan, J.; Hazarika, A.; Zhao, Q.; Ling, X.; Moot, T.; Ma, W.; Luther, J. M. Metal Halide Perovskites in Quantum Dot Solar Cells: Progress and Prospects. *Joule* **2020**, *4*, 1160−1185.

(34) Brivio, F.; Caetano, C.; Walsh, A. Thermodynamic Origin of Photoinstability in the $CH_3NH_3Pb(I_{1-X}Br_x)_3$ Hybrid Halide Perovskite Alloy. *J. Phys. Chem. Lett.* **2016**, *7*, 1083−1087.

(35) Noh, J. H.; Im, S. H.; Heo, J. H.; Mandal, T. N.; Seok, S. I. Chemical Management for Colorful, Efficient, and Stable Inorganic-Organic Hybrid Nanostructured Solar Cells. *Nano Lett.* **2013**, *13*, 1764−1769.

(36) Drozdowski, D.; Gągor, A.; Mączka, M. Methylhydrazinium Lead Iodide − One Dimensional Chain Phase with Excitonic Absorption and Large Energy Band Gap. *J. Mol. Struct.* **2022**, *1249*, 131660.

(37) Alberto López, C.; Consuelo Alvarez-Galván, M.; Abia, C.; Teresa Fernández-Díaz, M.; Antonio Alonso, J. Structural Phase Transitions of Hybrid Perovskites $CH_3NH_3PbX_3$ (X = Br, Cl) from Synchrotron and Neutron Diffraction Data. In *Perovskite and Piezoelectric Materials*; Pola, S.; Panwar, N.; Coondoo, I., Eds.; IntechOpen, 2021.

(38) Vegard, L. Die Konstitution Der Mischkristalle Und Die Raumfüllung Der Atome. *Z. Phys.* **1921**, *5*, 17−26.

(39) Vegard, L.; Dale, H. VIII. Untersuchungen Über Mischkristalle Und Legierungen. *Z. Krist. - Cryst. Mater.* **1928**, *67*, 239.

(40) Shannon, R. D. Revised Effective Ionic Radii and Systematic Studies of Interatomic Distances in Halides and Chalcogenides. *Acta Crystallogr., A* **1976**, *32*, 751−767.

(41) Fleet, M. E. Distortion Parameters for Coordination Polyhedra. *Mineral. Mag.* **1976**, *40*, 531−533.

(42) Spek, A. L. Single-Crystal Structure Validation with the Program PLATON. *J. Appl. Crystallogr.* **2003**, *36*, 7−13.

(43) Molak, A.; Paluch, M.; Pawlus, S.; Klimontko, J.; Ujma, Z.; Gruszka, I. Electric Modulus Approach to the Analysis of Electric Relaxation in Highly Conducting $(Na_{0.75}Bi_{0.25})(Mn_{0.25}Nb_{0.75})O_3$ Ceramics. *J. Phys. D: Appl. Phys.* **2005**, *38*, 1450−1460.

(44) Głowienka, D.; Miruszewski, T.; Szmytkowski, J. The Domination of Ionic Conductivity in Tetragonal Phase of the Organometal Halide Perovskite $CH_3NH_3PbI_{3-X}Cl_x$. *Solid State Sci.* **2018**, *82*, 19−23.

(45) Maeda, M.; Hattori, M.; Hotta, A.; Suzuki, I. Dielectric Studies on $CH_3NH_3PbX_3$ (X = Cl and Br) Single Cystals. *J. Phys. Soc. Jpn.* **1997**, *66*, 1508−1511.

(46) Yuan, Y.; Xu, R.; Xu, H. T.; Hong, F.; Xu, F.; Wang, L. J. Nature of the Band Gap of Halide Perovskites ABX_3 (A = CH_3NH_3, Cs; B = Sn, Pb; X = Cl, Br, I): First-Principles Calculations. *Chin. Phys. B* **2015**, *24*, 116302.

(47) Mączka, M.; Ptak, M.; Gągor, A.; Stefańska, D.; Sieradzki, A. Layered Lead Iodide of [Methylhydrazinium]$_2$PbI$_4$ with a Reduced Band Gap: Thermochromic Luminescence and Switchable Dielectric Properties Triggered by Structural Phase Transitions. *Chem. Mater.* **2019**, *31*, 8563−8575.

(48) Krishnamurthy, S.; Kour, P.; Katre, A.; Gosavi, S.; Chakraborty, S.; Ogale, S. Cystamine-Configured Lead Halide Based 2D Hybrid Molecular Crystals: Synthesis and Photoluminescence Systematics. *APL Mater.* **2018**, *6*, 114204.

(49) Yu, J.; Kong, J.; Hao, W.; Guo, X.; He, H.; Leow, W. R.; Liu, Z.; Cai, P.; Qian, G.; Li, S.; et al. Broadband Extrinsic Self-Trapped Exciton Emission in Sn-Doped 2D Lead-Halide Perovskites. *Adv. Mater.* **2019**, *31*, 1806385.

(50) Dai, J.; Zheng, H.; Zhu, C.; Lu, J.; Xu, C. Comparative Investigation on Temperature-Dependent Photoluminescence of $CH_3NH_3PbBr_3$ and $CH(NH_2)_2PbBr_3$ Microstructures. *J. Mater. Chem. C* **2016**, *4*, 4408−4413.

(51) Chen, C.; Hu, X.; Lu, W.; Chang, S.; Shi, L.; Li, L.; Zhong, H.; Han, J. B. Elucidating the Phase Transitions and Temperature-Dependent Photoluminescence of $MAPbBr_3$ Single Crystal. *J. Phys. D: Appl. Phys.* **2018**, *51*, No. 045105.

(52) Kurtz, S. K.; Perry, T. T. A Powder Technique for the Evaluation of Nonlinear Optical Materials. *J. Appl. Phys.* **1968**, *39*, 3798−3813.

Journal of
Materials Chemistry C

ROYAL SOCIETY
OF CHEMISTRY

PAPER

Check for updates

Cite this: *J. Mater. Chem. C*, 2024, **12**, 6653

Layered methylhydrazinium lead halide perovskites: new crystal polymorphs with a tailored band gap and photoluminescence colour *via* halide substitution†

Dawid Drozdowski,* Adam Kabański, Dagmara Stefańska, Maciej Ptak, Mirosław Mączka and Anna Gągor*

Received 4th March 2024,
Accepted 14th April 2024

DOI: 10.1039/d4tc00865k

rsc.li/materials-c

An unrelenting focus on improving stability and optoelectronic performance of lead halide three-dimensional hybrid organic–inorganic perovskites (3D HOIPs, ABX_3 formula) leads to the usage of many chemical engineering techniques, including X-site alloying. Formerly we have shown the usefulness of this approach in 3D HOIPs comprising methylhydrazinium (MHy^+); this time we prove it again in the layered (A_2BX_4) perovskites. Herein we report the synthesis, crystal structure and physicochemical characterization of $MHy_2PbBr_{4-x}I_x$ in a wide concentration range (x = 0.25, 0.3, 0.4, 1.1, 2.35, 2.5, 3.1). Reported compounds crystallise in the Ruddlesden–Popper phase with corner-sharing $[PbX_6]^{4-}$ (X = Br, I) octahedra, forming (010) layers, separated by MHy^+. An abundant temperature-driven polymorphism is observed, starting from the Br-rich compounds with a sequence of *Pnmm*, *Pnma* and $P2_1/c$ phases on cooling, through the region with the $P\bar{1}$ low-temperature phase, and ending with the I-rich compounds with an incommensurately modulated $Pnma(00\gamma)0s0$ superspace group. We also report, for the first time in the MHy-based perovskites, the 2D → 3D transition to $Pm\bar{3}m$ cubic symmetry and a 3D perovskite phase with a dominant presence of iodine. With the use of Raman spectroscopy, the dynamics of MHy^+ cations in particular phases is thoroughly analysed, revealing the positional disorder in room-temperature and high-temperature zones and its freezing at low temperatures. Linear optical studies demonstrate the decrease of the energy band gap (2.91 eV to 2.31 eV) and a strong change in photoluminescence colour (bluish-green to yellow-green) along with increasing iodine contribution.

Introduction

Since the first reports on photovoltaic devices based on three-dimensional hybrid organic–inorganic perovskites (3D HOIPs) back in 2009,[1] this class of materials has garnered significant interest on a global scale and has been thoroughly investigated until the present. The flagship 3D HOIPs, based on lead halides, adopt the perovskite-type structure of the ABX_3 formula and $Pm\bar{3}m$ prototype symmetry, where the 'A' components are situated in the 12-fold coordinated cavities between the corner-sharing BX_6 octahedra.[2,3] Notably, 3D lead halide HOIPs with methylammonium (MA^+) and formamidinium (FA^+) at the 'A' site have exhibited remarkable properties, *e.g.*, power conversion efficiencies (PCE) exceeding 25%, photoluminescence quantum yield (PLQY) up to 85% and long carrier diffusion lengths.[4–6] With their remarkable properties, they are considered a breakthrough in photovoltaics and light-emitting devices. However, the structural diversity of lead halide 3D HOIPs has been limited so far to only four organic cations (MA^+, FA^+, aziridinium (AZR^+) and methylhydrazinium (MHy^+))[7–11] and several other polytypes, *e.g.*, 4*H*-hexagons.[12–14] Furthermore, these materials suffer from sensitivity to outdoor factors, chemicals, *etc.*[15] To address these issues, 2D HOIPs have emerged as a potential solution.

In 2D HOIPs, octahedral slabs are separated by organic cations ('spacers'), creating a natural (for single-layer structures even perfect) quantum well character, resulting in narrower PL bands with higher PLQY when compared to 3D counterparts.[16,17] In contrast, the insulating spacers induce larger band gaps and exciton binding energies (typically >150 meV and *ca.* 10 meV for 2D and 3D HOIPs, respectively), and consequently – lower PCE.[18]

Institute of Low Temperature and Structure Research, Polish Academy of Sciences, Okólna 2, 50-422 Wrocław, Poland. E-mail: d.drozdowski@intibs.pl, a.gagor@intibs.pl

† Electronic supplementary information (ESI) available: Fig. S1–S20: PXRD diffractograms, Raman spectra, Fourier maps, crystal structures, absorption spectra, Tauc plots and integrated PL intensities *versus* temperature. Tables S1–S6: main details from SCXRD experiments and Raman wavenumbers. CCDC 2189681, 2307123–2307129, 2324607. For ESI and crystallographic data in CIF or other electronic format see DOI: https://doi.org/10.1039/d4tc00865k

With all their pros and cons, 2D HOIPs may be preferable for light-emitting (notably lasing) applications rather than photovoltaics. Nevertheless, an unprecedented advantage of 2D HOIPs is a plethora of the already-known spacers, allowing for the existence of numerous single-layered (n = 1) and multi-layered ($n \geq 2$, beyond the scope of this work) compounds. One may classify them relying on the relative stacking of layers and the type of introduced cation (formulae provided for n = 1): Ruddlesden–Popper (RP) phases of A_2BX_4 formula (A = monovalent cation), Dion–Jacobson (DJ) phases (ABX_4, A = divalent cation) and the alternating cation in the interlayer space (ACI) compounds ($AA'BX_4$, A and A′ denote monovalent cations).[19–21] The RP perovskites are an emerging type of compounds with the ability to tune the band gap across the wide spectrum range (~410–760 nm), as well as offering greater stability and an improved light absorption coefficient.[22,23] Compositional engineering with comprehensive, multitool analysis is another powerful way used to examine and modify the physicochemical properties of HOIPs, enhancing the desired and suppressing the undesirable ones. Amongst the A-site moieties, the aforementioned MHy^+ cation provides a good base for studies, as it is suitable for the development of both 3D and 2D lead halide HOIPs. The reports on $MHyPbBr_3$ and $MHyPbCl_3$ perovskites revealed the formation of heavily distorted 3D substructures, adopting the noncentrosymmetric alignment,[7,8] while the 2D counterparts reveal record-breaking low separation of the perovskite layers.[24–26] Furthermore, MHy_2PbBr_4 is a room temperature (RT) uniaxial ferroelectric adopting orthorhombic $Pmn2_1$ symmetry with a ferroelectric phase stable in a wide temperature range (from 350 K down to at least 100 K). MHy_2PbCl_4 adopts a sequence of centrosymmetric, modulated and polar phases with temperature lowering, while MHy_2PbI_4, which does not demonstrate polar properties, reveals a unique octahedral tilting system and an exceptionally low band gap of 2.20 eV. Given that altering the halide component in MHy_2PbX_4 perovskites leads to such significant changes in physicochemical properties, X-site alloying (two halides in one site) appears to be a promising method for obtaining materials with novel and intriguing characteristics. This technique has primarily proven its usefulness for $MAPbX_xX'_{3-x}$ and $FAPbX_xX'_{3-x}$ (X, X′ = Br^-, Cl^-, I^-) 3D HOIPs, tuning the PL bands, optical band gap and carrier diffusion lengths and improving the moisture resistance.[27–35] More recently, we have reported the studies on compounds of the formulae $MHyPbBr_xCl_{3-x}$ and $MHyPbBr_{2.8}I_{0.2}$, where the simple change of the halide ratio leads to and allows for modification of the absorption and PL emission bands, the activation energy of ionic conductivity and the intensity of the second harmonic generation (SHG) effect.[36] In the case of 2D compounds, halide-mixing also impacts certain physicochemical properties. For instance, in the $(PEA)_2Pb(I_{1-x}Br_x)_4$ series (PEA = phenethylammonium), increasing iodine concentration diminishes the exciton transport, especially noticeable in the bromine-rich region.[37] In another example, *i.e.*, (2-(1-cyclohexenyl)ethylammonium)$PbBr_{4-x}I_x$ 2D HOIPs, X-site alloying enables highly precise, tuneable, and linear changes of the band gap of the thin films, together with the redshift of the RT exciton absorbance band associated with the iodide incorporation.[22]

However, there is a significant lack of information regarding the influence of halide substitution on the structural changes of 2D HOIPs. Furthermore, in the 3D HOIPs comprising MHy^+ a series of Br-I systems has not been obtained hitherto and therefore, the iodine contribution to this specific class of materials remains an obscure field. Here, we report the synthesis of the RP perovskites of the $MHy_2PbBr_{4-x}I_x$ formula. Using two crystallisation methods, single crystals of a vast compositional range (x between 0.25 and 3.1) were obtained. The multitechnique analysis in the broad temperature range (80–420 K), *i.e.*, crystal structure determination on both single-crystal and powdered materials, Raman spectroscopy measurements and linear optical properties examination are the content of this contribution.

Experimental

Materials and methods

Synthetic procedures. $PbBr_2$ (98%) PbI_2 (99%), HBr (48 wt% in H_2O), HI (57 wt% in H_2O, stabilized with H_3PO_2), methylhydrazine (MHy, 98%), *N*,*N*-dimethylformamide (DMF, 99.8%) and propylene carbonate (PC, 99.7%) were commercially available (Sigma-Aldrich) and used without further purification. To grow $MHy_2PbBr_{4-x}I_x$ single crystals abundant in bromine (90% or more), a mixture of HBr and HI was added dropwise to 12 mmol of MHy until pH = 7. A 5 mmol of mixed together $PbBr_2$ and PbI_2 was subsequently added to the blend, and second DMF, upon stirring at 30 °C, until complete dissolution of lead halides. The solution was remained undisturbed at RT. The plate-like crystals were harvested after 2–3 days, separated from the mother fluid, and dried at RT. To obtain compounds with higher iodine contribution, the clear solution of lead halides, HBr, HI and MHy dissolved in PC was moved into a glass vial and stored at 50 °C. After 3–5 days, plate-like crystals were separated and dried at RT. The $PbBr_2$ to PbI_2 ratios were as follows: 9 : 1, 8 : 2, 7 : 3, 5 : 5, 4 : 6, 3 : 7 and 2 : 8. The energy dispersive X-ray analysis (EDAX) revealed the iodine content (x) of: 0.25, 0.3, 0.4, 1.1, 2.35, 2.5 and 3.1, confirmed with a good match *via* SCXRD experiments (Fig. S1, ESI†). The powder XRD diffractograms (Fig. S2, ESI†) prove the phase purity of the samples. The comparison of PXRD patterns for $MHyPbBr_{3.7}I_{0.3}$ (as-synthesized sample and stored *ca.* 2.5 years in a desiccator, RT) and patterns for $MHyPbBr_{1.65}I_{2.35}$ (stored *ca.* 2.5 years in a desiccator, RT) are presented in Fig. S3 (ESI†), demonstrating the stability of the reported materials. The Raman spectra (Fig. S4, ESI†) are in agreement with the ones recorded for MHy_2PbBr_4 and MHy_2PbI_4.

The elemental analysis was performed using the scanning electron microscope FEI Nova NanoSEM 230 (FEI Company, Hillsboro, OR, USA) equipped using an EDAX PegasusXM4 spectrometer, with the operating acceleration voltage in the range of 3.0–15 kV and spot of 2.5–3.0.

Single-crystal X-ray diffraction (SCXRD) experiments were carried out using an Xcalibur four-circle diffractometer (Oxford Diffraction) with an Atlas CCD detector and graphite-monochromated MoKα radiation ($\lambda = 0.7107$ Å). Absorption was corrected by multi-scan methods using CrysAlis PRO 1.171.41.93a (Rigaku Oxford Diffraction, 2020). Crystal structures were solved in Olex2 1.5 using SHELXT.[38,39] Refinement of non-modulated phases was performed in SHELXL.[40] Empirical absorption correction was applied using spherical harmonics, implemented in the SCALE3 ABSPACK scaling algorithm. H-atom parameters were constrained in all phases. Refinement of the incommensurately modulated phase was conducted in Jana2020.[41] The (3 + 1) superspace approach was applied. The studied structure was refined in the $Pnma(00\gamma)0s0$ superspace group with modulation vector $q^* = \gamma c^*$, where $\gamma = 0.44$–0.46 for $x = 2.35$, 2.5 and 3.1. As presented on Fourier maps (Fig. S5 and S6, ESI†), the positions of all atoms were modulated using first-order harmonics. All modulation waves were regarded as one-dimensional, *i.e.*, propagating along the [010] direction. The final R-factors, as well as other experimental and refinement details of selected compounds, are listed in Tables S1–S3 (ESI†).

Powder X-ray diffraction (PXRD) of the grounded compounds was measured in the reflection mode using an X'Pert PRO X-ray diffraction system equipped using a PIXcel ultrafast line detector and Soller slits for CuKα radiation ($\lambda = 1.5406$ Å). High-temperature (HT) experiments were performed using the Anton Paar Oven Chamber.

The RT diffuse reflectance spectra (DRS) of powdered samples were obtained using the Varian Cary 5E UV-VIS-NIR spectrometer. Measurements of temperature-dependent PL were performed using the Hamamatsu PMA-12 photonic multichannel analyser combined with a BT-CCD sensor while the temperature was controlled by the Linkam THMS600 stage. As an excitation source, the 375 nm laser beam was used.

The RT polycrystalline Raman spectra of $MHy_2PbBr_{4-x}I_x$ samples were collected in the 3500–50 cm^{-1} range using a Bruker FT MultiRam spectrometer with a YAG:Nd laser excitation at 1064 nm. The temperature-dependent Raman spectra in the 1700–100 cm^{-1} range were measured for the $x = 0.3$ sample using a Renishaw inVia Raman spectrometer, equipped with a confocal DM2500 Leica optical microscope, a CCD as a detector, and a diode laser operating at 830 nm.

Results and discussion

Crystal structure

$MHy_2PbBr_{4-x}I_x$ crystallises in 2D perovskite alignment, where the corner-sharing $[PbX_6]^{4-}$ (X = Br, I) octahedra forming (010) layers, separated by the MHy^+ cations, and reveals rich temperature-driven polymorphism. All crystal phases discerned between 100 K and the temperature limited by the decomposition, are presented in Fig. 1a in the form of a (x, T) phase diagram, which is divided into 3 regions with different iodine contributions. Starting from the lowest x, the boundaries are defined by the symmetry of low-temperature (LT) phases (between the 1st and 2nd regions) and RT phases (between the 2nd and 3rd regions). The HT phase in the first and second regions ($0.2 < x < 2.2$) is of orthorhombic *Pnmm* symmetry (**II**). This phase is isostructural to all formerly reported MHy_2PbX_4 (X = Br, Cl, I) single-halide analogues.[24–26] In **II**, MHy^+ are disordered over the m mirror plane. Consequently, the middle N1 atom of MHy^+ is split over two symmetrically equivalent positions with equal probability (Fig. S7a and S8, ESI†). The individual octahedra have C_{2v} symmetry, with C_{2v} site symmetry for Pb and bridging halides, and C_s for apical halide.

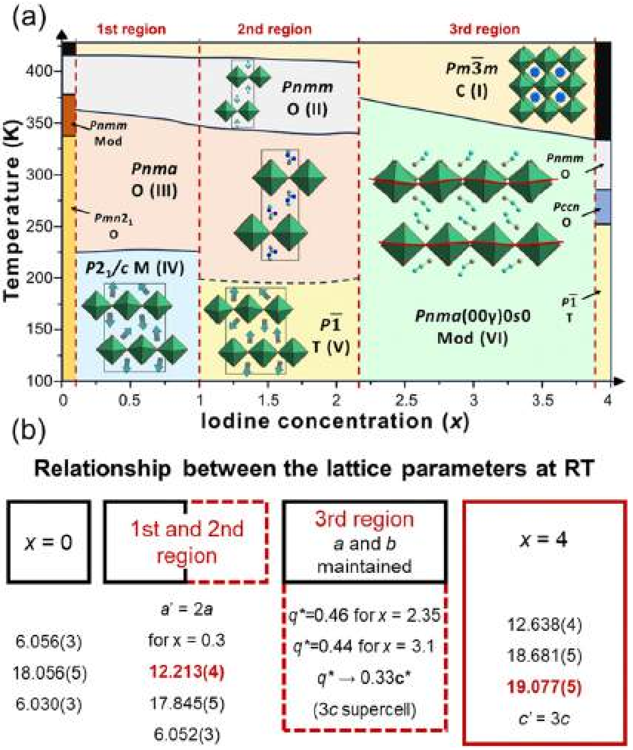

Fig. 1 (a) (x, T) Phase diagram of $MHy_2PbBr_{4-x}I_x$ 2D HOIPs divided into three regions depending on the halide concentration. Regions and phase boundaries were determined with respect to the XRD and (for selected samples) Raman experiments. (b) The relationship between lattice parameters of $MHy_2PbBr_{4-x}I_x$ 2D HOIPs at room temperature (RT).

The RT phase (**III**), for $0.2 < x < 1$, is $2a$ superstructure of **II** with orthorhombic *Pnma* symmetry (Fig. S7b and S9, ESI†) with the number of formula units per unit cell (Z) equal to 4. Fig. 2a demonstrates the fragment of a single perovskite slab. Three symmetrically inequivalent halides, namely X1, X2 (*i.e.*, bridging along [001] and [100], respectively) and an apical X3, are presented as octants. The site symmetry of Pb, X1 and X2 is reduced to C_s, while the X3 halides occupy general positions. The MHy^+ moieties are still disordered, but in **III**, they adopt two positions with a nonequal probability (0.65 : 0.35). Despite the disorder, MHy^+ may still interact with the inorganic substructure, creating several N–H···N and N–H···X hydrogen bonds (HBs), mostly involving the apical halides as acceptors (for distances see Table S4, ESI†). The individual octahedra are slightly distorted, which is expressed in the octahedral distortion parameters (calculated using the Fleet approach)[50] – bond length distortion $\Delta_d = 2.6 \times 10^{-4}$ and octahedral angle variance $\sigma^2 = 13.8$ deg^2 (Table 1). It is worth noting that even the smallest iodine concentration leads to the stabilization of

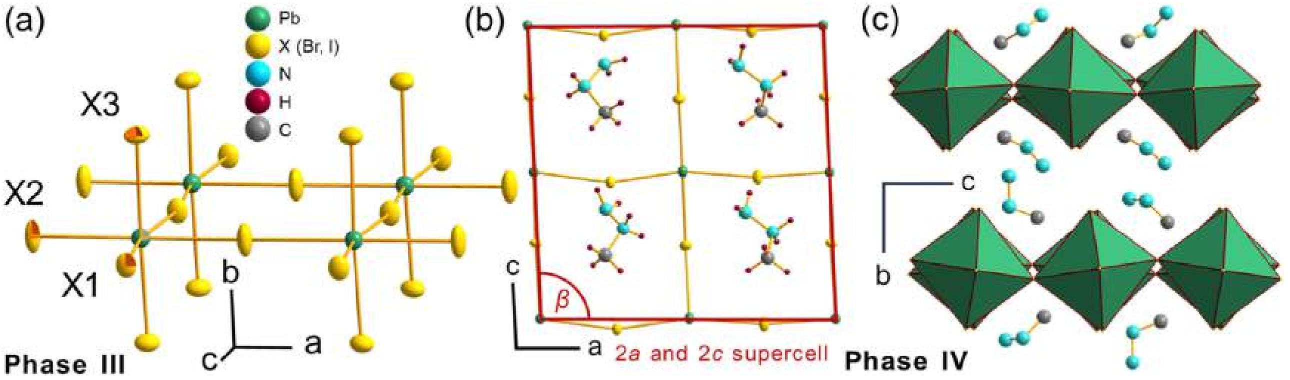

Fig. 2 (a) Fragment of the octahedra layer in phase **III**. (b) and (c) Example of the crystal structure with ordered MHy^+ cations – $MHy_2PbBr_{3.7}I_{0.3}$ in $P2_1/c$ (**IV**). View along (b) [010] and (c) [001] directions.

centrosymmetric phases and the disruption of ferroelectric ordering present in MHy_2PbBr_4, which possesses polar $Pmc2_1$ space group with ordered MHy^+ cations and σ^2 = 18.6 deg^2.[24] Both the polar symmetry breaking and smaller octahedra distortion arise from weaker intermolecular interactions in the presence of larger halides (*i.e.*, iodine).

$MHy_2PbBr_{4-x}I_x$, for $0.2 < x < 1$ and below 220–230 K, undergoes a phase transition related to symmetry breaking to the monoclinic $P2_1/c$. Symmetry reduction leads to twinning of the sample to a two-domain state (Fig. S7c, ESI†). The LT phase (**IV**) is a superstructure of **III** with $c' = 2c$ and $Z = 8$. In **IV**, all atoms occupy general positions and the MHy^+ cations are well-ordered (Fig. 2b, c and Fig. S10, ESI†). The amines are anchored *via* the network of numerous N–H···N and N–H···X HBs (Table S5, ESI†). Symmetry lowering also enhances the intermolecular interaction, affecting the single octahedra, as expressed in higher values of Δ_d and σ^2, and inducing the out-of-plane tilting of octahedral layers with D_{out} ($180 - \theta_{out}$) up to 17.94° (Fig. 2c and Table 1).

In the second region ($1 < x < 2.2$), a PT in the LT regime leads to more complex twinning, resulting in four ferroelastic domains (Fig. S7d, ESI†), with a *mmmF1* symmetry reduction, according to the Aizu notation.[51] Herein, the **LT** phase (**V**) adopts the triclinic $P\bar{1}$ space group (Fig. S11, ESI†). Analogously to **IV**, **V** is the $c' = 2c$ superstructure of **III** with $Z = 8$ and the network of multiple N–H···X and N–H···N HBs (Table S6, ESI†). The lower symmetry of **V** in comparison to **IV** enforces a higher number of inequivalent positions of MHy^+, increasing from 4 to 8. Owing to greater iodine contribution, **V** is characterized by slightly less distorted perovskite layers than in **IV**

Table 1 (Upper) Selected distortion parameters of $MHy_2PbBr_{4-x}I_x$ 2D HOIPs in particular polymorphic phases. (Lower) Comparison with selected analogues from the literature

x	Phase	T (K)	max^a θ_{out} (°)	D_{out} (°)	max Δ_d x 10^{-4}	max σ^2 (deg^2)	Ref.
0	$Pmn2_1$	300	180	0	2.2	18.6	24
0.3	$Pnmm$ (**II**)	380	180	0	1.9	10.3	This work
	$Pnma$ (**III**)	295	180	0	2.6	13.8	
	$P2_1/c$ (**IV**)	100	162.06	17.94	8.7	26.9	
1.1	$Pnma$ (**III**)	295	180	0	2.3	9.9	
	$P\bar{1}$ (**V**)	100	163.46	16.54	5.5	24.6	
3.1	$Pnma(00\gamma)0s0$ (VI)	295	165.55	14.45	1.8	11.1	
4	$Pnmm$	305	180	0	0.02	8.8	26
	$Pccn$	280	166.86	13.14	1.4	11.9	
	$P\bar{1}$	100	166.53	13.47	3.9	18.1	
Other analogues:							
$(C_6H_{10}N_2)_2PbBr_4$	$Pbca$	296	176.06	3.94	2.3	19.2	42
BA_2PbBr_4	$Pbca$	295	180	0	0.1	9.4	43
Tz_2PbBr_4	$C2/c$	298	180	0	0.2	33.6	44
BDA_2PbBr_4	$P\bar{1}$	173	149.43	30.57	0.6	8.8	45
PPr_2PbBr_4	$Pnma$	210	180	0	7.8	20.3	46
$(C_6H_{10}N_2)_2PbI_4$	$Pbca$	296	175.95	4.05	1.7	11.9	42
BA_2PbI_4	$Pbca$	295	180	0	0.1	5.6	47
PhE_2PbI_4	$P\bar{1}$	295	180	0	0.2	2.1	
$(C_6H_7ClN)_2PbI_4$	$P2_1/c$	295	143.53	36.47	0.3	9.6	48
$(C_6H_7BrN)_2PbI_4$	$P2_1/c$	295	144.34	35.66	1.2	8.8	49
BDA_2PbI_4	$C2/c$	295	147.18	32.82	0.05	3.8	45

[a] Maximum distortion parameters are given for the phases containing two or more inequivalent $[PbX_6]^{4-}$ octahedra. θ_{out} – out-of-plane Pb–X–Pb angle. $D_{out} = 180° - \theta_{out}$. Δ_d – bond length distortion. σ^2 – octahedra angle variance. $(C_6H_{10}N_2)$= 3-pyridinylmethylammonium, BA = butylammonium, Tz = 1,2,4-triazolium, BDA = 1,4-butyldiamine, PPr = piperidinium, PhE = phenethylammonium, (C_6H_7ClN) = 4-chloroanilinium, (C_6H_7BrN) = 4-bromoanilinium.

(Table 1). This is in agreement with the fact that undoped MHy_2PbI_4 distinguishes from its Br and Cl analogues by exhibiting the smallest distortion parameters.[26]

In the iodine-dominated region ($x > 2.2$), in the HT zone, a reconstructive transformation leads to a cubic phase with $Pm\bar{3}m$ symmetry (**I**), archetypal for 3D perovskites. The formerly layered substructure transforms into the 3D network of corner-sharing octahedra, while the heavily disordered organic cations are situated within the voids. $MHy_2PbBr_{4-x}I_x$ with $x = 2.5$ was stable enough to collect the diffraction intensities and refine the structure. Fig. S12 (ESI†) presents the reciprocal space reconstruction that corresponds to the cubic phase and crystal structure in phase **I**. The lattice parameter $a = 6.270(3)$ Å at 350 K, which is far closer to the one for $MAPbI_3$ (6.315(3) Å at 350 K)[52] than for $MHyPbBr_3$ (6.035(3) Å at 430 K),[7] confirms a dominant concentration of iodide in the crystal composition. The presence of the cubic 3D phase in $MHy_2PbBr_{1.5}I_{2.5}$ sheds light on the problem of stabilization of the 3D lead iodide perovskite comprising MHy^+,[36,53] providing a solution through the incorporation of bromine, also reported before for the FA-based compounds.[54] The reconstructive 2D to 3D transition was also observed for other $MHy_2PbBr_{4-x}I_x$ single crystals, after cooling down to RT from 420 K (400 K) for $x = 0.3$ (1.1). However, owing to poor thermal stability only preliminary experiments were conducted. The powder diffractograms of $MHy_2PbBr_{3.7}I_{0.3}$ collected after heating at different temperatures are presented in Fig. S13 (ESI†). The 3D perovskite structure (with $a = 5.992(3)$ Å) was recorded at RT, preceded by heating to 420 K.

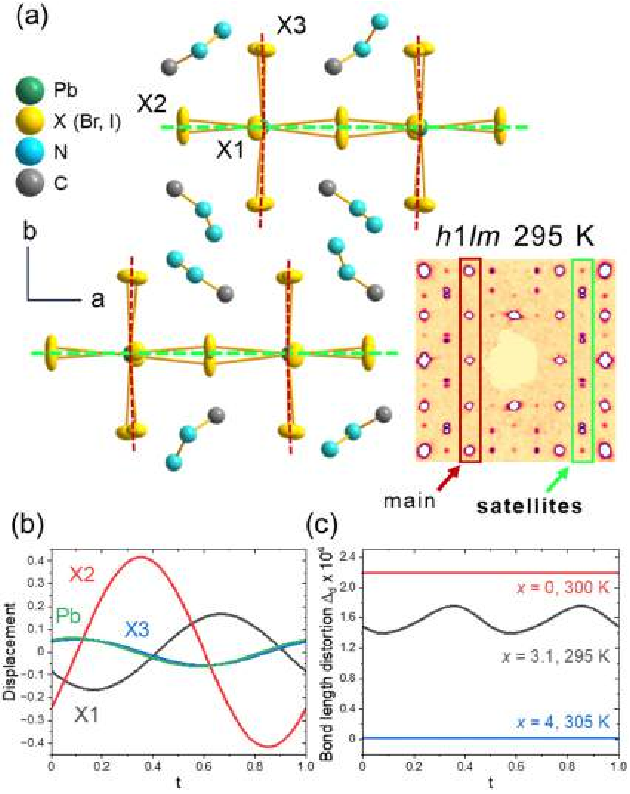

Fig. 3 $MHy_2PbBr_{0.9}I_{3.1}$ in the incommensurately modulated phase **VI**. (a) Snapshot at the phase of the modulation $t = 0.8$ and reciprocal space reconstruction of the *h*0*lm* layer at 295 K. Dashed lines represent coordinates of X1 (green) and X3 (red) in the averaged structure. (b) Displacement curves of independent Pb and X atoms along [010] direction and (c) bond length distortion (Δ_d) as a function of t. Δ_d values are compared with the single-halide analogues in $Pmn2_1$ ($x = 0$) and *Pmmn* ($x = 4$) phase, respectively.

For $x > 2.2$, $MHy_2PbBr_{4-x}I_x$ crystallise in the orthorhombic symmetry with the mean crystal structure and metrics of phase **III**. However, the satellite reflections in the diffraction patterns (Fig. S7e and f, ESI†) indicate that this phase (**VI**) is incommensurately modulated, with $\mathbf{q}^* = \gamma\mathbf{c}^*$. Modulation vector $\mathbf{q}^*$ does not depend on the temperature, nonetheless decreases along with augmenting iodine concentration (from 0.46 to 0.44 for $2.35 \leq x \leq 3.1$). According to the systematic absences, **VI** is described in the $Pnma(00\gamma)0s0$ superspace group. The modulation is associated with the positional displacement of all atoms along the [010] direction. In the case of the inorganic part, the highest amplitude of displacement was observed for the halides at the X2 site (Fig. 3 and Fig. S14, ESI†). Bearing in mind that both X1 and X3 sites act as proton acceptors in N–H···X HBs, bromines are more preferred at these positions. Consequently, X2 is almost fully occupied by iodine (Fig. 4a), being less affected by the intermolecular forces and therefore more prone to displacements. In the case of octahedra distortion parameters – Δ_d takes values between 1.4×10^{-4} and 1.8×10^{-4}, being within the range of single-halide analogues (Fig. 2c), while σ^2 (7.1–11.1 deg^2) oscillates around the value reported for MHy_2PbI_4 (Fig. S15, ESI†).[24,26] In contradiction to **III**, the octahedral layers exhibit tilting, reaching a maximum D_{out} of 14.45°, moderately lower than in **IV** and **V** (Table 1). Another difference in relation to **III** is the dynamics of MHy^+ cations, as in the modulated phase, the MHy^+ is ordered, which is also confirmed by the lack of PT on cooling.

The impact of the halides substitution on selected geometric parameters of $MHy_2PbBr_{4-x}I_x$ is presented in Fig. 4. First of all,

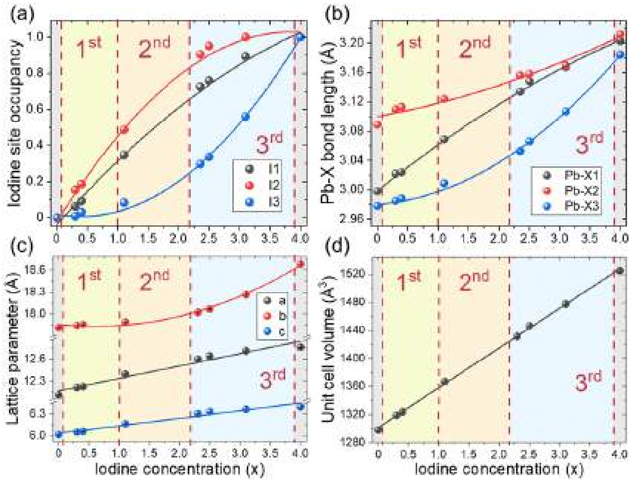

Fig. 4 Geometric parameters of $MHy_2PbBr_{4-x}I_x$ *versus* iodine concentration (x): (a) Iodine site occupancy in *Pnma* symmetry, (b) Pb–X bond length (X = Br, I), (c) lattice parameters and (d) unit cell volume. Values for the samples in the 3rd region are provided for the averaged structure of **VI**.

a site occupancy of the halides is non-uniform, as the iodine preferentially located on the bridging X2 site (Fig. 4a) which is not involved in the HBs interactions. For the $x > 2.2$ region, iodine occupancy at X2 is close to 1. Preferential occupation of certain sites by different anions has been recently reported for $(PEA)_2Pb(Br_xI_{1-x})_4$, $(t\text{-}BA)_2PbBr_2I_2$ and bilayer $(BA)_2MAPb_2(Br_xI_{1-x})_7$ RP perovskites (*t*-BA = *tert*-butylammonium).[55–57] Second, the growing iodine concentration leads to an expansion in Pb–X distances (Fig. 4b), which directly translates into an increase in lattice parameters. A linear unit cell volume vs x satisfies Vegard's law (Fig. 4c and d).[58] However, the preferential occupancy of the X2 bridging position by iodine for low x concentrations does not lead to significant changes in the distances between perovskite layers. Lattice parameter b, perpendicular to the layers, barely changes for $0 \leq x \leq 2.2$. It expands with the boost of iodine occupancy at the apical X3 site, which experiences a huge increase at high x values. It is also worth noting that high levels of iodine concentration suppress the octahedra deformation (Fig. S16, ESI†). The thermal equilibrium of crystal phases is affected as well, leading to the LT structures of different symmetry and stabilization of phases of lower translational symmetry at similar temperatures. Lastly, when all RT structures are juxtaposed with the single-halide analogues (Fig. 1b), one may find the relationship between the lattice parameters *versus* iodine concentration. Starting from the smallest x, a doubling of a direction occurs, while with arising x in phase **VI**, the modulation vector tends to $0.33c^*$ - the value corresponding to the $3c$ supercell, characteristic for the RT phase of MHy_2PbI_4.[26]

Raman spectroscopy

Raman spectra of $MHy_2PbBr_{4-x}I_x$ are presented in Fig. S3 (ESI†) and the observed wavenumbers listed are in Table S6 (ESI†) together with the assignment based on our previous works on end members, *i.e.*, $x = 0$ and 4 samples.[26,59] Qualitatively, the Raman spectra do not show any significant changes as a function of x, in spite of the fact that the RT symmetry of the phases changes from $Pmn2_1$ for $x = 0$ to three different $Pnma$ structures for $0 < x < 4$.[26,59] This behaviour indicates that MHy^+ cations possess similar hydrogen bonds networks in all these phases at RT. Nevertheless, weak increases in the full width at half maximum (FWHM) of the bands for intermediate compositions are noticeable due to the increasing substitutional disorder. Furthermore, a gradual shift of many bands toward lower wavenumbers occurs with increasing iodine content (see Table S6, ESI†). The strongest downshifts between the two end members are observed for the bands corresponding to skeletal vibrations of MHy^+, *i.e.*, δCNN (by 9 cm^{-1}), ν_sCNN (by 10 cm^{-1}), and ν_{as}CNN (by 13 cm^{-1}), as well as bending and stretching vibrations of both amino groups, *i.e.*, δNH_2 (by 8 cm^{-1}), δNH_2^+ (by 12 cm^{-1}), νNH_2 (by 12 cm^{-1}), and νNH_2^+ (by 9 cm^{-1}). The most sensitive to substitution is the τNH_2 band, which shows a downshift of 15 cm^{-1} when x changes from 0 to 4. This effect can be explained by a gradual increase in the space available to the MHy^+ cation in the inorganic substructure (V/Z). Namely, the value of this parameter for $x = 0$ is equal to 324.5 Å per formula unit (f.u.) at 300 K, while for the iodide analogue, it increases to 382.2 Åf.u.$^{-1}$ at 305 K.[26,59]

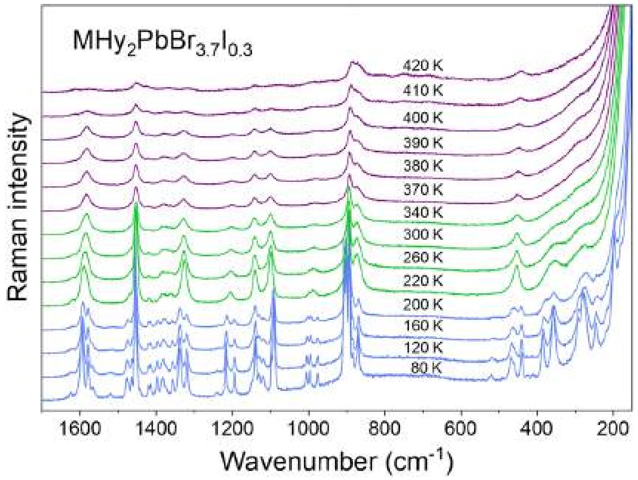

Fig. 5 Thermal evolution of Raman spectra for the $MHy_2PbBr_{3.7}I_{0.3}$ sample.

In order to obtain further insight into mechanisms and structural changes induced by the PTs in the first concentration region, the $x = 0.3$ sample was thoroughly measured by Raman spectroscopy as a function of temperature (see Fig. 5). At 80 K (monoclinic phase **IV**), Raman bands are very narrow (typically below 5–7.5 cm^{-1}, Fig. S17, ESI†), similarly as reported previously for pure MHy_2PbBr_4 ($x = 0$),[59] indicating the freezing of MHy^+ dynamics in the LT phase, where the cations are well-ordered. It is worth noting that many bands, which were observed as singlets at 80 K for pure MHy_2PbBr_4,[59] exhibit large splitting into doublets, triplets or quartets for $x = 0.3$ (Tab. S6 and Fig. 5 and 6). This behaviour is consistent with the XRD data, which revealed only one unique MHy^+ cation in the $Pmn2_1$ phase of MHy_2PbBr_4 and four unique MHy^+ cations in

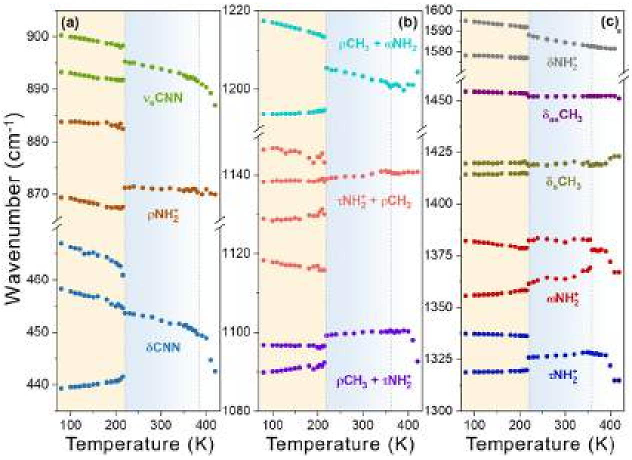

Fig. 6 Position dependence of selected Raman bands as a function of temperature for the $MHy_2PbBr_{3.7}I_{0.3}$ sample.

phase **IV** of the $P2_1/c$ symmetry for $x = 0.3$. On heating, the disappearance of splitting and broadening of Raman bands occurs at 220 K (Fig. 5 and 6). These abrupt changes are congruent with the first-order character of the PT to phase **III**, an increase in symmetry and unlocking of the MHy^+ cation dynamics. Indeed, X-ray diffraction data indicate partial disorder of the MHy^+ cations and the presence of only one crystallographically unique MHy^+ cation in this phase. Further heating causes a gradual and significant decrease in the intensity of the Raman bands to about 360 K, where the PT to phase **II** occurs. This change in intensity is accompanied by a slight broadening of the bands in the 230–355 K range. Similarly to pure MHy_2PbBr_4, the changes in band positions observed during PT at 360 K are almost imperceptible, indicating subtle structural changes.[59] However, the fitting and detailed examination of selected parts of the spectra revealed that a few bands exhibit weak shifts and an increase in FWHM at the PT to phase **II** (Fig. 5 and 6). This behaviour suggests a higher disorder of phase **II** compared to phase **III**.

When heated to about 400 K, slight changes occur suggesting the presence of another PT (Fig. 5 and 6). However, careful examination of the Raman data does not indicate a cubic phase **I**.[7] Both weak signal and large broadening of the bands of $MHy_2PbBr_{3.7}I_{0.3}$ hinder the evaluation of the crystal structure above 400 K using Raman spectroscopy. According to the SXCRD data, for the low iodine concentration ($0 < x < 1$), the 2D → 3D transition was observed above 420 K.

Optical studies

The collation of room-temperature absorption spectra of investigated materials containing various concentrations of iodine ions is presented in Fig. S18a (ESI†). The position of the bands, assigned to the excitonic absorption, shifts towards a higher wavelength as a result of an increase in x value – from 445 nm to 554 nm for 0.3 and 3.1, respectively. The influence of the iodine concentration (x) on the position of the maximum of the excitonic band is presented in Fig. S18b (ESI†). Similar behaviour has been reported recently for halide perovskites containing AZR^+, MHy^+, and IM^+/MHy^+ cations.[10,36,60]

The absorption results have been used to determine the energy band gaps (E_g) using the Kubelka–Munk relation. The values of E_g were estimated with Tauc plots (Fig. S19, ESI†).[61,62] Obtained values vary from 2.91 eV to 2.31 eV for x equal to 0.3 and 3.1, respectively. The influence of iodine concentration on the energy band gap values is presented in Fig. 7. What is more, investigated materials have been assigned to the specific regions according to the division proposed in Fig. 1a. To extend the scope of a subject, values of E_g of two reported materials – MHy_2PbBr_4 ($x = 0$)[24] and MHy_2PbI_4 ($x = 4$)[26] – have been added

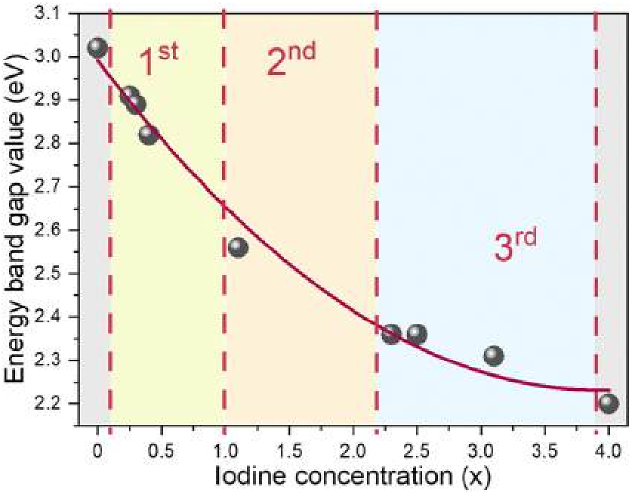

Fig. 7 The influence of the iodine concentration (x) on the value of the energy band gap in $MHy_2PbBr_{4-x}I_x$.

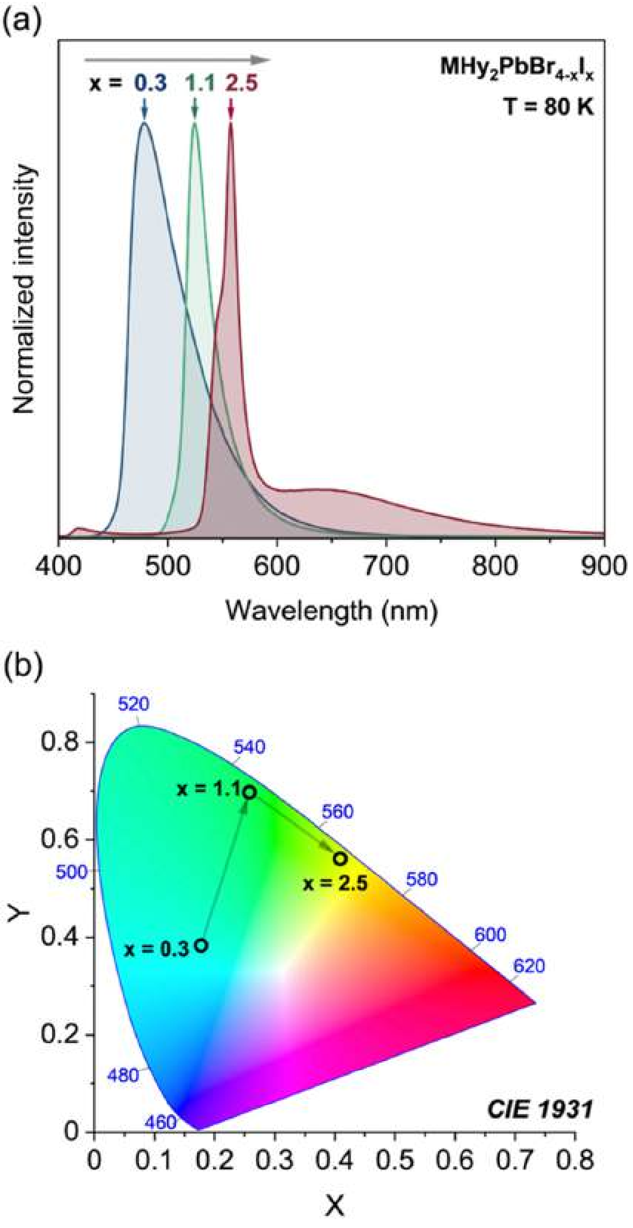

Fig. 8 (a) The normalized emission intensity for representative materials of $MHy_2PbBr_{4-x}I_x$ measured in 80 K, λ_{exc} = 375 nm; (b) CIE chromaticity coordinates of the investigated samples.

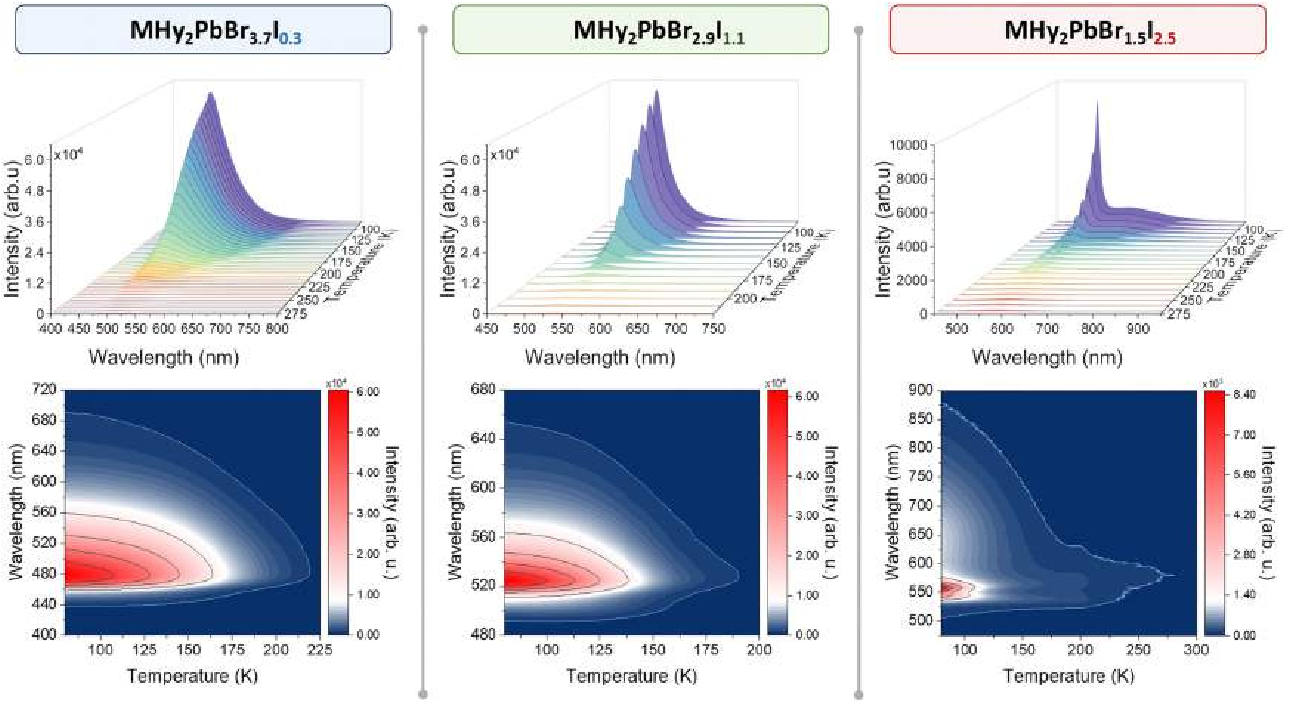

Fig. 9 The collation of temperature-dependent emission spectra and heat map for representative materials containing various iodine concentrations.

to Fig. 7 and Fig. S18b (ESI†). The value of E_g decreases with excess iodine, which increases interatomic distances and reduces octahedral distortion. Analogous relationships have been reported for several halide HOIPs.[10,36,60,63] The reduction in the band gap can be assigned to the smaller distortion of the inorganic substructure.[7,10,63]

The photoluminescence (PL) studies (λ_{exc} = 375 nm) were performed for three representative materials containing various iodine concentrations with x = 0.3; 1.1; 2.5. The LT emission spectra (Fig. 8a) exhibit a pronounced redshift as the iodine concentration increases. The position of the emission maximum varies from 478 nm (x = 0.3), and 524 nm (x = 1.1) to 557 nm (x = 2.5). The composition $MHy_2PbBr_{3.7}I_{0.3}$ exhibits an asymmetric emission band. The presence of an asymmetric luminescence spectrum has been reported for multiple lead halide perovskites and can be attributed to the existence of trap states (bound excitons, BEs) or domains with differing symmetries.[7,10,64] The FWHM is equal to 55.5 nm (0.30 eV), 27.0 nm (0.11 eV), and 21.8 nm (0.09 eV) for x = 0.3, 1.1, and 2.5, respectively. A comparable emission type is observed in the sample with x = 0.3 and 1.1; however, a smaller FWHM suggests a lower presence of trap states in x = 1.1. Unfortunately, for both samples $MHy_2PbBr_{3.7}I_{0.3}$ and $MHy_2PbBr_{2.9}I_{1.1}$, no free exciton (FE) band was observed.

The PL of $MHy_2PbBr_{1.5}I_{2.5}$ stands out from the other samples. It exhibits an intense emission band with a maximum at 557 nm, which is asymmetric, with a faintly outlined band at 546 nm. The position of this hump almost covers the excitonic band at the absorption spectrum. Moreover, the small energy separation between these two maxima and the small FWHM implies that the PL band originates from a superposition of FE and BE emissions. Furthermore, the presence of the additional band with a maximum of around 646 nm, assigned to the self-trapped exciton (STEx) emission, was observed. The coexistence of FE, BE and STEx emission bands has been reported also for $AZRPbCl_3$ and MHy_2PbBr_4.[10,24] PL spectra were used to calculate CIE chromaticity coordinates (Fig. 8b). An increase in iodine concentration leads to a significant change in the observed colour – from bluish-green, *via* yellowish-green (0.259; 0.695) to yellow-green (0.410; 0.559) for x = 0.3, 1,1, and 2.5, respectively.

The temperature-dependent luminescence measurements show a meaningful influence of temperature on the intensities of emission bands (Fig. 9). The increase in temperature induces a progressing decrease in the luminescence intensity, where the most rapid thermal quenching observed for $MHy_2PbBr_{1.5}I_{2.5}$ ($T_{0.5}$ = 94 K). On the other hand, the $T_{0.5}$ values for samples with x = 0.3 and 1.1 are 137 K and 119 K, respectively. The influence of the temperature increment on the change in luminescence intensity is presented in Fig. S20 (ESI†). Materials with x = 0.3 as well as 1.1 do not show a notable change in the shape of the luminescence spectra. However, the sample of $MHy_2PbBr_{1.5}I_{2.5}$ exhibits rapid quenching of the STEx emission. The change in the position of the emission bans due to the temperature increment is not observed. Similar positional stability has been noted for $AZRPbCl_3$ and $IMMHyPbCl_4$.[10,60]

Conclusions

We report the synthesis and comprehensive multi-technique studies investigating the influence of halide mixing on the structural and optical properties of 2D Ruddlesden–Popper Hybrid Organic–Inorganic Perovskites (HOIPs) of the $MHy_2PbBr_{4-x}I_x$ formula (x = 0.25, 0.3, 0.4, 1.1, 2.35, 2.5, 3.1). Crystal structure analysis revealed five crystal phases not observed in the single-halide analogues, including room temperature phases: orthorhombic *Pnma* (**III**) and incommensurately modulated $Pnma(00\gamma)0s0$ (**VI**), with the modulation vector dependent on x; LT phases: monoclinic $P2_1/c$ (**IV**) and triclinic $P\bar{1}$ (**V**); and the 3D archetypal perovskite phase of cubic $Pm\bar{3}m$ prototype symmetry (**I**). The observation of phase **I** represents the first report of 3D HOIPs comprising MHy^+ with a dominant iodine contribution. Geometric analysis across x demonstrated a selective halide site occupancy and a suppression of octahedral deformation and tilting with increasing iodine content. Raman spectroscopy revealed a change in MHy^+ dynamics at RT in mixed-halide compounds compared to single-halide analogues, and freezing of MHy^+ movements at LT, confirming observations from XRD measurements. Optical studies showed a redshift of the RT exciton absorption bands (445 to 554 nm) and a decrease in the energy band gap value from 2.91 eV to 2.31 eV (with increasing x from 0.3 to 3.1). Additionally, a profound change in emission colour (from bluish-green (0.178; 0.380) for $MHy_2PbBr_{3.7}I_{0.3}$ to yellow-green (0.410; 0.559) for $MHy_2PbBr_{1.5}I_{2.5}$) and a shift of PL bands (from 478 nm (x = 0.3) to 557 nm (x = 2.5)) were observed. Building upon previous studies on mixed-halide 3D HOIPs comprising MHy^+, the investigation of 2D analogues demonstrates the facile tuneability of selected physicochemical properties achieved *via* X-site alloying. Furthermore, we elucidate a novel aspect of halide mixing in the MHy-based HOIP family by uncovering new crystal polymorphs and understanding their formation mechanisms.

Author contributions

Conceptualization: D. D. & A. G.; data curation: D. D.; formal analysis, methodology, visualization and writing – original draft: D. D., M. P., A. K.; funding acquisition, project administration and resources: M. M.; supervision: A. G.; D. S.; validation: M. M., M. P., A. G.; D. S; investigation and writing – review & editing: all authors.

Conflicts of interest

There are no conflicts to declare.

Acknowledgements

We acknowledge the support from the National Science Centre (Narodowe Centrum Nauki) in Poland under Project No. 2019/35/B/ST5/00043.

References

1 A. Kojima, K. Teshima, Y. Shirai and T. Miyasaka, *J. Am. Chem. Soc.*, 2009, **131**, 6050–6051.

2 D. B. Mitzi, *Progress in Inorganic Chemistry*, wiley, 1999, vol. 48, pp. 1–121.

3 B. Saparov and D. B. Mitzi, *Chem. Rev.*, 2016, **116**, 4558–4596.

4 T. Yang, L. Gao, J. Lu, C. Ma, Y. Du, P. Wang, Z. Ding, S. Wang, P. Xu, D. Liu, H. Li, X. Chang, J. Fang, W. Tian, Y. Yang, S. Liu and K. Zhao, *Nat. Commun.*, 2023, **14**, 839.

5 L. Protesescu, S. Yakunin, M. I. Bodnarchuk, F. Bertolotti, N. Masciocchi, A. Guagliardi and M. V. Kovalenko, *J. Am. Chem. Soc.*, 2016, **138**, 14202–14205.

6 S. D. Stranks, G. E. Eperon, G. Grancini, C. Menelaou, M. J. P. Alcocer, T. Leijtens, L. M. Herz, A. Petrozza and H. J. Snaith, *Science*, 2013, **342**, 341–344.

7 M. Mączka, M. Ptak, A. Gągor, D. Stefańska, J. K. Zaręba and A. Sieradzki, *Chem. Mater.*, 2020, **32**, 1667–1673.

8 M. Mączka, A. Gagor, J. K. Zaręba, D. Stefańska, M. Drozd, S. Balciunas, M. Šimėnas, J. Banys and A. Sieradzki, *Chem. Mater.*, 2020, **32**, 4072–4082.

9 H. R. Petrosova, O. I. Kucheriv, S. Shova and I. A. Gural'skiy, *Chem. Commun.*, 2022, **58**, 5745–5748.

10 D. Stefańska, M. Ptak and M. Mączka, *Molecules*, 2022, **27**, 7949.

11 M. Mączka, M. Ptak, A. Gągor, J. K. Zaręba, X. Liang, S. Balčiūnas, O. A. Semenikhin, O. I. Kucheriv, I. A. Gural'skiy, S. Shova, A. Walsh, J. Banys and M. Šimėnas, *Chem. Mater.*, 2023, **35**, 9725–9738.

12 C. Elliott, J. A. McNulty, D. B. Cordes, A. M. Z. Slawin and P. Lightfoot, *J. Solid State Chem.*, 2021, **303**, 122466.

13 S. Smółka, M. Mączka, D. Drozdowski, D. Stefańska, A. Gągor, A. Sieradzki, J. K. Zaręba and M. Ptak, *Inorg. Chem.*, 2022, **61**, 15225–15238.

14 A. García-Fernández, E. J. Juarez-Perez, J. M. Bermúdez-García, A. L. Llamas-Saiz, R. Artiaga, J. J. López-Beceiro, M. A. Señarís-Rodríguez, M. Sánchez-Andújar and S. Castro-García, *J. Mater. Chem. C*, 2019, **7**, 10008–10018.

15 S. Shao, M. A. Loi, S. Shao and O. A. L. Photophysics, *Adv. Mater. Interfaces*, 2020, **7**, 1901469.

16 K. Wang, J. Y. Park, Akriti and L. Dou, *EcoMat*, 2021, **3**, e12104.

17 L. N. Quan, B. P. Rand, R. H. Friend, S. G. Mhaisalkar, T. W. Lee and E. H. Sargent, *Chem. Rev.*, 2019, **119**, 7444–7477.

18 M. D. Smith, B. A. Connor and H. I. Karunadasa, *Chem. Rev.*, 2019, **119**, 3104–3139.

19 C. C. Stoumpos, D. H. Cao, D. J. Clark, J. Young, J. M. Rondinelli, J. I. Jang, J. T. Hupp and M. G. Kanatzidis, *Chem. Mater.*, 2016, **28**, 2852–2867.

20 L. Mao, W. Ke, L. Pedesseau, Y. Wu, C. Katan, J. Even, M. R. Wasielewski, C. C. Stoumpos and M. G. Kanatzidis, *J. Am. Chem. Soc.*, 2018, **140**, 3775–3783.

21 C. M. M. Soe, C. C. Stoumpos, M. Kepenekian, B. Traoré, H. Tsai, W. Nie, B. Wang, C. Katan, R. Seshadri, A. D. Mohite, J. Even, T. J. Marks and M. G. Kanatzidis, *J. Am. Chem. Soc.*, 2017, **139**, 16297–16309.

22 S. Ahmad, M. Rahil, P. Rajput and D. Ghosh, *ACS Appl. Electron. Mater.*, 2020, **2**, 3199–3210.

23 Y. H. Chang, J. C. Lin, Y. C. Chen, T. R. Kuo and D. Y. Wang, *Nanoscale Res. Lett.*, 2018, **13**, 1–7.

24 M. Mączka, J. K. Zaręba, A. Gągor, D. Stefańska, M. Ptak, K. Roleder, D. Kajewski, A. Soszyński, K. Fedoruk and A. Sieradzki, *Chem. Mater.*, 2021, **33**, 2331–2342.

25 K. Fedoruk, D. Drozdowski, M. Mączka, J. K. Zaręba, D. Stefańska, A. Gagor and A. Sieradzki, *Inorg. Chem.*, 2022, **61**, 15520–15531.

26 M. Mączka, M. Ptak, A. Gągor, D. Stefańska and A. Sieradzki, *Chem. Mater.*, 2019, **31**, 8563–8575.

27 B. A. Rosales, L. Men, S. D. Cady, M. P. Hanrahan, A. J. Rossini and J. Vela, *Chem. Mater.*, 2016, **28**, 6848–6859.

28 M. Zhang, H. Yu, M. Lyu, Q. Wang, J. H. Yun and L. Wang, *Chem. Commun.*, 2014, **50**, 11727–11730.

29 M. E. A. Madjet, A. V. Akimov, F. El-Mellouhi, G. R. Berdiyorov, S. Ashhab, N. Tabet and S. Kais, *Phys. Chem. Chem. Phys.*, 2016, **18**, 5219–5231.

30 P. Fedeli, F. Gazza, D. Calestani, P. Ferro, T. Besagni, A. Zappettini, G. Calestani, E. Marchi, P. Ceroni and R. Mosca, *J. Phys. Chem. C*, 2015, **119**, 21304–21313.

31 L. Gil-Escrig, A. Miquel-Sempere, M. Sessolo and H. J. Bolink, *J. Phys. Chem. Lett.*, 2015, **6**, 3743–3748.

32 M. Karlsson, Z. Yi, S. Reichert, X. Luo, W. Lin, Z. Zhang, C. Bao, R. Zhang, S. Bai, G. Zheng, P. Teng, L. Duan, Y. Lu, K. Zheng, T. Pullerits, C. Deibel, W. Xu, R. Friend and F. Gao, *Nat. Commun.*, 2021, **12**, 1–10.

33 F. Brivio, C. Caetano and A. Walsh, *J. Phys. Chem. Lett.*, 2016, **7**, 1083–1087.

34 E. Edri, S. Kirmayer, M. Kulbak, G. Hodes and D. Cahen, *J. Phys. Chem. Lett.*, 2014, **5**, 429–433.

35 Y. Hassan, J. H. Park, M. L. Crawford, A. Sadhanala, J. Lee, J. C. Sadighian, E. Mosconi, R. Shivanna, E. Radicchi, M. Jeong, C. Yang, H. Choi, S. H. Park, M. H. Song, F. De Angelis, C. Y. Wong, R. H. Friend, B. R. Lee and H. J. Snaith, *Nature*, 2021, **591**, 72–77.

36 D. Drozdowski, A. Gągor, D. Stefańska, J. K. Zaręba, K. Fedoruk, M. Mączka and A. Sieradzki, *J. Phys. Chem. C*, 2022, **126**, 1600–1610.

37 M. Seitz, M. Meléndez, P. York, D. A. Kurtz, A. J. Magdaleno, N. Alcázar-Cano, A. S. Kshirsagar, M. K. Gangishetty, R. Delgado-Buscalioni, D. N. Congreve and F. Prins, *ACS Energy Lett.*, 2022, **7**, 358–365.

38 O. V. Dolomanov, L. J. Bourhis, R. J. Gildea, J. A. K. Howard and H. Puschmann, *J. Appl. Crystallogr.*, 2009, **42**, 339–341.

39 G. M. Sheldrick, *Acta Crystallogr., Sect. A: Found. Adv.*, 2015, **71**, 3–8.

40 G. M. Sheldrick, *Acta Crystallogr., Sect. C: Struct. Chem.*, 2015, **71**, 3–8.

41 V. Petříček, L. Palatinus, J. Plášil and M. Dušek, *Z. Kristallogr. - Cryst. Mater.*, 2023, **238**, 271–282.

42 C. Lermer, A. Senocrate, I. Moudrakovski, T. Seewald, A. K. Hatz, P. Mayer, F. Pielnhofer, J. A. Jaser, L. Schmidt-Mende, J. Maier and B. V. Lotsch, *Chem. Mater.*, 2018, **30**, 6289–6297.

43 Q. Tu, I. Spanopoulos, E. S. Vasileiadou, X. Li, M. G. Kanatzidis, G. S. Shekhawat and V. P. Dravid, *ACS Appl. Mater. Interfaces*, 2020, **12**, 20440–20447.

44 Y. Y. Guo, L. J. Yang, S. Biberger, J. A. McNulty, T. Li, K. Schötz, F. Panzer and P. Lightfoot, *Inorg. Chem.*, 2020, **59**, 12858–12866.

45 A. Lemmerer and D. G. Billing, *CrystEngComm*, 2012, **14**, 1954–1966.

46 S. Chai, J. Xiong, Y. Zheng, R. Shi and J. Xu, *Dalt. Trans.*, 2020, **49**, 2218–2224.

47 M. Menahem, Z. Dai, S. Aharon, R. Sharma, M. Asher, Y. Diskin-Posner, R. Korobko, A. M. Rappe and O. Yaffe, *ACS Nano*, 2021, **15**, 10153–10162.

48 Z. Liu, W. T. Yu, X. T. Tao, M. H. Jiang, J. X. Yang and L. Wang, *Z. Kristallogr. - New Cryst. Struct.*, 2004, **219**, 489–490.

49 H. Dai, Z. Liu, J. Fan, J. Wang, X. Tao and M. Jiang, *Z. Kristallogr. - New Cryst. Struct.*, 2009, **224**, 149–150.

50 M. E. Fleet, *Mineral. Mag.*, 1976, **40**, 531–533.

51 K. Aizu, *Phys. Rev. B: Solid State*, 1970, **2**, 754.

52 Y. Ren, I. W. H. Ostwald, X. Wang, G. T. McCandless and J. Y. Chan, *Cryst. Growth Des.*, 2016, **16**, 2945–2951.

53 D. Drozdowski, A. Gągor and M. Mączka, *J. Mol. Struct.*, 2022, **1249**, 131660.

54 M. Pratheek, P. Sujith, T. A. Shahul Hameed and P. Predeep, *Mater. Lett.*, 2022, **326**, 132903.

55 N. E. Wright, X. Qin, J. Xu, L. L. Kelly, S. P. Harvey, M. F. Toney, V. Blum and A. D. Stiff-Roberts, *Chem. Mater.*, 2022, **34**, 3109–3122.

56 J. Ovčar, T. L. Leung, L. Grisanti, Ž. Skoko, M. Vrankić, K. H. Low, S. Wang, P. Y. You, H. Ahn, I. Lončarić, A. B. Djurišić and J. Popović, *Chem. Mater.*, 2021, **34**, 42.

57 S. Toso, I. Gushchina, A. G. Oliver, L. Manna and M. Kuno, *ACS Energy Lett.*, 2022, **7**, 4242–4247.

58 L. Vegard and H. Dale, *Z. Kristallogr. - Cryst. Mater.*, 1928, **67**, 239.

59 M. Mączka and M. Ptak, *J. Phys. Chem. C*, 2022, **126**, 7991–7998.

60 D. Drozdowski, K. Fedoruk, A. Kabański, M. Mączka, A. Sieradzki and A. Gągor, *J. Mater. Chem. C*, 2023, **11**, 4907–4915.

61 P. Kubelka and F. Munk, *Z. Techn. Phys.*, 1931, **12**, 593–601.

62 A. Kabański, M. Ptak and D. Stefańska, *ACS Appl. Mater. Interfaces*, 2023, **15**, 7074–7082.

63 Y. Yuan, R. Xu, H. T. Xu, F. Hong, F. Xu and L. J. Wang, *Chin. Phys. B*, 2015, **24**, 1–5.

64 K. Galkowski, A. A. Mitioglu, A. Surrente, Z. Yang, D. K. Maude, P. Kossacki, G. E. Eperon, J. T. W. Wang, H. J. Snaith, P. Plochocka and R. J. Nicholas, *Nanoscale*, 2017, **9**, 3222–3230.

Inorganic Chemistry

pubs.acs.org/IC

Article

[Methylhydrazinium]$_2$PbCl$_4$, a Two-Dimensional Perovskite with Polar and Modulated Phases

Katarzyna Fedoruk, Dawid Drozdowski, Mirosław Maczka,* Jan K. Zareba, Dagmara Stefańska, Anna Gagor, and Adam Sieradzki*

Cite This: *Inorg. Chem.* 2022, 61, 15520−15531

Read Online

ACCESS | Metrics & More | Article Recommendations | Supporting Information

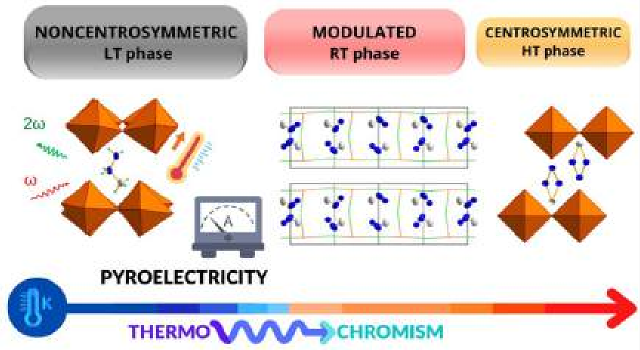

ABSTRACT: Two-dimensional (2D) lead halide perovskites are a family of materials at the heart of solar cell, light-emitting diode, and photodetector technologies. This perspective leads to a number of synthetic efforts toward materials of this class, including those with prescribed polar architectures. The methylhydrazinium (MHy$^+$) cation was recently presumed to have an unusual capacity to generate non-centrosymmetric perovskite phases, despite its intrinsically nonchiral structure. Here, we witness this effect once again in the case of the Ruddlesden−Popper perovskite phase of formula MHy$_2$PbCl$_4$. MHy$_2$PbCl$_4$ features three temperature-dependent crystal phases, with two first-order phase transitions at T_1 = 338.2 K (331.8 K) and T_2 = 224.0 K (205.2 K) observed in the heating (cooling) modes, respectively. Observed transitions involve a transformation from high-temperature orthorhombic phase **I**, with the centrosymmetric space group *Pmmn*, through the room-temperature modulated phase **II**, with the average structure being isostructural to **I**, to the low-temperature monoclinic phase **III**, with non-centrosymmetric space group $P2_1$. The intermediate phase **II** is a rare example of a modulated structure in 2D perovskites, with $Pmmn(00\gamma)s00$ superspace symmetry and modulation vector $\mathbf{q} \cong 0.25\mathbf{c}^*$. MHy$_2$PbCl$_4$ beats the previous record of MHy$_2$PbBr$_4$ in terms of the shortest inorganic interlayer distance in 2D perovskites (8.79 Å at 350 K vs 8.66 Å at 295 K, respectively). The characteristics of phase transitions are explored with differential scanning calorimetry, dielectric, and Raman spectroscopies. The non-centrosymmetry of phase **III** is confirmed with second harmonic generation (SHG) measurements, and polarity is demonstrated by the pyroelectric effect. MHy$_2$PbCl$_4$ also exhibits thermochromism, with the photoluminescence (PL) color changing from purplish-blue at 80 K to bluish-green at 230 K. The demonstration of polar characteristics for one more member of the methylhydrazinium perovskites settles a debate about whether this approach can present value for the crystal engineering of acentric solids similar to that which was recently adopted by a so-called fluorine substitution effect.

1. INTRODUCTION

Considering the unprecedented promise of hybrid organic−inorganic perovskites (HOIPs) for new types of solar cells[1] and other devices, it is an all-important task to have a more in-depth understanding of the connection between structure and properties in this class of compounds. Perhaps in the photovoltaic context, the most publicity has been gained so far by three-dimensional (3D) perovskites, spearheaded primarily by MAPbI$_3$ (MA = methylammonium).[2−5] 3D perovskites feature a general formula of ABX$_3$, where A is an organic or alkali metal cation, B is a divalent metal cation, and X stands for halogen. If A-site cation is organic, it must be small enough to fit into the cubic metal-halide BX$_3^-$ (ReO$_3$-type) network. Essentially, only a handful of organic cations are capable of serving as guests within 3D perovskite lattices, and the title methylhydrazinium (CH$_3$NH$_2$NH$_2^+$, MHy$^+$) is one of them. However, there is virtually unrestricted chemical space of 2D HOIPs and low-dimensional (1D, 0D) structures since in these topologies the steric hindrance of the coordination network does not restrict the size of organic cations anymore. This is so for 2D perovskites, which emerge as structurally more diverse alternatives to their 3D counterparts.[6] Indeed, in addition to changes in organic, metal, and halide components, there is also an opportunity to control the number and thickness of inorganic layers.[7−9] Critical to the functional properties are the physical implications arising from quantum effects associated with reduced dimensionality. The inorganic layers form slabs of 2D-confined quantum structures, and as a consequence, the formed quantum wells are separated by the

Received: June 26, 2022
Published: September 21, 2022

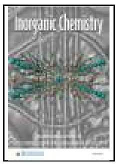

https://doi.org/10.1021/acs.inorgchem.2c02206

organic barriers. The resulting complex electronic structure is sensitive to structural inputs, which can assist in controlling the dielectric and optical properties of these structures.[10−14] Indeed, quantum and dielectric confinement effects in 2D perovskites increase the effective band gap and the exciton binding energy compared to 3D perovskites.[15] For instance, the exciton binding energies increase by more than an order of magnitude from ∼10 meV for 3D perovskites to typically >150 meV for conventional 2D perovskites,[15−18] leading to a radically improved photoluminescence quantum yield (PLQY) for layered analogues.[13,19,20]

It is the innumerable choices of organic components that make possible the tailoring of linear and nonlinear optical (NLO), electrical, and structural properties of perovskites. However, in some cases, simplicity, rather than complexity, yields the most intriguing results. A prime example of that is a small MHy^+ cation, which in its simplistic structure is unique in that it builds up both 2D and 3D lead halides.[21−26] In the case of 2D perovskites such as MHy_2PbBr_4 and MHy_2PbI_4, the small size of this cation translates to a record low separation between inorganic layers (8.91 Å at 300 K and 9.36 Å at 305 K, respectively) and a very small, as for 2D perovskites, estimated exciton binding energy (99.9 and 59.2 meV, respectively).[22,25] Quite an interesting aspect of using the MHy^+ cation for construction of perovskites is the apparent guided assembly of non-centrosymmetric perovskite phases. Indeed, the first 3D perovskite reported, with at least one unequivocally acentric phase was $MHyPbBr_3$,[21] soon after followed by the discovery of $MHyPbCl_3$ with two acentric crystal phases (monoclinic and orthorhombic), verified by pyrocurrent measurements and capable even for unusual temperature switching of a second-order NLO response of SHG-*low*−SHG-*high* type.[23] Mixed-halide analogues $MHyPbBr_3Cl_{(3\text{-}x)}$ mirror the phase behavior of the $MHyPbCl_3$ prototype in that they contain two polar crystal phases, irrespectively of Br content.[24] MHy_2PbBr_4 is ferroelectric at room temperature with orthorhombic $Pmn2_1$ symmetry.[22] Among 2D ($n = 1$) MHy^+-perovskites, only MHy_2PbI_4 does not reveal polar properties;[25] however, it features the unique octahedral tilt system.[6] The ability of MHy^+ to direct non-centrosymmetric structures does not work for the 2D and even low-dimensional iodides.[27] The same applies to other organic cations, such as benzylammonium[28−30] or cyclohexylammonium,[31,32] wherein only chloride or bromide analogues adopt polar phases. It may be possibly explained via weakening of hydrogen bonding (HB) strength with decreasing electronegativity of halides.[33] Thus, the N−H···I HBs are the weakest, and therefore for iodide systems the cations may adopt the most energetically favorable alignment, i.e., without inducing a resultant dipole moment. Polar structure, Cc, was also reported for 2D ($n = 3$) $BA_2MHy_2Pb_3Br_{10}$ perovskite (BA = butylammonium).[26] Accordingly, one sees that there is mounting evidence that the MHy^+ component promotes the formation of non-centrosymmetric phases, which however requires further experimental verification. Of large comparative value would be to explore the properties of unknown halide analogues of extant methylhydrazinium perovskites, one of which is a 2D analogue of formula MHy_2PbCl_4. Indeed, the multitechnique investigation of structural, polar, dielectric, nonlinear, and linear optical properties of all crystal phases of MHy_2PbCl_4 forms the content of the present contribution.

2. MATERIALS AND METHODS

Synthesis. $PbCl_2$ (98%, Sigma-Aldrich), methylhydrazine (98%, Sigma-Aldrich), hydrochloric acid (48 wt % in H_2O, POCH), methyl acetate (99.5%, Sigma-Aldrich), and *N*,*N*-dimethylformamide (DMF, 99.8%) were commercially available and used without further purification. In order to obtain single crystals of MHy_2PbCl_4, a reaction mixture containing 15 mmol of methylhydrazine neutralized with HCl (pH = 7), 5 mmol of $PbCl_2$, and DMF (about 12 mL) was stirred for an hour until the complete dissolution of $PbCl_2$. Then the solution was placed in a glass vial with the lid slightly loosened. This smaller vial was then placed in a second larger glass vial containing methyl acetate with a thoroughly sealed lid. Colorless, plate-like crystals with dimensions of up to 5 mm were harvested after 1 week, filtered from the mother liquid, and dried at RT. A good match of their powder XRD pattern with the calculated one based on the single-crystal data (Figure S1) confirmed the phase purity of the bulk sample. Caution! Methylhydrazine is toxic and must be handled with extreme caution and the appropriate protective gear.

Differential Scanning Calorimetry (DSC). Heat capacity was measured using a Mettler Toledo DSC-1 calorimeter with a high resolution of 0.4 μW. Nitrogen was used as a purging gas, and the heating and cooling rate was 5 K min^{-1}. The mass of the measured sample was 26.88 mg. The excess heat capacity associated with the PT was calculated by subtracting from the data a baseline representing the system variation in the absence of the PTs.

Single-Crystal X-ray Diffraction (SCXRD). SCXRD experiments were carried out using an Xcalibur four-circle diffractometer (Oxford Diffraction) with an Atlas CCD detector and graphite-monochromated Mo Kα radiation. Absorption was corrected by multiscan methods using CrysAlis PRO 1.171.41.93a (Rigaku Oxford Diffraction, 2020). Empirical absorption correction using spherical harmonics, implemented in the SCALE3 ABSPACK scaling algorithm, was applied. For all structures, H atom parameters were constrained. The crystal structures of phases **I** and **III**, and the average structure of phase **II** were solved in Olex2 1.5[34] using *SHELXT*.[35] Phases **I** and **III** were refined with *SHELXL*.[36] Refinement of modulated phase **II** was performed using *Jana2020*.[37] Experimental and refinement details for all phases are summarized in Table S1. Refinement of **I** ($Pmmn$ with $a = 5.7902(1)$, $b = 17.5814(6)$, $c = 5.8657(1)$ Å, $V = 597.13(3)$ Å^3, and $Z = 2$) converged to refinement factors $R_1 = 0.02$, $wR_2 = 0.04$, and $S = 1.13$. Phase **III** ($P2_1$ with $a = 11.6588(5)$, $b = 17.0423(6)$, $c = 12.7453(6)$ Å, $\beta = 114.16(1)°$, $V = 2310.65(6)$ Å^3 and $Z = 8$) was treated as a two-domain twin. Refinement converged to $R_1 = 0.06$, $wR_2 = 0.17$, and $S = 1.02$.

The refinement of modulated phase **II** requires a broader comment. As the satellite reflections appear along c^* in ca. one-fourth of the distance between the main reflections (Figure S2), one may treat this phase as a supercell of **I** with a four-fold multiplication of the c parameter. However, systematic absences of satellite peaks do not meet the extinction rules known for 3D space groups. Therefore, the (3 + 1) superspace approach was applied. The studied structure was refined in the $Pmmn(00\gamma)s00$ superspace group with modulation vector $\mathbf{q} \cong 0.25\mathbf{c}^*$ (Figure S3).[38] The refinement of the modulation waves started with the inorganic part. Based on Fourier maps (Figure S4), all of the Pb and Cl atoms were modulated with the assumption of a positional modulation using first-order harmonics. Later, the same approach was applied to the C1 and the terminal N2 atom of MHy^+, as derived from Fourier maps for MHy^+ (Figure S5). All of the positional modulation waves were treated as one-dimensional, i.e., propagating along the a direction. In the case of the N1 atom, a more accurate refinement was obtained when the occupational modulation was adopted. The occupancy of N1 was modulated with a crenel function with $\Delta x_4 = 0.5$, and the positional modulation functions were described as harmonics in the interval (0,1). Finally, hydrogen atoms were inserted from geometry and refined as riding atoms with $U_{iso} = 1.2U_{iso}$ of the maternal atom. The final R factors are $R_1 = 0.02$ (0.09) and $wR_2 = 0.03$ (0.12) for main reflections (satellites). The displacement of independent Pb and Cl atoms along the a direction as a function of the phase of the modulation t is shown in Figure S6a.

Cl2 demonstrates the highest displacement amplitude of ~0.20, which is greater than for Cl3 (~0.15) and for both Pb1 and Cl1 (~0.07). These displacements reveal variations of Pb−Cl bond lengths (Figure S6b) and Cl−Pb−Cl angles (Figure S6c). It is worth noting here that both from the symmetry relations and from the atomic positions of Pb and Cl atoms the 4c approximant structure of *Pcmn* symmetry is imposed for the II phase (*Pnma* in the standard setting). However, in the 4c superstructure of *Pcmn* symmetry, the amines are disordered over the *m* mirror plane, with two equally occupied positions. Thus, the conventional space group does not resolve the ordering of amines.

Raman Studies. Temperature-dependent Raman spectra were obtained in the 300−5 cm^{-1} range using a Renishaw InVia Raman spectrometer equipped with a confocal DM 2500 Leica optical microscope, a thermoelectrically cooled CCD as a detector, and an eclipse filter. The excitation was performed using a diode laser operating at 830 nm, and the temperature was controlled using a Linkam cryostat cell. The spectral resolution was 2 cm^{-1}.

Electrical Measurements. Dielectric measurements of the examined samples were carried out using a broadband impedance Novocontrol Alpha analyzer. Electric field-dependent polarization measurements were performed on a single-crystal sample of size 0.4 × 1 × 1 mm^3. The silver paste was used to ensure good electrical contact. A sinusoidal voltage with an amplitude of 1 V and a frequency in the range of 1 Hz to 1 MHz was applied across the sample. The studies were performed at quasi-static conditions in the temperature range of 150−360 K. The temperature was stabilized using nitrogen gas using the Novocontrol Quattro system. A pyrocurrent measurement was made on a single crystal with silver electrical contact. The crystal was cooled down to 150 K. During cooling, an electric poling field of 200 V/mm was applied. At 150 K, the sample electrodes were shorted for 10 min. Current measurements were performed using a Keithley 6514 electrometer during the heating of the sample from 150 to 300 K with a heating rate of 2 K/min. An aixACCT instrument was used to study the electric field-dependent electric polarization. A periodic triangular signal was used for the measurements. A high voltage was obtained using a Trek 609E6 voltage amplifier. Measurement of the polarization vs field (*P*−*E*) was carried out with a Precision Premier II Ferroelectric tester. The electrodes of conductive silver paste were placed on a single crystal with an area of 0.0226 cm^2 and a thickness of 345 μm. The measurement was made at a temperature of 180 K. The cooling gas was nitrogen. A maximum voltage of 500 V and frequency of 10^2 Hz were applied across the sample, and the data were recorded with the Virtual software.

SHG Studies. Temperature-resolved SHG studies and Kurtz-Perry powder test were performed using a laser system employing a wavelength-tunable Topaz Prime Vis-NIR optical parametric amplifier (OPA) pumped by a Coherent Astrella Ti:sapphire regenerative amplifier providing femtosecond laser pulses (800 nm, 75 fs) at a 1 kHz repetition rate. The output of OPA was set to 1300 nm and was used unfocused. The laser fluence at samples was equal to 0.17 mJ/cm^2. The single crystals of MHy_2PbCl_4 were crushed with a spatula and sieved through an Aldrich mini-sieve set, collecting a microcrystal size fraction of 125−177 μm. Next, size-graded samples were fixed in-between microscope glass slides to form tightly packed layers, sealed, and mounted to the horizontally aligned sample holder. No refractive index matching oil was used. The employed measurement setup operates in the reflection mode. Specifically, the laser beam delivered from OPA was directed onto the sample at 45 deg to its surface. Emission collecting optics consisted of a Ø25.0 mm plano-convex lens of focal length 25.4 mm mounted to the 400 μm 0.22 NA glass optical fiber and was placed along the normal to the sample surface. The distance between the collection lens and the sample was equal to 30 mm. The spectra of the NLO responses were recorded by an Ocean Optics Flame T fiber-coupled CCD spectrograph with a 200 μm entrance slit. Scattered pumping radiation was suppressed with the use of a Thorlabs 750 nm short-pass dielectric filter (FESH0750). Temperature control of the sample was performed using a Linkam LTS420 heating/freezing stage. Temperature stability was equal to 0.1 K. A Kurtz−Perry test was performed by comparing the integral SHG intensity of MHy_2PbCl_4 (measured at 160 K) to that of potassium dihydrogen phosphate (KDP) of the same particle size distribution. The same optical setup and laser beam parameters were employed for temperature-resolved studies.

One-Photon Absorption and Photoluminescence Studies. The RT absorption spectrum of the powdered sample was measured using a Varian Cary 5E UV−vis−NIR spectrophotometer. Emission spectra at various temperatures under 266 nm excitation provided by a diode laser were measured with the Hamamatsu photonic multichannel analyzer PMA-12 equipped with a BT-CCD linear image sensor. The temperature of the single-crystal sample was controlled using a Linkam THMS 600 heating/freezing stage. To record decay times, a femtosecond laser (Coherent Model Libra) was used as an excitation source.

3. RESULTS AND DISCUSSION

DSC. The performed calorimetric scans showed two reversible PTs at T_1 = 338.2 K (331.8 K) and T_2 = 224.0 K (205.2 K) visible in the heating (cooling) mode (Figure 1 and Figure S7). The symmetrical, strong peaks seen in ΔC_p plotted as a function of temperature, in combination with the thermal hysteresis between heating and cooling cycles, indicate the first-order type of PTs. This is also confirmed by the accompanying discontinuous change in the entropy (ΔS) (see inset in Figure 1b). The changes of entropy (ΔS) were estimated to be 0.38 J mol^{-1} K^{-1} (0.82 J mol^{-1} K^{-1}) for the PT at T_1 and 4.56 J mol^{-1} K^{-1} (3.33 J mol^{-1} K^{-1}) for the PT at T_2 in the heating (cooling) mode, respectively. The symmetry reduction during the transition from HT to modulated phase results in moderate entropy changes. A significantly higher value of ΔS at the second PT is associated with symmetry breaking from modulated orthorhombic to monoclinic (see SCXRD studies). Furthermore, the overall change of ΔS in MHy_2PbCl_4 is much greater than that reported recently for the MHy_2PbI_4 (~2.88 J mol^{-1} K^{-1}) and MHy_2PbBr_4 (~1.66 J mol^{-1} K^{-1}) analogues.[22,25] Because this material undergoes a first-order PT, its pressure dependence can be calculated using the indirect Clausius−Clapeyron method and the equation: $\frac{dT_2}{dp} = \frac{2\left(\frac{\Delta V}{V}\right)}{\Delta H_{molar}} V_{molar}$, where T_2 is the PT temperature, ΔH_{molar} (~1046 J mol^{-1}) represents the change in the molar enthalpy, estimated from calorimetric studies, $\Delta V/V$ (~1.8 × 10^{-2}) is the relative volume change at T_2, and V_{molar} (~1.75 × 10^{-4} m^3

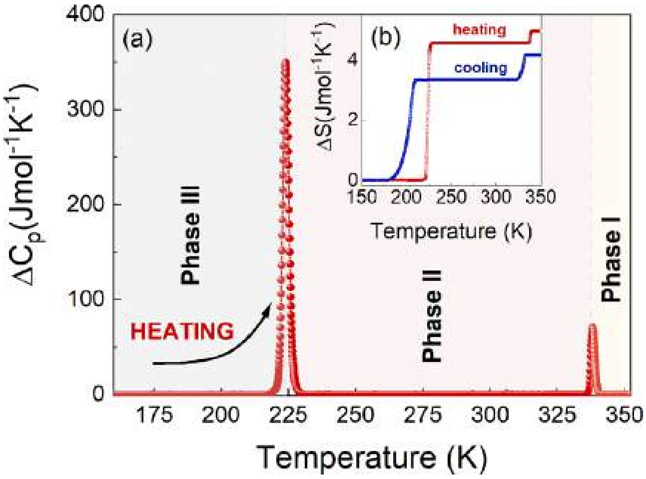

Figure 1. Changes in (a) C_p and (b) S related to the PT in the heating (red) and cooling (blue) runs.

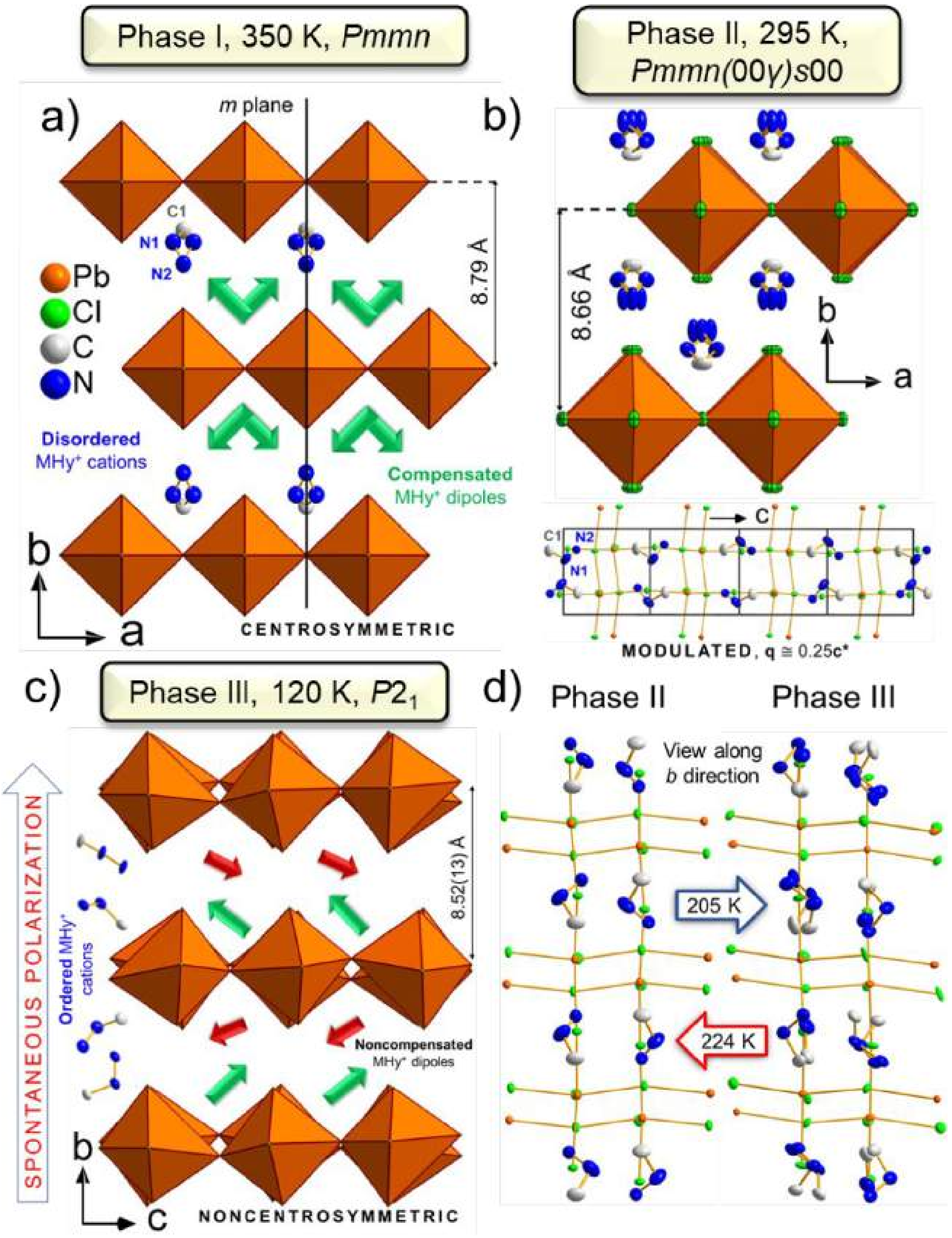

Figure 2. Details of the MHy_2PbCl_4 crystal structure in subsequent phases. (a) HT phase **I**, (b) 4-fold approximant of the modulated phase **II**, and (c) LT phase **III**. (d) Comparison of the atomic alignment in **II** and **III** along the [010] direction. The green and red arrows in (a, c) represent locations of the MHy^+ dipoles.

mol^{-1}) is the molar unit cell volume (structural data were taken from X-ray diffraction results described below). From the obtained data, the following pressure dependence of T_2 was calculated: $\frac{dT_2}{dp} = 64.7 \pm 0.3K\ kbar^{-1}$. The obtained results prove that this compound is an interesting material sensitive to both pressure and temperature changes. The obtained value is one order of magnitude higher than that for $[(CH_3CH_2CH_2)_4N][Mn(N(CN)_2)_3]$,[39] and two orders of magnitude higher than those for $(NH_4)MF_3$ perovskites (M = Mn, Co, Cd, Mg, and Zn).[40]

Single-Crystal X-ray Diffraction. MHy_2PbCl_4 adopts three temperature-controlled crystal phases. High-temperature (HT) phase **I** possesses the orthorhombic, centrosymmetric *Pmmn* space group. RT phase **II** adopts averaged structure isostructural to **I**; however, as derived from the diffraction pattern (Figure S3), it is a modulated structure with $Pmmn(00\gamma)s00$ superspace symmetry and vector $\mathbf{q} \cong 0.25\mathbf{c}^*$.[38] Low-temperature (LT) phase **III** is monoclinic with $P2_1$ symmetry. Given that this phase is polar, the second-order NLO effects can be expected, e.g., SHG (*vide infra*).

HT phase **I** is isostructural to the previously reported HT phases of the MHy_2PbI_4 and MHy_2PbBr_4 2D analogues.[22,25] The motif of **I** (Figure 2a) is composed of the corner-sharing $[PbCl_6]^{4-}$ octahedra forming (010) layers, separated by MHy^+ cations, which protrude out of the *m* mirror plane. Hence, the N1 atom is split into two equivalent positions with equal probability. The distance between the octahedra layers is equal to 8.79 Å.

The Pb1 coordination sphere consists of the Cl1 and Cl2 atoms (bridging along the *a* and *c* directions, respectively), and

Table 1. Distortion Parameters of the MHy_2PbCl_4 Perovskite in the Subsequent Polymorphic Phases

phase	T (K)	Pb−Cl−Pb direction	∠Pb−Cl−Pb (deg)	*a.d.* (deg)	D_{out} (deg)	max[a] $\Delta_d \times 10^{-3}$	max[a] σ^2 (deg^2)
I	350	[100]	168.27(1)	11.7	0	1.6	14.4
		[001]	180	0	0		
II[b]	295	[100]	165.78(1)	14.2	0	1.7	24.7
		[001]	172.34(1)	7.7	0		
III	120	[100]	166.1(5)	13.9	6.1	3.4	61.4
		[001][c]	160.9(5)	2.1	19.1		

[a] Maximum distortion parameters are provided due to the existence of four inequivalent $[PbCl_6]^{4-}$ octahedra in phase **III**. [b] Distortion parameters are given for modulated phase **II**. [c] The direction maintained from the axis setting of phases **I** and **II**. *a.d.* = 180 − $\angle_{Pb-Cl-Pb}$ along [100] and [001] directions; D_{out} = 180 − $\angle_{Pb-Cl-Pb}$ along [010]; Δ_d − bond length distortion; σ^2 − octahedral angle variance.[41]

the apical Cl3 atom. The individual octahedron is of C_{2v} symmetry with *mm*2 site symmetry for Pb1, Cl1, and Cl3, and *m*.. for Cl2. Pb−Cl distances vary from 2.74 to 3.12 Å. The difference between the longest and shortest Pb−Cl distances (0.38 Å) is relatively higher than the ones reported for the Br- and I- analogues (0.02 and 0.14 Å for the HT phases of MHy_2PbI_4 and MHy_2PbBr_4, respectively),[22,25] pointing to the higher octahedral distortion in the structure described herein. Indeed, both the bond length distortion (Δ_d) and octahedral angle variance (σ^2) values (Table 1) are 1.6×10^{-3} and $14.4^{\circ 2}$, which is greater than for MHy_2PbI_4 (6.8×10^{-6} and $5.6^{\circ 2}$) and MHy_2PbBr_4 (2.1×10^{-4} and $11.3^{\circ 2}$).[22,25] This distortion results in a decrease of the Pb−Cl−Pb angle along the [100] direction, and its value defined as *Def* = 180° − $\angle_{Pb-Cl-Pb}$ is the highest (*a.d.* = 11.7°) among the MHy_2PbX_4 (X = Cl, Br, I) perovskites (where *a.d.* = 9.3° and 10.7° for I and Br, respectively).[22,25] Observation of the octahedra distortion is strictly connected with intermolecular interactions between the perovskite layers and MHy^+ cations. However, the interlayer MHy^+ cation alignment in 2D perovskites diminishes the strength of these interactions when compared to their 3D counterparts. It is noticeable, for instance, in max. σ^2 values $-301^{\circ 2}$ ($314^{\circ 2}$) for $MHyPbBr_3$ ($MHyPbCl_3$).[23,24] Despite relatively weak intermolecular forces, several N−H···Cl hydrogen bonds (HBs) are formed with both N atoms as donors and the Cl1 and Cl3 atoms as acceptors (Table S2).

Lowering the temperature induces **I** → **II** PT. The effect of the unit-cell contraction as the temperature decreases leads to the reduction of the interlayer distance to approximately 8.66 Å. While the average structure of **II** is isostructural to **I**, satellite diffraction peaks along the **c*** direction appear in the diffraction pattern (Figure S2). As derived from the systematic absences (see caption to Figure S3), the (3 + 1)-dimensional superspace group of **II** is $Pmmn(00\gamma)s00$ with the modulation vector $\mathbf{q} \cong 0.25\mathbf{c}^*$. The 4-fold approximant of **II** is presented in Figure 2b. As compared to **I**, the atoms of the inorganic part slightly lean out of the mirror plane toward the [100] direction (Figure S8). This behavior brings consequences to the distortions of the perovskite layers. To start with, the change of the Pb−Cl−Pb angle along [001] appears with *a.d.* = 7.7°. Simultaneously, the maximum *a.d.* alongside [100] increases to 14.2°. Additionally, both Δ_d and σ^2 values increase to 1.73×10^{-3} and $24.7^{\circ 2}$, respectively (Table 1, Figure S9a,b). In the case of the organic part, the MHy^+ cation in **II** is ordered, and its distribution in the structure is governed by the additional translation component of the superspace group (intrinsic phase shift of 1/2) associated with the 2-fold axis (lower part of Figure 2b). This new configuration of amines is associated with the appearance of N−H···N and N−H···Cl HBs. However, the juxtaposition of distances between N atoms of neighboring MHy^+ as a function of the phase of the modulation *t* (Figure S9c) indicates that in **II** there are NH_2 groups that are not involved in hydrogen bonding. There is no N−H···Cl or N−H···N stable HBs network along the [001] direction (Figure S10a).

With further temperature lowering, the shrinking of interatomic distances strengthens the interactions between inorganic and organic constituents and eventually leads to the formation of a new phase with a stable configuration of HBs. Indeed, such a phase appears at 205.2 K (224.0 K) on cooling (heating). The LT phase **III** is monoclinic with a $P2_1$ polar space group and β = 114.16(1)° with an asymmetric unit consisting of 4 lead cations, 16 chloride anions, and 8 ordered MHy^+ cations (Figure S11). The main details of **III** are shown in Figure 2c and compared to modulated phase **II** in Figure 2d. Unlike the HT and RT phases, in **III**, certain MHy^+ cations are spontaneously rotated. From the viewpoint of polar characteristics, MHy^+ dipoles are no longer compensated. Instead, spontaneous polarization along the [010] direction occurs. Furthermore, due to the reduced interlayer gap of 8.52(13) Å, numerous HBs are formed (Table S3). One may distinguish two kinds of HBs. The first kind is N−H···Cl with N atoms acting as donors and Cl atoms (mainly apical) as acceptors. Contrarily to **II**, these HBs create the network alongside both directions of propagation of the octahedra (Figure S10b). The second kind of HBs is N−H···N, where both N atoms may serve as donors and acceptors for the hydrogen atoms. As the **II** → **III** PT is associated with symmetry reduction, all atoms in the unit cell adopt a general C_1 site. The synergistic effect of strengthened intermolecular interactions and the symmetry reduction remarkably influences the shape of the perovskite layers. Besides the in-plane Pb−Cl−Pb angle deformation (max. *a.d.* = 13.9°), the out-of-plane octahedra tilting is observed with the D_{out} value of 19.1°. At the same time, the octahedra distortion parameters significantly increase (Δ_d = 3.4×10^{-3} and σ^2 = $61.4^{\circ 2}$, Table 1). Lastly, the **II** → **III** PT provokes a step change in lattice parameters (Figure S12a) and an enlargement of a unit cell volume (Figure S12b).

In this paragraph, a wider comment is provided on the interlayer distances in the reported compound. As indicated above, the gap between perovskite layers decreases in the order **I** → **II** → **III** (8.79, 8.66, and 8.52 Å, respectively). It is worth noting that such small values were not recorded before in the 2D lead chloride perovskites with $[PbCl_6]^{4-}$ monolayers (Table S4). At the same time, MHy^+ is the smallest organic cation among the listed ones. This observation agrees with the hypothesis provided in our previous paper concerning the MHy_2PbBr_4 analogue,[21] that the MHy^+ cation is a key component developing 2D hybrid perovskites with a record-breaking low layer separation.

Raman Studies. In order to obtain further insight into the mechanism of the PTs and lattice dynamics, temperature-dependent Raman studies were performed on MHy_2PbCl_4 single crystals in the low-wavenumber range of 300−5 cm^{-1} (Figure 3). The observed Raman modes are tabulated in Table S5. According to previous studies of layered perovskites, PEA_2PbBr_4 and BA_2PbBr_4 (PEA = phenylethylammonium; BA = butylammonium) Raman spectra in the low-wavenumber range consist of five ranges. The lowest wavenumber narrow bands, which do not exhibit any splitting at LT, correspond to the octahedra rocking/twisting that could be alternatively assigned to $PbBr_6$ librational modes.[42] These modes were observed at near 27 and 22 cm^{-1} for PEA_2PbBr_4 and BA_2PbBr_4, respectively.[42] Raman spectra of MHy_2PbCl_4 show such narrow modes at 24 and 29 cm^{-1} (values at 80 K, Table S5). The corresponding modes of MHy_2PbBr_4 and MHy_2PbI_4 were observed at 23 and 17 cm^{-1}, respectively.[25,43] As can be seen, these modes shift weakly to higher wavenumbers with the decreasing size of the halide anion. The most intense Raman bands (weak bands), observed for PEA_2PbBr_4 and BA_2PbBr_4 in the 80−35 cm^{-1} range (140−83 cm^{-1} range), were attributed to Pb−Br bond bending modes (Pb−Br bond stretching modes).[25] These broad bands at RT exhibited splitting into many components at LT.[25] For the HT phase of MHy_2PbCl_4, Pb−Cl bending and stretching modes are located in the 105−54 and 186−164 cm^{-1}, respectively (Table S5). It is worth noting that these bands exhibit a very pronounced shift to lower wavenumbers with the increasing size of the halide anions, i.e., to 47−45 and 137−116 cm^{-1} for MHy_2PbBr_4 and 34−27 and 120−97 cm^{-1} for MHy_2PbI_4.[25,43]

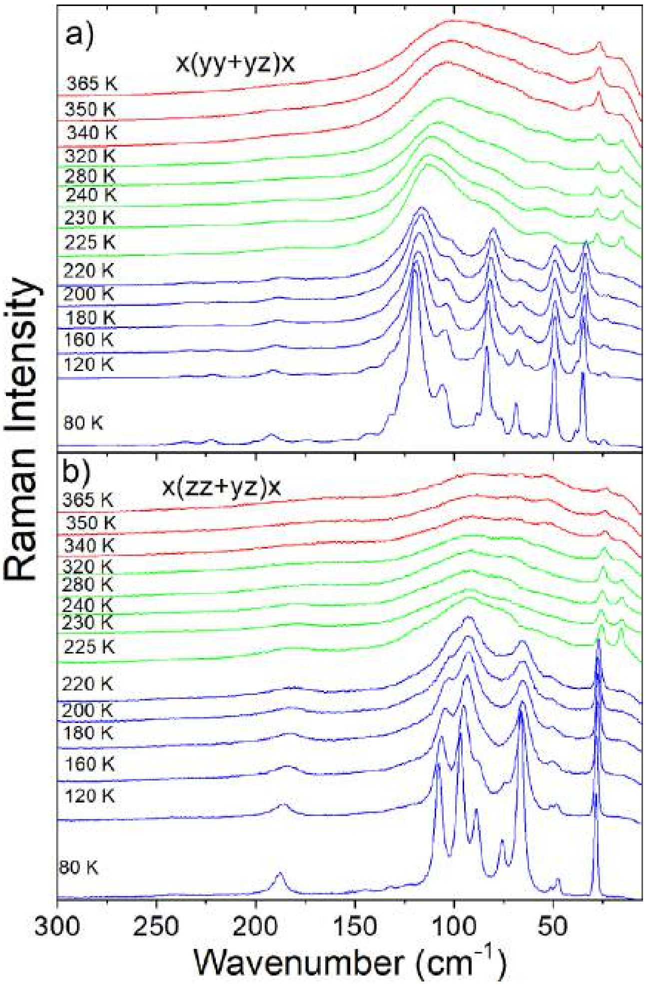

Figure 3. Temperature-dependent Raman spectra of MHy_2PbCl_4 crystals in a heating run for (a) $x(yy + yz)x$ and (b) $x(zz + yz)x$ polarization. Red, green, and blue colors correspond to the *Pmmn* phase **I**, modulated phase **II**, and $P2_1$ phase **III**, respectively.

According to the X-ray diffraction studies, MHy^+ cations are disordered in phase **I** and ordered in phase **II**. One would expect, therefore, to observe a significant narrowing of bands at the PT temperature. As can be noticed, Raman bands exhibit a rather weak narrowing at T_1 (see Figure 3). Interestingly, very similar behavior was also reported for MHy_2PbBr_4.[43] Thus, in both analogues, the dynamics of MHy^+ cations does not exhibit a sudden change at the PT temperature. Nevertheless, the PT leads to some changes in the intensity of Raman modes. For instance, a new $L(PbCl_6)$ band appears at 16 cm^{-1}, and in the $x(zz+yz)x$ polarization intensity of the 54 cm^{-1} band drastically decreases (Figure 3). However, the observed changes at T_1 are weak, providing a spectroscopic argument for the significant crystallographic similarity of phases **I** and **II**.

On further lowering of temperature, lattice modes exhibit very pronounced changes when the temperature decreases from 225 to 220 K (Figure 3). First, Raman modes exhibit significant shifts and split into many components. Second, Raman bands decrease fwhm, and they become very narrow at 80 K. All of these changes point to further slowing down of the MHy^+ cation dynamics and a significant decrease in crystal symmetry, associated with the change of distortion of $PbCl_6$ octahedra and appearance of out-of-plane tilting. Note that the number of Raman bands observed at 80 K is much larger for MHy_2PbCl_4 (24 in the $x(yy+yz)x$ polarization), compared to MHy_2PbBr_4 (nine bands).[41] This observation gives strong evidence that the crystal structure of the lowest temperature phase of MHy_2PbCl_4 features significantly lower symmetry than the crystal structure of its bromide analogue. This conclusion is consistent with X-ray diffraction data that revealed $Pmn2_1$ and $P2_1$ symmetry for the lowest temperature phases of MHy_2PbBr_4 and MHy_2PbCl_4, respectively.

Electrical Measurements. A broadband dielectric spectroscopy measurement was carried out to investigate the dipolar relaxation arising from the reorientation motions of molecular dipoles and conduction arising from the translational motions of electric charges (ions, electrons). Temperature-dependent complex dielectric permittivity ε^* ($\varepsilon^* = \varepsilon' - i\varepsilon''$, where ε' is the dielectric permittivity, and ε'' is the dielectric loss, respectively) is presented in Figure 4a,b. A slight, step-like anomaly of ε' can be observed at ∼224 K on heating, related to the structural PT from phase **II** to phase **III**. However, above the observed PT, frequency dispersion can be noticed for ε^*, which is probably associated with ionic/electrical conductivity processes. To reduce the contribution of the conductivity component at higher temperatures, the modulus representation ($M^* = 1/\varepsilon^*$) was used (Figure 4c,d).[44] The bell-shaped spectra of M″ and the step-like curves of M′ shift toward HTs with increasing frequency, which implies the presence of conduction and dielectric relaxation processes. The visible decrease in the value of the M″ coincides with the temperature of the PT from phase **I** to phase **II**. In order to investigate this behavior, the dependence of ε^* and M^* as a function of frequency in the temperature range of 140−360 K was performed (Figure S13). The visible bell-shaped spectra of M″ allow the activation energy to be

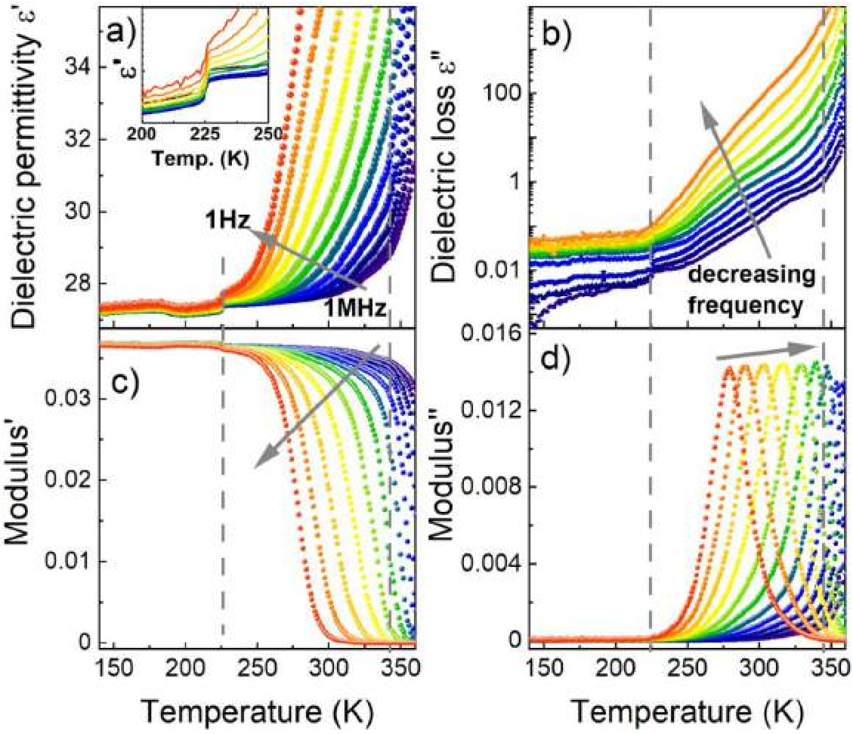

Figure 4. Temperature dependence of the (a) dielectric permittivity, (b) dielectric loss, (c) real M′, and (d) imaginary M″ components of electric modulus spectra as a function of the temperature of the MHy_2PbCl_4 single crystal along the [010] direction measured on heating. The representative curves are plotted in frequency decades between 1 Hz and 1 MHz. Dashed lines correspond to the structural PT temperatures. The changes in dielectric permittivity for the area near the PT are presented in the inset in a.

determined. The data were parametrized in the vicinity of the peak maximum with the use of the single Havriliak−Negami function. It was noticed that in the studied temperature range, the relaxation times (τ) exhibit linear tendencies as a function of the inverse temperature ($1000/T$). Therefore, the relaxation times can be modeled using the Arrhenius relation:

$$\tau = \tau_0 \exp\left(\frac{E_a}{k_B T}\right)$$

where τ_0, k_B, and E_a are relaxation times at the high temperature limit, Boltzmann constant, and activation energy, respectively. Based on this estimation, the E_a in phase **I** is 1.8 eV and in phase **II** is 0.7 eV (Figure S14). Taking into account the X-ray diffraction data, the mechanism of the observed dielectric relaxation process in MHy_2PbCl_4 can be related to the new configuration of MHy^+ and/or ionic conductivity. The obtained values of E_a are slightly higher than those reported for related compounds such as [triethylpropylammonium]PbI_3 (0.66 eV in the HT phase and 1.09 eV in the LT phase),[45] MHy_2PbI_4 (0.48, 0.80, and 0.70 eV from the HT phase to the LT phase, respectively).[25]

The temperature-dependent pyrocurrent of the MHy_2PbCl_4 single crystal measured along the [010] direction is presented in Figure 5. We observe a sudden increase in the value of the pyrocurrent during the heating of the sample at the PT temperature of about 224 K, confirming the material's polar properties. Despite repeated trials, we could not obtain a $P-E$ hysteresis loop for MHy_2PbCl_4, which indicates that it is a pyroelectric material. A similar case was observed for the related 3D compound $MHyPbCl_3$.[23]

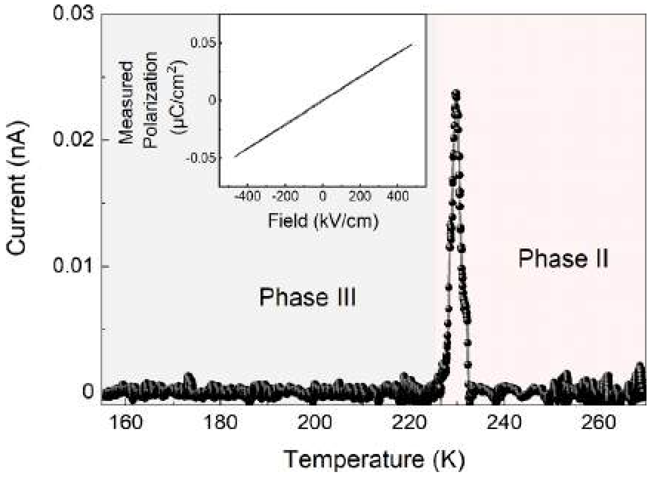

Figure 5. Temperature dependence of the pyroelectric current of a single crystal after poling in the DC electric field. Inset shows measured polarization as a function of the applied electric field at a temperature of 180 K.

Temperature-Resolved SHG Studies. Despite the fact that 2D HOIPs have been around for some time, their diverse NLO properties have gained significant interest only in the past few years. As is the case with the majority of the 2D materials, the NLO properties of 2D HOIPs are associated with their quantum-well structure; it is influenced by the quantum and dielectric confinement introduced by inorganic and organic layers, respectively.[46] Such systems typically possess strong two- and multiphoton excited PL due to large nonlinear absorption cross sections and luminescence quantum yields.[47] This is broadly true for the majority of 2D perovskites, particularly those comprising bromine, iodine, or a mixture of those at the so-called X-site.[48] The SHG phenomenon can also benefit from confinement effects but, on the other hand, has a strict non-centrosymmetry requirement imposed by the $\chi^{(2)}$ tensor, making this process possible only in acentric crystalline materials. For this reason, the SHG-active 2D HOIPs are not really common; the most notable examples include Ruddlesden−Popper phases such as $(PEA)_2(MA)_{n-1}Pb_nI_{3n+1}$ (PEA = phenylethylammonium),[49] $(BA)_2PbCl_4$ (BA = benzylammonium)[50] $(CH_3(CH_2)_3NH_3)_2(CH_3NH_3)_{n-1}Pb_nI_{3n+1}$ (n = 1, 2, 3, 4, ∞)[9] as well as MHy_2PbBr_4,[22] a bromine analogue of the title compound. For this reason, we set out to investigate SHG properties of all crystal phases of MHy_2PbCl_4, in particular, to check how they compare to those of MHy_2PbBr_4.

A temperature-resolved SHG study of MHy_2PbCl_4 was performed with the use of 1300 nm femtosecond laser pumping; this wavelength was chosen to enable comparisons with extant methylhydrazinum-based perovskites. First, we will discuss TR-SHG results for the RT phase **II** and LT phase **III**. Figure 6 presents integral areas of SHG signals (λ_{SHG} = 650 nm) plotted as a function of temperature for heating (148−268 K) and cooling run (268−148 K), while experimental spectra of NLO responses are displayed in Figure S15. These data show that MHy_2PbCl_4 is clearly SHG-active in its LT phase **III**, while PT to phase **II** (at ca. 223 K upon heating) results in a complete loss of SHG activity. Upon cooling at ca. 193 K, SHG starts to be restored due to a return to the non-centrosymmetric phase **III**. PT between phases **II** and **III** is therefore reversible, as well as features broad hysteresis, which confirms its first-order character. At this point, it should be noted that the LT phase **III** of MHy_2PbBr_4 is also non-centrosymmetric.[22]

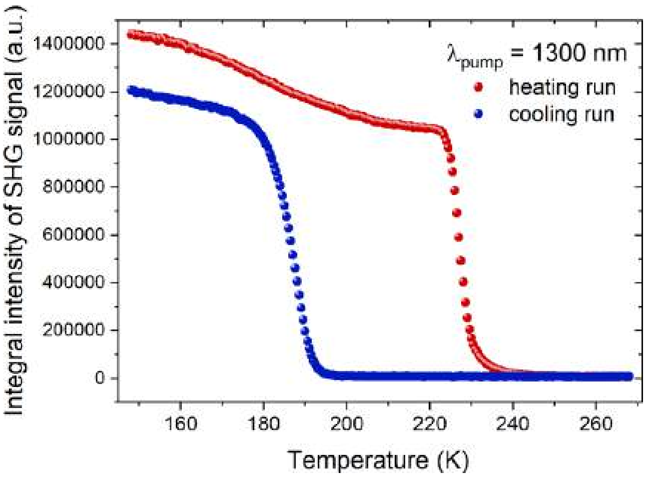

Figure 6. Plots of integral intensities of the SHG signal of MHy_2PbCl_4 for heating (red circles) and cooling (blue circles) runs.

In a separate experiment, we checked whether the HT phase **I** is SHG-active. To this end, we performed a temperature scan (300−355 K) using the same irradiation conditions and registered spectra of nonlinear emissions. As seen in Figure S16, spectra in this temperature range do not show any contribution of SHG at 650 nm, but only a third-harmonic generation (THG) signal at 433 nm, which is present for each phase regardless of its symmetry (compare with Figure S15). Accordingly, the centrosymmetric character of phase **I**, inferred from crystallographic data, is confirmed by these results.

In order to estimate the efficiency of the generation of the second harmonic of radiation by phase **III**, we performed the Kurtz−Perry powder test in which we compared the SHG emission of MHy_2PbCl_4 cooled down to 160 K with that of KDP of the same particle size, but measured at RT. It turns out that the relative efficiency of SHG is about 0.21 times that of KDP at 1300 nm. This value is two times higher than that found for MHy_2PbBr_4.[22]

From the viewpoint of NLO properties, the title compound is similar to its bromine analogue, MHy_2PbBr_4. The fundamental common feature is that both analogues possess three temperature-dependent crystal phases, among which only the LT phase **III** is SHG-active. In fact, in the case of MHy_2PbCl_4, the THG is present in addition to SHG. By contrast, phase **III** of MHy_2PbBr_4 showed multiphoton-excited luminescence of mixed 3- and 4-photon absorption origin in addition to SHG and THG emissions. This difference can be ascribed to the wide optical bandgap of MHy_2PbCl_4 (3.75 eV, see optical properties section) which effectively shifts nonlinear absorption resonances to shorter wavelengths.

All in all, the collected results demonstrate one more example of HOIP that contains MHy^+ cation and whose at least one crystal phase is SHG-active (acentric). While MHy_2PbCl_4 in its crystal architecture and phase behavior mirrors the MHy_2PbBr_4 analogue in many respects, it should be pointed out that MHy-containing 3D perovskites, $MHyPbCl_3$, $MHyPbBr_3$, and halide-mixed $MHyPbBr_3Cl_{(3\text{-}x)}$ analogues, possess acentric phases as well.[21,23,24] In fact, these materials are the only representatives of 3D perovskites that reveal clear polar order. The apparent accumulation of examples of MHy-containing perovskites which are non-centrosymmetric raises the question of whether the MHy^+ cation—a nonchiral molecule—facilitates crystallization of acentric perovskite phases. If there is indeed something to that, the MHy^+ component could play a similar role in materials science as recently adopted by amine fluorination,[51−54] and as such, could be seen as a useful tool for inducing non-centrosymmetry-driven properties, e.g., piezoelectricity or ferroelectricity.

Photoluminescence. The diffuse reflectance spectrum of MHy_2PbCl_4 shows a narrow band positioned at 344 nm (3.60 eV) (Figure S17), which can be assigned to the excitonic absorption. Based on this result, the energy band gap (E_g) of the investigated perovskite was calculated using the Kubelka−Munk equation:[55]

$$F(R) = \frac{(1-R)^2}{2R}$$

where R indicates reflectance. The estimated E_g value of MHy_2PbCl_4 is 3.75 eV (Figure S18); i.e., it is significantly larger than the E_g of the bromide ($MHy_2PbBr_4 \approx 3.02$ eV) and iodide ($MHy_2PbI_4 \approx 2.20$ eV) analogues.[22,25] The increase of the energy band gap when larger I^- are replaced by smaller Br^- or Cl^- ions can be attributed to the lower electronegativity of the smaller halogen atoms.[20] The band gap of MHy_2PbCl_4 is also larger than the band gap of its 3D $MHyPbCl_3$ analogue, for which E_g = 3.4 eV.[23] The same behavior, attributed to quantum confinement effects, was also observed for other lead halides.[56] It is worth adding that the energy band gap and the excitonic absorption of 2D lead halide perovskites with formula A_2PbX_4 also become larger with a decrease in the interlayer distance.[22,25,29,57,58] Thus, we showed that MHy_2PbI_4 and MHy_2PbBr_4 perovskites exhibit exceptionally small band gaps and the most red-shifted excitonic absorption among all known A_2PbI_4 and A_2PbBr_4 analogues.[22,25] The same applies to

https://doi.org/10.1021/acs.inorgchem.2c02206
Inorg. Chem. 2022, 61, 15520−15531

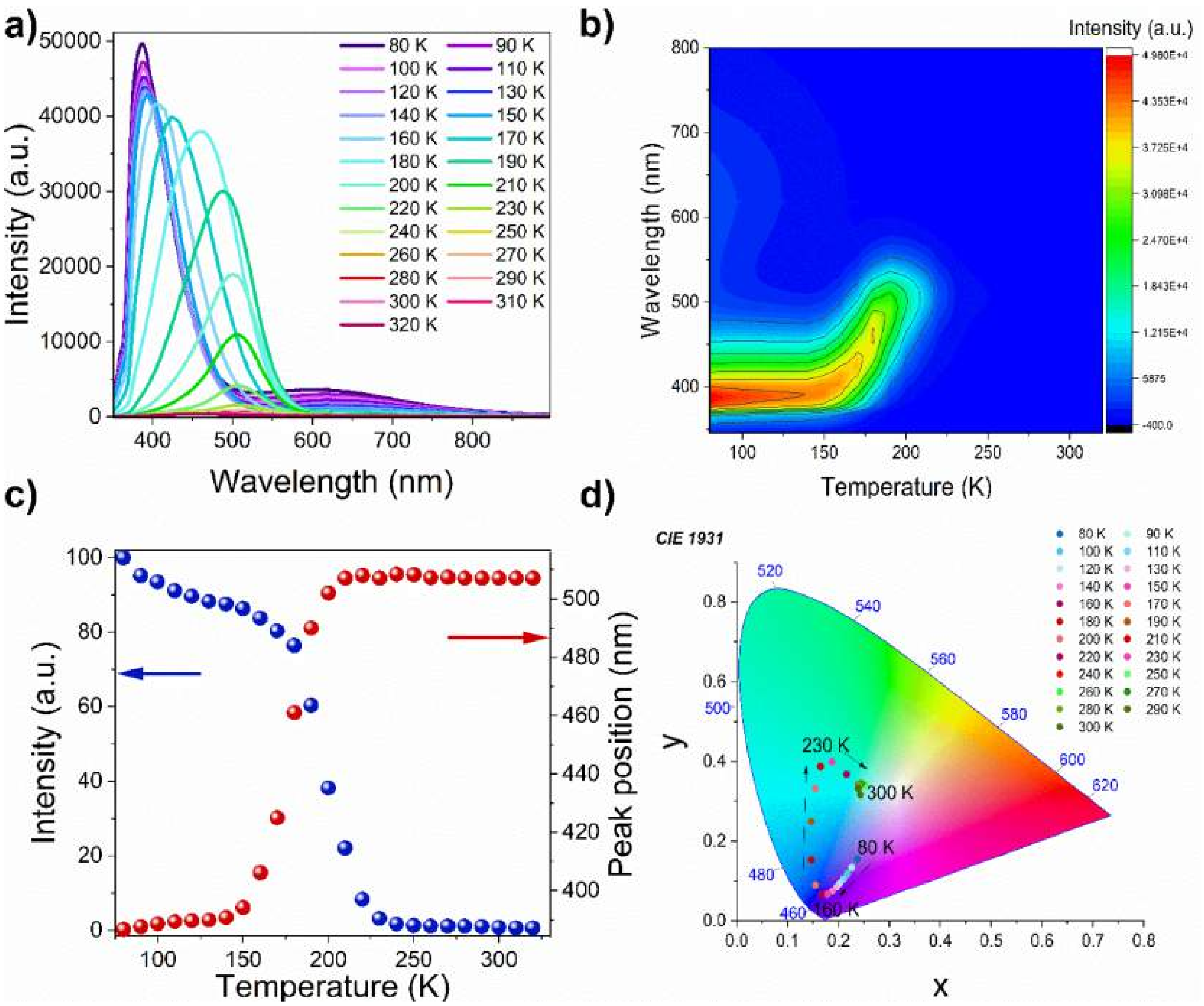

Figure 7. (a) Temperature-dependent emission spectra of MHy_2PbCl_4 measured every 10 K from 80 to 320 K, (b) the temperature dependence of band intensity (contour map), (c) the emission intensity as a function of temperature (left side) and the shift of the band center position with temperature, (d) CIE coordinates of MHy_2PbCl_4 at various temperatures.

MHy_2PbCl_4, wherein the band gap is smaller (excitonic absorption red-shifted) than the band gaps (excitonic absorption) of A_2PbCl_4 (100) perovskites containing large alkylammonium or aromatic cations.[29,59,60]

The PL spectrum recorded at 80 K presents a relatively broad band (full width at half-maximum, fwhm = 59.5 nm) centered at 387 nm and a very broad band (fwhm = 250 nm) located at 609 nm (Figure 7a). A significant fwhm and Stokes shift of the first band excludes its assignment to a free exciton (FE) recombination and suggests that it can be attributed to a bound exciton (BE) states or defects corresponding to imperfect stacking of layers (crumpled excitons, CE).[22,24,29,61,62] Previous studies of layered perovskites often revealed the presence of broad red-shifted bands, which were attributed to the self-trapped excitons (STEs) in the radiative centers.[63,64] Typically, the PL attributed to STE is observed below 150 K and was reported for some other two-dimensional lead chlorides with a strongly distorted framework as well as 3D $MHyPbCl_3$.[19,23,59] We assign, therefore, the broad band of MHy_2PbCl_4 near 609 nm to STEs. The emission decay times of the purplish-blue band (λ_{em} = 387 nm) and the red one (λ_{em}= 609 nm) recorded using a 266 nm line generated by the femtosecond laser are nonexponential with a time of τ_1 = 2.2 ns, τ_2 = 5.55 ns, and τ_1 = 0.69 ns; τ_2 = 3.0 ns, respectively (Figure S19).

As can be seen in Figure 7a−c, the intensity of the band located in the red region rapidly decreases on heating and becomes almost invisible above 130 K. The intensity of the purplish-blue band also decreases on heating, and this band exhibits significant broadening above 150 K. Furthermore, the position of the band maximum shows a pronounced red shift from 394 nm at 150 K to 507 nm at 210 K (Figure 7a−c). This pronounced broadening and the red shift of the PL above 150 nm can be most likely attributed to the light-induced permanent defects.

Based on temperature-dependent emission spectra, the activation energy for the thermal quenching was calculated as follows:

$$I(t) = \frac{I_o}{1 + A_e^{-E_a/k_BT}}$$

where, I_0, E_a, and k_B denote the emission intensity at LT, the activation energy, and the Boltzmann constant, respectively. After simple modification, the equation can be rewritten as

$$\ln\left(\frac{I_0}{I(t)} - 1\right) = \ln A \frac{-E_a}{k_B T}$$

Figure S20 presents $\ln(I_0/I(T) - 1)$ in a linear function of $1/k_BT$. The activation energy for the thermal quenching of the MHy_2PbCl_4 emission equals 366 meV, which is consistent with E_a values reported for many other A_2PbX_4 compounds[19,65] but is significantly larger than E_a reported for FE PL in MHy_2PbI_4 (59.2 meV) and MHy_2PbBr_4 (99.9 meV).[22,25]

The natural consequence of the broadening of the emission band and changing its position with temperature is the shift of the color rendering index CIE (Figure 7d). From 80 to 160 K sample exhibits purplish-blue emission but then the chromaticity coordinates (x, y) change more significantly and the color of the emission tunes rapidly with temperature. As a consequence, the sample glows bluish-green at 230 K.

4. CONCLUSION

HOIPs not only engender emerging technological interest but serve as a unique platform for fundamental studies of structure−property−function relationships. There are organic building units that facilitate the formation of specific types of structures, which can be intentionally employed to increase the likelihood of the generation of desired molecular arrangements. A growing body of evidence suggests that such a structure-directing role in HOIPs may be performed by the methylhydrazinium (MHy^+) cation in two aspects: (i) preferred formation of non-centrosymmetric perovskite phases; and (ii) self-assembly of 2D HOIPs with an unusually low separation between inorganic layers. With these working hypotheses in mind, in this work, we sought to employ MHy^+ for the construction of a missing member of the methylhydrazinium 2D perovskites, MHy_2PbCl_4.

Indeed, crystallographic results MHy_2PbCl_4 show that LT phase **III** is non-centrosymetric ($P2_1$ space group), while RT phase **II**, featuring the modulated phase of $Pmmn(00\gamma)s00$ superspace symmetry and HT phase **I** (orthorhombic, $Pmmn$) are both centrosymmetric. The acentric setting of phase **III** is corroborated by SHG studies as well as by the pyroelectric effect, showing the decay of spontaneous polarization along the [010] crystallographic direction upon PT. However, polarization could not be switched by the application of an external electric field; hence, MHy_2PbCl_4 cannot be considered ferroelectric.

Structural studies also demonstrate that MHy_2PbCl_4 establishes a new record for the short distance between inorganic layers in 2D HOIPs (8.79 Å at 350 K), breaking the previous one held by a bromine analog of the formula MHy_2PbBr_4. Nevertheless, in this case, the short interlayer distance does not translate to an unusually low exciton binding energy as was noted for bromine and iodine analogs. On the contrary, the value of exciton binding energy, estimated based on the activation energy for the thermal quenching equals 366 meV and is in the range typical for 2D perovskites. Further optical studies revealed that MHy_2PbCl_4 on heating displays a marked broadening and redshift of the higher energy band, which can most likely be attributed to light-induced permanent defects. The estimated E_g value of MHy_2PbCl_4 is 3.75 eV, which is significantly larger than those of the bromide and iodide analogues.

All in all, MHy_2PbCl_4 constitutes a plain example of MHy^+-directed formation of a non-centrosymmetric phase in 2D perovskite combined with the structural effect of an unusually low separation between inorganic layers. The guided formation of acentric phases by MHy^+ resembles that observed for ferroelectric materials comprising fluorine-substituted organic ligands. MHy_2PbCl_4 features a thermally responsive lattice, as revealed by dielectric and Raman measurements. By using the Clausius−Clapeyron relation, it was demonstrated that MHy_2PbCl_4 is not only responsive to temperature, but its structure should also display strong structural responsiveness to pressure stimuli, warranting further studies of pressure-dependent physical properties.

■ ASSOCIATED CONTENT

Supporting Information

The Supporting Information is available free of charge at https://pubs.acs.org/doi/10.1021/acs.inorgchem.2c02206.

Figures: DSC traces, projections of crystal structures, dielectric curves, energy activation, SHG spectra, THG spectra, diffuse reflectance, emission spectra. Tables: crystallographic data, hydrogen-bond parameters for the studied compound at different temperatures, structural and optical parameters for selected A_2PbBr_4 perovskites (PDF)

Video: Modulation movie of phase II (MPG)

Accession Codes

CCDC 2164381−2164383 (for the structure of MHy_2PbCl_4 at 350 K, for the averaged structure of MHy_2PbCl_4 at 295 K, or the structure of MHy_2PbCl_4 at 120 K, respectively) contain the supplementary crystallographic data for this paper. These data can be obtained free of charge via www.ccdc.cam.ac.uk/data_request/cif, or by emailing data_request@ccdc.cam.ac.uk, or by contacting The Cambridge Crystallographic Data Centre, 12 Union Road, Cambridge CB2 1EZ, UK; fax: +44 1223 336033.

■ AUTHOR INFORMATION

Corresponding Authors

Mirosław Maczka − *Institute of Low Temperature and Structure Research, Polish Academy of Sciences, 50-422 Wrocław, Poland;* orcid.org/0000-0003-2978-1093; Email: m.maczka@intibs.pl

Adam Sieradzki − *Department of Experimental Physics, Wrocław University of Science and Technology, 50-370 Wrocław, Poland;* orcid.org/0000-0003-4136-5754; Email: adam.sieradzki@pwr.edu.pl

Authors

Katarzyna Fedoruk − *Department of Experimental Physics, Wrocław University of Science and Technology, 50-370 Wrocław, Poland;* orcid.org/0000-0001-7485-7144

Dawid Drozdowski − *Institute of Low Temperature and Structure Research, Polish Academy of Sciences, 50-422 Wrocław, Poland;* orcid.org/0000-0001-5918-5503

Jan K. Zareba − *Advanced Materials Engineering and Modeling Group, Wrocław University of Science and Technology, 50-370 Wrocław, Poland;* orcid.org/0000-0001-6117-6876

Dagmara Stefańska − *Institute of Low Temperature and Structure Research, Polish Academy of Sciences, 50-422 Wrocław, Poland;* orcid.org/0000-0002-1051-3761

Anna Gagor − *Institute of Low Temperature and Structure Research, Polish Academy of Sciences, 50-422 Wrocław, Poland*

Complete contact information is available at:
https://pubs.acs.org/10.1021/acs.inorgchem.2c02206

Notes

The authors declare no competing financial interest.

■ ACKNOWLEDGMENTS

This research was supported by the National Science Center (Narodowe Centrum Nauki) in Poland under Project No. 2019/35/B/ST5/00043. J.K.Z. acknowledges support from Academia Iuvenum, Wroclaw University of Science and Technology.

■ REFERENCES

(1) Jena, A. K.; Kulkarni, A.; Miyasaka, T. Halide Perovskite Photovoltaics: Background, Status, and Future Prospects. *Chem. Rev.* **2019**, *119* (5), 3036−3103.

(2) Saparov, B.; Mitzi, D. B. Organic−Inorganic Perovskites: Structural Versatility for Functional Materials Design. *Chem. Rev.* **2016**, *116* (7), 4558−4596.

(3) Li, W.; Wang, Z.; Deschler, F.; Gao, S.; Friend, R. H.; Cheetham, A. K. Chemically Diverse and Multifunctional Hybrid Organic−Inorganic Perovskites. *Nat. Rev. Mater.* **2017**, *2* (3), 16099.

(4) Leguy, A. M. A.; Frost, J. M.; McMahon, A. P.; Sakai, V. G.; Kockelmann, W.; Law, C.; Li, X.; Foglia, F.; Walsh, A.; O'Regan, B. C.; Nelson, J.; Cabral, J. T.; Barnes, P. R. F. The Dynamics of Methylammonium Ions in Hybrid Organic−Inorganic Perovskite Solar Cells. *Nat. Commun.* **2015**, *6* (1), 7124.

(5) Šimėnas, M.; Balčiunas, S.; Svirskas, Š.; Kinka, M.; Ptak, M.; Kalendra, V.; Gagor, A.; Szewczyk, D.; Sieradzki, A.; Grigalaitis, R.; Walsh, A.; Maczka, M.; Banys, J. Phase Diagram and Cation Dynamics of Mixed $MA_{1-x}FA_xPbBr_3$ Hybrid Perovskites. *Chem. Mater.* **2021**, *33* (15), 5926−5934.

(6) McNulty, J. A.; Lightfoot, P. Structural Chemistry of Layered Lead Halide Perovskites Containing Single Octahedral Layers. *IUCrJ.* **2021**, *8* (4), 485−513.

(7) Straus, D. B.; Kagan, C. R. Electrons, Excitons, and Phonons in Two-Dimensional Hybrid Perovskites: Connecting Structural, Optical, and Electronic Properties. *J. Phys. Chem. Lett.* **2018**, *9* (6), 1434−1447.

(8) Boix, P. P.; Agarwala, S.; Koh, T. M.; Mathews, N.; Mhaisalkar, S. G. Perovskite Solar Cells: Beyond Methylammonium Lead Iodide. *J. Phys. Chem. Lett.* **2015**, *6* (5), 898−907.

(9) Stoumpos, C. C.; Cao, D. H.; Clark, D. J.; Young, J.; Rondinelli, J. M.; Jang, J. I.; Hupp, J. T.; Kanatzidis, M. G. Ruddlesden−Popper Hybrid Lead Iodide Perovskite 2D Homologous Semiconductors. *Chem. Mater.* **2016**, *28* (8), 2852−2867.

(10) Mao, L.; Stoumpos, C. C.; Kanatzidis, M. G. Two-Dimensional Hybrid Halide Perovskites: Principles and Promises. *J. Am. Chem. Soc.* **2019**, *141* (3), 1171−1190.

(11) Li, X.; Hoffman, J. M.; Kanatzidis, M. G. The 2D Halide Perovskite Rulebook: How the Spacer Influences Everything from the Structure to Optoelectronic Device Efficiency. *Chem. Rev.* **2021**, *121* (4), 2230−2291.

(12) Huo, C.; Cai, B.; Yuan, Z.; Ma, B.; Zeng, H. Two-Dimensional Metal Halide Perovskites: Theory, Synthesis, and Optoelectronics. *Small Methods* **2017**, *1* (3), 1600018.

(13) Chao, L.; Wang, Z.; Xia, Y.; Chen, Y.; Huang, W. Recent Progress on Low Dimensional Perovskite Solar Cells. *J. Energy Chem.* **2018**, *27* (4), 1091−1100.

(14) Ishihara, T. Optical Properties of PbI-Based Perovskite Structures. *J. Lumin.* **1994**, *60−61*, 269−274.

(15) Hong, X.; Ishihara, T.; Nurmikko, A. V. Dielectric confinement effect on excitons in PbI_4-based layered semiconductors. *Phys. Rev. B* **1992**, *45* (12), 6961−6964.

(16) Yang, Y.; Ostrowski, D. P.; France, R. M.; Zhu, K.; van de Lagemaat, J.; Luther, J. M.; Beard, M. C. Observation of a Hot-Phonon Bottleneck in Lead-Iodide Perovskites. *Nat. Photonics* **2016**, *10* (1), 53−59.

(17) Miyata, A.; Mitioglu, A.; Plochocka, P.; Portugall, O.; Wang, J. T.-W.; Stranks, S. D.; Snaith, H. J.; Nicholas, R. J. Direct Measurement of the Exciton Binding Energy and Effective Masses for Charge Carriers in Organic−Inorganic Tri-Halide Perovskites. *Nat. Phys.* **2015**, *11* (7), 582−587.

(18) Ishihara, T.; Hong, X.; Ding, J.; Nurmikko, A. V. Dielectric Confinement Effect for Exciton and Biexciton States in PbI4-Based Two-Dimensional Semiconductor Structures. *Surf. Sci.* **1992**, *267* (1−3), 323−326.

(19) Smith, M. D.; Connor, B. A.; Karunadasa, H. I. Tuning the Luminescence of Layered Halide Perovskites. *Chem. Rev.* **2019**, *119* (5), 3104−3139.

(20) Quan, L. N.; Rand, B. P.; Friend, R. H.; Mhaisalkar, S. G.; Lee, T.-W.; Sargent, E. H. Perovskites for Next-Generation Optical Sources. *Chem. Rev.* **2019**, *119* (12), 7444−7477.

(21) Drozdowski, D.; Gagor, A.; Stefańska, D.; Zareba, J. K.; Fedoruk, K.; Maczka, M.; Sieradzki, A. Three-Dimensional Methylhydrazinium Lead Halide Perovskites: Structural Changes and Effects on Dielectric, Linear, and Nonlinear Optical Properties Entailed by the Halide Tuning. *J. Phys. Chem. C* **2022**, *126* (3), 1600−1610.

(22) Maczka, M.; Zareba, J. K.; Gagor, A.; Stefańska, D.; Ptak, M.; Roleder, K.; Kajewski, D.; Soszyński, A.; Fedoruk, K.; Sieradzki, A. $[Methylhydrazinium]_2PbBr_4$, a Ferroelectric Hybrid Organic−Inorganic Perovskite with Multiple Nonlinear Optical Outputs. *Chem. Mater.* **2021**, *33* (7), 2331−2342.

(23) Maczka, M.; Gagor, A.; Zareba, J. K.; Stefanska, D.; Drozd, M.; Balciunas, S.; Šimėnas, M.; Banys, J.; Sieradzki, A. Three-Dimensional Perovskite Methylhydrazinium Lead Chloride with Two Polar Phases and Unusual Second-Harmonic Generation Bistability above Room Temperature. *Chem. Mater.* **2020**, *32* (9), 4072−4082.

(24) Maczka, M.; Ptak, M.; Gagor, A.; Stefanska, D.; Zareba, J. K.; Sieradzki, A. Methylhydrazinium Lead Bromide: Noncentrosymmetric Three-Dimensional Perovskite with Exceptionally Large Framework Distortion and Green Photoluminescence. *Chem. Mater.* **2020**, *32* (4), 1667−1673.

(25) Maczka, M.; Ptak, M.; Gagor, A.; Stefańska, D.; Sieradzki, A. Layered Lead Iodide of $[Methylhydrazinium]_2PbI_4$ with a Reduced Band Gap: Thermochromic Luminescence and Switchable Dielectric Properties Triggered by Structural Phase Transitions. *Chem. Mater.* **2019**, *31* (20), 8563−8575.

(26) Li, X.; Cuthriell, S. A.; Bergonzoni, A.; Dong, H.; Traoré, B.; Stoumpos, C. C.; Guo, P.; Even, J.; Katan, C.; Schaller, R. D.; Kanatzidis, M. G. Expanding the Cage of 2D Bromide Perovskites by Large A-Site Cations. *Chem. Mater.* **2022**, *34* (3), 1132−1142.

(27) Drozdowski, D.; Gagor, A.; Maczka, M. Methylhydrazinium Lead Iodide − One Dimensional Chain Phase with Excitonic Absorption and Large Energy Band Gap. *J. Mol. Struct.* **2022**, *1249*, 131660.

(28) Braun, M.; Frey, W. Crystal Structure of Bis(Benzylammonium) Lead Tetrachloride, (C7H7NH3)2PbCl4. *Z. Krist. - New Cryst. Struct.* **1999**, *214* (3), 331−332.

(29) Du, K.; Tu, Q.; Zhang, X.; Han, Q.; Liu, J.; Zauscher, S.; Mitzi, D. B. Two-Dimensional Lead(II) Halide-Based Hybrid Perovskites Templated by Acene Alkylamines: Crystal Structures, Optical Properties, and Piezoelectricity. *Inorg. Chem.* **2017**, *56* (15), 9291−9302.

(30) Kamminga, M. E.; Fang, H.-H.; Filip, M. R.; Giustino, F.; Baas, J.; Blake, G. R.; Loi, M. A.; Palstra, T. T. M. Confinement Effects in Low-Dimensional Lead Iodide Perovskite Hybrids. *Chem. Mater.* **2016**, *28* (13), 4554−4562.

(31) Billing, D. G.; Lemmerer, A. Inorganic−Organic Hybrid Materials Incorporating Primary Cyclic Ammonium Cations: The Lead Bromide and Chloride Series. *CrystEngComm* **2009**, *11* (8), 1549.

(32) Ye, H.-Y.; Liao, W.-Q.; Hu, C.-L.; Zhang, Y.; You, Y.-M.; Mao, J.-G.; Li, P.-F.; Xiong, R.-G. Bandgap Engineering of Lead-Halide

Perovskite-Type Ferroelectrics. *Adv. Mater.* **2016**, *28* (13), 2579−2586.

(33) Li, X.; Guo, P.; Kepenekian, M.; Hadar, I.; Katan, C.; Even, J.; Stoumpos, C. C.; Schaller, R. D.; Kanatzidis, M. G. Small Cyclic Diammonium Cation Templated (110)-Oriented 2D Halide (X = I, Br, Cl) Perovskites with White-Light Emission. *Chem. Mater.* **2019**, *31* (9), 3582−3590.

(34) Dolomanov, O. V.; Bourhis, L. J.; Gildea, R. J.; Howard, J. A. K.; Puschmann, H. *OLEX2*: A Complete Structure Solution, Refinement and Analysis Program. *J. Appl. Crystallogr.* **2009**, *42* (2), 339−341.

(35) Sheldrick, G. M. *SHELXT* − Integrated Space-Group and Crystal-Structure Determination. *Acta Crystallogr. Sect. A Found. Adv.* **2015**, *71* (1), 3−8.

(36) Sheldrick, G. M. Crystal Structure Refinement with *SHELXL*. *Acta Crystallogr. Sect. C Struct. Chem.* **2015**, *71* (1), 3−8.

(37) Petříček, V.; Dušek, M.; Palatinus, L. Crystallographic Computing System JANA2006: General Features. *Zeitschrift für Krist. - Cryst. Mater.* **2014**, *229* (5), 345−352.

(38) Janssen, T.; Janner, A.; Looijenga-Vos, A.; de Wolff, P. M. Incommensurate and Commensurate Modulated Structures. In *International Tables for Crystallography*; International Union of Crystallography: Chester, England, 2006; pp 907−955. DOI: 10.1107/97809553602060000624.

(39) Bermúdez-García, J. M.; Sánchez-Andújar, M.; Yáñez-Vilar, S.; Castro-García, S.; Artiaga, R.; López-Beceiro, J.; Botana, L.; Alegría, Á.; Señarís-Rodríguez, M. A. Role of Temperature and Pressure on the Multisensitive Multiferroic Dicyanamide Framework [TPrA][Mn-$(Dca)_3$] with Perovskite-like Structure. *Inorg. Chem.* **2015**, *54* (24), 11680−11687.

(40) Aleksandrov, K. S.; Bartolome, J.; Gorev, M. V.; Flerov, I. N. Hydrostatic Pressure Effect on Phase Transitions in Perovskites with Ammonium Cations. *Phys. status solidi* **2000**, *217* (2), 785−791.

(41) Fleet, M. E. Distortion Parameters for Coordination Polyhedra. *Mineral. Mag* **1976**, *40* (313), 531−533.

(42) Dhanabalan, B.; Leng, Y.-C.; Biffi, G.; Lin, M.-L.; Tan, P.-H.; Infante, I.; Manna, L.; Arciniegas, M. P.; Krahne, R. Directional Anisotropy of the Vibrational Modes in 2D-Layered Perovskites. *ACS Nano* **2020**, *14* (4), 4689−4697.

(43) Maczka, M.; Ptak, M. Lattice Dynamics and Structural Phase Transitions in Two-Dimensional Ferroelectric Methylhydrazinium Lead Bromide Investigated Using Raman and IR Spectroscopy. *J. Phys. Chem. C* **2022**, *126* (18), 7991−7998.

(44) Molak, A.; Paluch, M.; Pawlus, S.; Klimontko, J.; Ujma, Z.; Gruszka, I. Electric Modulus Approach to the Analysis of Electric Relaxation in Highly Conducting $(Na_{0.75}Bi_{0.25})(Mn_{0.25}Nb_{0.75})O_3$ Ceramics. *J. Phys. D. Appl. Phys.* **2005**, *38* (9), 1450−1460.

(45) Wang, M.-J.; Chen, X.-R.; Tong, Y.-B.; Yuan, G.-J.; Ren, X.-M.; Liu, J.-L. Phase Transition, Dielectrics, Single-Ion Conductance, and Thermochromic Luminescence of a Inorganic−Organic Hybrid of [Triethylpropylammonium][PbI_3]. *Inorg. Chem.* **2017**, *56* (16), 9525−9534.

(46) Zhou, F.; Ran, X.; Fan, D.; Lu, S.; Ji, W. Perovskites: Multiphoton Absorption and Applications. *Adv. Opt. Mater.* **2021**, *9* (23), 2100292.

(47) Xu, J.; Li, X.; Xiong, J.; Yuan, C.; Semin, S.; Rasing, T.; Bu, X. Halide Perovskites for Nonlinear Optics. *Adv. Mater.* **2020**, *32* (3), 1806736.

(48) Zareba, J. K.; Nyk, M.; Samoć, M. Nonlinear Optical Properties of Emerging Nano− and Microcrystalline Materials. *Adv. Opt. Mater.* **2021**, *9* (23), 2100216.

(49) Zhang, Q.; Solanki, A.; Parida, K.; Giovanni, D.; Li, M.; Jansen, T. L. C.; Pshenichnikov, M. S.; Sum, T. C. Tunable Ferroelectricity in Ruddlesden−Popper Halide Perovskites. *ACS Appl. Mater. Interfaces* **2019**, *11* (14), 13523−13532.

(50) Liao, W.-Q.; Zhang, Y.; Hu, C.-L.; Mao, J.-G.; Ye, H.-Y.; Li, P.-F.; Huang, S. D.; Xiong, R.-G. A Lead-Halide Perovskite Molecular Ferroelectric Semiconductor. *Nat. Commun.* **2015**, *6* (1), 7338.

(51) Zhang, H.-Y.; Zhang, Z.-X.; Song, X.-J.; Chen, X.-G.; Xiong, R.-G. Two-Dimensional Hybrid Perovskite Ferroelectric Induced by Perfluorinated Substitution. *J. Am. Chem. Soc.* **2020**, *142* (47), 20208−20215.

(52) Ai, Y.; Chen, X.-G.; Shi, P.-P.; Tang, Y.-Y.; Li, P.-F.; Liao, W.-Q.; Xiong, R.-G. Fluorine Substitution Induced High T_c of Enantiomeric Perovskite Ferroelectrics: (*R*)- and (*S*)-3-(Fluoropyrrolidinium)$MnCl_3$. *J. Am. Chem. Soc.* **2019**, *141* (10), 4474−4479.

(53) Xie, Y.; Ai, Y.; Zeng, Y.-L.; He, W.-H.; Huang, X.-Q.; Fu, D.-W.; Gao, J.-X.; Chen, X.-G.; Tang, Y.-Y. The Soft Molecular Polycrystalline Ferroelectric Realized by the Fluorination Effect. *J. Am. Chem. Soc.* **2020**, *142* (28), 12486−12492.

(54) Shi, P.-P.; Lu, S.-Q.; Song, X.-J.; Chen, X.-G.; Liao, W.-Q.; Li, P.-F.; Tang, Y.-Y.; Xiong, R.-G. Two-Dimensional Organic−Inorganic Perovskite Ferroelectric Semiconductors with Fluorinated Aromatic Spacers. *J. Am. Chem. Soc.* **2019**, *141* (45), 18334−18340.

(55) Kubelka, P.; Munk, F. Ein Beitrag Zür Optik Der Farbanstriche. *Z. Technol. Phys.* **1931**, *12*, 593−601.

(56) Wright, N. E.; Qin, X.; Xu, J.; Kelly, L. L.; Harvey, S. P.; Toney, M. F.; Blum, V.; Stiff-Roberts, A. D. Influence of Annealing and Composition on the Crystal Structure of Mixed-Halide, Ruddlesden−Popper Perovskites. *Chem. Mater.* **2022**, *34* (7), 3109−3122.

(57) Smith, M. D.; Jaffe, A.; Dohner, E. R.; Lindenberg, A. M.; Karunadasa, H. I. Structural Origins of Broadband Emission from Layered Pb−Br Hybrid Perovskites. *Chem. Sci.* **2017**, *8* (6), 4497−4504.

(58) Pradeesh, K.; Nageswara Rao, K.; Vijaya Prakash, G. Synthesis, Structural, Thermal and Optical Studies of Inorganic-Organic Hybrid Semiconductors, R-PbI_4. *J. Appl. Phys.* **2013**, *113* (8), 083523.

(59) Ji, C.; Wang, S.; Li, L.; Sun, Z.; Hong, M.; Luo, J. The First 2D Hybrid Perovskite Ferroelectric Showing Broadband White−Light Emission with High Color Rendering Index. *Adv. Funct. Mater.* **2019**, *29* (6), 1805038.

(60) Papavassiliou, G. C.; Mousdis, G. A.; Koutselas, I. B. Some New Organic-Inorganic Hybrid Semiconductors Based on Metal Halide Units: Structural, Optical and Related Properties. *Adv. Mater. Opt. Electron.* **1999**, *9* (6), 265−271.

(61) Lekina, Y.; Shen, Z. X. Excitonic States and Structural Stability in Two-Dimensional Hybrid Organic-Inorganic Perovskites. *J. Sci. Adv. Mater. Devices* **2019**, *4* (2), 189−200.

(62) Chen, C.; Hu, X.; Lu, W.; Chang, S.; Shi, L.; Li, L.; Zhong, H.; Han, J.-B. Elucidating the Phase Transitions and Temperature-Dependent Photoluminescence of $MAPbBr_3$ Single Crystal. *J. Phys. D. Appl. Phys.* **2018**, *51* (4), 045105.

(63) García-Fernández, A.; Juarez-Perez, E. J.; Bermúdez-García, J. M.; Llamas-Saiz, A. L.; Artiaga, R.; López-Beceiro, J. J.; Señarís-Rodríguez, M. A.; Sánchez-Andújar, M.; Castro-García, S. Hybrid Lead Halide [$(CH_3)_2NH_2$]PbX_3 (X = Cl^- and Br^-) Hexagonal Perovskites with Multiple Functional Properties. *J. Mater. Chem. C* **2019**, *7* (32), 10008−10018.

(64) Gautier, R.; Paris, M.; Massuyeau, F. Exciton Self-Trapping in Hybrid Lead Halides: Role of Halogen. *J. Am. Chem. Soc.* **2019**, *141* (32), 12619−12623.

(65) Chakraborty, R.; Nag, A. Correlation of Dielectric Confinement and Excitonic Binding Energy in 2D Layered Hybrid Perovskites Using Temperature Dependent Photoluminescence. *J. Phys. Chem. C* **2020**, *124* (29), 16177−16185.

Journal of
Materials Chemistry C

ROYAL SOCIETY
OF CHEMISTRY

PAPER

Check for updates

Cite this: *J. Mater. Chem. C*, 2023, **11**, 4907

Broadband yellow and white emission from large octahedral tilting in (110)-oriented layered perovskites: imidazolium-methylhydrazinium lead halides†

Dawid Drozdowski, *[a] Katarzyna Fedoruk, [b] Adam Kabanski, [a]
Mirosław Maczka, [a] Adam Sieradzki [b] and Anna Gagor *[a]

Hybrid organic–inorganic perovskites (HOIPs) are presently on the cutting edge of contemporary materials chemistry providing excellent and tuneable optoelectronic properties. Here we report the synthesis, crystal structures, and linear optical, and dielectric properties of two newcomers to the family of two-dimensional (2D) HOIPs – IMMHyPbBr$_4$ and IMMHyPbCl$_4$ (**IMPB** and **IMPC**), respectively, where IM = imidazolium, MHy = methylhydrazinium) which adopt rarely reported alignment of PbX$_6$ octahedral layers (X = Br, Cl), described as (110)-cut derivatives of 3D perovskites, with IM$^+$ situated at the interlayer and MHy$^+$ at intralayer sites. Both materials exhibit phase transitions with the high-temperature phase of monoclinic $P2/c$ symmetry with both organic cations and the linking halide anion being disordered. On cooling, at 344.5 K (375.4 K) for **IMPB** (**IMPC**) a $P2/c \rightarrow P2_1/c$ symmetry breaking occurs which induces strong tilting of octahedral layers, with the lowest Pb–X$_{\text{link}}$–Pb angle (143° for **IMPC**, X$_{\text{link}}$ = linking halide) ever reported for this class of compounds. Dielectric studies reveal a well-defined single dipolar relaxation process in the low temperature range from 150 K (170 K) to 188 K (230 K) for **IMPB** (**IMPC**), associated with the change in dynamics of the MHy$^+$ cation. With the use of linear optical measurements, we demonstrate that both compounds exhibit broadband emission with a large Stokes shift attributed to self-trapped excitons. The emission colour changes with temperature and **IMPB** is the first example of a mixed-organic cation perovskite showing white-light emission near 200 K. The structure–physiochemical property relationship is discussed with reference to other (110)-oriented lead halides.

Received 3rd February 2023,
Accepted 13th March 2023

DOI: 10.1039/d3tc00401e

rsc.li/materials-c

Introduction

Widespread exploration of hybrid organic–inorganic perovskites (HOIPs) – a family of materials with a variety of physiochemical properties and applications, gives rise to the development of compounds with vast structural diversity.[1–5] The flagship representatives, *i.e.*, three-dimensional (3D) HOIPs with ABX$_3$ formula and a high-temperature (HT) cubic $Pm\bar{3}m$ symmetry, built using corner-sharing PbX$_6$ octahedra (X = Br$^-$, Cl$^-$, I$^-$) and small monovalent organic cations (methylammonium (MA$^+$) and formamidinium (FA$^+$)) filling the voids in between the inorganic network,[6,7] exhibited remarkable optoelectronic properties (a power conversion efficiency of up to 25%, a photoluminescence quantum yield (PLQY) of up to 85%, long carrier diffusion lengths, *etc.*) and are increasingly placed as strong candidates for solar cells.[8–13] Apart from the aforementioned examples, only two newcomers appeared so far to meet the requirements of the 3D perovskite structure with lead halide octahedra, *i.e.*, aziridinium (Azr$^+$) and methylhydrazinium (MHy$^+$).[14–18] 3D HOIPs comprising MHy$^+$ are exceptional in terms of the polar crystal structure. They manifest the nonlinear optical effects, such as the second-harmonic generation (SHG), benefiting from the lack of the inversion centre.

The foregoing incorporation of different organic cations into the perovskite family leads to structures with reduced dimensionality: two-dimensional (2D, layered) HOIPs or 1D and 0D hybrid compounds. In 2D HOIPs, perovskite layers are separated by organic cations. Such a configuration improves the

---

[a] *Institute of Low Temperature and Structure Research, Polish Academy of Sciences, Okólna 2, 50-422 Wrocław, Poland. E-mail: d.drozdowski@intibs.pl, a.gagor@intibs.pl*

[b] *Department of Experimental Physics, Faculty of Fundamental Problems of Technology, Wrocław University of Science and Technology, Wybrzeże Wyspiańskiego 27, 50-370 Wrocław, Poland*

† Electronic supplementary information (ESI) available: Tables S1–S7: main details from SCXRD experiments and geometric comparison with literature compounds; Fig. S1–S10: powder X-ray diffractograms, geometric details *versus* temperature, dielectric spectra, diffuse reflectance spectra, Kubelka–Munk functions, and thermal evolution of luminescence. CCDC 2182360, 2182361 and 2236989 for **IMPB** and 2182518, 2182519 and 2235385 for **IMPC**. For ESI and crystallographic data in CIF or other electronic format see DOI: https://doi.org/10.1039/d3tc00401e

chemical stability and induces quantum well characteristics of the inorganic substructure with the insulating 'spacers'. It is also worth mentioning that another degree of structural flexibility is achieved *via* the incorporation of either one or two organic moieties, resulting in compositions of the ABX_4, A_2BX_4, or $AA'BX_4$ formula for single-layered ($n = 1$) analogues. Depending on the relative stacking of perovskite layers, one may distinguish three structural families: Ruddlesden–Popper (RP, A_2BX_4, A = monovalent cation),[19] Dion–Jacobson (DJ, ABX_4, A = divalent cation),[20] and alternating cations in the interlayer space (ACI, $AA'BX_4$, where A and A′ denote monovalent cations)[21] compounds. Facile manipulation of components, together with the quantum confinement effect brings more paths of tunability and flexibility of the dielectric and optical properties obtained *via* structural engineering.[4,22–24] When compared to their 3D counterparts, 2D HOIPs are usually characterized by higher exciton binding energies (typically >150 meV and *ca.* 10 meV for 2D and 3D perovskites, respectively),[25,26] leading to enhancement of the PL intensity and improved PLQY.[27–30] The mixing-amine approach may also improve the photovoltaic properties of hybrid perovskites. For instance, doping of imidazolium (IM^+) to MA^+-based 3D HOIPs increases solar cell efficiency.[31] Moreover, the imidazolium derivatives are also used for the improvement of resistance to moisture, taking advantage of their hydrophobic properties.[32,33]

Considering the structural diversity of the 2D lead halide perovskites, one may describe them as derivatives of 3D structures, created by 'slicing' along particular crystallographic planes (001) (*i.e.*, 'sliced' across the octahedral corners) and (110) ('sliced' across the octahedral edges).[3,5] As can be seen in Fig. 1, in the (110)-cut family the inorganic layers are corrugated. Depending on the corrugation type, these structures can be labelled as '$n \times n$' or '$n \times m$', as presented in Fig. 1(b).[34] Based on the online database of 2D perovskites published by Marchenko *et al.*[35] 633 representatives of (001)-cut lead halide HOIPs are found with only 25 (110)-oriented. The overwhelming majority of the (001)-cut perovskites proves that such a configuration is the most preferable and tolerant to the substitution of both inorganic and organic components.[36] Nevertheless, the (110)-derived compounds have proven their usefulness in optoelectronics, revealing, for instance, broadband white light emission with higher PLQY and larger Stokes shifts than their (001)-cut counterparts due to a greater degree of dielectric confinement and octahedral distortion.[37–40]

Our previous studies showed that MHy^+ may also be used as a 'spacer' for the layered lead halides with X = Br, Cl, I and that these compounds exhibit multiple functional properties like dielectric switching, ferroelectricity, PL, and nonlinear optical (NLO) properties.[41–43] We have also recently reported three distinct compounds comprising IM^+ cations and exhibiting broadband PL – $IMPbBr_3$ with the 4H-hexagonal perovskite structure built using face- and corner-shared $PbBr_6$; IM_2PbBr_4 adopting a 1D double-chain structure with edge-shared octahedra; and IM_3PbBr_5 adopting a 1D single-chain structure with corner-shared octahedra.[44]

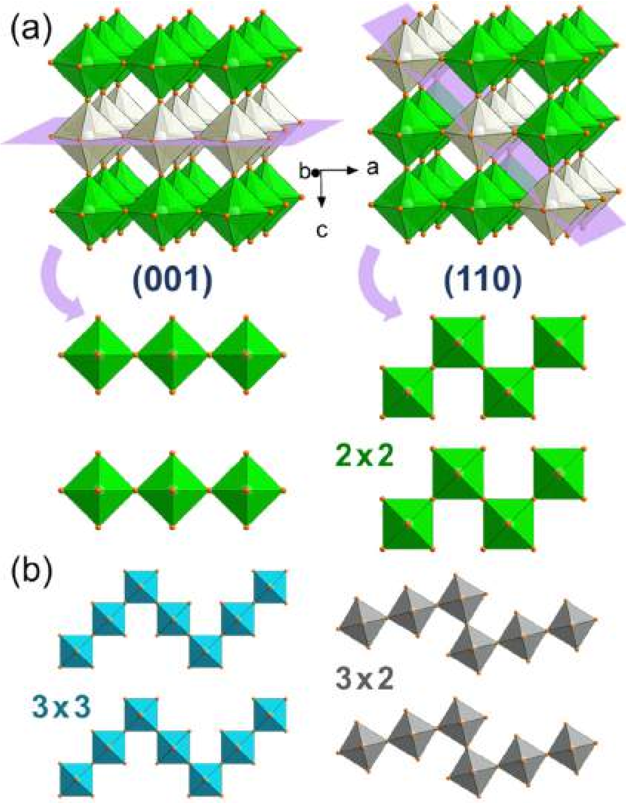

Fig. 1 (a) Schematic representation of 2D HOIPs as derived from the parental perovskite 3D lattice by slicing along the (001) and (110) crystallographic planes. (b) Other examples of corrugations in the (110)-oriented 2D HOIPs: 3 × 3 and 3 × 2.

To our best knowledge, only one example of hybrid lead chloride adopting the (110)-cut structure with two distinct organic moieties (*N*,*N*,*N*′,*N*′-tetramethylethylenediammonium (TMEDA) at the interlayer site and dimethylammonium (DMA) at the intralayer site) was reported so far.[45] However, this compound contains diammonium cations and its composition is $TMEDA_{0.5}DMAPbCl_4$, not $AA'BX_4$, as typically reported for the ACI perovskites. In the case of its bromine counterparts, there are 7 known ACI analogues, *i.e.*, two comprising IM^+ – $IMGUAPbBr_4$ and $IMTzPbBr_4$ (GUA = guanidinium, Tz = 1,2,4-triazolium),[36,46] and five comprising other organic cations – $FAHEAPbBr_4$, $PYGUAPbBr_4$, $PYTzPbBr_4$, $TzGUAPbBr_4$ and $FA_{1.5}AA_{0.5}PbBr_4$ (HEA = hydroxyethylammonium, PY = pyrazolium, AA = acetamidinium).[38,46,47] There are also several examples of (110)-oriented bromides and chlorides with one, mainly divalent organic cation.[36,39,40,48–54] One should note that there is no structure containing MHy^+ and that studies of ACI bromides and chlorides were limited principally to crystal structures and room-temperature (RT) absorption. Temperature-dependent PL was reported for only one representative, *i.e.*, $IMTzPbBr_4$.[36] Furthermore, there are no reports on dielectric properties, and the structural phase transition was revealed only in $TzGUAPbBr_4$.[46]

A short survey of literature data shows that the (110)-cut family of perovskites have great application potential but they are still very scarce, especially in the case of ACI analogues, and their properties are still poorly understood. Herein, we report for the first time two new representatives of 2 × 2 (110)-oriented

ACI layered HOIPs comprising MHy^+ and IM^+ cations, *i.e.*, $IMMHyPbBr_4$ ("IMPB") and $IMMHyPbCl_4$ ("IMPC"). Using multiple techniques we investigate the crystal structure and phase transition mechanisms as well as the dielectric and linear optical properties of these compounds.

Experimental

Synthetic procedures

$PbBr_2$ (98%, Sigma-Aldrich), $PbCl_2$ (98%, Sigma-Aldrich), methylhydrazine (98%, Sigma-Aldrich), imidazole (99.5%, Sigma-Aldrich), hydrochloric acid (37 wt % in H_2O, POCH), hydrobromic acid (48 wt% in H_2O, Sigma-Aldrich), and *N*,*N*-dimethylformamide (DMF, 99.8%, Sigma-Aldrich) were commercially available and used without further purification. In order to grow single crystals, HBr or HCl was added dropwise to 6 mmol of methylhydrazine and 5 mmol of imidazole until pH = 7. Then 5 mmol of $PbBr_2$ or $PbCl_2$ was added, the mixture was stirred at 30 °C and DMF was added until complete dissolution of lead halide. The solution was left undisturbed at RT. The plate-like crystals were harvested after 2 days, separated from the mother liquid, and dried at RT. Their powder X-ray diffraction patterns are in good agreement with the calculated ones based on single-crystal diffraction data (Fig. S1, ESI†), confirming the purity of the bulk sample.

Single-crystal X-ray diffraction (SCXRD)

SCXRD experiments were carried out using an Xcalibur four-circle diffractometer (Oxford Diffraction) with an Atlas CCD detector and graphite-monochromated Mo Kα radiation. Absorption was corrected by multi-scan methods using CrysAlis PRO 1.171.39.46 (Rigaku Oxford Diffraction, 2018). Empirical absorption correction was applied using spherical harmonics, implemented in the SCALE3 ABSPACK scaling algorithm. For the RT phases of both compounds, H atom parameters were constrained. All the crystal structures were solved in Olex2 1.5[55] using SHELXT[56] and refined with SHELXL.[57] Experiments were performed at 358 K (390 K) for the HT phase (**I**) of **IMPB** (**IMPC**) and at 295 K as well as 100 K for phase **II** of both compounds. The main experimental and geometric details are summarized in Tables S1–S4 (ESI†). The succinct structural details, *i.e.*, symmetry, unit cell parameters, and refinement factors, are as follows.

$IMMHyPbBr_4$ (**I**, 358 K): monoclinic, $P2/c$, a = 6.0384(4) Å, b = 13.970(1) Å, c = 8.5113(6) Å, β = 92.06(1)°; V = 717.53(8) Å^3, Z = 2, R_1 = 0.04, wR_2 = 0.12, S = 1.02; (**II**, 295 K): monoclinic, $P2_1/c$, a = 5.9753(7) Å, b = 28.414(4) Å, c = 8.2762(12) Å, β = 90.49(1)°; V = 1405.1(3) Å^3, Z = 4, R_1 = 0.06, wR_2 = 0.12, S = 1.09; (**II**, 100 K): a = 5.9431(2) Å, b = 28.182(1) Å, c = 8.1723(4) Å, β = 91.129(3)°; V = 1368.5(1) Å^3, R_1 = 0.04, wR_2 = 0.09, S = 1.17.

$IMMHyPbCl_4$ (**I**, 390 K): monoclinic, $P2/c$, a = 5.7615(4) Å, b = 13.725(1) Å, c = 8.1876(9) Å, β = 90.47(1)°; V = 647.4(1) Å^3, Z = 2, R_1 = 0.05, wR_2 = 0.11, S = 1.04; (**II**, 295 K): monoclinic, $P2_1/c$, a = 5.7168(2) Å, b = 27.883(1) Å, c = 8.0079(3) Å, β = 90.132(3)°; V = 1276.45(8) Å^3, Z = 4, R_1 = 0.03, wR_2 = 0.06, S = 1.24; (**II**, 100 K): a = 5.6652(2) Å, b = 27.388(2) Å, c = 7.9492(4) Å, β = 90.453(4)°; V = 1233.3(1) Å^3, R_1 = 0.03, wR_2 = 0.07, S = 1.16.

Powder X-ray diffraction (PXRD)

Powder X-ray diffraction (PXRD) patterns of the ground crystals were measured in the reflection modes using an X'Pert PRO X-ray diffraction system equipped with a PIXcel ultrafast line detector and Soller slits for CuKα_1 radiation (λ = 1.54056 Å).

Differential scanning calorimetry (DSC)

Heat flow was measured using a Mettler Toledo DSC-1 calorimeter with a high resolution of 0.4 μW. Nitrogen was used as a purging gas, and the heating and cooling rate was 5 K min^{-1}. The mass of the measured samples was 23.00 mg and 33.49 mg for **IMPB** and **IMPC**, respectively. The excess heat capacity associated with the phase transition was calculated by subtraction of the baseline from the data representing the system variation in the absence of phase transitions.

Broadband dielectric spectroscopy (BDS)

Dielectric measurements of the examined samples were carried out using a broadband impedance Novocontrol Alpha analyser. Since the obtained single crystals were not large enough, we did not perform single-crystal dielectric measurements. The powder was pressed into cylindrical pellets of 5 mm in diameter and about 0.5 mm in thickness. The silver paste was deposited on the pellet surface to ensure good electrical contact. A sinusoidal voltage with an amplitude of 1 V and a frequency in the range of 1 Hz–1 MHz was applied across the sample. The studies were performed in the temperature range of 150–400 K for **IMPB** and 175–425 K for **IMPC**. The temperature was stabilized using nitrogen gas using the Novocontrol Quattro system.

Optical measurements

The RT diffuse reflectance spectra (DRS) of powdered samples were obtained using the Varian Cary 5E UV-VIS-NIR spectrometer. Measurements of temperature-dependent PL were performed with the Hamamatsu PMA-12 photonic multichannel analyser combined with a BT-CCD sensor while the temperature was controlled using the Linkam THMS600 stage. As an excitation source, the 266 nm laser beam was used.

Results and discussion

Thermal properties

The calorimetric measurements showed one reversible phase transition (PT) at 344.5 K (356.9 K) and 375.4 K (383.3 K) visible in the cooling (heating) mode for **IMPB** (Fig. 2(a)) and **IMPC** (Fig. 2(b)), respectively. The symmetrical, sharp peaks seen in ΔC_p plotted as a function of temperature and the evident thermal hysteresis between heating and cooling cycles indicate the first-order type of PTs. This is also confirmed by the accompanying discontinuous change in the entropy (ΔS) (Fig. 2(a) and (b)). The changes of ΔS were estimated to be

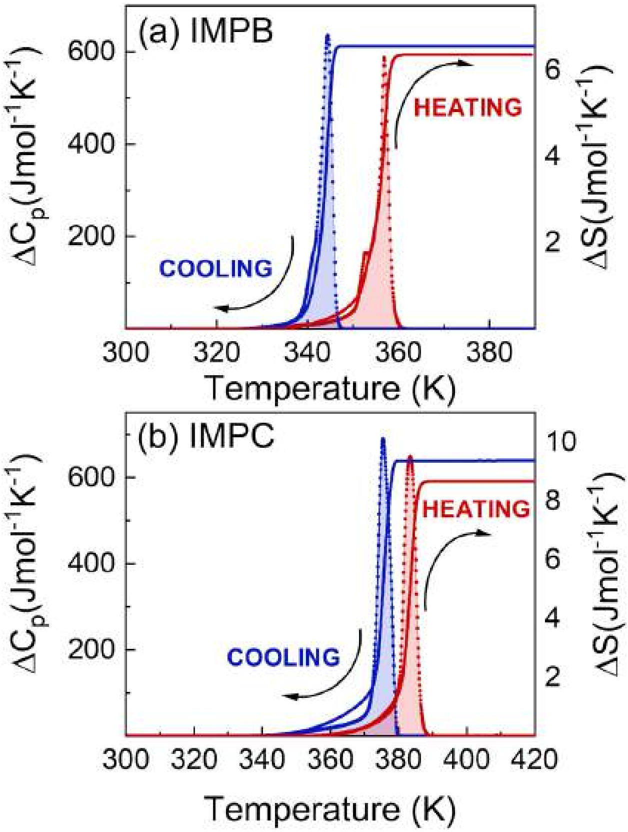

Fig. 2 Changes in heat capacity and entropy related to PT in the heating (red) and cooling (blue) runs for (a) **IMPB** and (b) **IMPC**.

6.6 J mol^{-1} K^{-1} (6.4 J mol^{-1} K^{-1}) for **IMPB** (Fig. 2(a)) and 9.37 J mol^{-1} K^{-1} (8.67 J mol^{-1} K^{-1}) for **IMPC** (Fig. 2(b)). For an order–disorder transition, $\Delta S = R\ln(N)$, where R is the gas constant and N is the ratio of the number of configurations in the disordered and ordered phase. The estimated N is 2.20 and 3.09 for **IMPB** and **IMPC**, respectively. These values imply an important contribution of order–disorder processes in the mechanism of PT. The temperature of the PT and the estimated entropy change are higher for the chloride analogue.

Crystal structure

Crystal structures of both **IMPB** and **IMPC** compounds represent the ACI family with IM$^+$ occupying the interlayer site and MHy$^+$ placed at the intralayer site. The HT phases (**I**) are isostructural, described in a monoclinic, centrosymmetric $P2/c$ space group, with the number of formula units per unit cell (Z) equal to 2. The crystal structure of **I** is presented in Fig. 3(a). The inorganic layers adopt a corrugated 2 × 2 (110)-oriented arrangement, composed of $[PbX_6]_\infty$ octahedra (X = Br, Cl) sharing *cis* ligands. The Pb–X distances are 2.898(1)–3.110(7) Å and 2.755(4)–2.99(4) Å for **IMPB** and **IMPC**, respectively. Both organic cations exhibit dynamic disorder. Consequently, there is no stable network of hydrogen bonding interactions (HBs). Bearing in mind that MHy$^+$ cations occupy the intralayer site, their dynamics might initiate disorder of the linking halides, which are split into two symmetrically equivalent positions with equal probability (Fig. S2a, ESI†). The organic components have a slight impact on the geometry of single octahedra, which is expressed in the octahedral distortion parameters (calculated using Fleet's approach)[58] – bond length distortion $\Delta d = 8.3 \times 10^{-4}$ (10.5×10^{-4}) and octahedral bond angle variance $\sigma^2 = 13.7$ deg^2 (15.1 deg^2) for **IMPB** (**IMPC**). These values are typical for the family of mixed-amine (110)-oriented lead halide 2D HOIPs (see Table S7, ESI†). The angular distortion results in deviations of Pb–X–Pb angles from 180°, with the largest deviation for the Pb–X–Pb angle with linking 'X' halogen (θ_{link}) equal to 167° for both **IMPB** and **IMPC**. It is worth noting that there is no octahedral tilting observed in this phase.

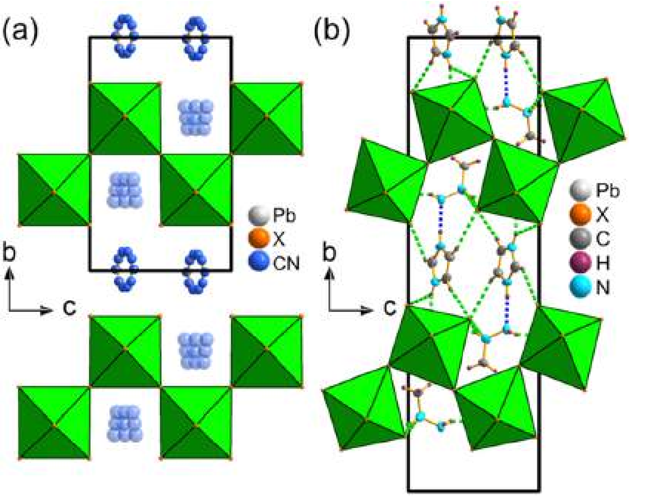

Fig. 3 Crystal structures of **IMPB** and **IMPC** in (a) HT phase **I** – $P2/c$ and (b) phase **II** – $P2_1/c$ at 100 K. Dashed lines in (b) represent the intermolecular interactions: green for N–H···X and C–H···X HBs, and blue for N–H···N HBs.

As the temperature decreases, both compounds undergo a PT to a monoclinic and centrosymmetric phase of $P2_1/c$ symmetry (phase **II**, Fig. 3(b)). The **I** → **II** PT is associated with a translational symmetry breaking and formation of the 2b superstructure (Z raises to 4). Analysis of the DSC curves suggests a change in the dynamics of the organic cations associated with this PT. Indeed, in **II** all the IM$^+$ moieties are well-ordered and anchored *via* N–H···X and C–H···X HBs (green dashed lines in Fig. 3(b), for distances see Tables S5 and S6, ESI†). At RT, the MHy$^+$ cations still exhibit a disorder which is, however, largely reduced compared to the HT phase – the CH_3 and terminal NH_2 groups are ordered, while the middle nitrogen is dynamically split into three distinct sites with equal probability (Fig. S2b, ESI†). Temperature decrease anchors one of the three positions and at 100 K the structure is well-ordered. One should also note that the creation of N–H···N HBs between IM$^+$ and the terminal N atom of the MHy$^+$ (blue dashed lines in Fig. 3(b)) might stabilize terminal NH_2 of MHy$^+$ at RT. The N atoms of MHy$^+$ take an active part in creating N–H···X HBs with the neighbouring halide ligands, including the linking one. The intermolecular forces mentioned above induce tilting of the octahedral layers with θ_{link} = 158° and 153° for **IMPB** and **IMPC**, respectively (Fig. S3, ESI†). Interestingly, the geometry of the single octahedra is not remarkably affected by the PT, as expressed in $\Delta d = 8.4 \times 10^{-4}$ (20.1×10^{-4}) and $\sigma^2 = 8.6$ deg^2 (17.3 deg^2) for **IMPB** (**IMPC**).

As the lowering of the temperature leads to the change of interatomic distances, both the distances between corresponding Pb atoms of the neighbouring layers (d_{inter}) and inside the layers measured along the [001] direction (d_{intra}) decrease with temperature within phase **II** (Fig. S4, ESI†). With a decrease of d_{intra}, increasing intermolecular forces between the inorganic part and MHy^+ cations cause gradual ordering of this organic moiety without a change in symmetry of the crystals, eventually leading to the formation of a stable network of N–H···X HBs (Fig. S2c, ESI†). Furthermore, with temperature lowering greater octahedral distortions and enlarged octahedral tilting are observed (Fig. S3, ESI†), with Δd, σ^2 and θ_{link} equal to 13.5×10^{-4} (31.5×10^{-4}), 28.7 deg^2 (44.7 deg^2) and 148° (143°) for **IMPB** (**IMPC**) at 100 K. The θ_{link} angles of both **IMPB** and **IMPC** are exceptionally low when compared to analogues found in the literature (152°–180° for related compounds, see Table S7, ESI†). In other words, the octahedral tilting in the structures reported herein is significantly larger. This anomaly is correlated with one of the lowest d_{intra} lengths for MHy^+ as the intralayer cation (8.16 Å (7.96 Å) for **IMPB** (**IMPC**) at 100 K *versus* 7.98–10.42 Å for related compounds) caused by strong intermolecular interactions, especially N–H···X HBs. This effect is also observed in (N-MEDA)PbBr_4 (N-MEDA = N-methylethane-1,2-diammonium)[40] with comparable $\theta_{\text{link}} = 152°$ and $d_{\text{intra}} = 8.39$ Å at 100 K, and in the monoclinic phase of FA_2PbBr_4 with $d_{\text{intra}} = 7.98$ Å at 100 K.[51] In terms of optoelectrical properties, massive octahedral tilting may manifest itself in a propensity for increased energy band gap and broader PL emission.[59,60]

Dielectric studies

The structural dynamics were investigated *via* broadband dielectric spectroscopy experiments. The temperature dependence of the complex dielectric permittivity $\varepsilon^* = \varepsilon' - i\varepsilon''$ of both compounds depict distinct changes at a temperature that corresponds to the PT confirmed by other experiments (Fig. 4). The dielectric curves of both samples show similar behaviour. Above 200 K, the observed strong frequency dispersion of ε^* is probably related to the induced ionic conductivity.[18,61,62] The occurrence of this process in the vicinity of the PT temperature (dashed lines in Fig. 4) obscures the experimental response of structural changes, resulting in slight changes observed in both real and imaginary dielectric permittivity values. In the investigated frequency range, at low temperatures, the anomalies indicate the occurrence of a single dipolar relaxation process. Close inspection of the complex dielectric permittivity data in the frequency domain confirms that in the temperature range from 150 K (170 K) to 188 K (230 K) for **IMPB** (**IMPC**), a well-defined single dipolar relaxation process appears (Fig. S5, ESI†). For both compounds, this relaxation is visible as a gradual step-like change in the frequency dependence of the dielectric permittivity ε' and a bell-like peak in the loss spectra ε'' (Fig. 5(a) and (b)). To parameterize the characteristic dipolar relaxation times, the data were fitted with the use of the single Havriliak–Negami function.[63] In order to understand the relaxation dynamics for both compounds, we compared the temperature-dependent behaviours of the dielectric relaxation times as a function of 1000/T (see Fig. 5(c)). In the investigated frequency range, the Arrhenius behaviour of the thermally activated single dipolar relaxation process for each sample can be recognized. The estimated activation energy for this process equals 0.269 eV and 0.326 eV, for **IMPB** and **IMPC**, respectively. The structural data indicate that the dipolar relaxation may be associated with

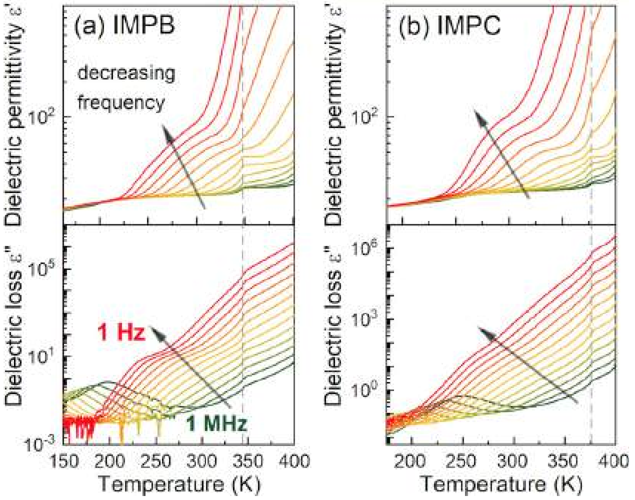

Fig. 4 Temperature dependence of dielectric permittivity and dielectric loss for (a) **IMPB** and (b) **IMPC** measured during cooling. The representative curves are plotted in frequency decay between 1 Hz and 1 MHz. The dashed lines correspond to the structural PT temperature as measured by DSC.

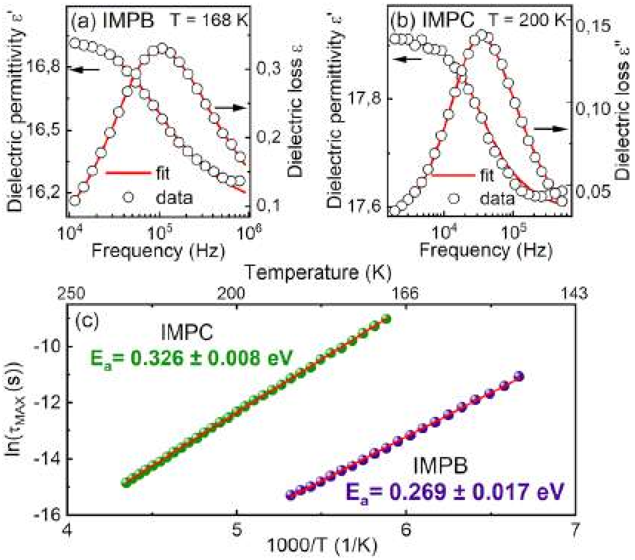

Fig. 5 Sample real and imaginary permittivity data fitted by means of the Havriliak–Negami function for (a) **IMPB** and (b) **IMPC**, respectively. (c) Relaxation map, *i.e.*, ln(τ_{max}) as a function of 1000/T.

the reorientational motion or angular jumps of the MHy^+ cation. A higher (smaller) value of the activation energy for **IMPC** (**IMPB**) is consistent with the presence of stronger (weaker) HBs between MHy^+ and Cl^- (Br^-) (Tables S5 and S6, ESI†), due to a smaller (larger) ionic size of Cl^- (Br^-) and thus a smaller (larger) size of the interlayer voids occupied by MHy^+. The obtained activation energy values are close to the value obtained for MHy^+ rotations in the metal–formate frameworks.[64] This is also consistent with the suspicion that the activation energy of the dipolar relaxation process is proportional to the number of broken hydrogen bonds.[65]

Optical studies

The RT diffuse reflectance spectra (DRS) of **IMPB** and **IMPC** are presented in Fig. S6a and b (ESI†). The bands at 391 nm (**IMPB**) and 334 nm (**IMPC**) can be attributed to excitonic absorption. Energy band gaps (E_g) of both samples were determined with the Kubelka–Munk[66] relation after subtraction of the low intensity peaks assigned to free excitons (FE), see Fig. S7a and b (ESI†). Graphical estimations of E_g were performed from Tauc plots (Fig. S6a and b, ESI†) and are equal to 3.22 eV and 3.79 eV for **IMPB** and **IMPC**, respectively. The E_g values are one of the largest amidst ACI (110)-oriented perovskites, however, they are similar to several single-amine examples (Table 1). The optical properties of the (001)-oriented perovskites depend on numerous factors, *e.g.*, the interlayer distance, in-plane and out-of-plane Pb–X–Pb angles, shifts between adjacent layers and octahedral central ion displacement.[41–43,59,67] In general, shorter interlayer distances and smaller tilting of the PbX_6 octahedra, indicate more reduced E_g. However, the former factor was found to be much more important.[59] In the (110)-cut family, the distortion of the perovskite layers seems to exert the predominant influence on the electro-optical properties, being even more important as the distance between the layers. In (110)-cut bromides and chlorides larger distortion (lower θ_{link}) increases E_g in most cases, as summarized in Table 1. For instance, the non-distorted $TzGUAPbBr_4$ and $IMGUAPbBr_4$ with $\theta_{link} = 180^\circ$ possess significantly lower E_g values than $MlaPbBr_4$ and **IMPB** (Mla = melammonium), which demonstrate much smaller or comparable interlayer distances but exhibit very strong deformation of the perovskite layer.[46,49,53] The greater band gap of **IMPC**, when compared to **IMPB**, is associated with the Br to Cl substitution effect, resulting in lower interatomic distances and greater octahedral distortion. Analogous dependence was also reported for the $3APRPbX_4$ (3APR = 3-aminopyrrolidinium; X = I, Br, Cl) series and in mixed-halide 3D HOIPs with MHy^+.[18,53]

Table 1 Relationship between selected geometric parameters and energy band gap values of **IMPB**, **IMPC** and analogous examples of (110)-oriented layered perovskites, all parameters are recorded at 295 ± 5 K

Compound	θ_{link} (°)	d_{inter} (Å)	E_g (eV)	λ_{em} (nm)	Stokes shift (nm)	Ref.
IMTzPbBr4	171.41(2)	12.93*	2.82	647	236	36
$TzGUAPbBr_4$	180	14.00	2.88	701	304	46
$APIPbBr_4$	162.68(4)	13.82	2.90	503	79	50
$IMGUAPbBr_4$	180	13.00	2.94	563	168	46
AA_2PbBr_4	166.45(2)	12.69	3.03	628	251	36
$EPZPbBr_4$	160.0(3)	12.51	3.12	596	∼215	39
$MlaPbBr_4$	159.85(3)	10.68	3.13	—	—	49
IMPB	157.80(7)	14.21	3.22	569.4	178	This work
$APIPbCl_4$	167.70(9)	13.02	3.49	573	∼193	52
$TMEDA_{0.5}DMAPbCl_4$	165.12(5)	13.12	3.50	447	72	45
IMPC	153.22(7)	13.94	3.79	586.6	252	This work
$3APRPbCl_4$	169.7(1)	10.88	3.85	617	282	53

θ_{link} – Pb–X–Pb angles for the linking 'X' halogen, d_{inter} – distances between corresponding Pb atoms of neighbouring layers, E_g – energy band gap, λ_{em} – wavelength of the maximum of emission band. * – structure with 3 × 3 corrugation type of octahedral layers, distances between the middle Pb atoms were taken into account. For the full names of the organic cations see Table S7 (ESI).

The PL spectra (λ_{exc} = 266 nm) of the investigated materials show single bands (Fig. 6(a), (b), (d) and (e)) with the maximum at λ_{em} = 569.4 nm (FWHM, 160 nm) and λ_{em} = 586.6 nm (FWHM, 166 nm) for **IMPB** and **IMPC**, respectively, and the Stokes shift equal to 178 nm (252 nm) for **IMPB** (**IMPC**). The broadband emissions with large Stoke shifts are usually attributed to self-trapped excitons (STEx).[27,68–72] Stability of STEx states increases with the enhancement of exciton–phonon coupling, and numerous studies showed that the intensity of STEx PL and Stokes shift increase with increasing distortion of the inorganic layers (decreasing θ_{link}).[27,68,72,73] Since the high level of structural distortions is typical of (110)-oriented perovskites,[36,46,53] these compounds often show STEx related broadband emission, including the white-light one.[39,40,45,47,48,51,53,69] Table 1 shows that for many (110)-cut bromides and chlorides, larger distortion leads to an increase of λ_{em} and Stokes shift. However, this trend is less regular than in the case of E_g.

In contrast to some (110)-oriented materials, **IMPB** and **IMPC** do not exhibit PL bands associated with FE recombination.[46,53] Furthermore, the observed PL is strongly temperature dependent (Fig. 6(a), (b), (d), (e) and Fig. S8, ESI†). The luminescent intensity decays with increasing temperature; the $T_{0.5}$ parameters, which stand for the temperature at which the PL intensity has decreased to half of its initial value, are equal to 111 K (**IMPB**) and 127 K (**IMPC**) (Fig. S9, ESI†). To acquire the activation energies of thermal quenching, the Arrhenius equation was implemented:

$$I(T) = \frac{I_0}{1 + c \cdot \exp\left(\frac{-E_a}{k_b T}\right)} \tag{1}$$

where I_0 is the initial intensity of luminescence (80 K), $I(T)$ is the intensity at a given temperature T, c is a constant value, E_a is the activation energy of thermal quenching, and k is Boltzmann's constant. The calculated values of activation energy of thermal quenching are equal to 123.2 meV and 306.3 meV, for **IMPB** and **IMPC**, respectively (Fig. S10, ESI†).

The increase in temperature induces a change in the position of the maximum emission intensity, which shifts toward higher wavelength values (Fig. 6(b), (e), Fig. S8, ESI†). To

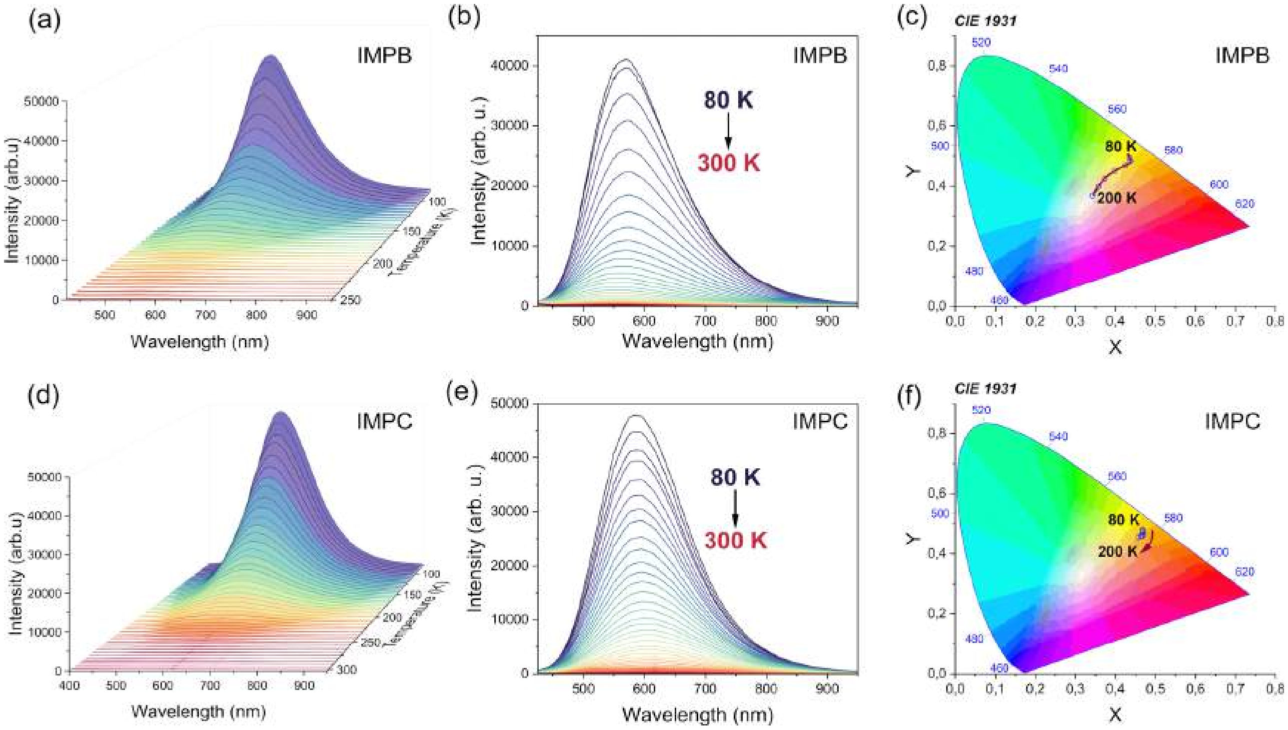

Fig. 6 Temperature-dependent optical properties of **IMPB**: (a and b) thermal quenching of the luminescence and (c) CIE colour coordinates in the 1931 colour space chromaticity diagram; and **IMPC**: (d and e) thermal quenching of the luminescence and (f) CIE colour coordinates in the 1931 colour space chromaticity diagram.

demonstrate this feature, the CIE (Commission Internationale de I'Echlairare) coordinates have been calculated (Fig. 6(c) and (f)). The shift of emission is especially visible for the **IMPB** sample, varying from warmer yellow (0.43, 0.49; 3666 K) at 80 K to colder white (0.34, 0.37; 5226 K) at 200 K. Such a strong dependence has not been observed for **IMPC**, where the CIE coordinates change from (0.47, 0.48) to (0.46, 0.46) in the 80–200 K range.

Conclusions

Two newcomers to the small family of ACI 2D HOIPs IMMHyPbBr$_4$ (**IMPB**) and IMMHyPbCl$_4$ (**IMPC**) have been synthesized. Both **IMPB** and **IMPC** adopt uncommon alignment of the perovskite layers, which may be treated as the (110)-cut derivative of 3D structures (*i.e.*, sharing *cis* ligands) with interlayer IM$^+$ and intralayer MHy$^+$ cations. HT phases are isostructural, of $P2/c$ symmetry (**I**), exhibiting disorder of both organic cations and linking halides. On cooling, both compounds undergo a $P2/c \rightarrow P2_1/c$ (**II**) symmetry breaking phase transition to a new monoclinic superstructure ($b' = 2b$) inducing the tilting of inorganic layers, ordering IM$^+$ cations and partial ordering of MHy$^+$. On further cooling the MHy$^+$ moieties stabilise their positions, eventually leading to structural alignment with record-breaking octahedral tilting ($\theta_{\text{link}} = 148°$ ($143°$) for **IMPB** (**IMPC**) at 100 K) in the family of (110)-oriented lead halide 2D HOIPs. The distortion of inorganic layers manifests in the broad PL (FWHM = 160 nm (166 nm) with a maximum at 569.4 nm (586.6 nm) for **IMPB** (**IMPC**) at 80 K) with huge Stokes shifts (178 nm (252 nm) for **IMPB** (**IMPC**)), and one of the largest energy band gaps (3.22 eV and 3.79 eV for **IMPB** and **IMPC**, respectively) amongst (110)-oriented compounds. Linear optical studies also demonstrate a change in the emission colour in the temperature gradient, especially noticeable for **IMPB** (yellow to white within the 80–200 K temperature range). Dielectric studies revealed a single dipolar relaxation process in the low temperature range from 150 K (170 K) up to 188 K (230 K) for **IMPB** (**IMPC**), originating from the gradual positional ordering of the MHy$^+$ cation.

Former studies showed that the MHy$^+$ cation has the ability to serve both as a 'spacer' (in (001) 2D perovskites[41–43]) and a 'perovskitizer' (in 3D analogues[16–18]) cation. The present results demonstrate a third feature of this cation, *i.e.*, it can also be employed in the synthesis of ACI phases with MHy$^+$ at intralayer sites exhibiting a record-breaking large out-of-plane distortion of the inorganic layers. Our results also demonstrate for the first time white-light emission in the ACI perovskite.

Author contributions

Conceptualization: D. D. & A. G.; data curation: D. D.; formal analysis, methodology, visualization and writing – original draft: D. D., K. F., A. K.; funding acquisition, project administration and resources: M. M.; supervision: A. G.; validation: M. M., A. S., A. G.; investigation and writing – review & editing: all authors.

Conflicts of interest

There are no conflicts to declare.

Acknowledgements

We acknowledge the support from the National Science Centre (Narodowe Centrum Nauki) in Poland under project no. 2019/35/B/ST5/00043.

References

1 B. Saparov and D. B. Mitzi, *Chem. Rev.*, 2016, **116**, 4558–4596.
2 W. Li, Z. Wang, F. Deschler, S. Gao, R. H. Friend and A. K. Cheetham, *Nat. Rev. Mater.*, 2017, **2**, 16099.
3 M. D. Smith, E. J. Crace, A. Jaffe and H. I. Karunadasa, *Annu. Rev. Mater. Res.*, 2018, **48**(1), 111–136.
4 L. Mao, C. C. Stoumpos and M. G. Kanatzidis, *J. Am. Chem. Soc.*, 2018, **141**, 1171–1190.
5 J. A. McNulty and P. Lightfoot, *IUCrJ*, 2021, **8**, 485–513.
6 T. Oku, *Rev. Adv. Mater. Sci.*, 2020, **59**, 264–305.
7 C. C. Stoumpos, C. D. Malliakas and M. G. Kanatzidis, *Inorg. Chem.*, 2013, **52**, 9019–9038.
8 J. Jeong, M. Kim, J. Seo, H. Lu, P. Ahlawat, A. Mishra, Y. Yang, M. A. Hope, F. T. Eickemeyer, M. Kim, Y. J. Yoon, I. W. Choi, B. P. Darwich, S. J. Choi, Y. Jo, J. H. Lee, B. Walker, S. M. Zakeeruddin, L. Emsley, U. Rothlisberger, A. Hagfeldt, D. S. Kim, M. Grätzel and J. Y. Kim, *Nature*, 2021, **592**, 381–385.
9 L. Protesescu, S. Yakunin, M. I. Bodnarchuk, F. Bertolotti, N. Masciocchi, A. Guagliardi and M. V. Kovalenko, *J. Am. Chem. Soc.*, 2016, **138**, 14202–14205.
10 S. D. Stranks, G. E. Eperon, G. Grancini, C. Menelaou, M. J. P. Alcocer, T. Leijtens, L. M. Herz, A. Petrozza and H. J. Snaith, *Science*, 2013, **342**, 341–344.
11 A. K. Jena, A. Kulkarni and T. Miyasaka, *Chem. Rev.*, 2019, **119**, 3036–3103.
12 Q. Chen, N. De Marco, Y. Yang, T. Bin Song, C. C. Chen, H. Zhao, Z. Hong, H. Zhou and Y. Yang, *Nano Today*, 2015, **10**, 355–396.
13 X. Zhao, J. D. A. Ng, R. H. Friend and Z. K. Tan, *ACS Photonics*, 2018, **5**, 3866–3875.
14 H. R. Petrosova, O. I. Kucheriv, S. Shova and I. A. Gural'skiy, *Chem. Commun.*, 2022, **58**, 5745–5748.
15 D. Stefańska, M. Ptak and M. Mączka, *Molecules*, 2022, **27**, 7949.
16 M. Mączka, M. Ptak, A. Gągor, D. Stefańska, J. K. Zaręba and A. Sieradzki, *Chem. Mater.*, 2020, **32**, 1667–1673.
17 M. Mączka, A. Gagor, J. K. Zaręba, D. Stefańska, M. Drozd, S. Balciunas, M. Šimėnas, J. Banys and A. Sieradzki, *Chem. Mater.*, 2020, **32**, 4072–4082.
18 D. Drozdowski, A. Gągor, D. Stefańska, J. K. Zaręba, K. Fedoruk, M. Mączka and A. Sieradzki, *J. Phys. Chem. C*, 2022, **126**, 1600–1610.
19 C. C. Stoumpos, D. H. Cao, D. J. Clark, J. Young, J. M. Rondinelli, J. I. Jang, J. T. Hupp and M. G. Kanatzidis, *Chem. Mater.*, 2016, **28**, 2852–2867.
20 L. Mao, W. Ke, L. Pedesseau, Y. Wu, C. Katan, J. Even, M. R. Wasielewski, C. C. Stoumpos and M. G. Kanatzidis, *J. Am. Chem. Soc.*, 2018, **140**, 3775–3783.
21 C. M. M. Soe, C. C. Stoumpos, M. Kepenekian, B. Traoré, H. Tsai, W. Nie, B. Wang, C. Katan, R. Seshadri, A. D. Mohite, J. Even, T. J. Marks and M. G. Kanatzidis, *J. Am. Chem. Soc.*, 2017, **139**, 16297–16309.
22 X. Li, J. M. Hoffman and M. G. Kanatzidis, *Chem. Rev.*, 2021, **121**, 2230–2291.
23 Z. Z. Zhang, T. M. Guo, Z. G. Li, F. F. Gao, W. Li, F. Wei and X. H. Bu, *Acta Mater.*, 2023, **245**, 118638.
24 F.-F. Gao, H. Song, Z.-G. Li, Y. Qin, X. Li, Z.-Q. Yao, J.-H. Fan, X. Wu, W. Li and X.-H. Bu, *Angew. Chem., Int. Ed.*, 2023, e202218675.
25 A. Miyata, A. Mitioglu, P. Plochocka, O. Portugall, J. T. W. Wang, S. D. Stranks, H. J. Snaith and R. J. Nicholas, *Nat. Phys.*, 2015, **11**, 582–587.
26 T. Ishihara, X. Hong, J. Ding and A. V. Nurmikko, *Surf. Sci.*, 1992, **267**, 323–326.
27 M. D. Smith, B. A. Connor and H. I. Karunadasa, *Chem. Rev.*, 2019, **119**, 3104–3139.
28 L. N. Quan, B. P. Rand, R. H. Friend, S. G. Mhaisalkar, T. W. Lee and E. H. Sargent, *Chem. Rev.*, 2019, **119**, 7444–7477.
29 L. Chao, Z. Wang, Y. Xia, Y. Chen and W. Huang, *J. Energy Chem.*, 2018, **27**, 1091–1100.
30 L. Gan, J. Li, Z. Fang, H. He and Z. Ye, *J. Phys. Chem. Lett.*, 2017, **8**, 5177–5183.
31 Q. Wang, F. Lin, C. C. Chueh, T. Zhao, M. Eslamian and A. K. Y. Jen, *Mater. Today Energy*, 2018, **7**, 161–168.
32 H. Lin, X. Zhang, L. Cai, J. Lao, R. Qi, C. Luo, S. Chen, H. Peng, R. Huang and C. Duan, *J. Mater. Chem. C*, 2020, **8**, 5594–5599.
33 M. Salado, F. J. Ramos, V. M. Manzanares, P. Gao, M. K. Nazeeruddin, P. J. Dyson and S. Ahmad, *ChemSusChem*, 2016, **9**, 2708–2714.
34 L. Mao, Y. Wu, C. C. Stoumpos, M. R. Wasielewski and M. G. Kanatzidis, *J. Am. Chem. Soc.*, 2017, **139**, 5210–5215.
35 E. I. Marchenko, S. A. Fateev, A. A. Petrov, V. V. Korolev, A. Mitrofanov, A. V. Petrov, E. A. Goodilin and A. B. Tarasov, *Chem. Mater.*, 2020, **32**, 7383–7388.
36 Y. Y. Guo, L. J. Yang, S. Biberger, J. A. McNulty, T. Li, K. Schötz, F. Panzer and P. Lightfoot, *Inorg. Chem.*, 2020, **59**, 12858–12866.
37 C. Katan, N. Mercier and J. Even, *Chem. Rev.*, 2019, **119**, 3140–3192.
38 Y. Y. Guo, C. Elliott, J. A. McNulty, D. B. Cordes, A. M. Z. Slawin and P. Lightfoot, *Eur. J. Inorg. Chem.*, 2021, 3404–3411.
39 L. Mao, P. Guo, M. Kepenekian, I. Hadar, C. Katan, J. Even, R. D. Schaller, C. C. Stoumpos and M. G. Kanatzidis, *J. Am. Chem. Soc.*, 2018, **140**, 13078–13088.
40 E. R. Dohner, E. T. Hoke and H. I. Karunadasa, *J. Am. Chem. Soc.*, 2014, **136**, 1718–1721.

41 M. Mączka, J. K. Zaręba, A. Gągor, D. Stefańska, M. Ptak, K. Roleder, D. Kajewski, A. Soszyński, K. Fedoruk and A. Sieradzki, *Chem. Mater.*, 2021, **33**, 2331–2342.

42 K. Fedoruk, D. Drozdowski, M. Mączka, J. K. Zaręba, D. Stefańska, A. Gagor and A. Sieradzki, *Inorg. Chem.*, 2022, **61**, 15520–15531.

43 M. Mączka, M. Ptak, A. Gągor, D. Stefańska and A. Sieradzki, *Chem. Mater.*, 2019, **31**, 8563–8575.

44 S. Smółka, M. Mączka, D. Drozdowski, D. Stefańska, A. Gągor, A. Sieradzki, J. K. Zaręba and M. Ptak, *Inorg. Chem.*, 2022, **61**, 15225–15238.

45 Y. Y. Ma, H. M. Pan, D. Y. Li, S. Wu and Z. Jing, *Z. Anorg. Allg. Chem.*, 2022, **648**, e202100334.

46 Y. Y. Guo, J. A. McNulty, N. A. Mica, I. D. W. Samuel, A. M. Z. Slawin, M. Bühl and P. Lightfoot, *Chem. Commun.*, 2019, **55**, 9935–9938.

47 M. B. H. Salah, N. Mercier, M. Allain, N. Zouari, U. Giovanella and C. Botta, *Eur. J. Inorg. Chem.*, 2019, 4527–4531.

48 E. R. Dohner, A. Jaffe, L. R. Bradshaw and H. I. Karunadasa, *J. Am. Chem. Soc.*, 2014, **136**, 13154–13157.

49 W. Huang, X. Zhang, Y. Li, Y. Zhou, X. Chen, X. Li, F. Wu, M. Hong, J. Luo, S. Zhao, W. Huang, Y. Li, Y. Zhou, X. Chen, X. Li, F. Wu, M. Hong, J. Luo, S. Zhao and X. Zhang, *Angew. Chem., Int. Ed.*, 2022, **61**, e202202746.

50 Y. Y. Li, C. K. Lin, G. L. Zheng, Z. Y. Cheng, H. You, W. D. Wang and J. Lin, *Chem. Mater.*, 2006, **18**, 3463–3469.

51 S. A. Fateev, A. A. Petrov, E. I. Marchenko, Y. V. Zubavichus, V. N. Khrustalev, A. V. Petrov, S. M. Aksenov, E. A. Goodilin and A. B. Tarasov, *Chem. Mater.*, 2021, **33**, 1900–1907.

52 Z. Wu, C. Ji, Z. Sun, S. Wang, S. Zhao, W. Zhang, L. Li and J. Luo, *J. Mater. Chem. C*, 2018, **6**, 1171–1175.

53 X. Li, P. Guo, M. Kepenekian, I. Hadar, C. Katan, J. Even, C. C. Stoumpos, R. D. Schaller and M. G. Kanatzidis, *Chem. Mater.*, 2019, **31**, 3582–3590.

54 A. Bonamartini Corradi, A. M. Ferrari, L. Righi and P. Sgarabotto, *Inorg. Chem.*, 2001, **40**, 218–223.

55 O. V. Dolomanov, L. J. Bourhis, R. J. Gildea, J. A. K. Howard and H. Puschmann, *J. Appl. Crystallogr.*, 2009, **42**, 339–341.

56 G. M. Sheldrick, *Acta Crystallogr., Sect. A: Found. Adv.*, 2015, **71**, 3–8.

57 G. M. Sheldrick, *Acta Crystallogr., Sect. C: Struct. Chem.*, 2015, **71**, 3–8.

58 M. E. Fleet, *Mineral. Mag.*, 1976, **40**, 531–533.

59 E. I. Marchenko, V. V. Korolev, S. A. Fateev, A. Mitrofanov, N. N. Eremin, E. A. Goodilin and A. B. Tarasov, *Chem. Mater.*, 2021, **33**, 7518–7526.

60 M. D. Smith and H. I. Karunadasa, *Acc. Chem. Res.*, 2018, **51**, 619–627.

61 M. F. Mostafa, S. S. El-Khiyami and A. K. Tammam, *Mater. Chem. Phys.*, 2022, **290**, 126526.

62 A. Walsh, D. O. Scanlon, S. Chen, X. G. Gong and S. H. Wei, *Angew. Chem., Int. Ed.*, 2015, **54**, 1791–1794.

63 A. Sieradzki, S. Pawlus, S. N. Tripathy, A. Gągor, M. Ptak, M. Paluch and M. Mączka, *Dalton Trans.*, 2017, **46**, 3681–3687.

64 A. Sieradzki, M. Mączka, M. Simenas, J. K. Zaręba, A. Gągor, S. Balciunas, M. Kinka, A. Ciupa, M. Nyk, V. Samulionis, J. Banys, M. Paluch and S. Pawlus, *J. Mater. Chem. C*, 2018, **6**, 9420–9429.

65 P. Peksa, A. Nowok, A. Gągor, M. Mączka, M. Drozd and A. Sieradzki, *Dalton Trans.*, 2021, **50**, 17906–17910.

66 P. Kubelka and F. Munk, *Z. Tech. Phys.*, 1931, **12**, 593–601.

67 X. Han, C. Jing, H. Zu and W. Zhang, *J. Am. Chem. Soc.*, 2022, **144**, 18595–18606.

68 M. D. Smith, A. Jaffe, E. R. Dohner, A. M. Lindenberg and H. I. Karunadasa, *Chem. Sci.*, 2017, **8**, 4497–4504.

69 Y. Lekina and Z. X. Shen, *J. Sci.: Adv. Mater. Devices*, 2019, **4**, 189–200.

70 C. Pareja-Rivera, J. A. Morán-Muñoz, A. P. Gómora-Figueroa, V. Jancik, B. Vargas, J. Rodríguez-Hernández and D. Solis-Ibarra, *Chem. Mater.*, 2022, **34**, 9344–9349.

71 M. Mączka, S. Sobczak, P. Ratajczyk, F. F. Leite, W. Paraguassu, F. Dybała, A. P. Herman, R. Kudrawiec and A. Katrusiak, *Chem. Mater.*, 2022, **34**, 7867–7877.

72 W. Yang, X. Xiao, H. He, G. Tong, J. Hu, X. Xiao, J. Chen, M. Li and Y. He, *Cryst. Growth Des.*, 2021, **21**, 5731–5739.

73 P. Shen, T. Vogt and Y. Lee, *J. Phys. Chem. Lett.*, 2020, **11**, 4131–4137.

Journal of Molecular Structure 1249 (2022) 131660

Contents lists available at ScienceDirect

Journal of Molecular Structure

journal homepage: www.elsevier.com/locate/molstr

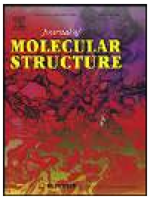

Methylhydrazinium lead iodide – one dimensional chain phase with excitonic absorption and large energy band gap

Dawid Drozdowski*, Anna Gągor, Mirosław Mączka

Institute of Low Temperature and Structure Research, Polish Academy of Sciences, Okólna 2, 50-422 Wrocław, Poland

ARTICLE INFO

Article history:
Received 8 July 2021
Revised 1 October 2021
Accepted 4 October 2021
Available online 7 October 2021

ABSTRACT

In this work the crystal structure of the new hybrid organic-inorganic compound has been studied using single-crystal X-ray diffraction (SCXRD). Methylhydrazinium lead iodide ($MHyPbI_3$) crystallizes in monoclinic, centrosymmetric $P2_1/c$ space group with $a = 4.5067(4)$ Å, $b = 19.1892(16)$ Å, $c = 12.0029(12)$ Å and $\beta = 98.178(8)°$. The structure is built of edge-sharing $[PbI_6]^{4-}$ octahedra forming parallel double chains along the [100] direction. MHy^+ cations are placed between the chains. The motif is stabilized via two kinds of N–H•••I hydrogen bonds. RT absorption studies reveal the excitonic absorption band at 413 nm (3.00 eV). The estimated energy band gap value E_g is 3.11 eV (400 nm). At 367 K $MHyPbI_3$ transforms to the new HT polymorph of $P2_1/m$ symmetry with $a = 8.895(1)$ Å, $b = 18.185(1)$ Å and $c = 13.197(1)$ Å and $\beta = 99.10(1)°$, that corresponds to the $2a$ monoclinic superstructure of the RT phase. The HT polymorph is metastable and returns to the pristine RT phase after ca. 50 min at room temperature.

1. Introduction

Recent years in materials science provided us with multiple studies on the hybrid organic-inorganic compounds. Such approach leads to employing new materials with fascinating and useful properties, taking advantages from both inorganic and organic constituents [1–5]. Among these compounds, hybrid organic-inorganic three-dimensional perovskites (3D HOIPs) with general formula ABX_3 where “A” is an organic cation, “B” is metal ion and “X” can be either organic or inorganic element/group are the object of intense studies [6–11]. To this day, 3D HOIPs with relatively small organic cations on “A” site, i.e., methylammonium (MA^+, 217 pm) and formamidinium (FA^+, 253 pm), lead cation (rarely tin, germanium) on “B” site and halide anion on “X” site proved to have fascinating properties, e.g., power conversion efficiency crossing 25% [12], high photoluminescence yields [13] and extraordinary mobility of charge carriers [14].

Very common way to explore new analogues of 3D HOIPs is through replacing organic cation on “A” site with e.g., hydrazinium (Hy^+, 217 pm) [15], imidazolium (IMI^+, 258 pm) [16] and dimethylammonium (DMA^+, 272 pm) [17–19]. However, one should note that the geometrical limitations (Goldschmidt Tolerance Factor, typically for perovskites TF = 0.8–1.0 [20]) and strong tendency to degradation limit the possibilities of such modification [21]. One of the most popular strategies for enhancing stability of HOIPs at ambient conditions is via dimensionality reduction [22]. Indeed, our group has recently reported two-dimensional hybrid compounds comprising methylhydrazinium cation (MHy^+, 264 pm), i.e., MHy_2PbI_4 and MHy_2PbBr_4 in which lead iodide or lead bromide layers are separated by MHy^+ cations [23,24]. We have also reported 3D lead halide HOIPs – $MHyPbBr_3$ [25] and $MHyPbCl_3$ [26]. Furthermore, using mixed-halide approach, $MHyPbBr_xCl_{3-x}$ crystals with 3D network were successfully synthesized [27].

Nevertheless, 3D HOIP with MHy^+ cation containing iodine, i.e., $MHyPbI_3$ has not been obtained yet, despite more suitable TF value (1.01) comparing to other halides – 1.03 (1.05) for $MHyPbBr_3$ ($MHyPbCl_3$). The anti-solvent crystallization conducted towards 3D $MHyPbI_3$ leads only to yellow needle-like crystals with 1D inorganic substructure. The same phase forms also as a main product of the $MHyPbBr_xI_{3-x}$ 3D HOIPs synthesis. Thus, the aim of this study is to describe in detail the synthesis and crystal structure of $MHyPbI_3$ needle-like phase based on single-crystal X-ray diffraction (SCXRD). Raman and powder X-ray diffraction (PXRD) experiments were made in order to examine purity of the bulk sample. DSC and high-temperature powder diffraction were used to examine phase transitions. We also apply RT absorption spectra measurements in order to investigate the optical properties and to calculate the energy band gap (E_g) value.

---

* Corresponding author at: Institute of Low Temperature and Structure Research, Polish Academy of Sciences, Okólna str. 2, 50-422 Wrocław, Poland.
E-mail address: d.drozdowski@intibs.pl (D. Drozdowski).

https://doi.org/10.1016/j.molstruc.2021.131660

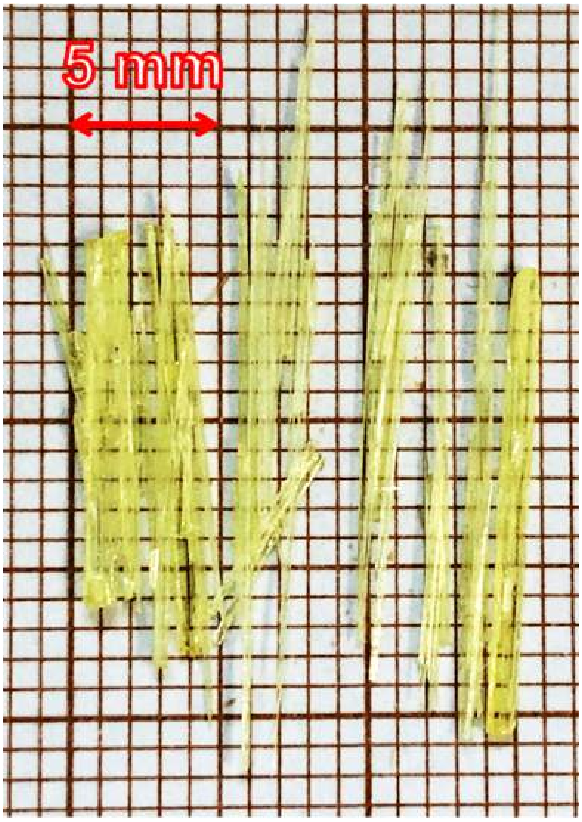

Fig. 1. Photograph of $MHyPbI_3$ needle-like phase on graph paper.

1.1. Experimental methods

Materials. PbI_2 (98%, Sigma-Aldrich), hydroiodic acid (57 wt% in H_2O, Sigma-Aldrich), methylhydrazine (98%, Sigma-Aldrich), and methyl acetate (99.5%, Sigma-Aldrich) were commercially available and used without further purification.

Synthesis. Crystals of $MHyPbI_3$ were grown using antisolvent crystallization. Hydroiodic acid was added dropwise under continuous stirring to mixture containing 10 mmol of PbI_2 and 10 mmol of methylhydrazine until complete dissolution of the mixture. The clear solution was transferred into glass vial and this vial was placed in a second, larger vial containing methyl acetate. The lid of the outer vial was thoroughly sealed, whereas the lid of the inner vial was loosened in order to allow diffusion of methyl acetate into the precursor solution. Yellow needle-like crystals (Fig. 1) with the length of 5–25 mm and diameter of 0.1–0.5 mm were harvested after 2–3 days, filtered from a mother liquid, and dried at RT. Analogously, single crystals of $MHyPbBr_xI_{3-x}$ were grown with the use of antisolvent crystallization. In this case the precursor contained 10 mmol mixture of $PbBr_2$ and PbI_2 in different ratio to a solution containing 10 mmol of methylhydrazine dissolved in 5 mL of HBr and HI (volumetric ratio adequate to the ratio of lead halides). After 5 min of continuous stirring at RT, the precursor solution became clear. For the iodine rich lead halide mixtures only yellow needle-like crystals have grown. SCXRD measurements proved the same crystal structure as 1D $MHyPbI_3$ (see Results and Discussion section) but with mixed occupancy of Br and I on halide sites. When increasing bromine contribution, additional phase of orange plates appears, associated with $MHyPbBr_xI_{3-x}$ 3D perovskites [27].

Raman spectra were measured using Bruker FT MultiRam spectrometer with the YAG:Nd laser excitation (1064 nm) and were recorded with a spectral resolution of 2 cm^{-1}.

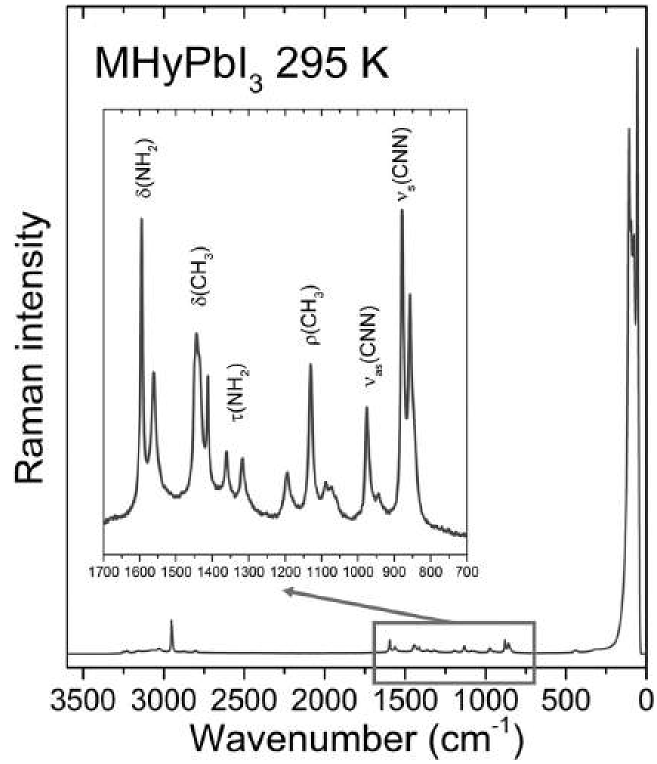

Fig. 2. Room temperature Raman spectra of $MHyPbI_3$ measured in the 3600–50 cm^{-1} wavenumber range.

Powder XRD (PXRD) pattern was obtained on an X'Pert PRO X-ray diffraction system equipped with a PIXcel ultrafast line detector. The powder was measured in the reflection mode, using CuKα radiation. High temperature (HT) experiments were performed with Anton Paar Oven Chamber.

Single-crystal X-ray diffraction (SCXRD) experiments were carried out with MoKα radiation using an Xcalibur, Atlas diffractometer. Absorption was corrected for by multi-scan methods, CrysAlis PRO 1.171.39.46 (Rigaku Oxford Diffraction, 2018). The room-temperature crystal structure was solved in Olex2 1.3 using SHELXT-2014/4 [28] and refined with SHELXL-2018/3 [29]. Empirical absorption correction using spherical harmonics, implemented in SCALE3 ABSPACK scaling algorithm was applied. H atom parameters were constrained. The HT data collection of the diffraction intensities was infeasible, due to the sample decomposition above 360 K.

RT absorption spectra was measured using the Varian Cary 5E UV–Vis-NIR spectrophotometer.

DSC measurements were performed using a Mettler Toledo DSC-1 calorimeter with a high resolution of 0.4 μW. Nitrogen was used as a purging gas, and the heating and cooling rates were 5 K/min.

2. Results and discussion

Initial characterization of the $MHyPbI_3$ needle phase using Raman spectroscopy reveals the existence of characteristic bands (Fig. 2) reported before for $MHyPbBr_3$ [25]. These bands are associated with vibrations of MHy^+ cation, i.e., scissoring (δ) and twisting (τ) of NH_2 group, scissoring (δ) and rocking (ρ) of CH_3 group and symmetric (ν_s) and antisymmetric (ν_s) stretching of CNN group. In addition, several sharp bands below 200 cm^{-1} are observed, associated with lattice vibrations. However, the shape of these bands differs from that recorded in $MAPbI_3$, in which a broad band at low frequencies is present, due to highly dynamic nature

Table 1
Selected experimental details of $MHyPbI_3$ (M_r = 634.98, Z = 4).

Crystal data	
Crystal system, space group	Monoclinic, $P2_1/c$
Temperature (K)	293
a, b, c (Å)	4.5067 (4), 19.1892 (16), 12.0029 (12)
β (°)	98.178 (8)
V (Å^3)	1027.45 (17)
Z	4
μ (mm^{-1})	25.36
Crystal size (mm)	0.22 × 0.04 × 0.03
Data collection	
T_{min}, T_{max}	0.599, 1.000
No. of measured, independent and observed [$I > 2\sigma(I)$] reflections	3599, 2051, 1557
R_{int}	0.031
$(\sin\theta/\lambda)_{max}$ (Å^{-1})	0.625
Refinement	
$R[F^2 > 2\sigma(F^2)]$, $wR(F^2)$, S	0.042, 0.055, 0.98
No. of reflections	2051
No. of parameters	67
No. of restraints	1
$\Delta\rho_{max}$, $\Delta\rho_{min}$ (e Å^{-3})	1.52 – 1.03

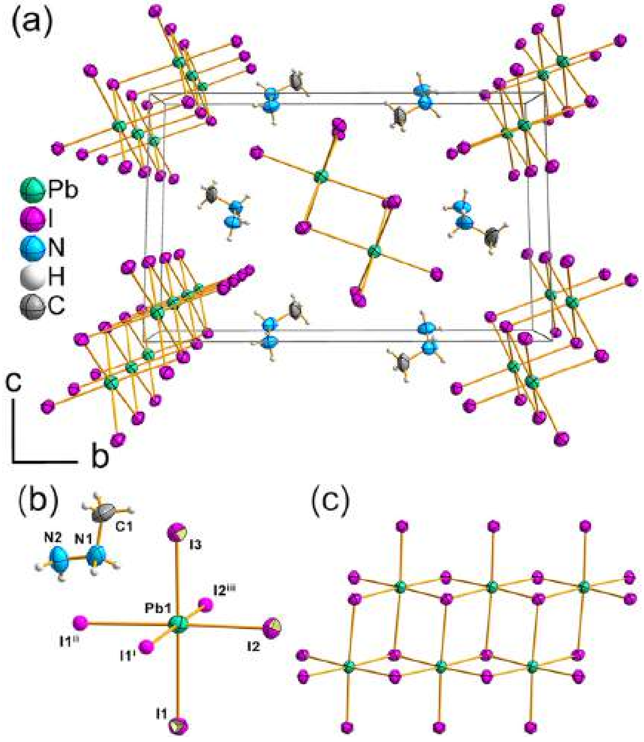

Fig. 3. (a) $MHyPbI_3$ crystal structure in central projection. (b) Main constituents of the structure: $[PbI_6]^{4-}$ edge-sharing octahedra and MHy^+ cation. (c) Octahedra forming double chains propagating along [100] direction.

Table 2
Selected geometric parameters (Å, º).

Pb1–I1^i	3.2892 (10)	Pb1–I2	3.1770 (9)
Pb1–I1	3.4383 (9)	Pb1–I2^{iii}	3.1615 (10)
Pb1–I1^{ii}	3.2924 (10)	Pb1–I3	3.0709 (9)
I1^{ii}–Pb1–I1	86.46 (2)	I3–Pb1–I1^i	90.00 (2)
I1^i–Pb1–I1	93.02 (2)	I3–Pb1–I1^{ii}	91.92 (2)
I1^i–Pb1–I1^{ii}	86.43 (2)	I3–Pb1–I2^{iii}	91.18 (2)
I2^{iii}–Pb1–I1^{ii}	91.57 (2)	I3–Pb1–I2	89.18 (2)
I2–Pb1–I1^i	91.35 (2)	Pb1^i–I1–Pb1^{ii}	86.43 (2)
I2^{iii}–Pb1–I1	85.74 (2)	Pb1^{ii}–I1–Pb1	93.54 (2)
I2–Pb1–I1	92.56 (2)	Pb1^i–I1–Pb1	86.98 (2)
I2^{iii}–Pb1–I2	90.63 (3)	Pb1^{iv}–I2–Pb1	90.63 (3)

Symmetry codes: (i) -*x* + 1, -*y* + 1, -*z* + 1; (ii) -x, -*y* + 1, -*z* + 1; (iii) x-1, y, z; (iv) *x* + 1, y, z.

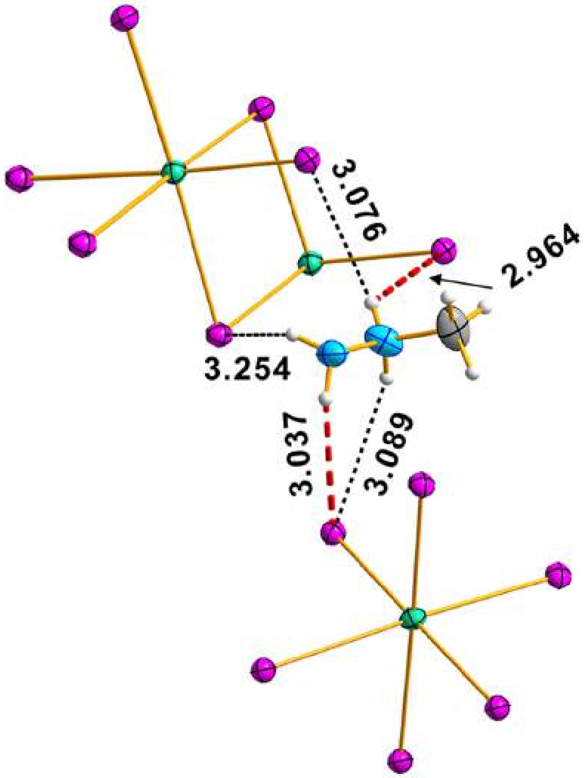

Fig. 4. The intermolecular interactions between the $[PbI_6]^{4-}$ octahedra and MHy^+cations – hydrogen bonds (red dashed lines) and weaker contacts (black dotted lines).

of MA^+ cation in RT phase [30]. This suggests that MHy^+ cation is ordered in the structure of $MHyPbI_3$ and does not exhibit any significant thermally induced motions.

According to SCXRD studies (main experimental details in Table 1), $MHyPbI_3$ crystallizes in monoclinic, centrosymmetric $P2_1/c$ space group (a = 4.5067(4) Å, b = 19.1892(16) Å, c = 12.0029(12) Å and β = 98.178(8)°). The motif (Fig. 3a) is composed of parallel double chains of edge-sharing $[PbI_6]^{4-}$ octahedra propagating along the [100] direction with the MHy^+ cations placed in between (Fig. 3b, c). In the octahedra, iodine atoms are in three inequivalent positions and thus, Pb – I bond lengths are not equal and spread in the range of 3.0709(9)–3.4383(9) Å (Table 2). Also, the I – Pb – I_{cis} angles slightly differ from 90º. In order to evaluate the degree of distortion, the octahedra angle variance (σ^2) parameter was calculated using Fleet's approach [31]. The σ^2 is equal to 6.32 deg^2 and it is significantly lower in comparison to 3D perovskites comprising MHy^+, i.e., 14 deg^2 and 301 deg^2 for $MHyPbBr_3$ [25], and 21 deg^2 and 314 deg^2 for $MHyPbCl_3$ [26], and slightly lower than in 2D analogue – MHy_2PbI_4 (11.87 deg^2 for more distorted octahedra) [23]. Therefore, low σ^2 value indicates that in 1D $MHyPbI_3$ the $[PbI_6]^{4-}$ units are less distorted and the cations does not affect remarkably the symmetry of the octahedra.

The MHy^+ amines interact with inorganic chains through hydrogen-bond interactions. Such interaction can be expressed through the N1–H1A···I3 and N2–H2B···I3^i (i: x-1, -y+3/2, z+1/2) hydrogen bonds (HBs, red dashed lines in Fig. 4, geometric parameters in Table 3) with H···A (D···A) distances of 2.96 (3.56) Å and 3.04 (3.48) Å, respectively. Apart from hydrogen bonding, the weaker contacts with H···A (D···A) distances below 3.28 (4.25) Å (black dotted lines in Fig. 4) between N1–H1A···I3^i, N1–H1B···I3^{ii} and N2–H2A···I1^{iii} (i: -x+1, y, z, ii: x, -y+3/2, z+1/2, iii: -x, -y+1,

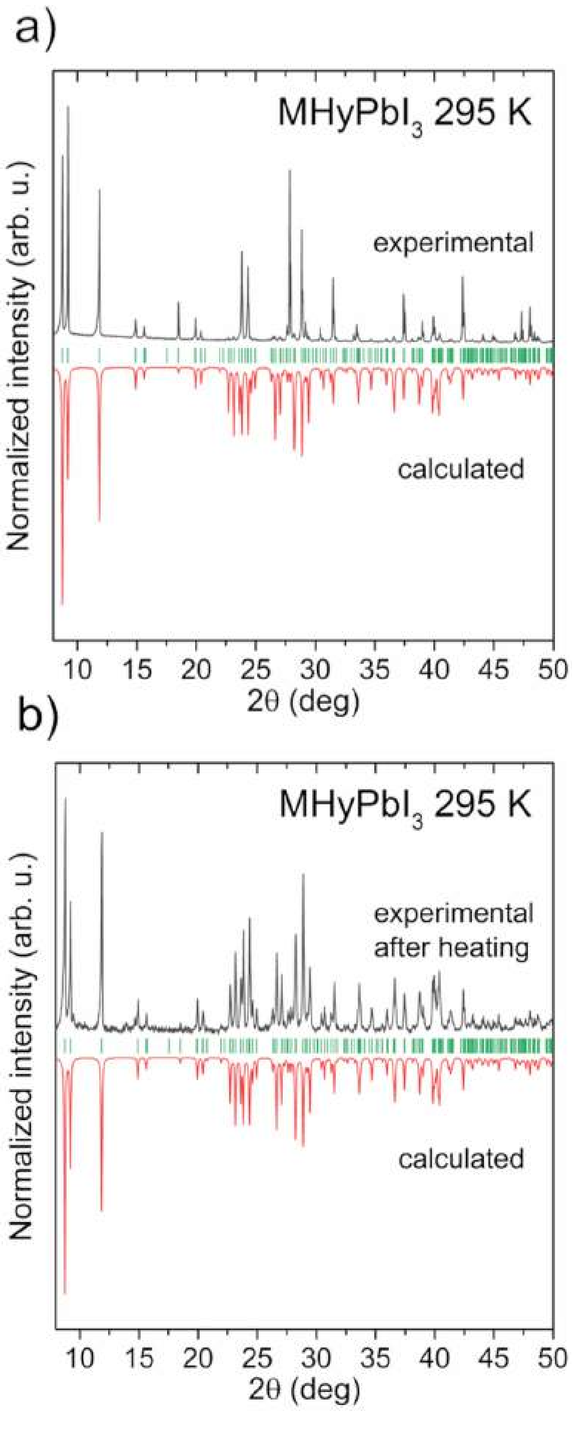

Fig 5. Powder X-ray diffraction (PXRD) patterns of $MHyPbI_3$ at room temperature of (a) virgin sample and (b) sample heated for 2 h in 373 K and measured after 24 h.

Table 3
Selected hydrogen bonds parameters (Å, º).

D–H···A	D–H (Å)	H···A (Å)	D···A (Å)
N1–H1A···I3	0.89	2.964	3.565 (9)
N2–H2B···I3^{i}	0.86	3.037	3.483 (10)

Symmetry codes: (i) x-1, -*y* + 3/2, *z* + 1/2.

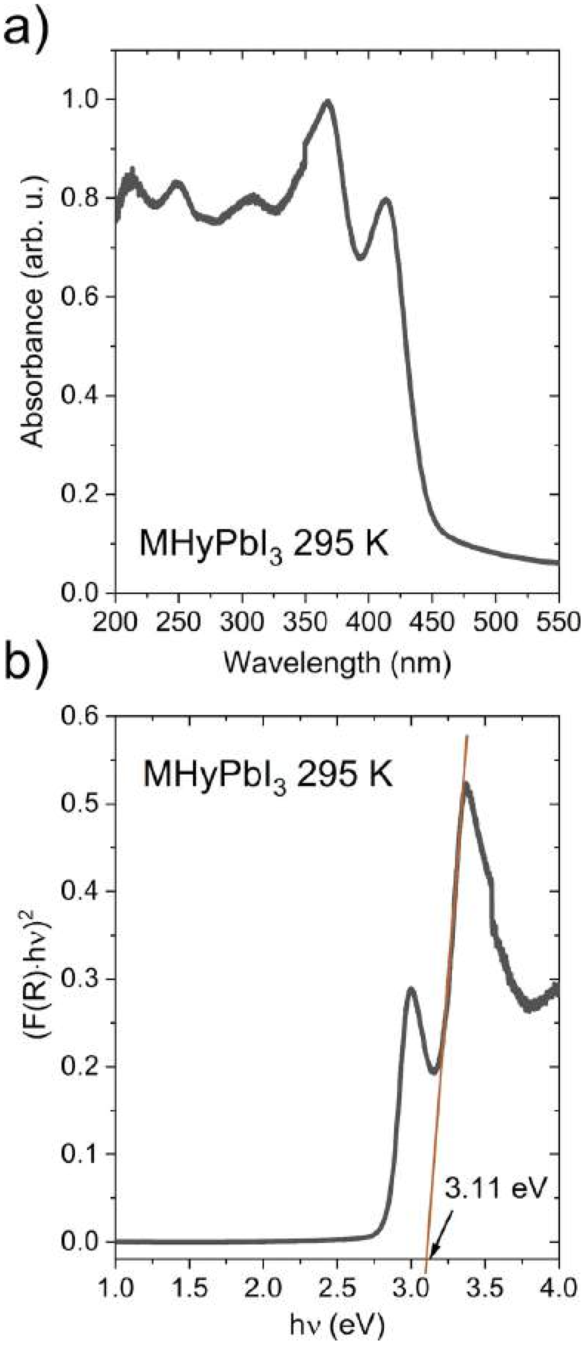

Fig. 6. (a) RT diffuse absorption spectra of $MHyPbI_3$ and (b) graphical presentation of the Kubelka-Munk function.

-z+1) cannot be omitted. All the above interactions stabilize the crystal structure. The number of interactions that may be classified as HBs is lower in the chain-structure of $MHyPbI_3$ compared to the RT phase of layered MHy_2PbI_4. Also, the strength of these interactions is lower. In the former material the H···A (D···A) distances are of 2.17–2.82 (3.04–3.62) Å. Therefore, lowering of dimensionality in the hybrid compounds with MHy^+ cation weakens the interatomic forces between organic and inorganic constituents.

Similar crystal packing to $MHyPbI_3$ has been reported by Campbell et al. for hydrazinium lead iodide ($HyPbI_3$) [32]. Contrarily to the structure reported herein, α-$HyPbI_3$ phase is orthorhombic with Pb – I distances of 3.025(3) – 3.3983(13) Å. Higher symmetry and slightly shorter Pb – I bond lengths can be explained by the difference in the intermolecular interactions between organic and

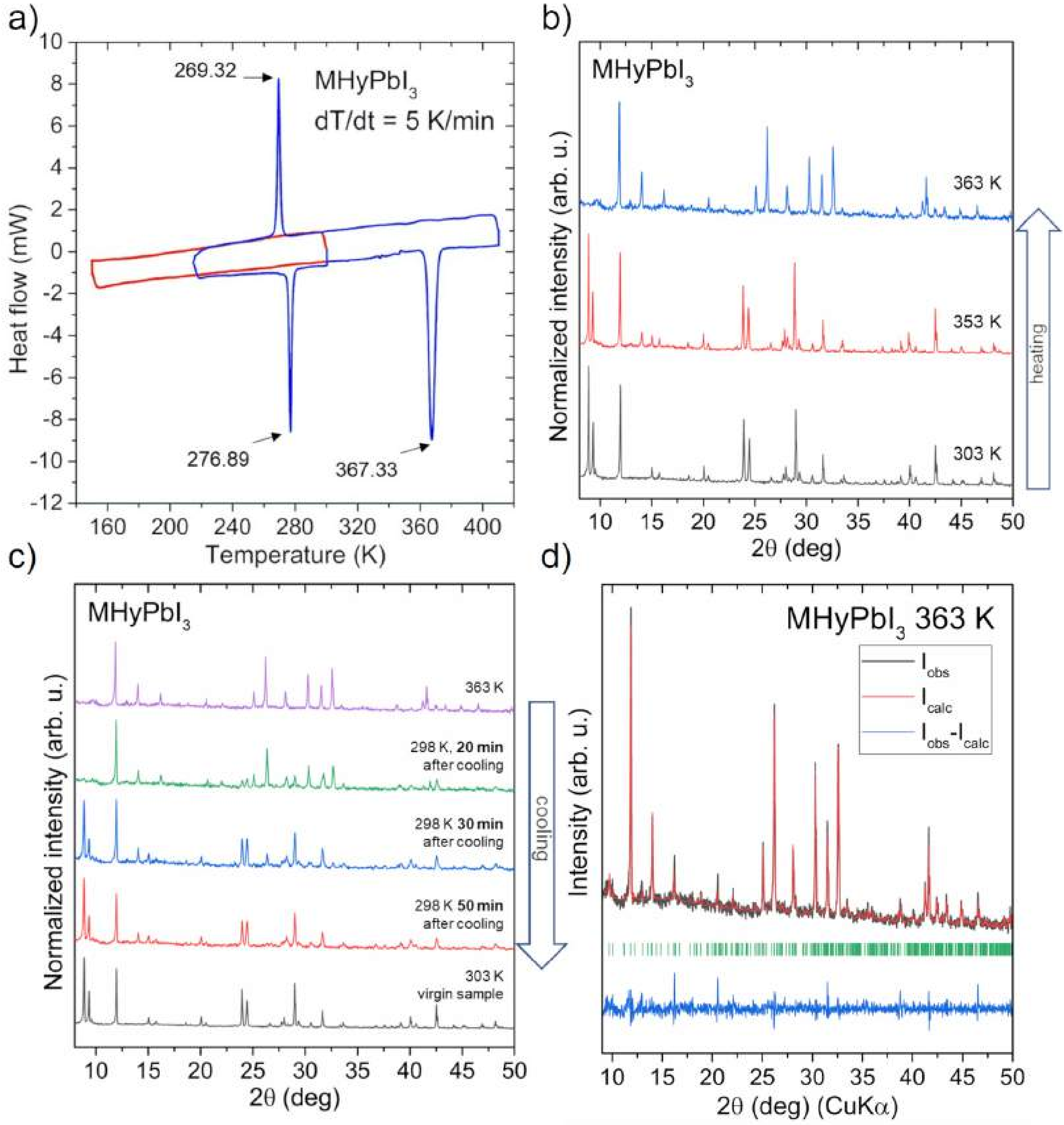

Fig 7. (a) DSC traces for the MHyPbI$_3$ sample in colling to 150 K followed by heating to 410 K (red and blue traces, respectively). (b,c) HT-PXRD patterns of MHyPbI$_3$. (d) The Le Bail refinement of the PXRD profile.

inorganic moieties. The determining factors are the size of cations and the distribution of the proton donor centres in the structure. Both amines differ in radius and geometry - the radius of Hy$^+$ cation (217 pm) is smaller, comparing to MHy$^+$ (264 pm). Additionally, the methyl group of MHy$^+$ is a steric hindrance that prevents the rotations of the whole amine along the NH$_2$–NH$_2$ bond, which is not the case of Hy$^+$. The latter amine may easily rotate and thus, change the direction of possible N–H···I HBs. This dynamic disorder results in the disorder of iodine atoms that interact with amines, while in MHyPbI$_3$ all atoms are ordered. Other analogous crystal structures were reported for MAPbI$_3$·DMF [33], (NH$_4$)PbI$_3$ [34] and (C$_6$H$_{10}$N$_2$)[PbI$_4$]·2H$_2$O [35].

The diffuse absorption of MHyPbI$_3$ was measured at RT with the use of powdered material. A good match of PXRD pattern (Fig. 5a) with the calculated model based on SXCRD measurements confirms the phase purity of the bulk sample. The differences between measured and calculated intensities, especially between 20° and 30° of 2θ diffraction angle arise from the preferred orientation effects. The absorption spectra are presented in Fig. 6a. As can be seen, the band representing the excitonic absorption is observed at 413 nm (3.00 eV). The absorption spectra were also used together with Kubelka-Munk relation to estimate the E$_g$ value of the studied crystal (Fig. 6b). By plotting $[F(R)\cdot h\nu]^2$ versus hν, the estimated $E_g = 3.11$ eV (400 nm). This value is larger than for MHy$_2$PbI$_4$ – 2.20 eV (564 nm) [23] and for other hybrid lead iodide compounds – 2.70 eV (459 nm) for HyPbI$_3$ [32] and 1.55 eV (800 nm) for the 3D perovskite MAPbI$_3$ [36].

In order to study thermal behavior of MHyPbI$_3$, the DSC measurements were performed. The obtained traces (Fig. 7a) show presence of a heat anomaly at 367 K upon heating with no adequate signal in the cooling mode. Besides, heat anomalies at 277 (269) K on heating (cooling) were observed exclusively for

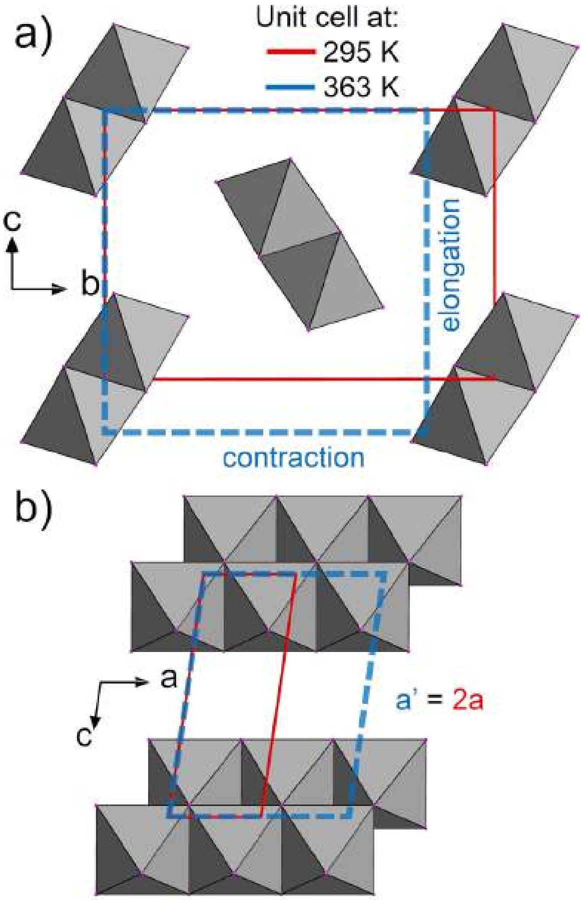

Fig 8. The structure transformations observed after the HT phase transition. View along (a) a axis and (b) b axis.

the samples heated above 367 K and then immediately cooled. The virgin sample (i.e., before the heat treatment), does not show any anomalies down to 150 K. Additionally, the low-temperature anomalies that are present for the immediately cooled sample do not appear after slow cooling. These observations point to the presence of a metastable phase that appears above $T_c = 367$ K and has its own, new sequence of phase-transitions (the low-temperature anomalies). This metastable phase transforms into initial, RT phase of the virgin crystal. To study in detail the temperature induced processes in $MHyPbI_3$ we performed HT-PXRD measurements. The results are presented in Fig. 7b-c. Above T_c at 367 K the crystal structure transforms to the new HT polymorph. The diffraction patterns of this new phase may be indexed in a monoclinic $P2_1/m$ symmetry and lattice parameters are equal to $a = 8.895(1)$ Å, $b = 18.185(1)$ Å and $c = 13.197(1)$ Å with $\beta = 99.10(1)°$, that corresponds to the $2a$ monoclinic superstructure of the RT phase. The Le Bail refinement of the profile (Fig. 7d) confirms a good match of the observed and calculated patterns in the chosen metrics and symmetry. It is worth noting that $P2_1/m$ symmetry is a maximal non-isomorphic supergroup of $P2_1/c$ for $a'=2a$ [37].

Doubling of the a-lattice parameter occurs without a fundamental change in the interatomic distances compared to the pristine phase (a small contraction of ca. 1.31% is observed). Bearing in mind that the a direction is the chains' propagation direction, we may suppose that the octahedral geometry of basic $[PbI_6]^{4-}$ units and the geometry of the chains change marginally. The foremost differences between the room temperature and HT phase are evident between the chains, as the b axis elongation by ca. 5.23% and the c axis contraction by ca. 9.89% results from the rearrangements of the chains' positions. Fig. 8 illustrates possible changes of the inorganic part of the structure at HT. The rearrangement of the structure most probably occurs in response to enhanced dynamics of the MHy^+ cations in HT phase.

One should note that the powder pattern confirming PT (blue trace in Fig. 7b) is recorded at lower temperature (363 K) than the PT temperature obtained from the DSC (367 K) measurements. This difference is caused by the fact that the sample measured by PXRD was heated directly from RT, while in DSC the heating run was preceded by cooling from RT. When the heating run in DSC measurements is performed without preceding cooling (Fig. S1 in the Supplementary materials), the PT temperature decreases to ~357 K, which lies in agreement with the PXRD experiments.

The restoration of the RT phase was also tracked by the PXRD experiments. It was recorded that the first traces of the virgin phase appear 20 min after cooling. The structure restores completely approx. 50 min after cooling. In between, the two-phase system is present. It is worth noting that after returning to the room temperature phase the PXRD pattern (Fig. 5b) fits much better to the calculated intensities generated from the model of the structure. This is because the high temperature transformation disturbs the preferred crystallite alignment observed for the thermally untreated material.

3. Conclusions

We report synthesis of the new hybrid organic-inorganic compound. $MHyPbI_3$ crystallizes in monoclinic, centrosymmetric $P2_1/c$ space group and consists of edge-sharing $[PbI_6]^{4-}$ octahedra forming parallel double chains along the [100] direction with MHy^+ cations placed in between. The motif is stabilized via N–H···I hydrogen bonds. Thermal behavior studies reveal a metastable phase of $MHyPbI_3$ above $T_c = 367$ K with its own, new sequence of phase-transitions, i.e., low-temperature anomalies at 277 (269) K upon heating (cooling). The metastable HT polymorph adopts monoclinic $2a$ superstructure of $P2_1/m$ space group which totally returns to the pristine RT phase after approx. 50 min. Unlike the perovskite counterparts with MHy^+, $MHyPbI_3$ chain phase does not show photoluminescence activity neither at RT nor 77 K. The energy band gap value is equal to 3.11 eV. Since the reported phase is the main (or the only) product of the methylhydrazinium lead iodide 3D perovskites synthesis, it is crucial to understand the nature of the thermodynamically preferred alignments in the continual searches for the new hybrid organic-inorganic perovskite analogues.

Declaration of Competing Interest

The authors declare that they have no known competing financial interests or personal relationships that could have appeared to influence the work reported in this paper.

CRediT authorship contribution statement

Dawid Drozdowski: Conceptualization, Methodology, Formal analysis, Investigation, Writing – original draft, Writing – review & editing, Visualization, Validation, Data curation. **Anna Gągor:** Writing – review & editing, Validation, Visualization, Methodology, Supervision, Formal analysis, Data curation. **Mirosław Mączka:** Resources, Funding acquisition, Project administration, Methodology.

Acknowledgements

This research was supported by the National Science Center (Narodowe Centrum Nauki) in Poland under project No. 2019/35/B/ST5/00043.

Supplementary materials

Crystallographic Information File (CIF), SCXRD experimental conditions and final refinement parameters of the structure at 295 K can be obtained from Cambridge Structural Database (CCDC, no. 2079119). Supplementary material associated with this article containing the additional DSC measurements and DTA plot of the reported compound can be found, in the online version, at doi:10.1016/j.molstruc.2021.131660.

References

[1] A.C.S. Alcântara, M. Darder, P. Aranda, E. Ruiz-Hitzky, Zein-fibrous clays biohybrid materials, Eur. J. Inorg. Chem. 2012 (2012) 5216–5224, doi:10.1002/ejic.201200582.

[2] L. Nicole, C. Laberty-Robert, L. Rozes, C. Sanchez, Hybrid materials science: a promised land for the integrative design of multifunctional materials, Nanoscale 6 (2014) 6267–6292, doi:10.1039/c4nr01788a.

[3] M.W.A. MacLean, L.M. Reid, X. Wu, C.M. Crudden, Chirality in ordered porous organosilica hybrid materials, Chem. An Asian J. 10 (2015) 70–82, doi:10.1002/asia.201402682.

[4] D.B. Mitzi, C.A. Feild, Z. Schlesinger, R.B. Laibowitz, Transport, optical, and magnetic properties of the conducting halide perovskite $CH_3NH_3SnI_3$, J. Solid State Chem. 114 (1995) 159–163, doi:10.1006/jssc.1995.1023.

[5] A. Mller-Schiffmann, H. Sticht, C. Korth, Hybrid compounds: from simple combinations to nanomachines, BioDrugs 26 (2012) 21–31, doi:10.2165/11597630-000000000-00000.

[6] B. Saparov, D.B. Mitzi, Organic-inorganic perovskites: structural versatility for functional materials design, Chem. Rev. 116 (2016) 4558–4596, doi:10.1021/acs.chemrev.5b00715.

[7] A. Poglitsch, D. Weber, Dynamic disorder in methylammoniumtrihalogenoplumbates (II) observed by millimeter-wave spectroscopy, J. Chem. Phys. 87 (1987) 6373–6378, doi:10.1063/1.453467.

[8] E. Sletten, L.H. Jensen, The crystal structure of dimethylammonium copper(II) formate, $NH_2(CH_2)_2[Cu(OOCH)_3]$, Acta Crystallogr. Sect. B Struct. Crystallogr. Cryst. Chem. 29 (1973) 1752–1756, doi:10.1107/s0567740873005480.

[9] M.L. Tong, J. Ru, Y.M. Wu, X.M. Chen, H.C. Chang, K. Mochizuki, S. Kitagawa, Cation-templated construction of three-dimensional α-Po cubic-type [M(dca)3]- networks. Syntheses, structures and magnetic properties of A[M(dca)3] (dca = dicyanamide; for A = benzyltributylammonium, M = Mn2+, Co2+; for A = benzyltriethylammonium, M = Mn2, New J. Chem. 27 (2003) 779–782. doi:10.1039/b300760j.

[10] X.H. Zhao, X.C. Huang, S.L. Zhang, D. Shao, H.Y. Wei, X.Y. Wang, Cation-dependent magnetic ordering and room-temperature bistability in azido-bridged perovskite-type compounds, J. Am. Chem. Soc. 135 (2013) 16006–16009, doi:10.1021/ja407654n.

[11] W. Li, Z. Wang, F. Deschler, S. Gao, R.H. Friend, A.K. Cheetham, Chemically diverse and multifunctional hybrid organic-inorganic perovskites, Nat. Rev. Mater. 2 (2017) 16099, doi:10.1038/natrevmats.2016.99.

[12] R. Lin, K. Xiao, Z. Qin, Q. Han, C. Zhang, M. Wei, M.I. Saidaminov, Y. Gao, J. Xu, M. Xiao, A. Li, J. Zhu, E.H. Sargent, H. Tan, Monolithic all-perovskite tandem solar cells with 24.8% efficiency exploiting comproportionation to suppress Sn(ii) oxidation in precursor ink, Nat. Energy. 4 (2019) 864–873, doi:10.1038/s41560-019-0466-3.

[13] H. Mehdi, A. Mhamdi, R. Hannachi, A. Bouazizi, $MAPbBr_3$ perovskite solar cells: via a two-step deposition process, RSC Adv. 9 (2019) 12906–12912, doi:10.1039/c9ra02036e.

[14] S.D. Stranks, G.E. Eperon, G. Grancini, C. Menelaou, M.J.P. Alcocer, T. Leijtens, L.M. Herz, A. Petrozza, H.J. Snaith, Electron-hole diffusion lengths exceeding 1 micrometer in an organometal trihalide perovskite absorber, Science 342 (80) (2013) 341–344, doi:10.1126/science.1243982.

[15] A.F. Akbulatov, L.A. Frolova, D.V. Anokhin, K.L. Gerasimov, N.N. Dremova, P.A. Troshin, Hydrazinium-loaded perovskite solar cells with enhanced performance and stability, J. Mater. Chem. A. 4 (2016) 18378–18382, doi:10.1039/c6ta08215g.

[16] A. Gabriel Tomulescu, L. Nicoleta Leonat, F. Neaţu, V. Stancu, V. Toma, S. Derbali, Ştefan Neaţu, A. Mihai Rostas, C. Beşleagă, R. Pătru, I. Pintilie, M. Florea, Enhancing stability of hybrid perovskite solar cells by imidazolium incorporation, Sol. Energy Mater. Sol. Cells 227 (2021) 111096, doi:10.1016/j.solmat.2021.111096.

[17] Y. Pei, Y. Liu, F. Li, S. Bai, X. Jian, M. Liu, Unveiling property of hydrolysis-derived $DMAPbI_3$ for perovskite devices: composition engineering, defect mitigation, and stability optimization, IScience 15 (2019) 165–172, doi:10.1016/j.isci.2019.04.024.

[18] M. Simenas, S. Balciunas, J.N. Wilson, S. Svirskas, M. Kinka, A. Garbaras, V. Kalendra, A. Gagor, D. Szewczyk, A. Sieradzki, M. Maczka, V. Samulionis, A. Walsh, R. Grigalaitis, J. Banys, Suppression of phase transitions and glass phase signatures in mixed cation halide perovskites, Nat. Commun. 11 (2020) 1–9, doi:10.1038/s41467-020-18938-z.

[19] C. Anelli, M.R. Chierotti, S. Bordignon, P. Quadrelli, D. Marongiu, G. Bongiovanni, L. Malavasi, Investigation of dimethylammonium solubility in $MAPbBr_3$ Hybrid perovskite: synthesis, crystal structure, and optical properties, Inorg. Chem. 58 (2019) 944–949, doi:10.1021/acs.inorgchem.8b03072.

[20] D.B. Mitzi, Synthesis, Structure, and Properties of Organic-Inorganic Perovskites and Related Materials, Progress in Inorganic Chemistry, 48, 1999, pp. 1–121, doi:10.1002/9780470166499.ch1.

[21] L. Chouhan, S. Ghimire, V. Biju, Blinking beats bleaching: the control of superoxide generation by photo-ionized perovskite nanocrystals, Angew. Chem. 131 (2019) 4929–4933, doi:10.1002/ange.201900061.

[22] C. Huo, B. Cai, Z. Yuan, B. Ma, H. Zeng, Two-dimensional metal halide perovskites: theory, synthesis, and optoelectronics, Small Methods 1 (2017) 1600018, doi:10.1002/smtd.201600018.

[23] M. Mączka, M. Ptak, A. Gągor, D. Stefańska, A. Sieradzki, Layered lead iodide of $[\text{Methylhydrazinium}]_2PbI_4$ with a reduced band gap: thermochromic luminescence and switchable dielectric properties triggered by structural phase transitions, Chem. Mater. 31 (2019) 8563–8575, doi:10.1021/acs.chemmater.9b03775.

[24] M. Mączka, J.K. Zaręba, A. Gągor, D. Stefańska, M. Ptak, K. Roleder, D. Kajewski, A. Soszyński, K. Fedoruk, A. Sieradzki, $[\text{Methylhydrazinium}]_2PbBr_4$, a ferroelectric hybrid organic-inorganic perovskite with multiple nonlinear optical outputs, Chem. Mater. 33 (2021) 2331–2342, doi:10.1021/acs.chemmater.0c04440.

[25] M. Mączka, M. Ptak, A. Gągor, D. Stefańska, J.K. Zaręba, A. Sieradzki, Methylhydrazinium lead bromide: noncentrosymmetric three-dimensional perovskite with exceptionally large framework distortion and green photoluminescence, Chem. Mater. 32 (2020) 1667–1673, doi:10.1021/acs.chemmater.9b05273.

[26] M. Mączka, A. Gagor, J.K. Zaręba, D. Stefanska, M. Drozd, S. Balciunas, M. Šimėnas, J. Banys, A. Sieradzki, Three-dimensional perovskite methylhydrazinium lead chloride with two polar phases and unusual second-harmonic generation bistability above room temperature, Chem. Mater. 32 (2020) 4072–4082, doi:10.1021/acs.chemmater.0c00973.

[27] D. Drozdowski, A. Gągor, D. Stefańska, J.K. Zaręba, K. Fedoruk, M. Mączka, A. Sieradzki, To be published - mixing halides in 3D methylhydrazinium lead halide perovskites: structural changes and effects on dielectric, linear and nonlinear optical properties entailed by the halide tuning, 2021.

[28] G.M. Sheldrick, SHELXT – integrated space-group and crystal-structure determination, Acta Crystallogr. Sect. A Found. Adv. 71 (2015) 3–8, doi:10.1107/S2053273314026370.

[29] G.M. Sheldrick, Crystal structure refinement with SHELXL, Acta Crystallogr. Sect. C Struct. Chem. 71 (2015) 3–8, doi:10.1107/S2053229614024218.

[30] P. Pistor, A. Ruiz, A. Cabot, V. Izquierdo-Roca, Advanced Raman spectroscopy of methylammonium lead iodide: development of a non-destructive characterisation methodology, Nat. Publ. Gr. (2016), doi:10.1038/srep35973.

[31] M.E. Fleet, Distortion parameters for coordination polyhedra, Mineral. Mag. 40 (1976) 531–533, doi:10.1180/minmag.1976.040.313.18.

[32] E.V. Campbell, B. Dick, A.L. Rheingold, C. Zhang, X. Liu, Z.V. Vardeny, J.S. Miller, Structures of a complex hydrazinium Lead Iodide, $(N_2H_5)_{15}Pb_3I_{21}$, Possessing $[Pb_2I_9]^{5-}$, $[PbI6]^{4-}$, and I− Ions and α- and β-$(N_2H_5)PbI_3$, Chem. A Eur. J. 24 (2018) 222–229, doi:10.1002/chem.201704356.

[33] F. Hao, C.C. Stoumpos, Z. Liu, R.P.H. Chang, M.G. Kanatzidis, Controllable perovskite crystallization at a gas-solid interface for hole conductor-free solar cells with steady power conversion efficiency over 10%, J. Am. Chem. Soc. 136 (2014) 16411–16419, doi:10.1021/ja509245x.

[34] L.Q. Fan, J.H. Wu, NH_4PbI_3, Acta Crystallogr. Sect. E Struct. 63 (2007) Reports Online i189–i189, doi:10.1107/S1600536807050581.

[35] A. Lemmerer, D.G. Billing, Two packing motifs based upon chains of edge-sharing PbI_6 octahedra, Acta Crystallogr. Sect. C Cryst. Struct. Commun. 62 (2006) m597–m601, doi:10.1107/S0108270106039746.

[36] F. Hao, C.C. Stoumpos, R.P.H. Chang, M.G. Kanatzidis, Anomalous band gap behavior in mixed Sn and Pb perovskites enables broadening of absorption spectrum in solar cells, J. Am. Chem. Soc. 136 (2014) 8094–8099, doi:10.1021/ja5033259.

[37] T. Hahn, International Tables for Crystallography Volume A: Space-Group Symmetry, Fifth, Springer, 2005, doi:10.1107/97809553602060000100.

INORGANIC CHEMISTRY
FRONTIERS

CHINESE CHEMICAL SOCIETY
ROYAL SOCIETY OF CHEMISTRY

RESEARCH ARTICLE

View Article Online
View Journal | View Issue

Cite this: *Inorg. Chem. Front.*, 2023, **10**, 7222

Zero-dimensional mixed-cation hybrid lead halides with broadband emissions†

Mirosław Mączka, * Dawid Drozdowski, Dagmara Stefańska and Anna Gągor

Received 30th August 2023,
Accepted 20th October 2023

DOI: 10.1039/d3qi01749d

rsc.li/frontiers-inorganic

Zero-dimensional (0D) metal halides have received significant attention in recent years due to their attractive light-emitting properties derived from the presence of isolated building units. Here we report the synthesis, crystal structures, and linear optical and phonon properties of three newcomers to the family of 0D lead halides – $Cs_2MHy_2PbBr_6$, $Cs_2MHy_2PbI_6$ and $Cs_2MHy_2PbBr_3I_3$ (MHy^+ = methylhydrazinium) which are the first examples of 0D lead halides with mixed cations. These compounds crystallize in the orthorhombic *Cmce* structure with isolated PbX_6^{4-} octahedral units and statistically disordered MHy^+ cations. X-ray diffraction revealed the selective substitution of halide ions in $Cs_2MHy_2PbI_3Br_3$ with Br^- occupying the positions of ions acting as hydrogen-bond (HB) acceptors and I^- occupying non-interacting sites. This preferential occupation leads to a giant increase of the octahedral distortion (27- and 249-fold, compared to the bromide and iodide, respectively). Raman spectra confirm the static disorder of MHy^+ and preferential occupation of halide sites. With the use of linear optical measurements, we demonstrate that all compounds exhibit broadband orange-yellow emission attributed to self-trapped excitons (STEs). The observed Stokes shifts of $Cs_2MHy_2PbBr_6$ and $Cs_2MHy_2PbBr_3I_3$ are record large among 0D lead halides. A large increase of the octahedral distortion due to the preferential occupation of halide sites in $Cs_2MHy_2PbBr_3I_3$ is reflected in the spectra by broadening and red-shift of its emission. This study paves the way for developing a new class of light-emitting 0D lead halides by synthesizing mixed-cation analogues.

1. Introduction

Inorganic and hybrid organic–inorganic lead halides have attracted a lot of attention in recent years due to their functional properties. In this respect, three-dimensional (3D) perovskites of general formula $APbX_3$ (A = methylammonium (MA^+), formamidinium (FA^+), aziridinium (AZR^+), MHy^+, Cs^+; X = Cl^-, Br^-, I^-) are attractive solar cell, light-emitting and nonlinear optical (NLO) materials.[1–11] These 3D perovskites can be obtained for a few above-mentioned small cations only whereas for other organic cations two-dimensional (2D), one-dimensional (1D) and discrete (0D) structures can be prepared. Lowering of dimensionality leads to widening of the bandgap and increase of the exciton binding energy, limiting their photovoltaic performance.[12–14] Low-dimensional lead halides are, however, attractive materials for NLO,[15,16] dielectric switching,[17] ferroelectric[16,18] and light-emitting applications.[13,14,19,20] It is worth adding that low dimensional structures can also be obtained using a mixed cation approach. The most famous families of compounds containing two cations are the alternating cations in the interlayer (ACI, $(B)A_nPb_nX_{3n+1}$) perovskites as well as multilayered ($n \geq 2$) Dion–Jacobson (DJ, $A''A_{n-1}Pb_nX_{3n+1}$) and Ruddlesden–Popper (RP, $A'_2A_{n-1}Pb_nX_{3n+1}$) compounds (A′ and A″ are large monovalent and divalent cations, respectively; B is a small or large monovalent cation; *n* indicates the number of octahedral layers within each inorganic slab).[12,15,18,19,21] The two-cation approach in these layered perovskites allows the narrowing of the bandgap, which is beneficial for solar cell applications.[12] This approach is also an efficient way for tuning photoluminescence (PL) colour as well as inducing polar (ferro- or antiferroelectric) order and second-order NLO properties.[15,18,19,21,22] Although numerous examples of layered lead halide perovskites comprising two cations have been reported, we are not aware of any mixed-cation analogues in the family of 1D and 0D lead halides.

The PL of 3D and non-corrugated 2D lead halides usually consists of narrow bands attributed to free exciton (FE) recombination.[10,11,13,14,16,19] Unfortunately, this narrow emis-

---

*W. Trzebiatowski Institute of Low Temperature and Structural Research of the Polish Academy of Sciences, Okólna 2, 50-422 Wroclaw, Poland.
E-mail: M.Maczka@intibs.pl*

† Electronic supplementary information (ESI) available: Tables S1–S6: details of structural parameters, Raman wavenumbers together with the proposed assignment and comparison of optical parameters for 0D lead halides. Fig. S1–S11: powder X-ray diffractograms, temperature evolution of lattice parameters for $Cs_2MHy_2PbBr_6$, Raman spectra, PL excitation spectra, decay curves and the logarithm of $I_0/I - 1$ as a function of $1/kT$ plots for $Cs_2MHy_2PbX_6$ compounds. CCDC 2269853–2269855. For ESI and crystallographic data in CIF or other electronic format see DOI: https://doi.org/10.1039/d3qi01749d

sion has a relatively low PL quantum yield (PLQY). Lowering the dimensionality to 1D and 0D promotes self-trapping of excitons, leading to the appearance of heavily Stokes shifted broadband PL from STEs with high PLQYs.[12–14,23] In particular, high PLQYs can be realized in 0D lead halides since due to the fact that they are composed of isolated PbX_6^{4-} octahedra or lead halide clusters, they usually have a strong exciton binding energy that increases radiative recombination.[12–14,23] 0D perovskites are also much more stable under ambient conditions than 3D, 2D or 1D analogues, which is beneficial for applications.[13] The stability can be further increased by partially replacing organic cations with inorganic ones, as reported for the lead-free $DFPD_2CsBiI_6$ compound (DFPD = 4,4-difluoropiperidine).[24]

Although 0D metal halides have received much attention in recent years, the number of discovered 0D lead halides is still scarce. The most famous are all-inorganic Cs_4PbX_6 compounds, composed of isolated PbX_6 octahedra surrounded by Cs^+ ions.[13,23,25–27] PL was reported for Cs_4PbBr_6 but it consisted of a relatively narrow green emission.[13,23,25–27] Therefore, its mechanism is still controversial and some reports attributed it to $CsPbBr_3$ impurities, inclusion-induced emission or defect state-induced emission.[23] Recent studies supported the assignment of the green emission to the presence of luminescent $CsPbBr_3$ inclusions.[27] Among iodides and chlorides, the known examples are $MA_4PbI_6\cdot 2H_2O$, which consists of isolated octahedral units,[28] $(C_9NH_{20})_7(PbCl_4)Pb_3Cl_{11}$, which consists of $PbCl_4^{2-}$ tetrahedra and $Pb_3Cl_{11}^{5-}$ trimer clusters,[29] and $(TAE)_2[Pb_2Cl_{10}]Cl_2$ (TAE = tris(2-aminoethyl) ammonium), containing isolated lead chloride edge sharing bioctahedra $Pb_2Cl_{10}^{6-}$.[30] $(C_9NH_{20})_7(PbCl_4)Pb_3Cl_{11}$ exhibited blue emission near 470 nm with a very high PLQY (near 83%),[29] whereas $(TAE)_2[Pb_2Cl_{10}]Cl_2$ showed white emission.[30] There are also several bromides composed of isolated $PbBr_6^{4-}$ octahedra,[31] isolated $PbBr_4^{2-}$ units,[32,33] and lead–bromide clusters,[34–36] which exhibit broadband emissions.

In this paper, we report a new approach to developing 0D lead halides by employing both organic (MHy^+) and inorganic (Cs^+) cations. We investigate the crystal structures and optical properties of the obtained 0D mixed organic–inorganic lead halides.

2. Experimental section

2.1. Synthesis

In order to obtain single crystals of $Cs_2MHy_2PbBr_6$, 1 mmol $PbBr_2$ (98%, Sigma Aldrich) was dissolved in 8 mL of HBr (48 wt% in H_2O, Sigma-Aldrich). Then 2 mmol Cs_2CO_3 and 1 mL of methylhydrazine (98%, Sigma Aldrich) were added under vigorous stirring. The solution was heated to 50 °C and then 10 mL of propylene carbonate (PC, 99.7%, Sigma-Aldrich) was added. The reaction mixture was cooled down to room temperature (RT) and left undisturbed. Colourless transparent crystals, which grew at the bottom of the glass vial, were separated from the mother liquid, washed 3 times with ethanol and dried at RT. Colourless $Cs_2MHy_2PbBr_3I_3$ and light yellow $Cs_2MHy_2PbI_6$ crystals were grown using the same procedure but with smaller amounts of PC, *i.e.*, 7 and 5 mL, respectively. PbI_2 (99%, Sigma Aldrich) and HI (57 wt% in H_2O, stabilized with H_3PO_2) were purchased from Sigma-Aldrich.

We also grew single crystals of inorganic $CsPbBr_3$ and Cs_4PbBr_6. In order to grow single crystals of $CsPbBr_3$, 5 mmol CsBr (99.9%, Sigma-Aldrich) and 6 mmol $PbBr_2$ were dissolved in 10 mL of dimethyl sulfoxide (DMSO, 99.9%, Sigma-Aldrich) under stirring for 24 h at RT. The reaction mixture was then left at 40 °C and the orange crystals, which grew in the vial after 4 days, were separated from the mother liquid, washed with ethanol and dried at RT. Yellow crystals of Cs_4PbBr_6 were prepared in the same procedure but the reaction mixture contained 2 mmol of $PbBr_2$ and 10 mmol of CsBr.

The powder X-ray diffraction patterns of the obtained crystals are in good agreement with the calculated ones based on single-crystal diffraction data (Fig. S1, ESI†), confirming the purity of the bulk sample.

2.2. Powder X-ray diffraction

Powder X-ray diffraction (PXRD) patterns of the ground crystals were measured in the reflection modes using an X'Pert PRO X-ray diffraction system equipped with a PIXcel ultrafast line detector and Soller slits for $CuK\alpha_1$ radiation (λ = 1.54056 Å).

2.3. Single-crystal X-ray diffraction

The single-crystal X-ray diffraction experiments were conducted using a conventional Xcalibur four-circle diffractometer from Oxford Diffraction. The experiments utilized Mo $K_{\alpha1\alpha2}$ radiation and a CCD (Atlas) camera. The empirical absorption correction using spherical harmonics was done in the SCALE3 ABSPACK scaling algorithm implemented in CrysAlis PRO 1.171.39.46 (Rigaku Oxford Diffraction, 2018). For solving and refining the structures, the ShelxT and ShelXL were employed, respectively.[37,38] Hydrogen atoms were introduced at calculated positions and refined as riding atoms. The measurements were conducted both at RT (295 K) and 100 K, and no symmetry changes were observed, confirming the temperature stability of new materials. The details on the measured samples and refinement are shown in ESI, Table S1.† Pb–X distances are given in Table S2,† whereas Table S3† shows the geometry of possible hydrogen-bond interactions. Fig. S2† presents the temperature evolution of lattice parameters and unit cell volume in $Cs_2MHy_2PbBr_6$, which confirms the stability of the RT structure at low-temperatures. The refinements show the regions of negative electron density with the highest of -2.54 e A^{-3} at 0.65 Å from Cs^+ in $Cs_2MHy_2PbI_6$, which may denote the presence of MHy^+ also at Cs^+ sites. CCDC deposition numbers: 2269853–2269855.†

2.4. Raman spectroscopy

The RT Raman spectra of powdered crystals in the 3500–100 cm^{-1} range were recorded using a Bruker FT 100/S spectrometer with YAG:Nd laser excitation (λ_{exc} = 1064 nm) and 2 cm^{-1} spectral resolution. Additional low-wavenumber

Raman spectra in the 500–10 cm^{-1} range were measured using a Renishaw inVia Raman spectrometer (Renishaw, UK), equipped with a confocal DM2500 Leica optical microscope, a thermoelectrically cooled CCD as a detector, an eclipse filter and a diode laser operating at 830 nm.

2.5. Optical absorption and photoluminescence (PL) studies

The RT diffuse reflectance spectra of the powdered samples were recorded using a Varian Cary 5E UV–Vis–NIR spectrophotometer (Varian, Palo Alto, CA, USA). Temperature-dependent emission spectra were recorded under 266 nm excitation from a laser diode and with a Hamamatsu PMA-12 photonic multichannel analyser, equipped with a BT-CCD linear image sensor (Hamamatsu Photonics, Iwata, Japan). The temperature of the samples was controlled using a Linkam THMS 600 heating/freezing stage (Linkam, Tadworth, UK). To record decay times, a femtosecond laser (Coherent Model Libra) (Coherent, Pennsylvania, USA) was used as an excitation source.

3. Results and discussion

3.1 Single-crystal X-ray diffraction

The crystal structure of ternary lead halides of the Cs_4PbX_6 formula, where X = Cl, Br, or I was initially reported by C. K. N. Moller,[39] and subsequently confirmed by R. H. Andrews *et al.*[40] and K. Nitsch *et al.*[41] These compounds exhibit a rhombohedral crystal structure belonging to the $R\bar{3}c$ space group (no. 167). The Pb and halogen atoms form slightly distorted PbX_6^{4-} octahedra, which are isolated (0D). Notably, the Pb–X distances in Cs_4PbX_6 are longer compared to those observed in the 3D $CsPbX_3$ structures. Recent synchrotron and X-ray diffraction experiments, along with Raman and PL spectroscopy conducted on Cs_4PbBr_6, confirmed the rhombohedral packing under normal conditions.[27] These experiments also revealed high-pressure phase transition occurring at P = 2.9 GPa to an orthorhombic crystal structure belonging to the *Cmce* space group. This orthorhombic phase remains stable within the pressure range of 2.9 to 4.2 GPa. Above the triclinic symmetry is thermodynamically favoured. It is worth noting that octahedral coordination is only slightly disturbed by I to II high-pressure phase transition.

$Cs_2MHy_2PbX_6$ compounds, where X = Br and I, adopt crystal structures analogous to ternary Cs_4PbX_6. However, the symmetry of these hybrid crystals is related to the high-pressure modification of Cs_4PbBr_6. The presence of larger and highly anisotropic counterions in the crystal structure creates internal pressure on the inorganic component, leading to the octahedral distortions of *Cmce* symmetry. Until now, there have been no reports on the discrete 0D structures of MHy-based metal-halide hybrids.

The crystal packing of $Cs_2MHy_2PbX_6$ is shown in Fig. 1. The characteristic feature is the layered arrangement of the structure components. The MHy^+ selectively substitute for Cs^+ ions forming hydrogen bonded (HB) layers interacting *via* N–H⋯X bonds with the inorganic part. In $Cs_2MHy_2PbBr_6$ the presence of the organic component significantly changes the a and c unit cell parameters, which expands from a = 13.2887(20) Å, b = 12.6058(20) Å, and c = 9.5105(20) Å in all-inorganic Cs_4PbBr_6,[27] to a = 14.280(4) Å, b = 12.876(4) Å, and c = 10.772 (4) Å in the hybrid.

The inherent property of the crystal structure of $Cs_2MHy_2PbX_6$ is the disorder of MHy^+ cations. It is present both at 295 K and 100 K, has statistical character and results in two equivalent positions of MHy^+ related by the mirror m plane, which makes terminal CH_3 and NH_2 groups undistinguishable. The selective substitution of halide ions in $Cs_2MHy_2PbI_3Br_3$ mixed crystals is also worth noting where the positions of ions acting as HB acceptors are preferentially occupied by Br^-. The best refinement results were obtained for the model with full occupancy of Br^- at interacting sites, and mixed occupancy of non-interacting sites with 0.75 and 0.25 of I and Br, respectively. The Pb–Br bond lengths also seem to positively verify this model, as in $Cs_2MHy_2PbBr_6$ as well as in the mixed-halide $Cs_2MHy_2PbI_3Br_3$ the Pb–Br distances to Br^- interacting with MHy^+ are roughly the same (3.011 *vs.* 3.037 Å). Additionally, this preferential substitution leads to a significantly larger octahedral distortion parameter in mixed crystals as it grows from 0.12×10^{-5} and 1.1×10^{-5} in $PbBr_6^{4-}$ and PbI_6^{4-}, respectively, to 29.9×10^{-5} in $[PbBr_3I_3]^{4-}$. Fig. 2 shows the HB layers, disordered MHy^+ positions and illustrates the preferential location of halogen Br^- and I^- ions in mixed $Cs_2MHy_2PbI_3Br_3$.

3.2. Raman study

Raman spectra of $Cs_2MHy_2PbX_6$ and Cs_4PbBr_6 samples are shown in Fig. 3 and S3, S4,† and the observed modes are listed in Tables S4 and S5† together with the assignment based on previous studies of MHy-based 3D, 2D and 1D lead halide perovskites and all-inorganic Cs_4PbBr_6.[6,27,42–45] Fig. 3 and S3, and Table S4† show that bands related to vibrations of the CH_3 groups are observed at very similar wavenumbers as previously reported for 3D, 2D and 1D analogues whereas bands related to vibrations of the NH_2 and NH_2^+ groups are much more sen-

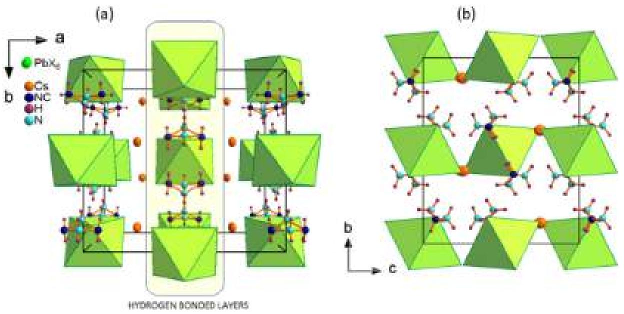

Fig. 1 The crystal structures of $Cs_2MHy_2PbX_6$ and MHy^+ are disordered. (a) Discrete (0D) Pb $(Br/I)_6$ units interact through HBs with MHy^+ cations forming HB layers perpendicular to the a direction, coulombic interactions between caesium ions and $Pb(Br/I)_6$ units stabilize the structure perpendicular to the layers. (b) The view along the a direction.

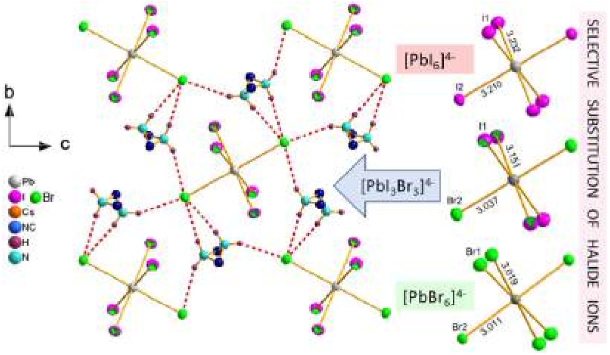

Fig. 2 The N–H⋯Br HB network in $Cs_2MHy_2Pb(Br/I)_6$. In each $Pb(Br/I)_6$ there are two sites for halogen ions interacting with middle-chain NH_2^+ groups. In $Cs_2MHy_2PbI_3Br_3$ they are preferentially occupied by Br^-.

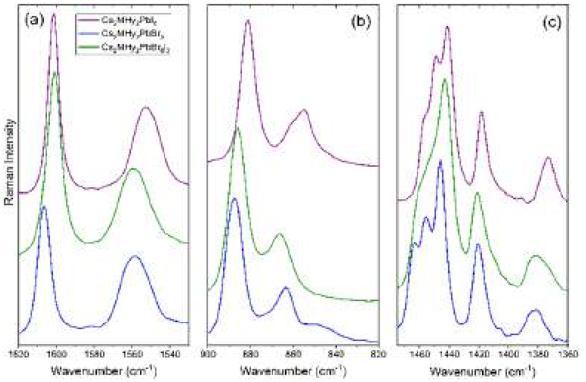

Fig. 3 Raman spectra of $Cs_2MHy_2PbX_6$ compounds in the (a) 1620–1530 cm^{-1}, (b) 900–820 cm^{-1} and (c) 1475–1360 cm^{-1} wavenumber range showing behaviour of NH_2^+-related modes (bands near 1560, 860 and 1360 cm^{-1}), the NH_2-related mode (band near 1600 cm^{-1}), CH_3-related modes (bands in the 1463–1418 cm^{-1} range) and the ν_s(CNN) mode near 890 cm^{-1}.

sitive on the crystal structure. For instance, the $\nu_s(NH_2)$ mode of the terminal NH_2 group exhibits shift to a lower wavenumber when going from 2D MHy_2PbBr_4 (3247 cm^{-1}) to 0D $Cs_2MHy_2PbBr_6$ (3236 cm^{-1}), 1D $MHyPbI_3$ (3217 cm^{-1}) and 3D $MHyPbBr_3$ (3217 cm^{-1}) (Table S4†). This shift indicates that the strength of the HB between the halogen anion and the NH_2 group increases in the order 2D < 0D < 1D < 3D. In general, the strong sensitivity of the NH_2 and NH_2^+ modes on the type of crystal structure points to significantly different HB networks in these compounds.

Former temperature-dependent studies of MHy-based perovskites showed that the disorder of MHy^+ cations is reflected in the spectra by broadening of Raman bands, especially pronounced for those related to the NH_2^+ and NH_2 groups.[6,42,43,46,47] These bands are narrow for $Cs_2MHy_2PbX_6$ analogues, *i.e.*, their widths are comparable to Raman widths of well-ordered $MHyPbBr_3$ and $MHyPbI_3$. For instance, the full width at half maximum (FWHM) of the $\rho(NH_2^+)$ mode is about 11.3 cm^{-1} for $Cs_2MHy_2PbBr6_6$, 10.6 cm^{-1} for $MHyPbBr_3$ and 7.5 cm^{-1} for $MHyPbI_3$. Narrow Raman bands confirm that the disorder revealed by X-ray diffraction is not dynamic but static.

Raman spectra of $Cs_2MHy_2PbX_6$ compounds in the internal mode region are very similar (Fig. 3 and S3†), confirming the same crystal structure. Replacement of Br^- by I^- leads to a weak shift of Raman bands to lower wavenumbers (Table S4†) due to a larger size of the latter anion. In case of the mixed halide compound, $Cs_2MHy_2PbBr_3I_3$, a clear shift to lower wavenumbers compared to $Cs_2MHy_2PbBr_6$ is observed for bands related to vibrations of the CH_3 and terminal NH_2 groups (Table S4, Fig. S3† and Fig. 3). Positions of bands related to the middle NH_2^+ groups are, however, close to those observed for pure bromide (Table S4,† Fig. 3 and S3†). Raman spectra confirm, therefore, the X-ray diffraction model with preferential occupation by Br^- at the sites interacting *via* HBs with the NH_2^+ groups. Closer inspection of the Raman spectra also shows that some bands become broader and less resolved for the mixed-halide compound. This behaviour, observed for instance for the $\delta_{as}(CH_3)$ bands in the 1463–1441 cm^{-1} (Fig. 3c), reflects compositional disorder at sites occupied by both Br^- and I^-.

A comparison of low-wavenumber Raman spectra shows that the majority of modes exhibit large shifts to lower wavenumbers when Br^- is replaced by I^-. This behaviour is related to a larger size and atomic mass of I^- compared to Br^-. Raman modes of all-inorganic Cs_4PbBr_6 show weak shifts to higher wavenumbers when compared to $Cs_2MHy_2PbBr_6$. This effect can be attributed to the smaller unit-cell size of the former compound. It is worth noting that the bands of Cs_4PbBr_6 are narrower than the corresponding bands of $Cs_2MHy_2PbBr_6$. This behaviour is consistent with more pronounced dynamics of MHy^+ compared to Cs^+.

3.3. Optical properties

The RT diffuse absorption spectra of the investigated samples consist of two bands positioned in the UV region (Fig. 4). The lower energy and less intense band is observed at 332 nm (3.73 eV), 372 nm (3.33 eV) and 395 nm (3.14 eV) for $Cs_2MHy_2PbBr_6$, $Cs_2MHy_2PbBr_3I_3$, and $Cs_2MHy_2PbI_6$, respectively. The second higher energy and more intense band appeared at 305 nm (4.07 eV), 331 nm (3.75 eV) and 357 nm (3.47 eV) for $Cs_2MHy_2PbBr_6$, $Cs_2MHy_2PbBr_3I_3$, and $Cs_2MHy_2PbI_6$, respectively. This band is broadened for the mixed-halide $Cs_2MHy_2PbBr_3I_3$. The spectrum of all-inorganic Cs_4PbBr_6 also shows two bands at 329 nm (3.77 eV) and 307 nm (4.04 eV), *i.e.*, this spectrum is very similar to the spectrum of $Cs_2MHy_2PbBr_6$. Very similar two bands were previously reported by other authors for samples prepared from single crystals by grinding,[48,49] but studies of nanocrystalline and thin films usually showed the presence of only one band at 284 nm (4.37 eV) for Cs_4PbCl_6, 310–314 nm (3.95–3.99 eV) for Cs_4PbBr_6, and 365–367 nm (3.38–3.4 eV) for Cs_4PbI_6.[26,50,51] Based on literature data and DFT calculations performed for Cs_4PbBr_6,[48,50] the observed absorption bands can be attributed to the localized absorption from the isolated PbX_6 octahedra. DFT calculations proved that the localized density of states (DOS) corresponding to these bands is mainly composed of Br-

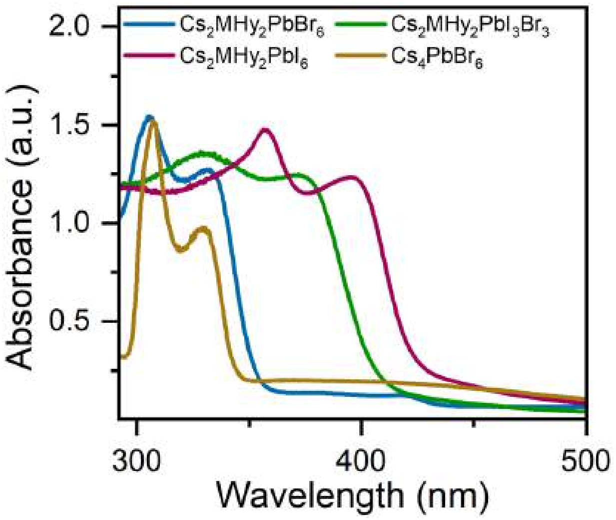

Fig. 4 The 300 K diffuse absorption spectra of the investigated perovskites.

4p and Pb-6s orbitals whereas Cs orbitals almost have no contribution to the DOS near the valence band and conduction band.[48,50] In general, the absorption bands of 0D halides are observed in narrow ranges, *i.e.*, 367–395 nm (3.14–3.47 eV), 305–348 nm (3.56–4.07 eV) and 284–348 nm (3.56–4.37 eV) for the iodides, bromides and chlorides, respectively (Table S6†).

The PL excitation (PLE) and emission (PL) spectra of the synthesized hybrid crystals recorded at 80 K are shown in Fig. 5a. As can be seen, PL spectra consist of one broad band centred at 637 nm and 647 nm with FWHM values of 158 and 175 nm for $Cs_2MHy_2PbI_6$ and $Cs_2MHy_2PbBr_6$, respectively (Table S6†). The emission of the mixed-halide compound is much broader with an FWHM of 230 nm and is red-shifted to 680 nm. This behaviour can be attributed to significantly larger octahedral distortion in $Cs_2MHy_2PbBr_3I_3$, as revealed by the X-ray diffraction study. The large Stokes shift and broad emission are characteristic of STE emission.[52,53] The excitation spectra monitored at the maximum of the emission contain three bands located in the 300–450 nm spectral range and indicate the presence of additional states below the bottom of the conduction band (Fig. 5a). The emission-wavelength-dependent PL excitation spectra of the representative $Cs_2MHy_2PbBr_6$ sample exhibit various profiles at different monitored wavelengths (Fig. S5†). This confirms the presence of more than one PL centre, which could be assigned to STE emission. Similar broadband and strongly Stokes shifted emissions have been reported for many low-dimensional lead halide perovskites,[19,20,44,52,54–56] including 0D.[29–36,53,57] Table S6† shows that $Cs_2MHy_2PbBr_6$ and $Cs_2MHy_2PbBr_3I_3$ exhibit a record large Stokes shift among 0D lead halides.

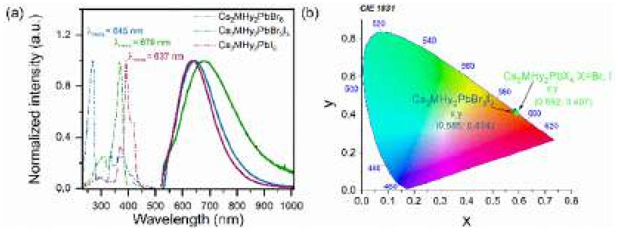

Fig. 5 (a) Low temperature (80 K) PLE (dashed) and PL spectra (solid) and (b) CIE coordinates of $Cs_2MHy_2PbX_6$ (X = Br, I) and $Cs_2MHy_2Br_3I_3$ crystals.

To confirm the origin of the PL bands, we have also performed time-resolved measurements at 80 K under a 266 nm excitation line generated with a femtosecond laser. It can be seen that the registered decay curves were non-exponential with faster (around 0.33 μs) and longer components. The longest lifetime of 1.16 μs is observed for the Br-analogue and it decreases to 0.87 μs and 0.79 μs for $Cs_2MHy_2PbBr_3I_3$ and $Cs_2MHy_2PbI_6$, respectively (Fig. S6†). A longer lifetime of 7.79 μs is observed for all-inorganic Cs_4PbBr_6 (Fig. S7†). The obtained lifetimes are much longer than the values reported for the HOMO–LUMO electronic transitions of the organic cation, proving that the observed emission comes from trapped states.[6,46] Similarly long lifetimes of 5.8 and 16.4 μs were, however, reported for 0D *N*-benzylpyridinium$_6$$Pb_3Br_{12}$ and $(C_{13}H_{19}N_4)_2PbBr_4$.[33,34]

It is worth noting that in spite of very similar crystal structures of $Cs_2MHy_2PbBr_6$ and all-inorganic Cs_4PbBr_6, the latter compound shows significantly different emissions. As can be seen in Fig. S8,† the PL of Cs_4PbBr_6 is narrow (FWHM = 9 nm) and centred at 531 nm. Furthermore, the band at 531 nm corresponds well to the 530 nm band of $CsPbBr_3$. Our results are, therefore, consistent with the assignment of Cs_4PbBr_6 PL to $CsPbBr_3$ inclusions and lack of efficient emission from the Cs_4PbBr_6 matrix.[27] They also show that partial replacement of Cs^+ by organic cations (*e.g.*, MHy^+) is an effective way to induce efficient broadband PL in these perovskites. Based on the PL spectra, the CIE coordinates of $Cs_2MHy_2PbX_6$ (X = Br, I) and $Cs_2MHy_2PbBr_3I_3$ crystals were calculated and are shown in Fig. 5b. The calculated values are characteristic of the orange-yellow emission.

The emission intensity of all investigated lead halides strongly depends on temperature (Fig. 6). The position and shape of the emission bands do not change upon heating. However, the emission intensity significantly decreases with an increase in temperature with $T_{0.5}$ = 105 K. To estimate the activation energies of thermal quenching, the Arrhenius equation was used (Fig. S9–S11†):

$$I(T) = \frac{I_0}{1 + c \cdot \exp\left(\frac{-E_a}{k_b T}\right)} \tag{1}$$

where I_0 is the initial intensity of luminescence (80 K), $I(T)$ is the intensity at a given temperature T, c is a constant value, E_a is the activation energy of thermal quenching, and k is Boltzmann's constant. The emission of $Cs_2MHy_2PbBr_3I_3$ is less stable with an E_a value of 51 meV, while the emissions of the iodide and bromide analogues are more stable with E_a values of 57 meV and 65 meV, respectively. These values are similar

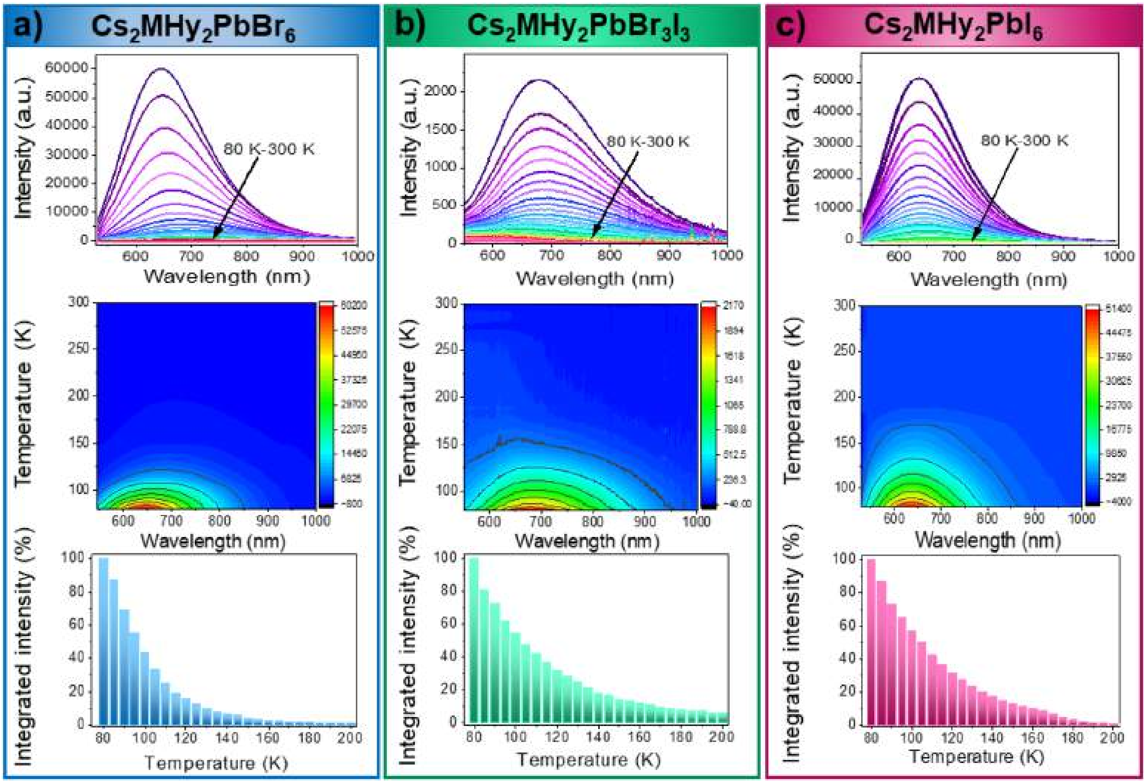

Fig. 6 Temperature-dependent emission spectra recorded from 80 to 300 K, the PL intensity contour map, and the integrated emission intensity at various temperatures of (a) $Cs_2MHy_2PbBr_6$, (b) $Cs_2MHy_2PbBr_3I_3$, and (c) $Cs_2MHy_2PbI_6$, respectively.

to that reported for 3D $MHyPbBr_3$ (63 meV),[6] smaller than that of 2D MHy_2PbBr_4 (99.9 meV)[16] and significantly larger than that of 0D $(TAE)_2[Pb_2Cl_{10}]Cl_2$ (5 meV).[30]

4. Conclusions

For the first time, a mixed-cation approach has been successfully employed to synthesize three newcomers to the small family of 0D lead halides. The obtained $Cs_2MHy_2PbBr_6$, $Cs_2MHy_2PbBr_3I_3$, and $Cs_2MHy_2PbI_6$ isostructural compounds crystallize in orthorhombic structures (space group *Cmce*). The structures are built up of isolated PbX_6^{4-} octahedral units. The characteristic feature of these structures, not reported for other MHy-based perovskites, is the static disorder of MHy^+ cations, which form HBs with halide anions. X-ray diffraction also reveals that in the mixed halide analogue, $Cs_2MHy_2PbI_3Br_3$, Br^- (I^-) anions preferentially occupy the sites acting (non-acting) as HB acceptors. This preferential substitution leads to a significantly larger octahedral distortion parameter in $Cs_2MHy_2PbBr_3I_3$ crystals.

Raman studies show that the HB strength in the discovered 0D lead halides is stronger than in 2D MHy_2PbBr_4 but weaker than in 1D $MHyPbI_3$ and 3D $MHyPbBr_3$. Raman data also confirm the preferential occupation of anionic sites by Br^- and I^- in the mixed-halide analogue as well as the static character of MHy^+ disorder in all compounds.

Linear optical studies demonstrate that $Cs_2MHy_2PbBr_6$ and $Cs_2MHy_2PbI_6$ exhibit broadband orange-yellow PL with maxima (FWHM) at 637 (158) and 647 nm (175 nm), respectively, and vast Stokes shifts of 342 and 280 nm for $Cs_2MHy_2PbBr_6$ and $Cs_2MHy_2PbI_6$, respectively. To the best of our knowledge, $Cs_2MHy_2PbI_6$ is the first 0D iodide for which PL was reported. Much larger octahedral distortion in mixed-cation $Cs_2MHy_2PbBr_3I_3$ manifests a red-shift of PL to 680 nm and an increase of FWHM to 230 nm. For this compound, the Stokes shift is 349 nm. The observed Stokes shifts for $Cs_2MHy_2PbBr_6$ and $Cs_2MHy_2PbBr_3I_3$ are record large among the family of 0D lead halides. The PL of $Cs_2MHy_2PbX_6$ compounds shows strong temperature dependence and analysis of these data reveals that the activation energies required for thermal quenching are 51, 57 and 65 meV for $Cs_2MHy_2PbBr_3I_3$, $Cs_2MHy_2PbI_6$ and $Cs_2MHy_2PbBr_6$, respectively.

Overall, our results demonstrate that the mixed-cation approach is a promising way to develop novel 0D lead halides with efficient broadband PL. They also show that MHy^+ cations have unusual ability to form lead halides of vast structural diversity and properties, *i.e.*, 3D ($MhyPbX_3$, X = Cl, Br)[6–8] and quasi-2D RP ($BA_2MHy_2Pb_3Br_{10}$, BA^+ = butylammonium)[58] with MHy^+ serving as a 'perovskitizer' cation, 2D of formula MHy_2PbX_4 (X = Cl, Br, I)[16,46,47] and the 2D ACI phase ($IMMHyPbX_4$, X = Cl, Br, IM = imidazolium)[22] with MHy^+ as a 'spacer' cation and 1D ($MHyPbI_3$)[45] and 0D (this work), in which MHy^+ cations separate inorganic chains or PbX_6^{4-} octahedra.

Author contributions

Conceptualization: M. M. Data curation: D. D., D. S. and A. G. Formal analysis: D. D., D. S. and A. G. Funding acquisition: M. M. Investigation: D. D., D. S. and A. G. Methodology: all authors. Project administration: M. M. Resources: M. M. Supervision: M. M. Validation: D. D., D. S. and A. G. Writing – original draft: all authors. Writing – review and editing: all authors. All the authors have given their approval to the final version of the manuscript.

Conflicts of interest

There are no conflicts to declare.

Acknowledgements

This research was supported by the National Science Center (Narodowe Centrum Nauki) in Poland under project no. 2019/35/B/ST5/00043.

References

1 Y. Tu, J. Wu, G. Xu, X. Yang, R. Cai, Q. Gong, R. Zhu and W. Huang, Perovskite Solar Cells for Space Applications: Progress and Challenges, *Adv. Mater.*, 2021, **33**, 2006545.

2 T. Yang, L. Gao, J. Lu, C. Ma, Y. Du, P. Wang, Z. Ding, S. Wang, P. Xu, D. Liu, *et al.*, One-Stone-for-Two-Birds Strategy to Attain Beyond 25% Perovskite Solar Cells, *Nat. Commun.*, 2023, **14**, 839.

3 Y. Zhou, Y. Huang, Z. Fan, J. B. Khurgin and Q. Xiong, Nonlinear Optical Properties of Halide Perovskites and Their Applications, *Appl. Phys. Rev.*, 2020, 041313.

4 H. Liu, H. Zhang, H. Xu and L. Zhang, The Opto-Electronic Functional Devices Based on Three-Dimensional Lead Halide Perovskite, *Appl. Sci.*, 2021, **11**, 1453.

5 W. Chen, S. Bhaumik, S. A. Veldhuis, G. Xing, Q. Xu, M. Grätzel, S. Mhaisalkar, N. Mathews and T. C. Sum, Giant Five-Photon Absorption from Multidimensional Core-shell Halide Perovskite Colloidal Nanocrystals, *Nat. Commun.*, 2017, **8**, 15198.

6 M. Mączka, M. Ptak, A. Gągor, D. Stefańska, J. K. Zaręba and A. Sieradzki, Methylhydrazinium Lead Bromide: Noncentrosymmetric Three-Dimensional Perovskite with Exceptionally Large Framework Distortion and Green Photoluminescence, *Chem. Mater.*, 2020, **32**, 1667–1673.

7 M. Mączka, A. Gągor, J. K. Zaręba, D. Stefańska, M. Drozd, S. Balciunas, M. Simenas, J. Banys and A. Sieradzki, Three-Dimensional Perovskite Methylhydrazinium Lead Chloride with Two Polar Phases and Unusual Second-Harmonic Generation Bistability above Room Temperature, *Chem. Mater.*, 2020, **32**, 4072–4082.

8 D. Drozdowski, A. Gągor, D. Stefańska, J. K. Zaręba, K. Fedoruk, M. Mączka and A. Sieradzki, Three-Dimensional Methylhydrazinium Lead Halide Perovskites: Structural Changes and Effects on Dielectric, Linear, and Nonlinear Optical Properties Entailed by the Halide Tuning, *J. Phys. Chem. C*, 2022, **126**, 1600–1610.

9 H. R. Petrosova, O. I. Kucheriv, S. Shova and I. A. Gural'skiy, Aziridinium Cation Templating 3D Lead Halide Hybrid Perovskites, *Chem. Commun.*, 2022, **58**, 5745–5748.

10 D. Stefańska, M. Ptak and M. Mączka, Photoluminescence and Vibrational Properties of Aziridinium Lead Halide Perovskites, *Molecules*, 2022, **27**, 7949.

11 O. A. Semenikhin, O. I. Kucheriv, L. Sacarescu, S. Shova and I. A. Gural'skiy, Aziridinium Cation Templating 3D Lead Halide Hybrid Perovskites, *Chem. Commun.*, 2023, **59**, 3566–3569.

12 T. Niu, Q. Xue and H. L. Yip, Advances in Dion-Jacobson Phase Two-Dimensional Metal Halide Perovskite Solar Cells, *Nanophotonics*, 2021, **10**, 2069–2102.

13 S. Sun, M. Lu, X. Gao, Z. Shi, X. Bai, W. W. Yu and Y. Zhang, 0D Perovskites: Unique Properties, Synthesis, and Their Applications, *Adv. Sci.*, 2021, **8**, 2102689.

14 Y. Han, S. Yue and B. B. Cui, Low-Dimensional Metal Halide Perovskite Crystal Materials: Structure Strategies and Luminescence Applications, *Adv. Sci.*, 2021, **8**, 2004805.

15 X. Han, Y. Zheng, S. Chai, S. Chen and J. Xu, 2D Organic-Inorganic Hybrid Perovskite Materials for Nonlinear Optics, *Nanophotonics*, 2020, **9**, 1787–1810.

16 M. Mączka, J. K. Zaręba, A. Gągor, D. Stefańska, M. Ptak, K. Rolder, D. Kajewski, A. Soszyński, K. Fedoruk and A. Sieradzki, [Methylhydrazinium]$_2$PbBr$_4$, a Ferroelectric Hybrid Organic-Inorganic Perovskite with Multiple Nonlinear Optical Outputs, *Chem. Mater.*, 2021, **33**, 2331–2342.

17 M. M. Lun, F. L. Zhou, D. W. Fu and Q. Ye, Multi-functional Hybrid Perovskites with Triple-Channel Switches and Optical Properties, *J. Mater. Chem. C*, 2022, **10**, 11371–11378.

18 P. Siwach, P. Sikarwar, J. S. Halpati and A. K. Chandiran, Design of Above-Room-Temperature Ferroelectric Two-Dimensional Layered Halide Perovskites, *J. Mater. Chem. A*, 2022, **10**, 8719–8738.

19 M. D. Smith, B. A. Connor and H. I. Karunadasa, Tuning the Luminescence of layered Halide Perovskites, *Chem. Rev.*, 2019, **119**, 3104–3139.

20 S. Smółka, M. Mączka, D. Drozdowski, D. Stefańska, A. Gągor, A. Sieradzki, J. K. Zaręba and M. Ptak, Effect of Dimensionality on Photoluminescence and Dielectric Properties of Imidazolium Lead Bromides, *Inorg. Chem.*, 2022, **61**, 15225–15238.

21 S. Shao, X. Cui and Z. Li, Recent Progress in Understanding the Structural, Optoelectronic, and Photophysical Properties of Lead Based Dion-Jacobson Perovskites as Well

as Their Application in Solar Cells, *ACS Mater. Lett.*, 2022, **4**, 891–917.

22 D. Drozdowski, K. Fedoruk, A. Kabanski, M. Maczka, A. Sieradzki and A. Gagor, Broadband Yellow And White Emission from Large Octahedral Tilting in (110)-Oriented Layered Perovskites: Imidazolium-Methylhydrazinium Lead Halides, *J. Mater. Chem. C*, 2023, **11**, 4907.

23 M. Li and Z. Xia, Recent Progress of Zero-Dimensional Luminescence Metal Halides, *Chem. Soc. Rev.*, 2021, **50**, 2626–2662.

24 T. Bai, X. Wang, Y. He, H. Wei, Y. Su and J. Chen, Turning Self-Trapped Exciton Emission to Near-Infrared Regionin Thermochromism Zero-Dimensional Hybrid Metal Halides, *Adv. Opt. Mater.*, 2023, 2301110.

25 A. A. Akkerman, A. L. Abdelhady and L. Manna, Zero-Dimensional Cesium Lead Halides: History, Properties, and Challenges, *J. Phys. Chem. Lett.*, 2018, **9**, 2326–2337.

26 U. Thumu, M. Piotrowski, B. Owens-Baird and Y. V. Kolen'ko, Zero-Dimensional Cesium Lead Halide Perovskites: Phase Transformations, Hybrid Structures, and Applications, *J. Solid State Chem.*, 2019, **271**, 361–377.

27 W. Castro Ferreira, B. S. Araujo, M. A. P. Gomez, F. E. O. Medeiros, C. W. de Araujo Paschoal, C. B. da Silva, P. T. C. Freire, U. F. Kaneko, F. M. Ardito, N. M. Souza-Neto and A. P. Ayala, Pressure-Induced Structural and Optical Transitions in Luminescent Bulk Cs_4PbBr_6, *J. Phys. Chem. C*, 2022, **126**, 541–550.

28 B. R. Vincent, K. N. Robertson, T. Stanley Cameron and O. Knop, Alkylammonium lead iodides. Part 1. Isolated PbI_6^{4-} ions in $(CH_3NH_3)_4PbI_6 \cdot H_2O$, *Can. J. Chem.*, 1987, **65**, 1042–1046.

29 C. Zhou, H. Lin, M. Worku, J. Neu, Y. Zhou, Y. Tian, S. Lee, P. Djurovich, T. Siegrist and B. Ma, Blue Emitting Single Crystalline Assembly of Metal Halide Clusters, *J. Am. Chem. Soc.*, 2018, **140**, 13181–13184.

30 S. Elleuch, A. Lusson, S. Pillet, K. Boukheddaden and Y. Abid, White Light Emission from a Zero-Dimensional Lead Chloride YHybrid Material, *ACS Photonics*, 2020, **7**, 1178–1197.

31 B. B. Cui, Y. Han, B. Huang, Y. Zhao, X. Wu, L. Liu, G. Cao, Q. Du, N. Liu, W. Zou, M. Sun, L. Wang, X. Liu, J. Wang, H. Zhou and Q. Chen, Locally Collective Hydrogen Bonding Isolates Lead Octahedra for White Emission Improvement, *Nat. Commun.*, 2019, **10**, 5190.

32 V. Morad, Y. Shynkarenko, S. Yakunin, A. Brumberg, R. D. Schaller and M. V. Kovalenko, Disphenoidal Zero-Dimensional Lead, Thin and Germanium Halides: Highly Emissive Singlet and Triplet Self-Trapped Excitons and X-ray Scintillation, *J. Am. Chem. Soc.*, 2019, **141**, 9764–9768.

33 H. Lin, C. Zhou, M. Chaaban, L. J. Xu, Y. Zhou, J. Neu, M. Worku, E. Berkwits, Q. He, S. Lee, X. Lin, T. Siegrists, M. H. Du and B. Ma, Bulk Assembly of Zero-Dimensional Organic Lead Bromide Hybrid with Efficient Blue Emission, *ACS Mater. Lett.*, 2019, **1**, 594–598.

34 B. Febriansyah, C. S. D. Neo, D. Giovanni, S. Srivastava, Y. Lekina, T. M. Koh, Y. Li, Z. X. Shen, M. Asta, T. C. Sum, N. Mathews and J. England, Targeted Synthesis of Trimeric Organic-Bromoplumbate Hybrids That Display Intrinsic Highly Stokes-Shifted, Broadband Emission, *Chem. Mater.*, 2020, **32**, 4431–4441.

35 D. Tian, Z. Lai, H. Xu, F. Lin, Y. Jiang, Y. Huang, S. Wang, Y. Cai, J. Jin, R. J. Xie and X. Chen, Low-Dimensional Organic Lead Halides with Organic-Inorganic Collaborative Luminescence Regulated by Anion in Dimension, *Chem. Mater.*, 2022, **34**, 5224–5231.

36 Y. Takeoka, K. Asai, M. Rikukawa and K. Sanui, Hydrothermal Synthesis and Structure of Zero-Dimensional Organic-Inorganic Perovskites, *Chem. Lett.*, 2005, **34**, 602–603.

37 G. M. Sheldrick, SHELXT - Integrated Space-Group and Crystal-Structure Determination, *Acta Crystallogr., Sect. A: Found. Adv.*, 2015, **71**, 3–8.

38 G. M. Sheldrick, Crystal Structure Refinement with SHELXL, *Acta Crystallogr., Sect. C: Struct. Chem.*, 2015, **71**, 3–8.

39 C. K. N. Moller, On the structure of caesium hexahalogeno-plumbates(II), *Mat. Fys. Medd. Dan. Vid. Selsk.*, 1960, **32**, 1–13.

40 R. H. Andrews, S. J. Clark, J. D. Donaldson, J. C. Dewan and J. Silver, Solid-State Properties of Materials of the Type Cs_4MX_6 (where M = Sn or Pb and X=Cl or Br), *J. Chem. Soc., Dalton Trans.*, 1983, 767–770.

41 K. Nitsch, M. Dousek, M. Nikl, K. Polak and M. Rodova, Ternary Alkali Lead Chlorides: Crystal Growth, Crystal Structure, Absorption and Emission Properties, *Prog. Cryst. Growth Charact. Mater.*, 1995, **30**, 1–22.

42 M. Mączka, J. Zienkiewicz and M. Ptak, Comparative Studies of Phonon Properties of Three-Dimensional Hybrid Organic–Inorganic Perovskites Comprising Methylhydrazinium, Methylammonium, and Formamidinium Cations, *J. Phys. Chem. C*, 2022, **126**, 4048–4056.

43 M. Mączka and M. Ptak, Lattice Dynamics and Structural Phase Transitions in Two-Dimensional Ferroelectric Methylhydrazinium Lead Bromide Investigated Using Raman and IR Spectroscopy, *J. Phys. Chem. C*, 2022, **126**, 7991–7998.

44 M. Mączka, S. Sobczak, P. Ratajczyk, F. F. Leite, W. Paraguassu, F. Dybała, A. P. Herman, R. Kudrawiec and A. Katrusiak, Pressure-Driven Phase Transition in Two-Dimensional Perovskite MHy_2PbBr_4, *Chem. Mater.*, 2022, **34**, 7867–7877.

45 D. Drozdowski, A. Gągor and M. Mączka, Methylhydrazinium Lead Iodide – One Dimensional Chain Phase with Excitonic Absorption and Large Energy Band Gap, *J. Mol. Struct.*, 2022, **1249**, 131660.

46 M. Mączka, M. Ptak, A. Gagor, D. Stefańska and A. Sieradzki, Layered Lead Iodide of $[Methylhydrazinium]_2PbI_4$ with a Reduced Band Gap: Thermochromic Luminescence and Switchable Dielectric Properties Triggered by Structural Phase Transitions, *Chem. Mater.*, 2019, **31**, 8563–8575.

47 K. Fedoruk, D. Drozdowski, M. Mączka, J. K. Zaręba, D. Stefańska, A. Gągor and A. Sieradzki, [Methylhydrazinium]$_2$PbCl$_4$, a Two-Dimensional Perovskite with Polar and Modulated Phases, *Inorg. Chem.*, 2022, **61**, 15520–15531.

48 Z. Zhang, Y. Zhu, W. Wang, W. Zheng, R. Lin, X. Li, H. Zhang, D. Zhong and F. Huang, Aqueous Solution Growth of Milimiter-Sized Nongreen-Luminescent Wide Bandgap Cs$_4$PbBr$_6$ Bulk Crystal, *Cryst. Growth Des.*, 2018, **18**, 6393–6398.

49 X. Chen, F. Zhang, Y. Ge, L. Shi, S. Huang, J. Tang, Z. Lv, L. Zhang, B. Zou and H. Zhong, Centimeter-Sized Cs$_4$PbBr$_4$ Crystals with Embedded CsPbBr$_3$ Nanocrystals Showing Superior Photoluminescence: Nonstoichiometry Induced Transformation and Light-Emitting Applications, *Adv. Funct. Mater.*, 2018, **28**, 1706567.

50 K. A. Akkerman, S. Park, E. Radicchi, F. Nunzi, E. Mosconi, F. De Angelis, R. Brescia, P. Rastogi, M. Prato and L. Manna, Nearly Monodispersed insulator Cs$_4$PbX$_6$ (X=Cl, Br, I) Nanocrystals, Their Mixed Halide Compositions, and Their Transformation into CsPbX$_3$ Nanocrystals, *Nano Lett.*, 2017, **17**, 1924–1930.

51 O. I. Yunakova, V. K. Miloslavskii and E. N. Kovalenko, Exciton Absorption Spectrum of Thin CsPbI3 and Cs4PbI6 Films, *Opt. Spectrosc.*, 2012, **112**, 91–96.

52 C. Ji, S. Wang, L. Li, Z. Sun, M. Hong and J. Luo, The First 2D Hybrid Perovskite Ferroelectric Showing Broadband White-Light Emission with High Color Rendering Index, *Adv. Funct. Mater.*, 2018, **29**, 1805038.

53 B. A. H. Huisman, F. Palazon and H. J. Bolink, Zero-Dimensional Hybrid Organic-Inorganic Lead Halides and Their Post-Synthesis Reversible Transformation into Three-Dimensional Perovskites, *Inorg. Chem.*, 2021, **60**, 5212–5216.

54 H. Gu, J. Xia, C. Liang, Y. Chen, W. Huang and G. Xing, Phase-Pure Two-Dimensional Layered Perovskite Thin Films, *Nat. Rev. Mater.*, 2023, **8**, 533–551.

55 Z. Zhang, J. F. Liao and G. Xing, Regulating the Coordination Geometry of Polyhedra in Zero-Dimensional Metal Halides for Tunable Emission, *Nanaoscale*, 2023, **15**, 5241–5248.

56 J. F. Liao, Z. Zhang, B. Wang, Z. Tang and G. Xing, Full-Color-Tunable Phosphorescence of Antimony-Doped Lead Halide Single Crystal, *npj Flexible Electron.*, 2022, **6**, 57.

57 S. K. Sharma, C. Phadnis, T. K. Das, A. Kumar, B. Kavaipatti, A. Chowdhury and A. Yella, Reversible Dimensionality Tuning of Hybrid Perovskites with Humidity: Visualisation and Application to Stable Solar Cells, *Chem. Mater.*, 2019, **31**, 3111–3117.

58 X. Li, S. A. Cuthriell, A. Bergonzoni, H. Dong, B. Traore, C. C. Stoumpos, P. Guo, J. Even, C. Katan, R. D. Schaller and M. G. Kanatzidis, Expanding the Cage of 2D Bromide Perovskites by Large A-Site Cations, *Chem. Mater.*, 2022, **34**, 1132–1142.